Doped ceria nanostructures for the oxidation of pollutants: investigations into the role of defect sites

Doctoral Dissertation
Doctoral Program in Chemical Engineering (33rd Cycle)

Doped ceria nanostructures for the oxidation of pollutants: investigations into the role of defect sites

Enrico Sartoretti
* * * * * *

Supervisors
Prof. Samir Bensaid, Supervisor
Prof. Marco Piumetti, Co-Supervisor

Doctoral Examination Committee:
Prof. Agustín Bueno López, Referee, Universidad de Alicante
Prof. Alessandro Trovarelli, Referee, Università degli Studi di Udine

Politecnico di Torino
March 1, 2021

I hereby declare that the contents and organization of this dissertation constitute my own original work and does not compromise in any way the rights of third parties, including those relating to the security of personal data.

…….....

Enrico Sartoretti

Turin, March 1, 2021

Summary

Air pollution is a worldwide phenomenon strictly connected to severe risks to human health. Among the anthropic activities linked to the production of noxious compounds, road transport is one of the most impacting, especially in highly populated urban areas. In order to preserve air quality and the environment, strict regulations in terms of emission limits have been adopted by several nations. As a consequence, most vehicles are today equipped with a complex aftertreatment line in which the pollutants can be converted into harmless substances.

To this end, oxidation catalysts are needed to convert CO and unburned hydrocarbons into CO_2; moreover, proper catalysts can also be deposited inside particulate filters to promote soot oxidation at lower temperature, reducing the fuel consumption and thermal shock during regeneration. Among the attractive alternatives to expensive noble metals, ceria-based materials have exhibited promising oxidative performances. Ceria activity is linked to its unique redox behavior and oxygen storage capacity, but several other factors, such as morphology, reducibility or defectiveness, concur in determining the final catalytic properties. All these features can be tuned by adjusting the synthesis conditions or by doping.

In this thesis, different ceria-based nanostructured catalysts have been examined, with the intent of shedding light on the relevant structural and physico-chemical properties defining the catalytic activity and on the reaction pathways involved. The materials, prepared via hydrothermal synthesis, were extensively characterized and tested following the procedures reported in Chapter 2.

A first set of catalysts was obtained by doping ceria with Cu and Mn. The defect sites formed in ceria structure upon doping were investigated via in situ Raman spectroscopy, monitoring their behavior throughout thermal cycles and during soot oxidation (Chapter 3) and CO oxidation (Chapter 4). Three different types of structural defects were recognized, namely oxygen vacancies, Frenkel interstitial-vacancy pairs and vacancy-free substitutional sites. The defectiveness was correlated with catalytic activity towards CO oxidation, while an increase of vacancy-free sites after soot oxidation suggested that peroxides and superoxides

deactivation can occur on catalysts presenting excessive oxygen vacancy concentration. Hence, Cu-doped ceria was characterized by the best CO oxidation activity, thanks to its high specific surface area, reducibility and amount of defects; however, it featured poor soot oxidation activity; conversely, Mn-doped ceria exhibited the best soot oxidation activity, thanks to an intermediate density of oxygen vacancies and to its well-defined morphology. Spectral evolution also suggested that CO dissociative adsorption may occur at ceria surface. Moreover, oxygen vacancy clusters can form in reducing atmosphere, which could reorganize not only in the presence of O_2 but also upon a temperature decrease, forming isolated vacancies and then evolving into Frenkel and dopant-containing oxidized sites when exposed to oxygen. The extent of this dynamic defect behavior seemed to be correlated with the material reducibility.

In Chapter 5, equimolar ceria-praseodymia was compared to pure CeO_2 in view of the possible application of this mixed oxide in a gasoline particulate filter. The weakening of the Ce – O bonds associated to Pr addition resulted in a high reducibility, promoting the catalytic activity towards CO, VOCs and soot oxidation. Thanks to its ability to release active oxygen, ceria-praseodymia exhibited a greater activity and CO_2-selectivity with respect to pure ceria also at low O_2 concentration, proving to be a promising catalyst for coated filters.

Rare earth-doped ceria samples containing different quantities of La and Nd were also prepared and analyzed in Chapter 6. La and Nd ions were well incorporated in ceria structure, but the final morphology was significantly altered: in fact, doping fostered the formation of smaller nanocubes and elongated particles, resulting in a higher specific surface area. The introduction of trivalent cations was also associated with a higher abundance of defects and oxygen vacancies, but a too high oxygen deficiency detrimentally affected the material reducibility and catalytic activity for CO and NO oxidation. Conversely, soot oxidation generally benefited from La and Nd addition. In particular, the Ce-La equimolar oxide exhibited outstanding performances in all the tested conditions, thanks to its optimal morphology and surface acidity. The presence of NO_x promoted soot oxidation in loose contact while it had detrimental effects in tight contact, giving insights on the active species and reaction mechanisms involved.

In conclusion, CO oxidation is highly promoted by the presence of active oxygen vacancies, like those associated to Cu doping. However, a high density of these sites favors reactive oxygen species deactivation, with detrimental effects in case of a poor catalyst-pollutant contact. Hence, rare earths-doped CeO_2 exhibits better soot oxidation activity thanks to its less dynamic vacancies.

Acknowledgments

First of all, I would like to thank very much prof. Samir Bensaid and prof. Marco Piumetti for guiding my work during the last three years with their invaluable expertise. I would also like to acknowledge prof. Fabrizio Giorgis, prof. Nunzio Russo and prof. Debora Fino for supervising my activities and contributing to the scientific discussions.

A heartfelt thanks goes to Dr. Chiara Novara, for introducing me to Raman spectroscopy and for always being at my side during long experiments, data analysis and interpretation, paper writing, and so on. Thank you for having been not only an expert guide but also a good friend.

I gratefully thank all the people which I collaborated with at Politecnico di Torino during my PhD, especially all the members of CREST research group. I would like to acknowledge prof. Fabio Deorsola and Dr. Camilla Galletti for XRD measurements, Mauro Raimondo for FESEM investigations, Dr. Marco Fontana for TEM analysis and Ing. Salvatore Guastella for XPS measurements. A great thanks to Dr. Tahrizi Andana and Dr. Alessandro Monteverde for their precious help in the lab. A special thanks to my friends Fabio Salomone, for our continuous and fruitful exchange of ideas and for having endured my daily presence for nearly eight years, and Melodj Dosa, for our fantastic collaboration and for always supporting each other, sharing the good times and facing together the difficulties. Thanks also to Fabio Martini, Gabriele Viglianco, Sabrina Ballauri and Elena Valli for everything we learned together working side by side.

Furthermore, thanks to all my friends for their irreplaceable role throughout these years, and especially to Francesca, Elisa and Emanuele for all the happy moments we shared. Finally, the most important acknowledgement goes to all my family, to whom I would like to dedicate this achievement. Thanks for your unconditional support and affection, for constantly putting my needs first, and for encouraging me to always do my best in every situation. None of this would have been possible without you. Thank you!

Contents

List of Tables

List of Figures

Chapter 1

Introduction: background and objectives

1.1 The problem of air pollution: new regulations and possible solutions in the automotive field

Air pollution is the result of the excessive emission of certain substances into the atmosphere, causing changes in the air natural properties that can have harmful effects on the living beings and ecosystems. Atmospheric pollution is one of the most important environmental risks to human health [1] and is therefore an issue which should be urgently addressed [2].

Some air pollutants are produced by natural sources, such as fires or volcanic eruptions, but the main causes of air pollution are linked to anthropogenic activities [1,3]. In particular, energy production, households heating, transports, industrial activities, agriculture and waste treatment are among the most impactful human-related sources of pollution [4,5].

Air contamination is today a worldwide phenomenon, but the most affected regions are the large urban areas [6]. In these densely populated sites the impact of noxious emissions linked to traffic is remarkable and road vehicles constitute the primary source of certain pollutants (e.g. nitrogen oxides) [1,7]. In fact, despite the increasing diffusion of electric cars in the last years, the largest part of new vehicles is still equipped with an internal combustion engine (ICE). An ICE can be fed with different fuels (usually gasoline or diesel, but also natural gas or liquefied petroleum gas are quite commonly used in Europe) which are burned to obtain mechanical energy; however, several toxic substances are produced during the combustion [8], and this is one the main drawbacks of this technology.

1.1.1 Main pollutants emitted by road vehicles

Carbon monoxide (CO)

Carbon monoxide (CO) is a colorless and odorless gas which forms via incomplete combustion of organic substances. CO production is more significant when the combustion occurs in oxygen shortage: higher CO quantities are therefore generated in gasoline engines, since they are fed with a stoichiometric air-fuel mixture.

Carbon monoxide is very toxic when inhaled, since it can combine with hemoglobin, the oxygen-transport protein in our blood, hindering the delivery of oxygen to bodily tissues. Breathing excessive doses of CO hence results in headache, nausea, dizziness, drowsiness and can even lead to death [9,10]. Moreover, also a prolonged exposure to low concentrations of CO, like those in the polluted air of some big metropolises, has been associated with a higher mortality for cardiovascular diseases [11].

Unburned hydrocarbons (HC)

Some unreacted or only partially-burned hydrocarbons are always present in an ICE exhaust gas, since the combustion reaction can never reach a 100% efficiency for different reasons. For instance, the portion of fuel trapped in engine crevices or adsorbed by the lube oil layer cannot react with oxygen; furthermore, the combustion reaction does not occur in a quench layer at combustion chamber walls [12].

Unburned hydrocarbons include many classes of compounds, e.g. methane, benzene, formaldehyde or polycyclic aromatic hydrocarbons (PAHs) [13]; some of these substances are also often referred to as volatile organic compounds (VOCs). While some hydrocarbons are quite harmless, some others can cause irritation of the respiratory tract or have teratogenic, mutagenic or carcinogenic effects [14–16]. Furthermore, these substances (e.g. methane) usually have a high global warming potential (GWP), i.e. they significantly contribute to global warming and climate change. Some VOCs can also foster the photochemical generation of secondary pollutants, such as ozone [17].

Nitrogen oxides (NO_x)

In every combustion process at high temperature in which air is used as oxidizing agent, oxygen and nitrogen can react producing some NO and smaller quantities of NO_2. Three main mechanism of NO_x formation have been identified [18,19]:

- Prompt NO_x form from the reaction between molecular nitrogen and radicals (e.g. CH or CH_2) derived from fuels in the earliest stages of combustion.

- Thermal NO_x form since at temperatures above 1500 °C the O_2 and N_2 molecules can dissociate and participate in a series of radical reactions leading to the formation of NO. The reaction rate increases with the temperature and the residence time of air at that temperature. This is the prevalent mechanism of NO_x production in an ICE.
- Fuel NO_x are the result of the oxidation of nitrogen-containing compounds in the fuel, which are more abundant in heavy oils.

Once in the environment, NO can spontaneously convert to NO_2. The latter gas can react with atmospheric water producing nitric acid, which is a responsible of acid rain [20]. Moreover, NO_x take part, together with VOCs, in a series of reactions catalyzed by the UV rays in sun light, leading to the formation of secondary pollutants such as aldehydes or ozone; this phenomenon is known as photochemical smog [17].

Concerning the effects on human health, NO_2 is a strong irritant: direct exposure to high NO_x concentrations can thereby cause skin and eye irritation, cough and pulmonary edema, which can result in irreversible damages to lungs or even death [21]. Also the prolonged exposure to relatively lower NO_x concentrations, like those found in many cities, is harmful and it has been associated with a higher incidence of respiratory, cardiovascular and neurological diseases and with increased mortality [22–26].

Sulphur oxides (SO_x)

When the fuel contains some sulfur compounds, SO_2 is produced during combustion and it can be easily converted to SO_3 in an oxidizing atmosphere. The latter gas is extremely corrosive, since it can react with water forming sulfuric acid: SO_x are therefore irritating for people [27] and they are the main culprits for acid rain [28]. Moreover, SO_x can foster the deactivation of some catalysts used for exhaust gas aftertreatment [29–31] and the sulfates forming after combustion can increase the mass of the particulate matter [32]. For all these reasons, only few ppm of sulfur are today allowed inside the fuels used for road vehicles (e.g., 10 ppm of sulfur for diesel fuel in the European Union).

Particulate matter (PM)

Particulate matter consists of a complex mixture of different substances in the form of an aerosol of fine particles. It mainly forms in the fuel-rich regions of the combustion chamber, where in oxygen shortage some polycyclic carbon compounds can grow and generate carbonaceous nuclei, known as soot [33]; a simplified scheme describing this mechanism is depicted in Figure 1.1. Several other species can then deposit on the carbon core, such as condensed hydrocarbons (namely the soluble organic fraction, SOF), sulfates and ashes [33–35]. Soot formation is fostered when the air-fuel mixture is not homogeneous, as it happens in the non-premixed flames created in direct injection gasoline or diesel engines.

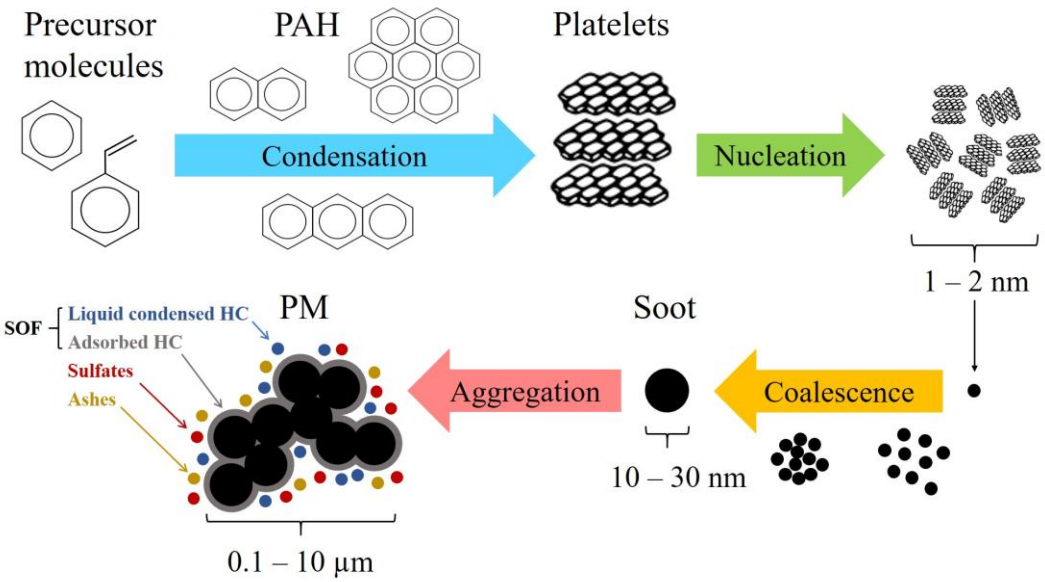

Figure 1.1. Different phases of the soot formation mechanism (picture adapted from [33] with modifications).

Due to their small size, PM particles below 10 µm (PM10) and 2.5 µm (PM2.5) can penetrate the respiratory system and even reach pulmonary alveoli and blood, causing respiratory or cardiovascular diseases and cancer [22,23,36–42]. Recent studies have also concluded that PM pollution contributed to the high level of lethality in the Northern Italy during the SARS-CoV-2 pandemic in the first months of 2020 [43,44].

Carbon dioxide (CO_2)

Carbon dioxide is the desired final product of the complete combustion of every carbon-based fuel, so it is generated during most of the anthropic activities. It is also one of the products of cellular respiration in animals and plants, as well as a carbon source for photosynthetic organisms, thus it plays a fundamental role for life. It is the fourth most abundant gas in the atmosphere and is the main responsible for the greenhouse effect, a very important phenomenon which is critical in regulating the planet temperature: in fact, CO_2 molecules can redirect part of the radiation emitted by the Earth towards its surface, warming it and thus promoting life [45,46].

Being non-toxic (except that in high concentrations) and naturally present in air, CO_2 is not actually a pollutant. However, its concentration has been increasing since the industrial revolution [47,48], as a result of the massive consumption of fossil fuels, and starting from the pre-industrial level of about 280 ppm has recently exceeded 410 ppm [49]. The accumulation of CO_2 in the atmosphere is associated to enhanced greenhouse effect, which is causing a rise in the average planet temperature (i.e. global warming) [50]. This phenomenon is the main responsible for climate change, which is affecting the whole planet in several different but interconnected ways. Some effects are, for instance, the retreat of glaciers and permafrost, the rise in sea levels and ocean temperature, more

frequent droughts and heat waves, wildfires, desertification of lands, stronger hurricanes and changes in the precipitation patterns [51–56]. All these events are having strong impacts on ecosystems and biodiversity, resulting in the relocation or extinction of many species [57–60], and they are also causing the migration and death of many people [60–64]. For all these reasons, the excessive production of CO_2 can be considered indirectly harmful for human health and life, and the CO_2 emissions should be therefore limited or reduced as much as possible.

1.1.2 Regulations on vehicle emissions

In the last decades new regulations in terms of emission limits have been adopted by several nations all over the world, concerning both stationary and mobile pollution sources. Following the growing concern for air quality, these limits have become stricter and stricter over time, pushing the manufacturers to develop new solutions in order to comply with the law [65–67]. As an example, the evolution of the regulations adopted by the European Union (EU) regarding vehicle emission limits will be briefly presented.

Polluting emissions: the EURO directives

The EURO directives, introduced in 1992, establish the maximum quantity of pollutants that can be released in the atmosphere by a vehicle per km traveled. These regulations have become more demanding over the years, as can be observed in Table 1.1 and Table 1.2, which report the emission limit values for gasoline and diesel cars, respectively. In particular, with EURO 4 the limits were almost halved, and EURO 5 and 6 directives further reduced the limits for PM and NO_x. The latter regulations also introduced a limit for the number of particles emitted by both gasoline and diesel vehicles [68].

Table 1.1. Emission limits in the EU for gasoline-fueled passenger cars.

Directive	Year of application	CO (g km^{-1})	HC + NO_x (g km^{-1})	HC (g km^{-1})	NO_x (g km^{-1})	PM (g km^{-1})	Particles (no. km^{-1})
EURO 1	1992	2.72	0.97	-	-	-	-
EURO 2	1996	2.2	0.5	-	-	-	-
EURO 3	2000	2.3	-	0.2	0.15	-	-
EURO 4	2005	1.0	-	0.1	0.08	-	-
EURO 5	2009	1.0	-	0.1	0.06	0.005	-
EURO 6	2014	1.0	-	0.1	0.06	0.005	6×10^{11}

Table 1.2. Emission limits in the EU for diesel-fueled passenger cars.

Directive	Year of application	CO (g km^{-1})	HC + NO_x (g km^{-1})	NO_x (g km^{-1})	PM (g km^{-1})	Particles (no. km^{-1})
EURO 1	1992	2.72	0.97	-	0.14	-
EURO 2	1996	1.0	0.7	-	0.08	-
EURO 3	2000	0.64	0.56	0.5	0.05	-
EURO 4	2005	0.5	0.3	0.25	0.025	-
EURO 5	2009	0.5	0.23	0.18	0.005	6×10^{11}
EURO 6	2014	0.5	0.17	0.08	0.005	6×10^{11}

Each new model of car has to respect these EURO limits, so it is subjected to type approval tests on a chassis dyno, consisting in the simulation of a model driving cycle. The New European Driving Cycle (NEDC) was used until some years ago, but this type of cycle does not allow to evaluate the emissions in real driving conditions, which are usually much higher due to more intense accelerations and decelerations. Furthermore, some manufacturers developed illegal defeat devices able to recognize the homologation cycle and activate some aftertreatment systems only during the lab test [69,70], resulting in a greater gap between measured and real emissions. Hence, after this fraud had been discovered in 2015 (with the so called Dieselgate), the EURO 6 directive was revised in order to better monitor the real emissions.

In 2017 the NEDC was replaced by a new cycle, the Worldwide harmonized Light vehicles Test Cycle (WLTC), which is more dynamic and similar to real world driving conditions [71]. Moreover, Real Driving Emission (RDE) tests were introduced, measuring the pollutants emitted in real conditions using a portable emissions measurement system (PEMS) [72]. Comparing the results of the two different tests, a conformity factor can be calculated as the ratio between the RDE and WLTC emissions. From 2019 the conformity factor must be lower than a certain threshold (e.g. 2.1 in 2019 and 1.43 from 2020 for NO_x) [66], guaranteeing that emission limits are respected, with a certain tolerance, also in real conditions [73]. Furthermore, the life required to the catalytic converters has been extended from 80000 to 160000 km and the on board diagnostic systems should alert the driver in case of a suspect increase of the pollutants emitted.

Concerning heavy duty vehicles, they have to comply with the EURO directives too, albeit with different limits. In this case, the type approval procedure is not carried out by putting the entire vehicle on a chassis dyno, but only the engine is tested, investigating some specific operating points at different power required [74].

CO_2 emissions: new challenging targets

In order to fight against the global warming and climate change effects previously discussed, the EU has recently set mandatory CO_2 emission reduction targets for new passenger cars [75]. Each car manufacturer has to reach a different fleet-average CO_2 emission target, depending on the average mass of the cars sold. Starting from 2015, a target of 130 grams of CO_2 per km was set for the fleet-wide average emission of new cars [71]; this goal had already been reached in 2013 and was achieved also in the following years. The average CO_2 emission of new cars sold in 2019 in Europe was 122.4 g km^{-1} of CO_2 [76], a value not much lower than the imposed limit. However, a much more challenging target was introduced in 2020, i.e. 95 g km^{-1} of CO_2 [71]; this limit will initially apply for each manufacturer's 95% least emitting new cars, while the average will be calculated on the whole fleet from 2021. CO_2 emission limit will then be further lowered from 2025 [77].

If a manufacturer is not able to comply with the target in a given year, it has to pay a penalty for each car registered consisting in € 95 for each g km^{-1} of CO_2 exceeding the target [75]. These quite high fines are pushing car manufacturers to invest in the development of different new technologies and powertrains in order to lower fuel consumption. A high electrification of the fleets will likely be needed to achieve the goal and avoid costly penalties [78].

1.1.3 Aftertreatment technologies

In order to comply with the actual regulations in terms of polluting emissions, all the vehicles must today be equipped with complex aftertreatment systems [79], since the latest engine advancements alone are not sufficient to meet the targets.

Diesel engines are ignited by compression and can be fed with a high excess of air with respect to fuel, providing high efficiency and low fuel consumption. The oxygen surplus ensures low production of CO and unburned HC, but at the same time the air excess is associated to remarkable generation of NO_x; moreover, since the fuel is directly injected into the combustion chamber without possible premixing, a significant quantity of PM is produced in the fuel rich regions of the flame.

Gasoline engines are instead spark-ignited and work with a stoichiometric air to fuel ratio, which is achieved using a lambda probe. As a consequence, these engines produce more CO but a lower quantity of NOx. Furthermore, a premixed combustion occurs in port fuel injection (PFI) engines, which is associated to very low PM production; soot generation is instead significant in non-premixed gasoline direct injection (GDI) engines.

Depending on the type of fuel and on the engine size and configuration, different solutions can be adopted for exhaust aftertreatment. A short description of the main available technologies will be provided in the next subsections.

Three way catalyst (TWC)

The TWC is the main catalytic unit in gasoline vehicles. Since the exhaust gas contains a very low quantity of O_2, this system is able to oxidize CO and unburned HC and to reduce NO_x at the same time [80,81]. Several different interconnected reactions can occur [82,83]: NO is mainly reduced by CO, HC and H_2, while CO and HC can convert to CO_2 by reacting with catalyst-provided oxygen; however, other parallel reactions are possible, such as HC steam reforming, water gas shift or NO reduction to ammonia and N_2O. The TWC abatement efficiency is very high (approaching 100%), but only in a thin window of air to fuel ratio around the stoichiometry (see Figure 1.2) [81,84,85]; hence, this parameter must be actively and accurately controlled with a lambda probe. The TWC light off temperature is usually in the 150 – 250 °C range.

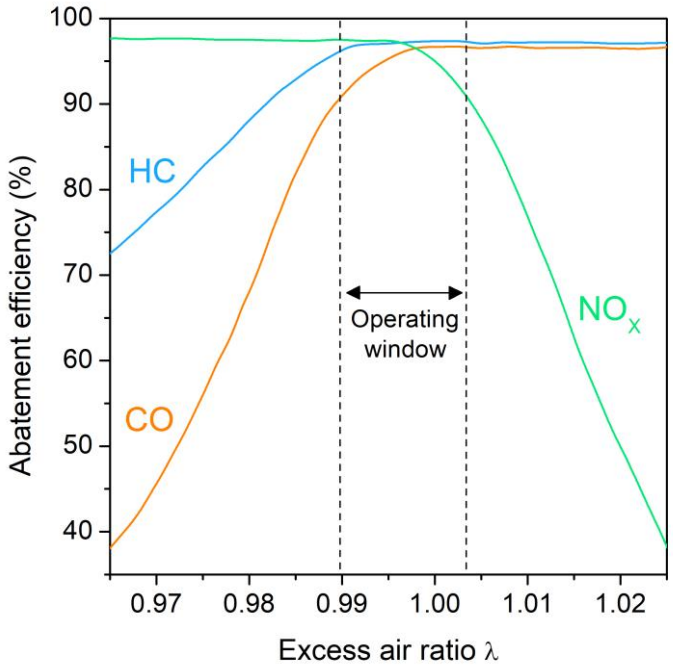

Figure 1.2. TWC steady state conversion efficiency of the different pollutants as a function of λ, which is the ratio between the actual and the stoichiometric air to fuel ratios. Picture adapted from [84], with modifications.

The TWC consists of a honeycomb monolith, usually made of a ceramic material such as cordierite, through which the exhaust gas flows. The inner walls of the monolith channels are covered with a catalytic washcoat, containing an active phase supported by a high surface area carrier [86]. This carrier usually consists in γ-Al_2O_3 doped with other oxides (e.g. La_2O_3, Y_2O_3 or ZrO_2) which promote alumina stability by hindering high temperature sintering and phase transition. The active phase is instead a mixture of platinum group metals (PGMs), such as Pt, Rh and Pd, with a variable composition tuned according to the applications and the actual costs of these very expensive elements. The seeking for cheaper alternatives is tricky, since high reliability and durability of

the catalyst are required for this application. Also cerium oxide can be profitably included in the washcoat formulation [86–89]: in fact, thanks to its unique redox properties, this material can behave as an oxygen buffer, releasing or storing oxygen depending on the exhaust gas composition [84]; furthermore, CeO_2 can strongly interact with dispersed PGMs, promoting their activity and enhancing their stability to sintering [90,91].

Diesel oxidation catalyst (DOC)

Since diesel engine exhausts contain a high quantity of residual oxygen, the different pollutants cannot be abated simultaneously. CO and unburned HC are converted in the DOC, a honeycomb monolith analogous to the TWC in which however only oxidation reactions take place [80]. This monolith can be ceramic (e.g. cordierite) or metallic (e.g., Fe-Cr-Al alloys can be used for a quicker heating) and is coated with γ-Al_2O_3 or zeolites supporting a PGM-based active phase, which usually contains Pt and Pd [92,93]. Again, ceria can be fruitfully employed as active support and catalyst promoter [94].

Besides CO and HC, also NO can be oxidized in the DOC, and the thus obtained NO_2 is a strong oxidant that can take part in other parallel reactions [95,96]. Moreover, also the PM composition is modified in the DOC: the soluble organic fraction is converted, while sulfates resulting from SO_2 oxidation can deposit on soot particles [97,98]. Sulfur can also act as a poison promoting catalyst deactivation, so the sulfur concentration allowed in diesel fuel has been gradually decreased over the years.

In order to speed up the heating phase after a cold start, the DOC is usually mounted in close-coupled position, just downstream the engine exhaust manifold [66,81]. Furthermore, specific adsorbent materials (e.g. some zeolites) can be added to the washcoat formulation, in order to retain the pollutants produced just after the vehicle start-up, when the catalyst is cold and inactive; adsorbed molecules are then released once the light off temperature has been reached, so that they can be effectively abated [98–100].

NO_x abatement systems for diesel vehicles (LNT and SCR)

In the past, NO_x emissions were mainly controlled using exhaust gas recirculation (EGR), i.e. recirculating a fraction of the exhaust gas into the engine in order to lower the combustion temperature and the associated production of thermal NO_x; nevertheless, soot generation is promoted by this process. Nowadays, EGR alone is not sufficient, thus the aftertreatment line of a diesel vehicle has at least one section dedicated to the abatement of NO_x. Two main technologies are available for this purpose.

The lean NO_x trap (LNT) has a moderate efficiency and is usually used only for small passenger cars. It is made of a ceramic monolith containing noble metals (Pt and Rh) together with alkaline metal oxides (especially BaO) supported by high surface area carriers (e.g. γ-Al_2O_3 or zeolites) [93,101–103]. This trap allows

to reduce the NO_x concentration via a two-step process, also referred to as NO_x storage and reduction (NSR) [101,102,104–106]. During normal operation, the diesel engine is fed with a fuel-lean mixture and a remarkable quantity of NO_x is generated; when the exhaust gas enters the LNT channels, NO is oxidized on Pt and the thus-obtained NO_2 molecules react with BaO getting trapped in the form of nitrates. When the NO_x adsorption capacity is saturated, a regeneration step is needed. The engine is thus fed with a fuel-rich mixture, producing a reducing exhaust; under reducing conditions, the LNT releases NO, which converts to N_2 by reacting with the CO, HC and H_2 generated in the engine. The LNT can also be coupled to the DOC: in fact, by adding NSR catalysts to the DOC formulation it is possible to reduce the NO_x emission after cold starts [107].

A good alternative to NSR is represented by selective catalytic reduction (SCR), which is mainly used in big cars and heavy duty vehicles. This technology requires a bigger, more complex and more expensive system [108], but offers a higher conversion efficiency. Actually, SCR is based on the addition to the exhaust gas of a proper reducing agent, such as ammonia or the fuel itself, which is able to directly react with NO_x. The use of an appropriate catalyst is crucial to maximize the selectivity towards N_2: usually, Cu- and Fe-exchanged zeolites are used for vehicles, while metal oxides (e.g. V_2O_5 and WO_3 on TiO_2) are preferred for stationary sources [109–112]. Most automotive SCR systems use NH_3 as reductant, obtained by the hydrolysis of urea in aqueous solution (commercially known as AdBlue®). An appropriate quantity of fluid is injected in the exhaust gas and carefully mixed to it upstream the SCR monolith [79]. Each urea molecule decomposes generating two molecules of NH_3, which can combine with NO, NO_2 and O_2 following different possible reactions [93]. Urea dosing and mixing are fundamental operations in order to achieve high abatement efficiency avoiding at the same time the emission of NH_3; anyway, the last section of the SCR monolith can accommodate an ammonia slip catalyst (ASC) able to oxidize residual NH_3 [93].

In order to obtain the best NO_x abatement performances, LNT and SCR can be coupled. Different configurations are possible, e.g. with two independent units or with a mixed multifunctional catalyst [79,93,108,113]. In this way, NO_x can be stored at low temperature, when the SCR system is inactive, and the NH_3 generated by the LNT can be exploited by the SCR catalyst.

Particulate filters (DPF and GPF)

As discussed above, the production of PM is a critical issue, especially for diesel engines. In order to meet the strict requirements in terms of PM abatement, diesel particulate filters (DPFs) have been developed and are today installed in every diesel road vehicle in the EU [35,114–116]. A DPF usually consists in a wall-flow honeycomb monolith (commonly made of SiC) with alternatively plugged channels, even if some other configurations (e.g. metallic or ceramic foams or fibers) have been proposed [114,117]. The exhaust gas is forced to cross the porous walls between two channels and the PM particles are trapped inside the

pores (see Figure 1.3) with a very high efficiency (> 95%) [35]. PM deposition entails the formation of a soot cake and this layer becomes thicker over time, resulting in higher pressure drops [118]; hence, the filter must be periodically regenerated by burning the trapped particles. A temperature above 600 °C is required for soot combustion, but the usual exhaust gas temperature during normal engine operation is quite lower (< 400 °C) [115,119]. Therefore, the DPF is heated by post-injecting into the exhaust some fuel, which then burns in the DOC increasing the gas temperature; to reduce heat losses, DOC and DPF are usually close-coupled [79,120].

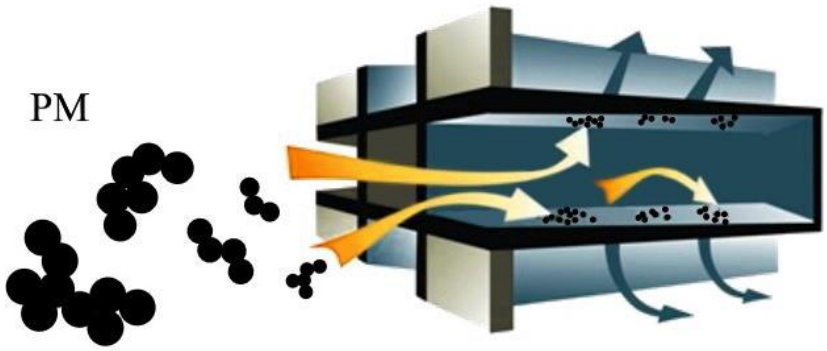

Figure 1.3. Scheme of PM trapping in a wall-flow particulate filter.

Since soot combustion is a highly exothermic reaction, very high temperatures may be reached in certain hot spots of the filter during the regeneration, with possible damage to the SiC monolith. In order to reduce the thermal shock for the materials as well as the post-injected fuel consumption, soot oxidation can be promoted at lower temperatures by depositing proper catalysts on the filter walls. To this end, PGMs can be employed, but also metal oxides offer an attractive and less expensive alternative; in particular, ceria-based catalysts are considered promising candidates for catalyzed DPF (cDPF) [35,87,115].

Similarly, also SCR catalysts can be accommodated in a DPF; such a technology is already commercially available and is known as SCR on filter (SCRF or SDPF) [79,121–123]. Coupling the two functions into a unique wall-flow monolith allows to reduce the total dimensions and to speed up the SCR catalyst heating, since this SCRF is usually in close-coupled position with the DOC just downstream the engine exhaust manifold [123]. However, the complexity of this system is much higher: in fact, effective urea mixing in the little space between the DOC and the SCRF can be tricky [79], and the possible interactions between NO_x, NH_3, soot and the SCR catalyst have to be evaluated [124]. Anyway, to avoid uncontrolled emissions in certain operating conditions (e.g. during the regeneration) a second SCR monolith is usually present in the aftertreatment line.

Concerning gasoline vehicles, the PM production is very low for PFI engines, which therefore do not need any filter. However, soot formation is higher in GDI engines and an intervention is thus required to comply with the emission limits, especially in terms of particle number [68,125]. For this reason, gasoline

particulate filters (GPFs) have been developed, with a structure analogous to that of DPFs. However, the operating conditions of a GPF are different [126] and the regeneration phase may be tricky because of the lack of oxygen. In fact, while the O_2 concentration is usually around 10% in Diesel exhaust, it is lower than 5% in stratified-charge GDI engines and it is barely measurable in homogeneous-charge GDI engines, due to the stoichiometric air-to-fuel ratio employed [127]. Nevertheless, soot oxidation can be promoted by coating the GPF walls with a proper catalyst. Again, CeO_2 can be profitably included in the washcoat formulation since its oxygen buffer behavior can compensate the low oxygen concentration, as in a TWC [128,129].

1.2 Ceria-based catalysts: properties and potentialities

As discussed in the previous section, ceria-based catalysts find application in different types of automotive aftertreatment systems and are among the most promising materials which can be employed in catalyzed particulate filters. In addition, ceria can be used as catalyst or active support for promoting several other reactions, such as methane reforming, water gas shift, CO preferential oxidation, photocatalytic water splitting or oxidation of pollutants in wastewater [87,130].

The growing interest attracted by ceria in the last decades is primarily due to the unique redox properties of this material. In fact, cerium can easily switch its oxidation state from Ce^{4+} to Ce^{3+}, and for two Ce ions reduced an oxygen vacancy is formed. This capability provides CeO_2 with a high oxygen storage capacity (OSC) [130]: this means that in reducing atmosphere this oxide can release a considerable amount of oxygen (often in the form of highly reactive species), while when gaseous O_2 is available again the oxygen vacancies previously formed in the crystal lattice can be refilled. Thanks to these redox properties, ceria can be profitably employed as oxygen buffer (e.g. in a TWC or GPF).

The just described behavior is also at the basis of the peculiar catalytic activity of ceria. In fact, while heterogeneous catalysis often proceeds via a Langmuir-Hinshelwood mechanism in the case of metal catalysts [131–133], i.e. with the reaction between two species adsorbed at the solid surface, different catalytic pathways have been recognized when ceria-based oxides are used as catalysts or active carriers. For instance, mechanisms involving the formation of carbonates or CO disproportionation have been proposed in the case of CO oxidation [134,135]. However, many authors believe that different reactions proceed via a two-step Mars – van Krevelen (MvK) mechanism over ceria-based catalysts [135–138]. A simplified scheme illustrating this catalytic pathway is reported in Figure 1.4: initially, a reactant is oxidized by oxygen directly released by ceria lattice and an oxygen vacancy is generated; afterwards, this vacancy is refilled by the O_2 coming from the gas bulk and the initial lattice configuration is restored.

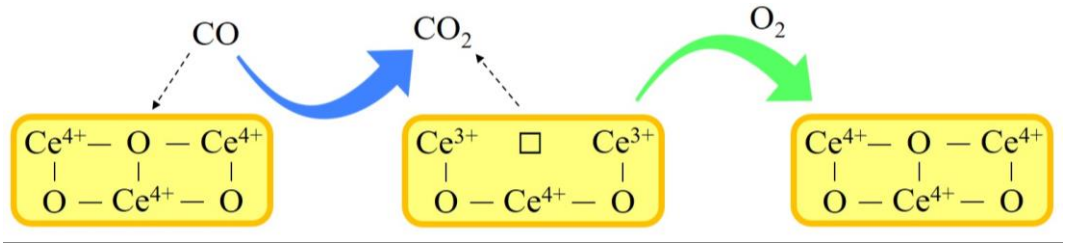

Figure 1.4. Scheme of the MvK mechanism during CO oxidation over ceria.

The oxygen mobility inside the lattice is therefore a key parameter in defining the catalytic performances of ceria-based materials, since a higher mobility from the bulk to the surface is associated with a greater oxygen release and a thereby enhanced oxidizing activity. This parameter is usually affected by the presence of reticular defects [139,140], which can weaken the Ce – O bonds. Actually, ceria crystallizes in a regular face-centered cubic lattice, also known as fluorite (*Fm3m*) crystal structure, in which each Ce^{4+} ion is coordinated with eight O^{2-} [140]. However, different types of point defects can be hosted in this lattice, such as those illustrated in Figure 1.5. Besides oxygen vacancies, always present because of the partial reduction of some Ce^{4+} to Ce^{3+}, also Frenkel pairs can form when an oxygen ion is dislocated in an octahedral interstitial position, generating a vacancy; moreover, the presence of foreign elements results in the formation of substitutional sites, which are in some cases accompanied by nearby oxygen vacancies. All these defect sites might be directly involved in the catalysis, even if their role has not been completely understood yet [141]. For instance, a higher abundance of oxygen vacancies in ceria-based catalysts has been correlated to a higher catalytic activity towards CO oxidation [142,143].

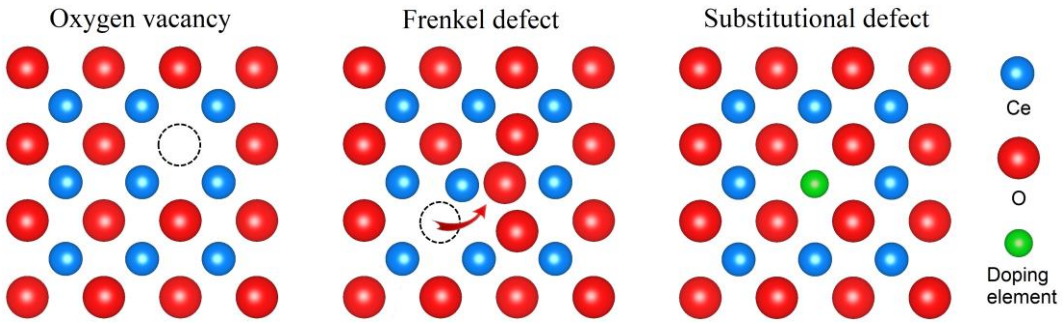

Figure 1.5. Some types of point defects which can be found in the ceria lattice.

Another key parameter which influences many properties of ceria, from the OSC and defect abundance to the surface reactivity and the favored catalytic mechanisms, is morphology. It is indeed possible to tune the synthesis procedure in order to obtain tailored ceria nanoparticles with a well-defined shape, whose reactivity depends not only on the particle size but also on the crystalline planes exposed at the surface, as pointed out in several studies [144–147]. Some examples of ceria-based materials with very different morphological and topological properties are shown in Figure 1.6.

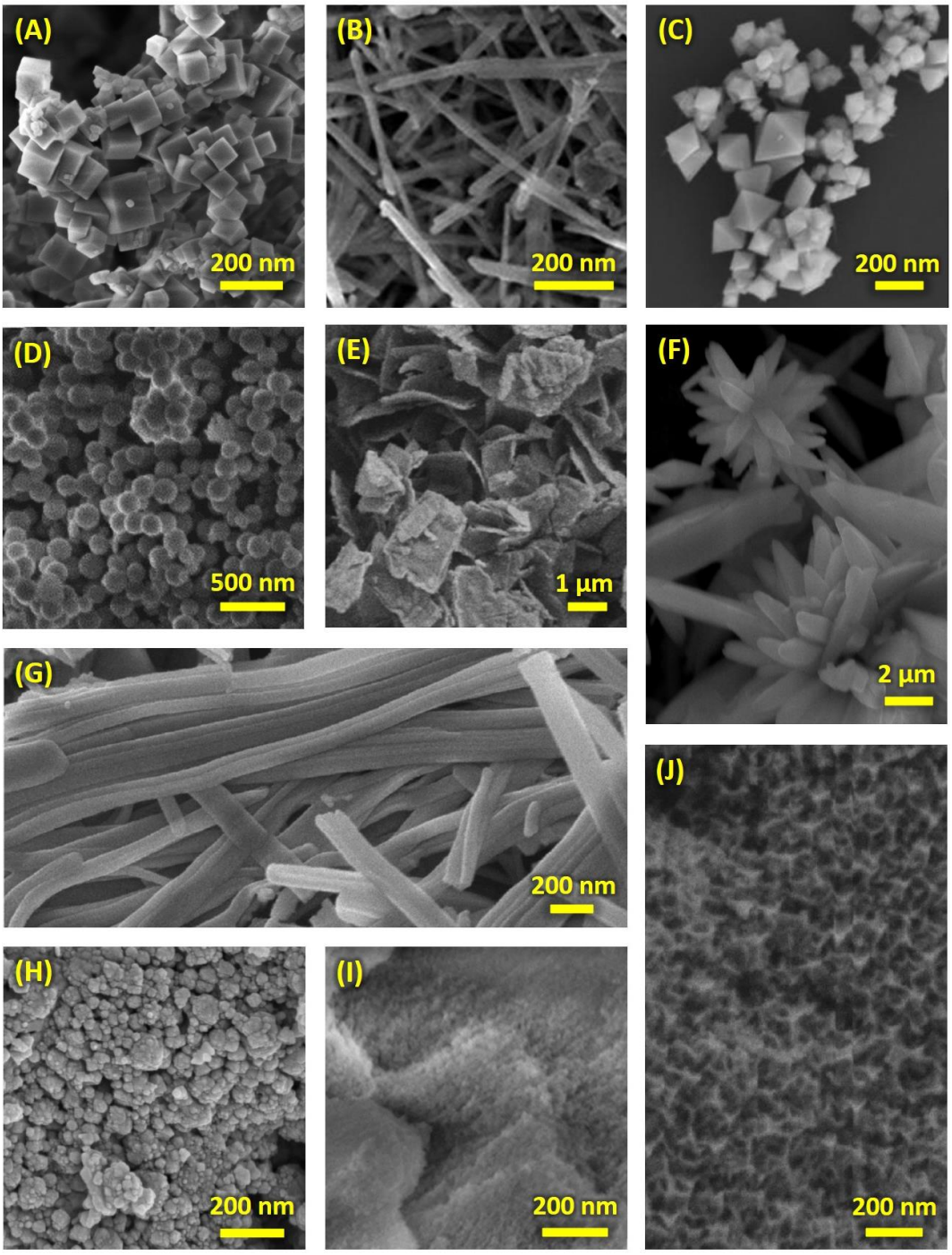

Figure 1.6. SEM pictures of ceria-based materials exhibiting very different morphologies (some images are adapted from published literature as herein detailed): cubes (A), rods (B) [148], octahedra (C) [149], spheres (D) [150], flakes (E) [151], self-assembled stars (F) [152], fibers (G) [151], SCS (solution combustion synthesis) nanoparticles (H), mesoporous (I) [146], 3-DOM (three dimensionally ordered macroporous) (J) [153].

The differences in reactivity are primarily linked to the different degrees of coordinative unsaturation of the atomic sites at the exposed surfaces. In particular, the oxygen reactivity is thought to be higher on the less thermodynamically stable facets and it is supposed to follow this trend among the low-index surfaces: (1 1 1) < (1 1 0) < (1 0 0) [154]. The vacancy formation energy depends on the type of exposed planes too, and it is believed to conform to this trend:

(1 1 0) < (1 0 0) < (1 1 1) [154]. Consistently, ceria particles featuring (1 0 0) and (1 1 0) facets, such as nanocubes and nanorods, were found to be more reactive and defective than polycrystalline ceria and octahedra, which mainly expose (1 1 1) crystal planes [136,147,155]. Also some catalytic pathways are believed to be facet-dependent [134,135]: for instance, the MvK mechanism is promoted over the highly active (1 0 0) crystal planes typical of ceria nanocubes, which present a lower oxygen vacancy formation energy [137]. All these aspects must be carefully considered for the effective design of ceria-based catalysts.

1.2.1 The role of doping

The properties of ceria can be further customized by adding some other elements to the catalyst formulation. Different kinds of interaction can actually arise between ceria and other oxides or metals, conferring a unique behavior to the mixed system.

Ceria-based materials are widely used as active supports, e.g. for carrying PGMs nanoclusters. With respect to other oxides like silica or alumina, ceria can develop strong electronic interactions at the interface with the supported metal, binding the metallic clusters to its surface with a high strength and thereby hindering displacements and sintering at high temperature [156]. This phenomenon can be particularly intense in some conditions, e.g. after a reduction treatment at high temperature, and it is not only linked to high stability but also to increased catalytic activity or selectivity of the supported metals [157]. In fact, mechanisms involving an exchange of oxygen species between ceria and the supported metal via spillover have been identified [158]. Hence, during an oxidation reaction ceria can provide the active phase with the oxygen required, offering a faster route for oxygen supply.

Sometimes, the compatibility between ceria and a metal is so good that solid solutions can be obtained. For instance, Danielis et al. have recently found out that an amorphous layer containing both ceria and Pd can form around ceria nanoparticles via mechanochemical synthesis [90,159]; a high stability and catalytic activity towards methane oxidation were ascribed to this phase. Interestingly, a similar effect was not observed when replacing ceria with zirconia, confirming that the phenomenon is connected with the unique redox properties of the former oxide.

Solid solutions can also be prepared by adding some dopants during the ceria synthesis. In fact, thanks to its flexibility, ceria crystal lattice is able to accommodate great amounts of dopant ions, forming a single phase with many substitutional sites. However, this leads to a strong distortion of the structure, accompanied by weakening of the Ce – O bonds. As a result, the material can obtain an improved thermal stability accompanied by increased reducibility and oxygen mobility, with beneficial effects on the OSC and catalytic activity [140,145,160,161].

Different types of metals can be chosen as dopants, depending on the final application. For instance, alkali metals can promote soot oxidation, by increasing

the surface mobility and thus improving the soot-catalyst contact [119]. Doping with transition metals, such as Cu, Fe, Mn or Co, is beneficial for several reactions: the redox cycles of these elements can indeed be coupled to that of ceria, synergistically enhancing the final redox properties [162–169]. Despite being an isovalent non-reducible element, also Zr is widely employed as dopant [170]: indeed, Zr^{4+} ions can be well-incorporated into ceria structure and the resulting lattice distortion is accompanied by higher oxygen mobility and reducibility [145,171]; moreover, ceria-zirconia features a better thermal stability [172].

Analogous effects have been observed for ceria-based oxides containing other rare earth elements. In this case, solid solutions are often obtained even at high dopant loading, thanks to the similar ion dimensions [173]. Like Zr, most of these dopants exhibit a single stable oxidation state, hence showing little redox ability; an excessive substitution of Ce may therefore be detrimental for the oxidation activity, due to the loss of active redox centers and the reduced total OSC [145,174]. However, unlike Zr, rare earths usually have 3+ ions, thus their incorporation in ceria structure is accompanied by the formation of a great amount of oxygen vacancies for charge compensation, which can improve oxygen mobility from bulk to surface and dynamic OSC [174,175].

Moreover, also some co-doped systems have been investigated, suggesting that eventual synergistic effects can arise by coupling two suitable dopants [166,176]. This further expands the possible range of properties which can be obtained by ceria-based materials.

1.2.2 Ceria-catalyzed CO oxidation

CO oxidation is a key reaction in the field of pollutants abatement and environment protection. Noble metals are known to be very active towards CO to CO_2 conversion, but ceria-based materials represent a lower-cost attractive alternative.

As previously discussed, different reactions are believed to occur via a MvK pathway over ceria-based oxides (see Figure 1.4). Such a mechanism has been directly observed for CO oxidation through experiments with labelled oxygen [135]: when a ceria catalytic bed is fed with a mixture containing $C^{16}O$ and $^{18}O_2$, the main oxidation product at the beginning is $C^{16}O_2$, indicating that CO mainly reacts with oxygen supplied by the catalyst; however, the oxygen vacancies formed in ceria lattice are then refilled by $^{18}O_2$ and so the production of $C^{16}O^{18}O$ gradually increases in time. If gaseous $^{18}O_2$ is eventually replaced by $^{16}O_2$, the concentration of $C^{16}O^{18}O$ only slowly decreases, since some ^{18}O atoms are still present in the ceria lattice, confirming the direct role played by lattice oxygen in the oxidation mechanism.

Modified MvK-like pathways have also been proposed, e.g. considering the involvement of carbonate species in the catalytic cycle [134,176]. These mechanisms are considered facet-sensitive and can also be affected by the density of superficial oxygen vacancies [134]. CO_2 formation and desorption,

accompanied by the generation of an oxygen vacancy, are usually considered the rate determining step of the reaction; hence, the oxygen vacancy formation energy is expected to be correlated to the catalytic activity [175].

A good solution for promoting vacancy formation, and thus increasing the reaction rate, is represented by aliovalent doping. To this end, both transition metals and rare earths can be employed, but with different results. In fact, while rare earth-doping mainly improves CO oxidation as a consequence of a higher specific surface area, the inclusion of transition metals in ceria structure allows to really lower the oxygen vacancy formation energy [175]. In addition, redox synergies can arise from the interaction between cerium and some transition metals, while the surface area does not seem to always control the final performances [161,165]. Consequently, better results in terms of CO oxidation activity are usually achieved with transition metal-doped ceria [161].

1.2.3 Ceria-catalyzed soot oxidation

The oxidation of particulate matter in the presence of a catalyst is a complex heterogeneous reaction involving three different phases and various possible reaction pathways. Among the possible catalysts capable of promoting soot combustion, ceria-based oxides have attracted an increasing attention in the recent years, as shown in Figure 1.7.

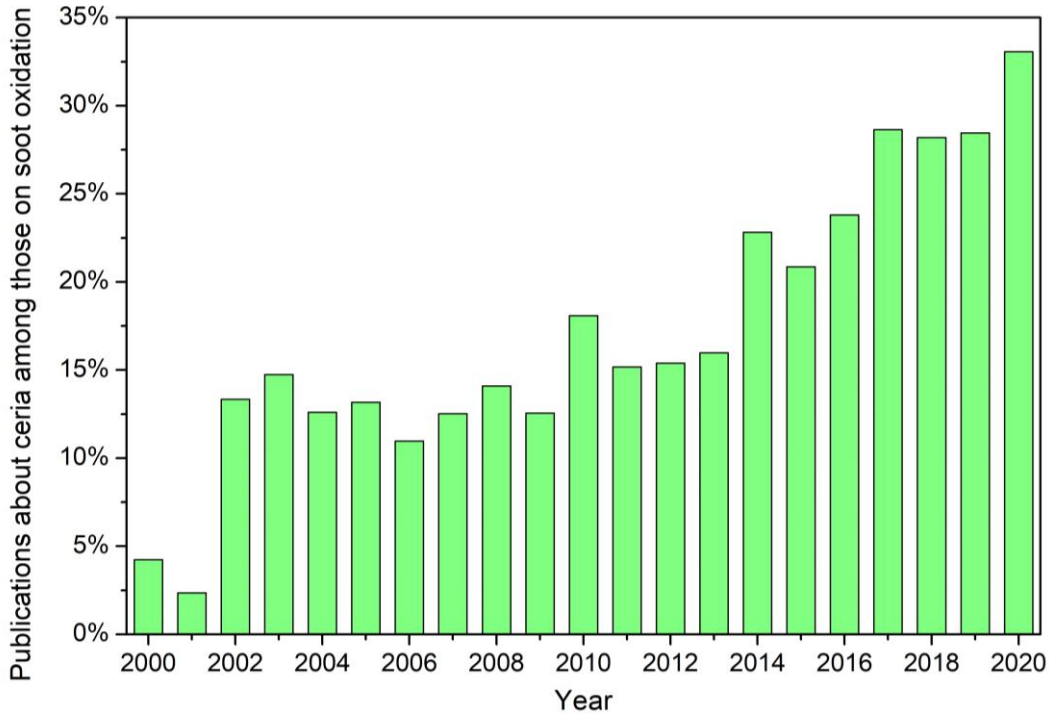

Figure 1.7. Percentages of the publications dealing with ceria-based catalysts among those about soot oxidation over the last twenty years. The data have been obtained using Google Scholar (https://scholar.google.com, accessed on November 27, 2020), searching for the publications containing the string "ceria" among those containing the string "soot oxidation".

Despite the great advances and new discoveries made in the last decades, these materials remain among the most studied for this application and are still object of many investigations. In fact, the catalytic activity towards soot oxidation of ceria-based samples is the result of all the different properties described so far. Due to the complexity of these systems, several questions still require an adequate answer, which should be found in order to acquire further knowledge useful for improving the performances of these oxides.

Morphology and solid-solid contact

Soot combustion can be considered a surface-sensitive reaction, namely affected by the superficial crystal planes exposed by ceria nanoparticles. A higher specific soot oxidation rate was indeed measured when the stable (1 1 1) facets typical of polycrystalline ceria were partially replaced by (1 0 0) or (1 1 0) planes upon high temperature treatments in air, despite the decrease of the specific surface area [172]. Actually, the surface area may be correlated with the catalytic activity at low temperature, but the morphology seems to play a much more important role at the significant temperatures for soot combustion (i.e. above 350 – 400 °C) [145,146]. As a result, nanocubes or nanorods rich in reactive (1 0 0) and (1 1 0) facets were found to be more active than other ceria structures with different topological properties, such as octahedra, polycrystalline, mesoporous or SCS samples [146,155].

Particle size and morphology are even more relevant in the case of soot oxidation, since these properties crucially define not only the reaction mechanisms and catalytic activity but also the possible degree of contact between the catalyst and soot. The latter aspect is critical for a reaction involving two solid phases: in fact, the catalyst is able to deliver active oxygen species to particulate matter only close to the contact points. This can be a strong limitation during the regeneration of a cDPF, in which a large part of the soot cake deposited in the filter channels may be totally isolated from the catalytic materials at the walls, thus being converted via a less efficient thermal combustion pathway [177]. The number of contact points must be therefore maximized in order to overcome this critical issue.

Different strategies have been adopted in order to enhance the interaction between ceria and soot. For instance, alkali metals can be profitably included in the catalyst formulation: in fact, these elements can promote soot oxidation and carbon gasification by increasing the surface mobility of the mixed oxides [119,178–180]. However, the main drawback connected to alkali-doped ceria consists in the low stability of these systems: the alkali metal loss at high temperature indeed results in a quick deactivation of the material, especially in the presence of water [179,181].

A peculiar approach adopted by some car manufacturers is the use of a so-called fuel-borne catalyst [182,183]. In this case, an additive containing organic molecules with some Ce or Fe atoms in their structure is added to diesel fuel, so that metal oxides are produced when the mixture burns in the engine. The such

obtained solid particles are trapped by the DPF and incorporated in the soot cake, so they can act as highly-dispersed catalysts intimately-mixed with soot during the regeneration. This allows to greatly promote the carbon combustion; nevertheless, the solid ashes can accumulate in the filter pores, causing obstructions and an increase in the pressure drops over time, until a manual cleaning of the filter is required.

Also tailoring the catalyst morphology can help in achieving better performances: in fact, nanocatalysts with a proper shape can better accommodate soot particles in their voids, reaching a more intimate solid-solid contact. For instance, engineered structures such as ceria nanofibers or self-assembled stars have proven to be highly effective for soot combustion also in case of low-intensity contact, despite a relatively low specific surface area [151,152,184]. Also ceria nanocubes are considered excellent catalysts, as they offer a low surface area which is however highly-accessible to soot particles [185]; moreover, this benefit is combined with the exposure of highly reactive facets further promoting the catalytic performances. For these reasons, the cubic morphology was chosen as starting point for the nanostructured catalysts which will be object of this thesis.

Reaction mechanisms

Two main reaction mechanisms have been identified for soot oxidation over ceria-based catalysts [136,186]. A MvK-like mechanism, as previously described, involves the reduction of the catalyst through the direct transfer of lattice oxygen at the ceria-soot interface; oxygen vacancies are formed, but they can be successively refilled by gaseous O_2 or by mobile lattice oxygen coming from the material bulk. In parallel, oxygen spillover can occur: in fact, reactive oxygen O_2^{x-} can form on reduced Ce^{3+} (or reduced substitutional cations) associated with the presence of oxygen vacancies, and these species can then move across the surface until they are delivered to soot particles.

Both these mechanisms are affected by the catalyst morphology or chemical composition, i.e. by the exposed facets and by the quantity and type of dopants added in the ceria structure [142,143,187,188]. Also the abundance of oxygen vacancies and other structural defects is expected to influence soot oxidation, even if their role has not been fully clarified yet [189–191]. In fact, different kinds of vacancies can be hosted in ceria lattice, and while some of them may play a key role directly participating in the catalysis, others might behave as simple spectators [189]. Furthermore, the work of Liu et al. has recently raised doubts about the actual convenience of a high defect abundance in ceria-based catalysts [191,192]. Deeper investigations are therefore required for elucidating the role of the different defect sites.

The situation is even much more complicated in real applications, since the catalytic pathways promoted by ceria-based oxides may change upon variations in the O_2 concentration or in the presence of the different species which are commonly found in an exhaust gas. Indeed CO, CO_2, unburned hydrocarbons,

NO_x, SO_x and water can be expected to interact with ceria or soot in different ways [193]. For instance, the effect of water can be either beneficial or detrimental, depending on the catalyst properties and on the operating conditions [171,179,194,195]: indeed, water vapor may foster the catalyst deactivation (e.g. in the case of alkali-doped ceria), but it could also improve the oxygen mobility at the catalyst surface and promote carbon gasification. Sulphur entails the formation of stable sulphates, inevitably resulting in catalyst poisoning [193]; the presence of water or alkali dopants can however help in retarding this phenomenon [180,196].

Also NO_x can take part in catalytic soot oxidation and two main mechanisms have been identified. An indirect pathway involves NO oxidation over the catalyst, producing NO_2 molecules which can reach and convert soot from the gas phase [169,197]; at the end, NO is obtained again and the whole cycle may be repeated multiple times [198,199]. Besides, soot oxidation can also occur via a direct pathway involving the NO_x adsorbed on the catalyst: in fact, nitrites or nitrates at the solid surface can decompose in the proximity of soot particles, generating active species able to attack soot directly from the solid phase [199,200].

Hence, all these possible interactions must be taken into account when investigating the soot oxidation mechanisms. Fortunately, new in situ and operando techniques have been developed, which allow to trace the changes undergone by the catalyst during the reaction. The new insights gained through these experiments will help in reducing the gap between the lab-scale results and the real performances measured on field.

1.3 Raman spectroscopy: some basic concepts

In the recent years, Raman spectroscopy has become a widespread characterization technique in various research fields concerning materials science, including catalysis. Regarding ceria-based oxides, this technique has been used to investigate the interaction of molecules with the catalyst surface or the defects present in the lattice [201]. Moreover, some in situ Raman analyses have been employed to gain new insights into the modification of ceria structure under variable conditions [201–204].

Hence, this powerful technique will be extensively used in this thesis in order to characterize the defects in ceria-based materials and follow their evolution in different conditions. Indeed, although understanding the nature of the defect sites involved in the catalysis is crucial for the rational design of active materials, as explained in the previous section, the identification of the various lattice defects, of their arrangement and of the associated catalytic mechanisms is still under debate, so it will be further addressed within this thesis. However, since this analytic technique is not so common in the field of chemical engineering, a short description of the phenomena involved will be provided here.

The Raman effect consists in the inelastic scattering of light by matter and was described for the first time in 1928 by the Indian physicists C. V. Raman and

K. S. Krishnan. Thanks to this important discovery, Raman was awarded the Nobel Prize for physics in 1930.

When light interacts with matter, it can be absorbed, reflected, transmitted or scattered. Most of the scattered photons are elastically scattered, i.e. they have the same energy and wavelength as the incident light, but a different direction; this effect is called Rayleigh scattering. However, a very small fraction of the scattered photons (approximately 1 in 10 million) can be inelastically scattered, i.e. they feature a different energy, usually lower, with respect to the incident beam. This is Raman scattering and is the consequence of an exchange of energy between light and matter involving vibrational levels.

For the sake of clarity, a simplified scheme of the possible interactions between light and matter during scattering is depicted in Figure 1.8. In detail, when a system (e.g. a molecule) in a certain vibrational level is excited by an impinging photon, it reaches a virtual level at higher energy; upon relaxation, the system usually comes back to the initial energy level, generating a photon with the same energy of the incident one (Rayleigh scattering). However, after relaxation the system can also move to a vibrational energy level different from the initial one: when the new level has higher energy than the previous one, a lower-energy photon will be emitted (Stokes Raman scattering); more rarely, the new level has a lower energy than the starting one, hence a higher-energy photon will be generated (anti-Stokes Raman scattering) [205]. Moreover, when the incident light has an energy close to that required for an electronic transition of the analyzed material, Raman effect is greatly enhanced. In this case, resonance Raman occurs, which allows to detect the presence of the resonant species even at very low concentrations.

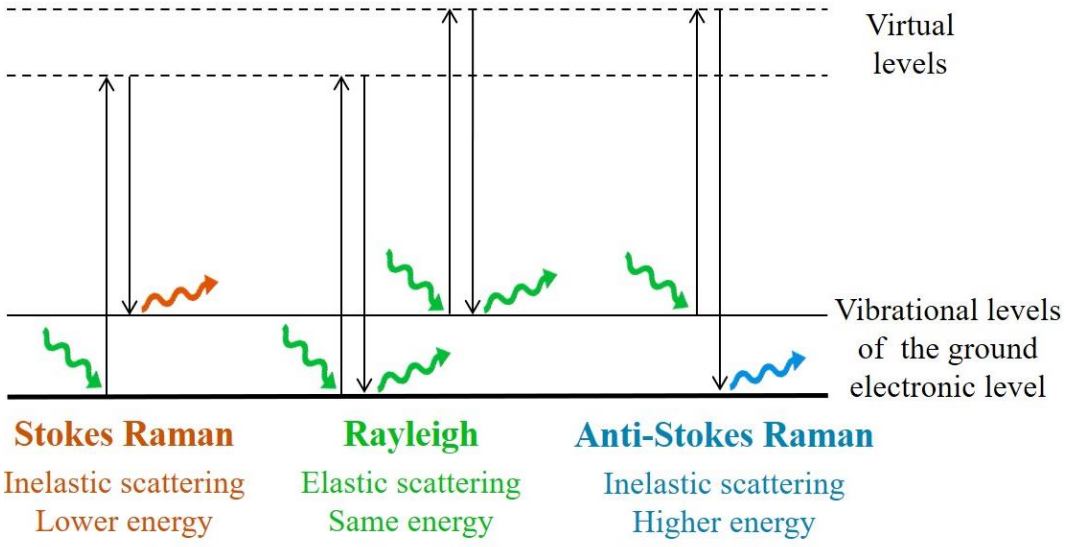

Figure 1.8. Simplified scheme of the vibrational levels involved in light scattering.

When light interacts with a solid crystal, scattering involves phonons, namely the collective vibrations in an ordered lattice [206]. In this case, during Stokes Raman scattering the incident photon transfers some of its energy to a generated

phonon, so it is then scattered with a lower energy. For anti-Stokes Raman scattering, instead, the impinging photon combines with a phonon and thus acquires energy. Hence, Raman spectroscopy can be suitably employed also for the study of solids.

In a common Raman spectrometer, the analyzed sample is irradiated with a monochromatic light beam and the scattered light is collected; the Rayleigh photons are then removed with a proper filter before the light reaches the detector. A Raman spectrum can be obtained by plotting the intensity of the inelastically scattered light as a function of the Raman shift, i.e. the difference in wavenumber between the incident and scattered photons. Stokes Raman components are usually considered, since they are more intense than the corresponding anti-Stokes ones. The Raman peaks are related to energy differences between the vibrational levels of a molecule or crystalline lattice, so they can provide information on the composition and microstructure of the analyzed sample.

1.4 Objectives of this PhD thesis

As described so far, ceria-based materials are among the most interesting catalysts for the oxidation of environmental pollutants, thanks to their fascinating properties and promising performances. However, despite these oxides have been widely studied in the last decades, different questions are still demanding an answer and some of them will be addressed in this thesis.

On the one hand, in situ Raman spectroscopy will be employed to gain new insights into the types of defects which can form in ceria lattice upon Cu or Mn doping. The evolution of these defect sites will be monitored throughout thermal cycles and during CO and soot oxidation. The link between defect abundance and catalytic activity will be examined, investigating the role played by oxygen vacancies during the reactions.

On the other hand, well-defined nanostructures will be prepared by doping ceria with different rare earths, in order to boost its catalytic activity for soot oxidation. The structural and physico-chemical properties of the mixed materials will be studied, looking for the reasons behind improved oxidation performances. Equimolar ceria-praseodymia will be tested in low-O_2 conditions, in order to assess the adequacy of this catalytic system in view of its possible use in coated GPFs. Moreover, novel La- and Nd-doped nanocatalysts will be prepared and the effects of dopant type and loading on ceria properties will be evaluated. Tests carried out in different conditions will help in understanding the main catalytic pathways involved when the soot oxidation reaction is performed over these oxides.

The results obtained will bring new knowledge of the ceria-based materials behavior during oxidation reactions, providing useful indications for the improvement of these high-potential systems.

Chapter 2

Experimental methods

This chapter is aimed at providing a detailed description of the experimental methods employed to carry out the research presented in this thesis. The catalyst synthesis procedure will be reported, together with a general overview of the operating conditions used for the characterization techniques and the catalytic tests. Some further specific details will be also presented at the beginning of next chapters.

2.1 Synthesis of the catalytic materials

Ceria-based nanocatalysts with different composition were obtained via hydrothermal synthesis, following a procedure previously used by my research group [143,207] adapted from [208]. The hydrothermal treatment promotes the growth of specific crystal facets, allowing to produce nano-shaped particles. The synthesis parameters (i.e. pH and temperature) were optimized in order to obtain nanocubes in the case of pure ceria [207]. A scheme resuming the main operating conditions is reported in Figure 2.1.

Appropriate amounts of $Ce(NO_3)_3 \cdot 6H_2O$, $Cu(NO_3)_2 \cdot 5H_2O$, $Mn(NO_3)_2 \cdot 4H_2O$, $Pr(NO_3)_3 \cdot 6H_2O$, $La(NO_3)_3 \cdot 6H_2O$ or $Nd(NO_3)_3 \cdot 6H_2O$ (all provided by Sigma-Aldrich) were dissolved in a beaker containing 10 mL of deionized water, stirring the solution for some minutes. Separately, another solution was prepared by adding 48 g of NaOH (Carlo Erba Reagents) to 70 mL of deionized water, stirring for 30 min to dissipate the released heat. The nitrate-containing solution was then slowly added drop by drop to the second solution and hydroxide crystals started to precipitate. The thus obtained mixture was stirred for 1 h at room temperature (RT), then it was poured into a 150 mL Teflon liner, which was placed in a stainless-steel autoclave. Subsequently, an aging treatment was carried out by heating the autoclave in an oven at 180 °C for 24 h. The slurry obtained was centrifuged and rinsed several times, using alternately deionized water and ethanol to remove impurities; the precipitate was then dried at 60 °C overnight.

Finally, the dry powder was gently crushed in a mortar and calcined in an oven at 550 or 650 °C in air for 4 h.

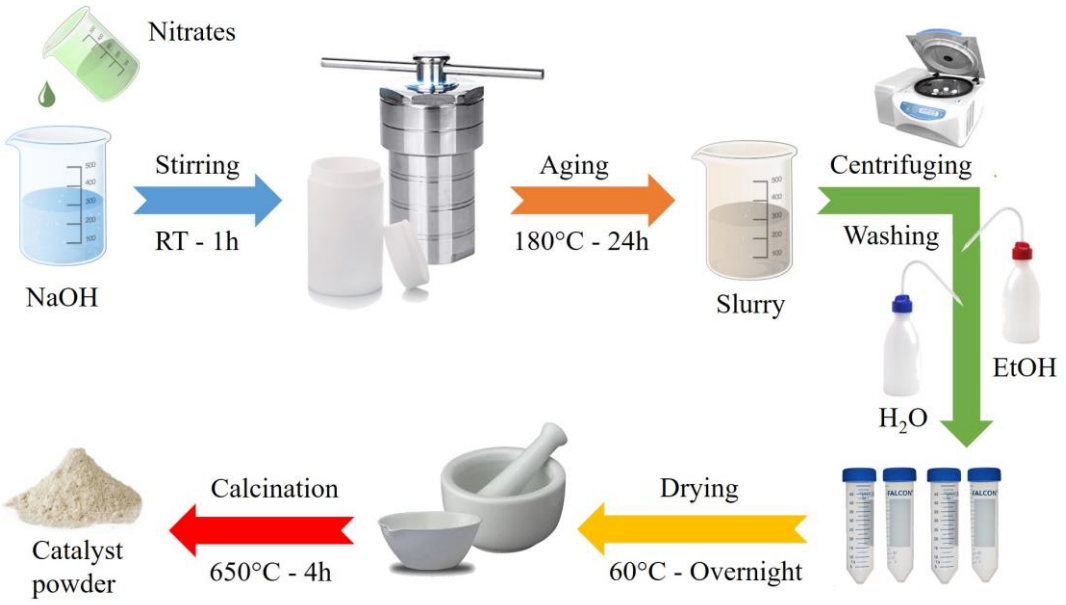

Figure 2.1. Different phases of the hydrothermal synthesis procedure.

2.2 Characterization techniques

The catalysts were studied using several complementary characterization techniques, to investigate the properties of each sample.

2.2.1 X-ray diffraction (XRD)

Powder X-ray diffraction (XRD) was performed in a Philips X'Pert PW3040 diffractometer using Cu Kα radiation (λ = 1.5418 × 10^{-10} m), with values of 2θ ranging between 20° and 70°, a step size of 0.013° and an acquisition time of 0.2 s per step. The diffraction peaks were indexed according to the Powder Data File database (PDF 2000, International Centre of Diffraction Data, Pennsylvania, USA).

The crystal average size (D_c) was estimated using Scherrer's formula, reported in equation (2.1):

$$\boldsymbol{D_c = \frac{0.9\,\lambda}{\beta\,\cos\theta}} \qquad (2.1)$$

where 0.9 is the shape factor for spheres, λ is the Cu Kα wavelength, β is the full width at half maximum FWHM and θ is the Bragg angle [209]. The FWHM data were previously corrected using lanthanum hexaboride (LaB_6) as a calibration standard to compensate the instrumental peak broadening.

The lattice parameter of the face-centered cubic structure (a) was determined using the Nelson-Riley extrapolation function.

2.2.2 Nitrogen physisorption

The surface area and pore-related properties of the prepared catalysts were investigated via nitrogen physisorption at -196 °C, which was performed in a Micromeritics Tristar II 3020 apparatus. Before the analysis, the samples were pre-treated at 200 °C for 2 h under nitrogen flow in a Micromeritics FlowPrep 060, in order to remove the adsorbed gases. The specific surface area (SSA) was estimated using the Brunauer–Emmett–Teller (BET) method [210], while the pore (V_p) volume and pore average size (D_p) were evaluated applying the Barrett-Joyner-Halenda (BJH) algorithm to the desorption branch of the adsorption isotherm [211].

2.2.3 X-ray photoelectron spectroscopy (XPS)

X-ray photoelectron spectroscopy (XPS) was carried out in a PHI Versa Probe apparatus, using a 187.85 eV band-pass energy, a 45° take-off angle and an X-ray spot size of 100.0 μm. Data analysis was performed using Casa XPS software.

2.2.4 Field emission scanning electron microscopy (FESEM)

The morphology of the different catalysts was investigated via field emission scanning electron microscopy (FESEM), using a Zeiss Merlin equipped with a Gemini-II column. Prior to the morphological analysis, the powder was coated with a 5 – 7 nm thick layer of Cr or Pt via sputter deposition, to improve the surface conductivity.

2.2.5 Energy dispersive X-ray spectroscopy (EDX)

The sample composition was estimated via energy-dispersive X-ray spectroscopy (EDX) using the Zeiss Merlin FESEM equipment and an Oxford x-act X-ray detector; this analysis was performed on non-coated powder.

2.2.6 Transmission electron microscopy (TEM)

The morphology of some catalysts was further investigated by means of Transmission Electron Microscopy on a FEI Tecnai F20 Super-Twin microscope equipped with a EDAX detector (30 mm^2 active area) for Energy Dispersive X-ray Spectroscopy (EDX). Concerning the sample preparation, the powders were dispersed in high-purity ethanol via sonication and subsequently drop-casted on Au holey carbon TEM grids.

2.2.7 Diffuse reflectance UV-Visible-NIR spectroscopy

Diffuse reflectance UV-Visible-NIR spectra of some catalysts were collected in the 200 – 1500 nm range with an Agilent CARY 5000 spectrophotometer.

2.2.8 Temperature programmed techniques

Different types of temperature programmed techniques were employed to investigate the oxygen availability, the reducibility or the acid-base properties of the catalysts.

CO temperature programmed reduction (CO-TPR)

The release of oxygen from the catalyst lattice during CO oxidation in the absence of gaseous O_2 was observed via CO-TPR. This analysis was carried out in a quartz U-tube reactor (4 mm internal diameter) containing a bed of 150 mg of SiO_2 (Sigma-Aldrich) and 45 mg of catalyst powder, placed inside a PID-controlled furnace. Before the analysis, the catalytic bed was pre-treated at 150 °C, flowing 100 mL min^{-1} of air for 1 h and then flushing with pure N_2 for 30 min. The reactor was then heated from room temperature to 700 °C with a rate of 10 °C min^{-1} under a 100 mL min^{-1} flow of 2000 ppm of CO in N_2. The concentration of CO and CO_2 in the outlet was continuously monitored with an ABB Uras 14 non-dispersive infrared (NDIR) analyzer.

Soot temperature programmed reduction (soot-TPR)

The release of oxygen from the catalyst lattice during soot oxidation in the absence of gaseous O_2 was observed via soot-TPR. This analysis was carried out with the same set-up used for CO-TPR, i.e. using a quartz U-tube reactor in a PID-controlled furnace. This time, the bed was prepared with 150 mg of silica, 45 mg of catalyst powder and 5 mg of Printex-U synthetic soot (Degussa), mixed together in a ball mill at 290 rpm for 15 min. Before the analysis, the catalytic bed was pre-treated at 100 °C, flowing 100 mL min^{-1} of pure nitrogen for 1 h. The reactor was then heated from room temperature to 800 °C at a rate of 10 °C min^{-1} under a 100 mL min^{-1} flow of pure N_2. The concentration of CO and CO_2 in the outlet was continuously monitored with an ABB Uras 14 NDIR analyzer.

H_2 temperature programmed reduction (H_2-TPR)

The catalyst reducibility was studied via H_2-TPR in a Thermo Scientific 1100 TPDRO equipped with a TCD detector. Some catalyst powder (50 mg) was placed in a quartz reactor, between two quartz wool layers. An oxidative pre-treatment was carried out by heating the sample up to 550 °C with a 10 °C min^{-1} ramp in O_2 flow, maintaining this temperature for 50 min and then flushing the reactor with N_2. During the analysis, the sample was heated from room temperature up to 900 °C with a 10 °C min^{-1} ramp, under a 20 mL min^{-1} flow of 5% H_2 in Ar.

O_2 temperature programmed desorption (O_2-TPD)

Oxygen release was further studied via O_2-TPD, which was performed in a Thermo Scientific 1100 TPDRO equipped with a TCD detector. Some catalyst powder (100 mg) was pretreated in O_2 at 550 °C for 30 min, keeping the oxygen flow during the successive cooling and then flushing the reactor with He for 30 min. The desorption was performed by heating the reactor from room temperature up to 950 °C with a 5 °C min^{-1} ramp under a 20 mL min^{-1} flow of He.

NH_3 temperature programmed desorption (NH_3-TPD)

In order to study the acid sites at the surface of the catalysts, NH_3-TPD was performed in the Thermo Scientific 1100 TPDRO. Some catalyst powder (100 mg) was pretreated at 550 °C for 2 h in He flow, then the acid sites at the surface were saturated by flowing 20 mL min^{-1} of a mixture containing 10% NH_3 in He at 100 °C for 30 min. After flushing away physisorbed ammonia by flowing pure He for 30 min at 120 °C, desorption was carried out by heating the reactor up to 600 °C with a 10 °C min^{-1} ramp under a 20 mL min^{-1} flow of He.

CO_2 temperature programmed desorption (CO_2-TPD)

In order to study the basic sites at the surface of the catalysts, CO_2-TPD was performed in the Thermo Scientific 1100 TPDRO. Some catalyst powder (100 mg) was pretreated at 550 °C for 2 h in He flow, then the basic sites at the surface were saturated by flowing 20 mL min^{-1} of pure CO_2 at RT for 30 min. After flushing away physisorbed CO_2 by flowing pure He for 30 min at 50 °C, desorption was carried out by heating the reactor up to 600 °C with a 10 °C min^{-1} ramp under a 20 mL min^{-1} flow of He.

2.2.9 Raman spectroscopy

The defectiveness of the catalysts was studied through Raman spectroscopy, carrying out both ex situ and in situ analyses.

All the Raman measurements were performed using a Renishaw InVia Reflex micro-Raman spectrometer, equipped with a cooled CCD detector. Excitation was obtained with a solid-state laser emitting monochromatic light at a wavelength of 514.5 nm. The spectra were collected under a 5x objective with a total acquisition time of 225 s, using a laser power of 10 mW.

The data were carefully analyzed with the Renishaw software WiRE 3.4. Fitting and deconvolution of the spectra allowed to monitor position, intensity, width and area of the Raman peaks. The D/F_{2g} value, representative of the defect abundancy, was calculated as the ratio between the area of the deconvolved defect-associated Raman bands (D) and the area of the main vibrational feature of ceria lattice (F_{2g}).

In situ Raman analyses at high temperature

In situ Raman analyses were performed using a Linkam TS1500 cell connected to a temperature controller. A 45 mL min^{-1} gas flow was sent into the cell during the tests, exposing the sample to the desired atmosphere. In order to avoid powder displacement during the analysis, catalyst tablets were prepared by compressing some powder into a press. The morphology of the nano-powders was not altered by this procedure, as demonstrated by Figure 2.2. A small part of a tablet was placed in a tungsten crucible inside the Linkam cell, which was then inserted in the Raman spectrometer as shown in Figure 2.3.

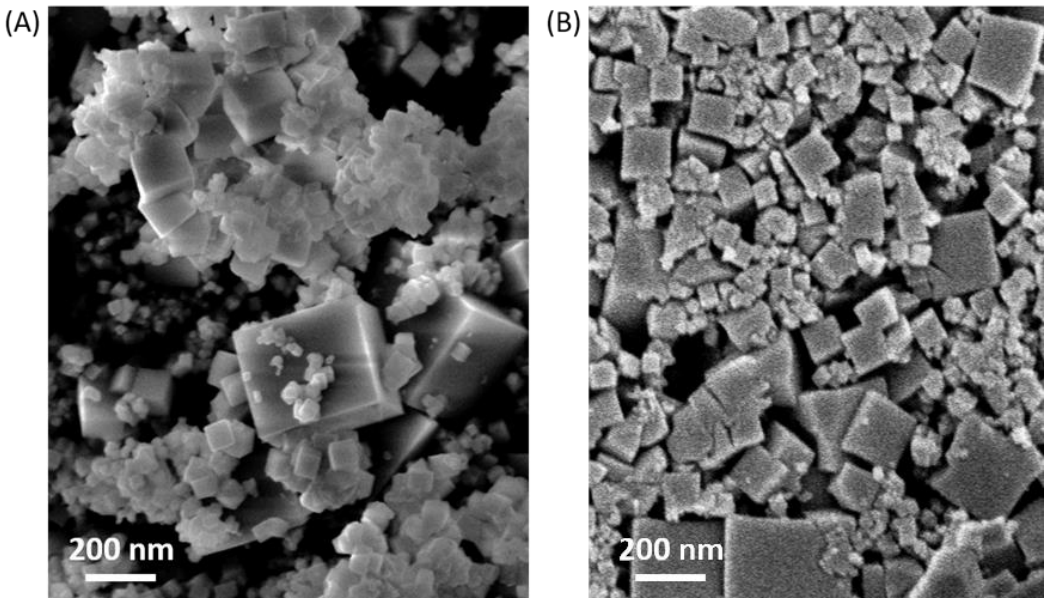

Figure 2.2. FESEM micrographs of a CeO_2 catalyst in powder (A) and after compression to prepare a tablet (B). The pictures show no significant morphological changes due to the applied pressure [212].

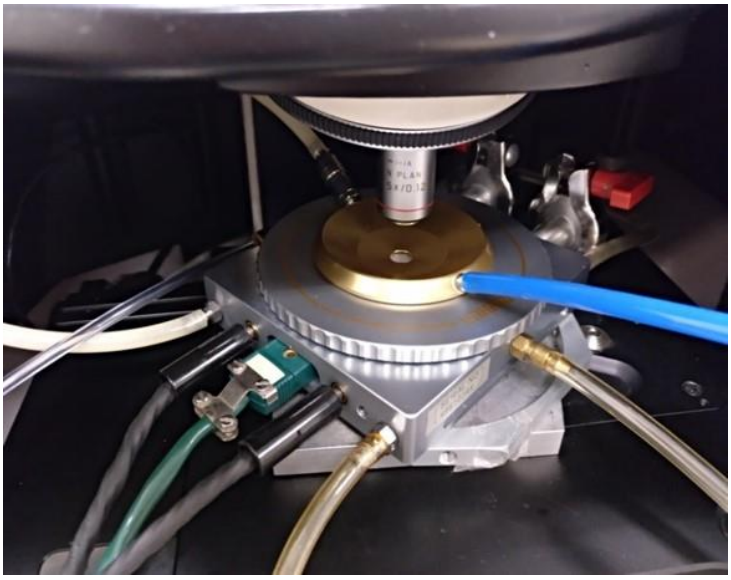

Figure 2.3. Linkam cell mounted in the Raman spectrometer.

Different types of test were carried out in the in situ cell, changing both the temperature and the gas atmosphere, in order to observe how the catalyst structure varies during and after a reaction. Further details about the operating conditions will be provided in the following chapters.

2.3 Catalytic activity

Different types of temperature programmed oxidation (TPO) tests were carried out in order to assess the catalytic activity of the samples towards various oxidation reactions.

The general setup used for TPO catalytic tests consisted of a quartz U-tube reactor with a 4 mm inner diameter, housed in a PID-controlled furnace. A K-type thermocouple was placed into the U-tube, with the sensor tip as close as possible to the fixed catalytic bed in the reactor. A by-pass line was used to let the feed gas concentration stabilize before starting the tests. The CO and CO_2 concentration in the reactor outlet was monitored with an ABB Uras 14 continuous NDIR gas analyzer; furthermore, an Emerson XStream X2GP NDIR/paramagnetic analyzer was employed for measuring the concentration of NO, NO_2 or O_2.

Temperatures corresponding to 10%, 50% and 90% of conversion (denoted as $T_{10\%}$, $T_{50\%}$ and $T_{90\%}$, respectively) were often taken as indices of activity to compare the performances of different samples.

2.3.1 CO oxidation

For CO oxidation tests, the catalytic bed was prepared with 100 mg of catalyst. The bed was pre-treated at 100 °C for 30 min under a 50 mL min^{-1} flow of air. The reactor was then cooled to 50 °C, while a mixture containing 1000 ppm of CO and 10% or 1% of O_2 in N_2 was sent to the by-pass line, with a flow rate of 50 mL min^{-1}. After the concentration of CO, CO_2 and O_2 had stabilized, the flow was sent to the reactor. Upon reaching the steady state, the gas composition at the outlet was recorded and then the oven temperature was increased by 50 °C or less. This procedure was repeated several times, sampling a sequence of steady states until total CO conversion was reached.

A blank test was performed in the same way, except preparing the reactor bed with 100 mg of SiO_2.

2.3.2 NO oxidation

For NO oxidation tests, the catalytic bed was prepared by mixing with a spatula 45 mg of catalyst and 150 mg of SiO_2. The bed was pre-treated at 100 °C for 30 min under a 100 mL min^{-1} flow of air. The reactor was then cooled to 50 °C, while a 100 mL min^{-1} flow of a mixture containing 550 ppm of NO and 10% of O_2 in N_2 was sent to the by-pass line. After the concentrations of NO, NO_2 and O_2 had stabilized, the flow was sent to the reactor. After reaching the steady state, the gas composition at the outlet was recorded and then the oven temperature was

increased by 50 °C. This procedure was repeated several times, sampling a sequence of steady states between 50 and 650 °C.

2.3.3 VOCs oxidation

Two different tests were carried out to investigate the catalytic activity towards ethylene and propylene complete oxidation. The catalytic bed was prepared with 100 mg of catalyst, and it was pre-treated at 100 °C for 30 min under a 50 mL min^{-1} flow of air. The reactor was then cooled to 50 °C, while a mixture containing 500 ppm of the VOC (ethylene or propylene) and 1% or 10% of O_2 in N_2 was sent to the bypass line, with a flow rate of 50 mL min^{-1}. After the concentrations of CO, CO_2 and O_2 had stabilized, the flow was sent to the reactor. Upon reaching the steady state, the gas composition at the outlet was recorded and the oven temperature was increased by 50 °C or less. The procedure was then repeated several times, in order to sample a sequence of steady states at different temperatures, until total VOC oxidation was reached.

For the sake of comparison, blank tests were performed in the same way, except preparing the reactor bed with 100 mg of SiO_2.

2.3.4 Soot oxidation

The soot oxidation tests were performed on a catalytic bed containing 45 mg of catalyst, 150 mg of SiO_2 and 5 mg of Printex-U synthetic soot (Degussa). Two different contact conditions were investigated: *loose contact* (LC) conditions were obtained by gently mixing the solid mixture with a spatula for 3 min, while *tight contact* (TC) conditions were achieved by mixing the powders in a ball mill (Giuliani Tecnologie) at 290 rpm for 15 minutes. The catalytic bed was then inserted in the reactor and pre-treated at 100 °C for 30 min under a 100 mL min^{-1} flow of air. Afterwards, a mixture of 1% or 10% of O_2 in N_2 was sent to the reactor with a flow rate of 100 mL min^{-1}. The furnace temperature was then raised continuously with a 5 °C min^{-1} ramp from 100 up to 750 °C.

For the sake of comparison, uncatalyzed soot oxidation was also performed with the same procedures, except preparing the bed with 195 mg of SiO_2 and 5 mg of Printex-U soot.

Soot oxidation tests in isothermal mode were carried out by pretreating the bed of catalyst and soot at 100 °C for 60 min under a 100 mL min^{-1} flow of pure nitrogen. Afterwards, the furnace was heated up to 450 °C while flowing a mixture of O_2 (1, 5 or 10 %) in N_2 into the bypass line. After reaching a stationary state, the flow was directed to the hot reactor and the quantity of CO and CO_2 produced over time were recorded, keeping the temperature constant.

Soot oxidation tests in the presence of additional gaseous species were also performed; further details will be provided in the concerned chapter.

Chapter 3

In situ Raman analyses of the soot oxidation reaction over ceria-based nanocatalysts

The study presented in this chapter was published, with modifications, as [203]:

Sartoretti, E.; Novara, C.; Giorgis, F.; Piumetti, M.; Bensaid, S.; Russo, N.; Fino, D. In situ Raman analyses of the soot oxidation reaction over nanostructured ceria-based catalysts. *Sci. Rep.* **2019**, *9*, 3875, doi:10.1038/s41598-019-39105-5.

3.1 Introduction

As discussed in the general introduction of this thesis (Chapter 1), diesel vehicles, which are appreciated for their great efficiency and fuel economy, are nowadays equipped with a particulate filter that can entrap fine dusts. This filter must be periodically regenerated, and 600 °C should be reached to cause the combustion of carbon particles, while the exhaust gas temperature of a diesel engine is usually much lower [115,119]. The use of catalysts dispersed on the filter walls allows to lower the regeneration temperature, reducing fuel consumption and the associated CO_2 emission, besides avoiding excessive thermal shock for the materials [33,114].

To this end, many studies have been focused on ceria-based materials, since they offer a good activity due to their ability to release or absorb oxygen atoms, which confers them a high oxygen storage capacity [213–215]. The ability of a catalyst to lower the temperature required for particulate combustion does not only depend on its intrinsic activity; actually, since the reaction involves two solid phases, the efficiency of contact between catalyst and particulate matter also plays a fundamental role [152,184]. For this reason, many advances have been made in

the synthesis of nanostructured ceria-based catalysts, whose reactivity depends not only on the particle size but also on the crystalline planes exposed on the surface, as pointed out in several studies [144–146]. The presence of surface defects, e.g. oxygen vacancies, can affect the final activity too [141,216]. To increase the number of surface defects, dopant atoms can be inserted into the crystalline lattice, and this often also provides the material with greater thermal stability, increased oxygen mobility and reducibility of cerium atoms [140]. Both rare earth elements and transition metals can be used as dopants [142,217]. In particular, previous studies have demonstrated the positive effects of Cu or Mn addition, ascribed to the coupled redox cycles between cerium and copper or manganese ions [31,165,218,219].

Thanks to its remarkable sensitivity to the microstructural evolution of the analyzed samples, Raman spectroscopy has become widespread in recent years in various research fields concerning materials science, including catalysis. Regarding ceria-based catalysts, this technique has been used to investigate the interaction of molecules with their surface or the defects present in the lattice [201]. Indeed, defect sites have been found to influence ceria catalytic activity, playing an important role in catalysis [141]. However, up to now the evolution of defects with temperature in doped systems and during the catalytic activity has been poorly investigated. In particular, monitoring the defect sites throughout the soot oxidation reaction presents several complexities [202] and only few observations of this process have been reported [189].

In this chapter, four nanostructured ceria-based catalysts (pure CeO_2 nanocubes, 5% Cu doped CeO_2 , 5% Mn doped CeO_2, 2.5% Cu and 2.5% Mn doped CeO_2) prepared through hydrothermal synthesis [143] were studied by in situ Raman spectroscopy at high temperature and during soot oxidation. Temperature-dependent Raman analyses were performed on the catalysts, studying the evolution of the identified defect sites in different atmospheres. The performance of the ceria-based nanoparticles in soot oxidation was then investigated and the results compared to standard activity tests, through the calculation of Raman-based soot conversion curves. The role of the different defect sites was discussed, analyzing their behavior in terms of the proposed mechanisms for soot oxidation.

3.2 Experimental methods

A general description of the experimental methods used for catalyst preparation, characterization and testing was provided in Chapter 2. However, for the sake of clarity and simplicity, a brief presentation of the studied samples is reported here, together with some further details about the analyses which were performed.

In the present chapter, four different catalysts are considered: the CeO_2 sample is made of pure ceria, while the other samples, named Ce95Cu5, Ce95Mn5 and Ce95Cu2.5Mn2.5, are made of ceria doped with 5% Cu, 5% Mn, and 2.5% Cu together with 2.5% Mn, respectively. All the catalysts were obtained via the

hydrothermal procedure described in Chapter 2 and were calcined in air at 550 °C for 4 h [143].

The four catalysts were studied using different characterization techniques, to identify the main physico-chemical and morphological characteristics of each sample; in detail, XRD, N_2-physisorption, FESEM and XPS analyses were performed. The catalytic activity towards soot oxidation was evaluated as well. Some of the results obtained (except for Ce95Mn5) were published in [143], but a brief summary will be reported in the next section for the sake of completeness.

3.2.1 Raman analyses

A deep study via ex situ and in situ Raman spectroscopy was carried out, in order to study the material defectiveness and its evolution during soot oxidation.

Raman spectra were acquired using a 514.5 nm excitation wavelength and were carefully analyzed with the Renishaw software WiRE 3.4, in order to perform the fitting and deconvolution of the peaks and to calculate for each of them position, intensity, width and area. Except for the pure ceria catalyst, three Lorentzian curves were used to fit the defect (D) band, whose centers were initially set at the typical Raman shifts reported by the previous literature for the different defect sites. The final contribution (null for the D3 peak for some catalysts) and the parameters of each curve were determined by the software optimization algorithm (using the Root Mean Square method). The D/F_{2g} value, representative of the defect density, was calculated as the ratio between the integrated areas of the deconvoluted defect-related Raman bands (D) and the main vibrational component related to the ceria lattice (F_{2g}). RT measurements were repeated in different points of each catalyst and the deconvolution of the spectra led to reproducible results.

Static Raman analyses at high temperature

These analyses were carried out using the Linkam TS1500 cell housed in the Raman spectrometer. Some powder was placed in a tungsten crucible, which was then inserted in the Linkam cell. After having recorded a spectrum at RT (RT_i), the cell was heated up to 100 °C with a rate of 10 °C min^{-1}, and it was then left at this temperature for ten minutes before recording a new Raman spectrum. This procedure was similarly repeated for the other considered temperatures, up to 700 °C. Afterwards, the cell was cooled to 350 °C, and after waiting ten minutes a spectrum was collected ($350°C_{cool.}$). Finally, the sample was cooled to RT, and ten minutes later a spectrum was recorded ($RT_{cool.}$).

Raman analyses in air flow at high temperature

These analyses were carried out heating the cell with a constant rate of 3 °C min^{-1}, continuously, up to 700 °C. Furthermore, a 45 mL min^{-1} air flow was sent into the cell during the heating phase, while a 45 mL min^{-1} pure nitrogen flow was flushed during the cooling phase. In order to prevent the gas flow from displacing

the powder, the tests were performed on catalyst tablets, obtained by compressing some powder into a press. A small portion of a tablet was inserted into the cell crucible, perpendicular to the laser beam. After recording the spectrum at RT (RT_i), the cell was heated and spectra at various temperatures were collected. Once the 700 °C spectrum had been recorded, the temperature was kept constant and pure nitrogen was fluxed for 15 min; then a new spectrum was acquired at 700 °C, that would allow to detect any changes induced by the variation of the atmosphere. Finally, during the cooling phase two spectra were measured at 350 °C ($350°C_{cool.}$) and after reaching RT ($RT_{cool.}$).

In situ Raman analyses of soot oxidation

These measurements were carried out on tablets of catalyst and soot, prepared by mixing adequate quantities of catalyst and Printex-U particulate in a ball mill and then compressing the resulting powder in a press. In this way, "tight" contact conditions were obtained, with a high degree of contact between the two solids. A catalyst-soot weight ratio of 40:1 was chosen, so that the Raman signal of the soot did not completely cover the peaks associated to the presence of defects in the catalyst. A 45 mL min^{-1} air flux was sent into the cell during both the heating and cooling phases. After all the soot in the tablet had been converted, the cell was cooled down and two spectra were measured at 350 °C ($350°C_{cool.}$) and at RT ($RT_{cool.}$).

3.3 Results and discussion

3.3.1 Catalyst characterization

The synthesized catalysts were first characterized through complementary techniques in order to investigate their morphology, crystalline structure, surface area and surface species; some of the results obtained were previously reported elsewhere [143], but are briefly resumed in Table 3.1 to present a complete description of the investigated materials.

Figure 3.1 shows the FESEM micrographs of the four catalysts. The CeO_2 sample presents a well-defined nanocubic morphology, with the size of the cubes ranging from 100 to 300 nm and many (1 0 0) planes exposed [220,221]. The presence of nanocubes has been linked to better performances in the catalytic oxidation of both carbon monoxide and particulate matter [135,146,215]; concerning the latter reaction, the effect of morphology is more evident, since the shape of ceria nanoparticles directly affects the density of contact points between the catalyst and soot [185]. Also the 5% Mn doped catalyst (Ce95Mn5) maintains a morphology similar to that of CeO_2, but with smaller nanocubes, whose size ranges from 50 to 100 nm. On the contrary, when copper is introduced into ceria lattice, the nanocubes disappear. Both the 5% Cu doped (Ce95Cu5) and 2.5% Cu, 2.5% Mn doped (Ce95Cu2.5Mn2.5) catalysts are formed by small particle

agglomerates, probably consisting of nanoparticles characterized by high-index planes, like nanopolyhedra [155]; for both of the samples, the nanoparticles have average sizes between 20 and 40 nm.

Table 3.1. Some properties of the synthesized catalysts obtained by XRD, N_2-physisorption and XPS [143].

Catalyst	D_C [a] [nm]	SSA [b] [$m^2\,g^{-1}$]	V_p [b] [$cm^3\,g^{-1}$]	D_p [b] [nm]	O_α [c] [% at.]	O_β [c] [% at.]	Ce^{3+} [c] [% at.]
CeO_2	135	9	0.03	12	31	69	21
Ce95Cu5	34	46	0.16	14	29	71	26
Ce95Mn5	79	17	0.05	12	33	67	22
Ce95Cu2.5Mn2.5	23	52	0.15	11	40	60	26

[a] Average crystallite size (D_C) estimated via XRD

[b] Specific surface area (SSA), pore volume (V_p) and pore diameter (D_p) obtained via N_2-physisorption

[c] Superficial O_α, O_β and Ce^{3+} abundance evaluated via XPS

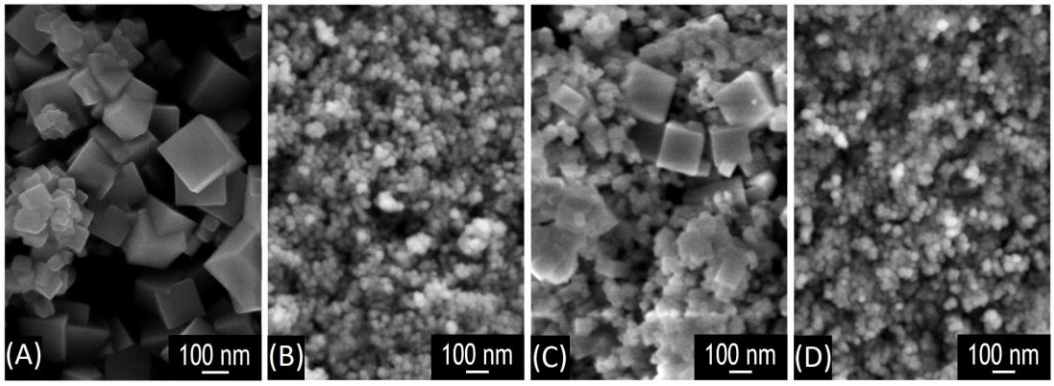

Figure 3.1. FESEM micrographs of the CeO_2 (A), Ce95Cu5 (B), Ce95Mn5 (C) and Ce95Cu2.5Mn2.5 (D) catalysts.

The crystallite size was also investigated through XRD and the D_c values calculated with the Scherrer's equation, reported in Table 3.1, are in good agreement with the FESEM observations. Mixed oxides have indeed a smaller D_c than pure CeO_2, and the two Cu-doped catalysts present the lowest D_c values. However, all the powder XRD diffractograms, displayed in Figure 3.2, exhibit the typical pattern of the crystalline fluorite structure of ceria. A shift of the (1 1 1) peak to higher 2θ values is visible for the doped samples, and it is probably due to ceria lattice shrinkage, since the ionic radii of copper and manganese are smaller than those of cerium ions [222].

Previous results are in accordance with those obtained from N_2-physisorption, reported in Table 3.1. The pure ceria sample has the lowest specific surface area, while this is definitely higher for all the doped catalysts. In particular, copper seems to have a greater tendency to increase SSA, and this can be explained considering the lower crystallite size of the Ce95Cu5 and Ce95Cu2.5Mn2.5

samples revealed by the XRD and FESEM results. The total pore volume V_p follows the same order of the specific surface area, while the average pore diameter D_p presents comparable values for the four samples.

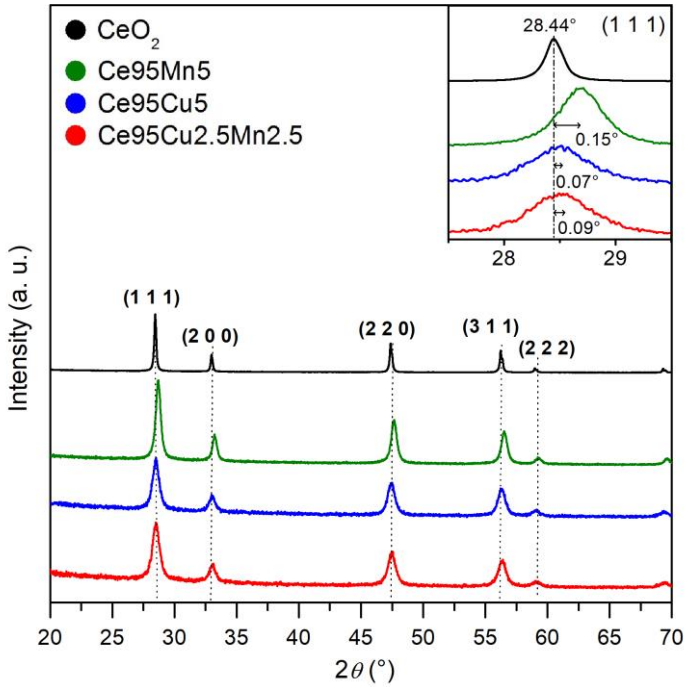

Figure 3.2. XRD diffractograms of the prepared samples, with a magnification of the (1 1 1) peak in the inset.

Surface oxygen species of the four catalysts were investigated by analyzing the O 1*s* XPS spectra, shown in Figure 3.3 A. Their deconvolution allows to estimate the amount of capping oxygen species on the surface, the so-called "O_α", compared to the quantity of "O_β" oxygen atoms in the ceria lattice [223,224]; the relative abundances of these two oxygen species in the four catalysts are reported in Table 3.1. The CeO_2, Ce95Cu5 and Ce95Mn5 samples present similar relative quantities of O_α species. Instead, in the Ce95Cu2.5Mn2.5 catalyst, the quantity of O_α is significantly higher. An increase of O_α atoms can favor oxygen spillover at solid surfaces.

The presence of reduced Ce^{3+}, often associated with oxygen vacancies, was instead investigated by the analysis of Ce 3*d* XPS spectra, which are reported in Figure 3.3 B. Eight peaks can be identified; only the v_1 and u_1 peaks are ascribed to Ce^{3+} species, while the other peaks are associated with the presence of Ce^{4+} species [217,225]. Through the deconvolution of the peaks, the relative abundance of the Ce^{3+} species in the four synthesized catalysts can be estimated; such values are summarized in Table 3.1. The CeO_2 and Ce95Mn5 catalysts have similar relative amounts of Ce^{3+} species at the surface, while the Ce95Cu5 and Ce95Cu2.5Mn2.5 samples contain higher percentages of Ce^{3+}. This observation suggests that copper addition promotes the formation of Ce^{3+} and redox sites at the surface more than manganese insertion; moreover, this effect is already

evident for low Cu percentages, since there are minimal differences between the Ce95Cu5 and Ce95Cu2.5Mn2.5 samples [143].

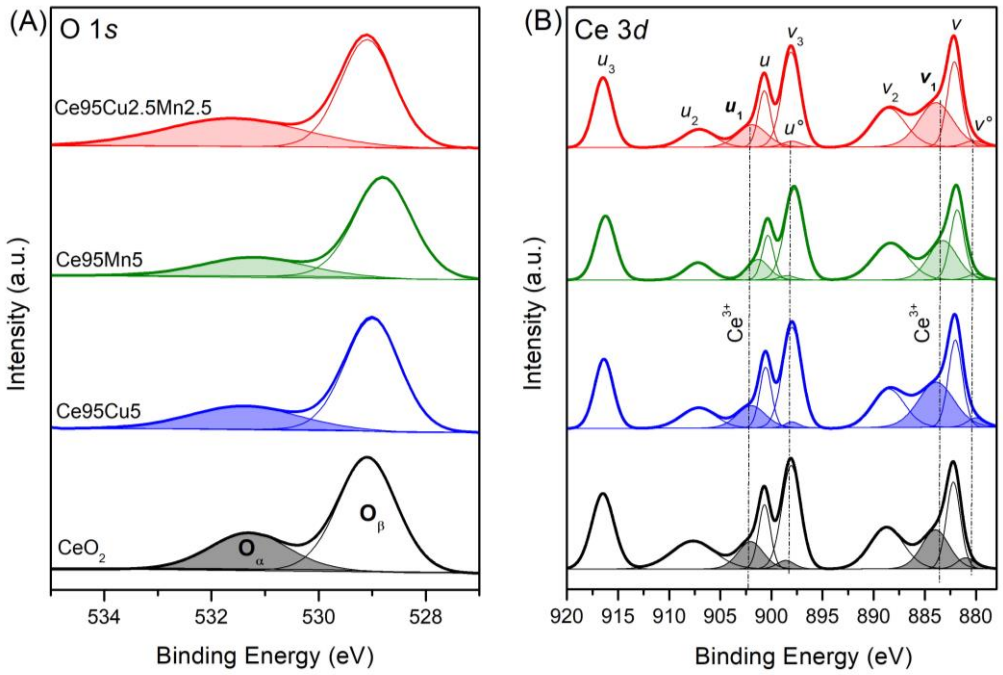

Figure 3.3. XPS spectra of the four samples in the O 1*s* (A) and Ce 3*d* (B) core levels. The traces obtained by curve fit and deconvolution of the bands are also reported.

The XPS Cu 2*p* and Mn 2*p* spectra are not shown, since the low quantities of doping elements (5% or 2.5%) are associated with peaks characterized by very low intensities and hard to be observed or deconvoluted.

3.3.2 Catalytic activity

Soot oxidation tests in tight contact conditions were carried out to investigate the performances of the four catalysts [143]. The soot conversion as a function of temperature, reported in Figure 3.4 A, was calculated by monitoring the concentration of CO and CO_2 at the reactor outlet (Figure 3.4 B and C). Temperatures corresponding to 10%, 50% and 90% conversion (denoted as $T_{10\%}$, $T_{50\%}$ and $T_{90\%}$, respectively) were taken as indices of activity and are reported in Table 3.2. The inset in Figure 3.4 A shows the magnification of the curves between 260 and 340 °C. In this range, soot conversion appears higher for Ce95Cu2.5Mn2.5 and Ce95Cu5 and this is probably related to their higher specific surface area and the initial availability of reduced D3 sites, as detailed in the successive discussion. Above 400 °C, the Ce95Mn5 sample is the most performing catalyst in the series, since the trend of $T_{50\%}$ follows this order: Ce95Mn5 < CeO_2 < Ce95Cu5 < Ce95Cu2.5Mn2.5 (Table 3.2). At high temperature the effect of morphology seems thus to overcome the effect of dopants and a structure-sensitive behavior can be observed. The nanocubic structure of Ce95Mn5 and CeO_2, characterized by reactive low-index planes,

apparently plays an important role in soot oxidation, as already supposed in previous investigations [146,155].

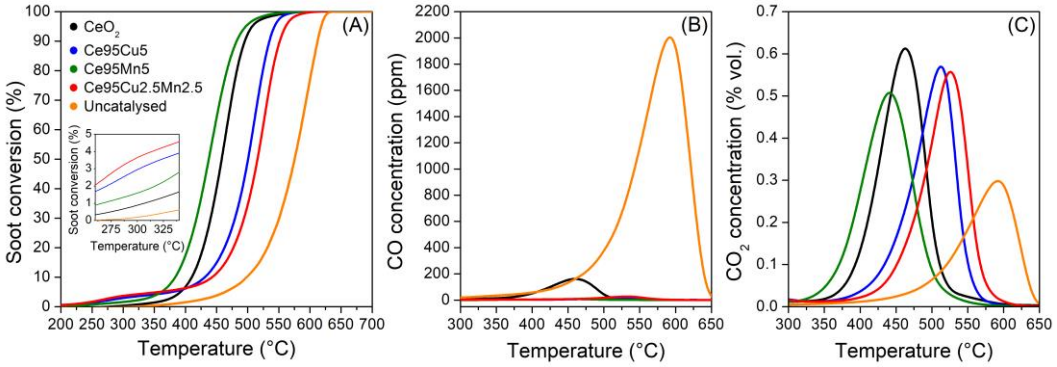

Figure 3.4. Conversion of soot as a function of the temperature during the oxidation tests in tight contact (A), with a magnification of the curves between 260 and 340 °C in the inset; concentration of CO (B) and CO_2 (C) produced during the soot oxidation tests [143].

Table 3.2. Catalytic performance parameters obtained from the soot oxidation tests.

Catalyst	$T_{10\%}$ [°C]	$T_{50\%}$ [°C]	$T_{90\%}$ [°C]
CeO_2	409	455	494
Ce95Cu5	430	503	533
Ce95Mn5	382	436	481
Ce95Cu2.5Mn2.5	441	516	552

All these catalysts are able not only to lower the reaction temperature but also to enhance the selectivity of the reaction towards CO_2, as can be concluded observing Figure 3.4 B and C showing the CO and CO_2 concentration produced during the soot oxidation tests. CeO_2 is the most unselective catalyst as it produces the highest CO concentration, while Ce95Cu5 is the most selective towards CO_2.

3.3.3 Raman analyses

Raman analyses at room temperature

Raman spectroscopy can provide useful information about the influence of dopants on ceria structure and on the formation of new defective sites. Raman spectra recorded on ceria-based materials can show several peaks related to both bulk ceria vibrational modes and surface defects. Some of the most significant and sometimes controversial assignments provided by the literature are gathered in Table 3.3.

Table 3.3. Peak assignments of Raman spectra recorded on ceria-based materials at RT.

Raman shift [cm^{-1}]	Assignments of the peaks
404	Shoulder due to distortion in the lattice [201]
460 - 465	Symmetrical stretching of the Ce-O_8 crystal unit (F_{2g} mode), characteristic of the fluorite lattice structure [143,201,234–239,226–233]
487	Shoulder due to distortion in the lattice [201]
540	Defect spaces which include an O^{2-} vacancy, observed when 3+ dopant cations are introduced in the CeO_2 lattice [226]
	Extrinsic oxygen vacancy complexes [234]
550	Oxygen vacancies [143,235,236]
	Extrinsic oxygen vacancies [227,229]
560	Oxygen vacancies [230,237,238]
570	Oxygen vacancies in pure and cation-doped ceria [228,232]
580	Intrinsic oxygen vacancies [239]
590 - 600	Defect spaces including a dopant cation in 8-fold coordination of O^{2-}, without any O^{2-} vacancy [226,227,230,235]
	Vacancy-interstitial Frenkel-type oxygen intrinsic defects in ceria [143,201,228,238]
	Oxygen vacancies and reduced Ce^{3+} cations in the ceria lattice [229,231,233,234,236]
620	Extrinsic MO_8 sites capable of delivering oxygen under reducing conditions i.e. part of a Frenkel defect [231]
630	Extrinsic defect band [143]

Figure 3.5 A shows the Raman spectra of the four different samples collected at RT, each obtained from the average of three spectra recorded in different points of the sample. All the spectra have been normalized to the most intense peak, namely the F_{2g} peak, located at about 464 cm^{-1} and ascribed to the symmetric stretch mode of the $Ce - O_8$ crystal unit, characteristic of the fluorite lattice structure typical of ceria-based materials [143,201,234–239,226–233]. The absence of the characteristic signatures of Mn and Cu oxides in Raman spectra indicates that the doping elements are well integrated into the ceria lattice, confirming the XRD results. However, the addition of dopants causes several changes in ceria microstructure, which can be noticed in the Raman spectra.

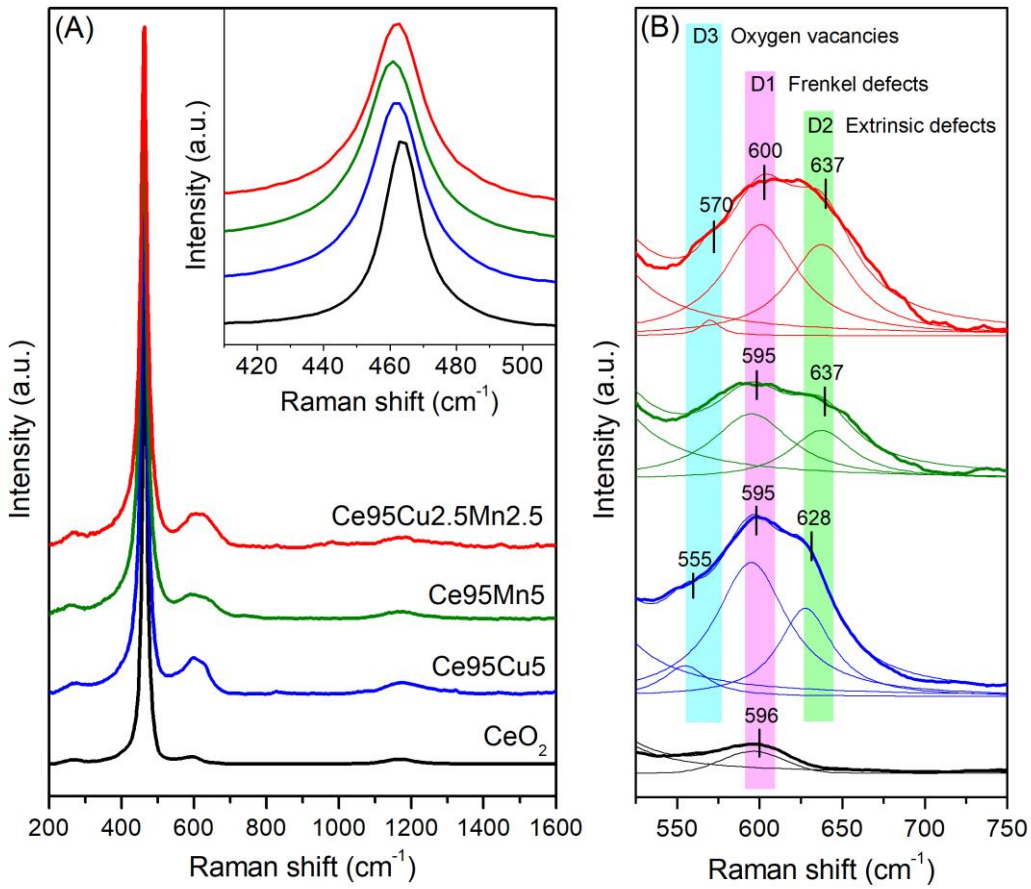

Figure 3.5. Average Raman spectra of the four catalysts at RT (A), with magnifications of the F_{2g} peak (inset) and of the defects band region (B). The traces obtained by curve fit and deconvolution of the defect-induced band are also reported (thin lines). All the spectra were normalized to the F_{2g} band.

Besides a blue-shift and a broadening of the F_{2g} band (inset of Figure 3.5 A), which may depend on the increase of topological disorder and on a higher defectiveness [240], new defect-induced bands can be identified in the 500 to 700 cm^{-1} range; Figure 3.5 B shows a magnification of this region. CeO_2 spectrum presents a single peak located at 596 cm^{-1}, previously assigned by different authors to oxygen vacancies dealing with a Frenkel anion pair, in which an oxygen atom has moved into an octahedral interstitial position generating a vacancy [143,201,228,238]. Other authors ascribed such band to oxygen vacancies associated to the presence of reduced Ce^{3+} cations [229,231,233,234,236], or to defect spaces including a dopant cation without any O^{2-} vacancy [226,227,230,235]. This vibrational feature, which from now on will be referred to as "D1", can be considered anyway "intrinsic", i.e. already present in the structure of pure ceria.

For the doped catalysts, the disorder-associated band becomes broader and more intense, and it can be deconvoluted into two different peaks. Besides the already mentioned D1, a "D2" component can be identified, centered at 628 cm^{-1} for the Ce95Cu5 sample and at 637 cm^{-1} for the Ce95Mn5 and Ce95Cu2.5Mn2.5 samples. Since the position of this band depends on the doping element, it is

probably linked to "extrinsic" defects, generated by the dopant addition. In some previous literature reports this Raman component has been ascribed to the presence of MO_8 units without associated oxygen vacancies, where M is a foreign cation [230,231]. Interestingly, in presence of dopants, also the D1 peak at 595 cm^{-1} becomes more intense, suggesting that the addition of the doping elements causes an increase in the amount of both intrinsic and extrinsic defects.

Finally, only for the Cu-containing samples a third "D3" peak can be detected, centered at about 555-570 cm^{-1} and much weaker than the other two. This component is usually assigned to oxygen vacancies coupled with the presence of Ce^{3+} or other aliovalent cations [227,229,235,236]. The presence of this peak only in Ce95Cu5 and Ce95Cu2.5Mn2.5 spectra can be linked to the higher abundance of Ce^{3+} in these samples, proved by the XPS results reported in Table 3.1. Schematic structures of the three defect types are displayed in Figure 3.6. It should be noted that a closer inspection of the defect-induced Raman band reveals that each identified component is the result of the convolution of more bands, which cannot be however clearly resolved and account for the heterogeneous environment in which a particular defect type can be found.

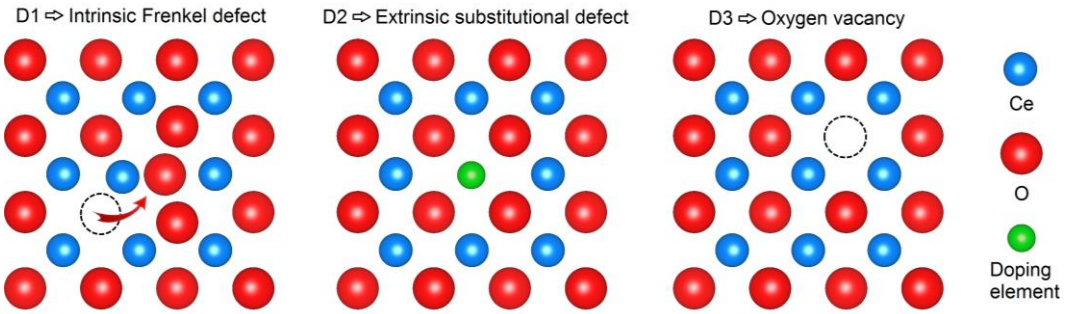

Figure 3.6. Typical literature assignments of the observed Raman components to the different types of defect sites which can be found in the ceria lattice.

The amount of defects in the four samples was estimated by calculating the ratios between the area of the D1, D2 or D3 peak and the one of the F_{2g} band; these parameters, called $D1/F_{2g}$, $D2/F_{2g}$ and $D3/F_{2g}$, respectively, are summarized in Table 3.4, together with their sum, D/F_{2g}. The data reported in Table 3.4 confirm that the addition of dopants fosters both D1 and D2 defects formation. The two Cu-doped samples show the highest D/F_{2g} ratios, due to a greater defectiveness accompanied by their higher specific surface area. The major abundance of defects in these materials is probably an effect of the strong interaction between ceria and copper, which fosters microstructural changes, and it is affected also by the type of planes exposed by the nanoparticles [241].

Several papers report that the D/F2g ratio order reflects well the trend of the catalytic activity for the CO and other gas phase oxidation reactions [142,242,243]. Such a correlation was observed also for the analyzed set of catalysts [143], suggesting that the presence of a greater number of defects promotes the conversion of CO to CO_2; indeed the specific reaction rates of CO

conversion increased according to the order CeO_2 < Ce95Mn5 < Ce95Cu2.5Mn2.5 < Ce95Cu5, in analogy to the D/F_{2g} ratio and the specific surface areas (this topic will be better discussed in Chapter 4). Instead, the trend of catalytic activity for the soot oxidation reaction is usually different, suggesting that other factors, such as the catalyst morphology or the contact points between catalyst and soot, play a more important role; in particular, ceria nanocubes and nanorods usually exhibits better performances when compared to nanopolyhedra, spindles or mesoporous polycrystalline ceria samples [146,155,192].

Table 3.4. Raman parameters calculated at RT for the four catalysts.

Catalyst	$D1/F_{2g}$	$D2/F_{2g}$	$D3/F_{2g}$	D/F_{2g}
CeO_2	0.022	-	-	0.022
Ce95Cu5	0.156	0.077	0.023	0.256
Ce95Mn5	0.078	0.046	-	0.124
Ce95Cu2.5Mn2.5	0.116	0.096	0.013	0.225

Static Raman analyses at high temperature

The four catalysts were analyzed in the 25 – 700 °C range in order to monitor the evolution of their vibrational spectral features at the catalytic temperatures. Figure 3.7 A shows the Raman spectra of the CeO_2 sample acquired in air under a static atmosphere.

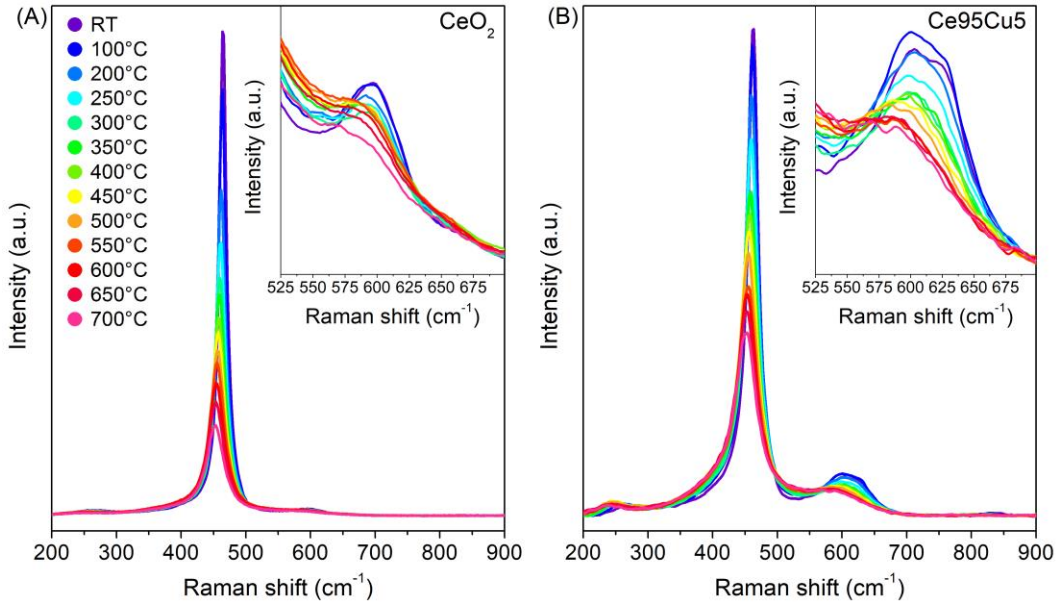

Figure 3.7. Raman spectra collected at different temperatures on the CeO_2 (A) and Ce95Cu5 (B) samples during the static tests. The insets show magnifications of the defect region.

As the temperature increases, the Raman peaks move to lower Raman shift and their width increases, while their intensity decreases. Both the position and the width of the peaks vary almost linearly with temperature. The red-shift of the peaks is mainly due to thermal induced strain; the spectral broadening and the intensity quenching are instead due to anharmonicity effects [231,244]. The temperature, however, affects differently the intensity of the Raman bands for collective and more localized modes: for this reason, it is not possible to determine if the amount of defects increases or decreases by comparing the ratios between the areas of the peaks calculated at different temperatures, as the comparison could be unreliable [207].

Similar effects are observed on the doped catalysts, as shown in Figure 3.7 B for Ce95Cu5. An unresolved D band is detected at high temperatures, due to the broadening of the three components.

After reaching 700 °C, the samples were cooled to RT. During the cooling phase, two spectra were collected at 350 °C (350°$C_{cool.}$) and 25 °C ($RT_{cool.}$). For what concerns CeO_2, the spectra recorded at the same temperatures during the heating and cooling ramp are almost overlapped, as shown in Figure 3.8 A and C. This correspondence suggests that any structural change caused by the heating is completely reversible: thus, there is no defects evolution after the thermal cycle. This could be a further confirmation of the assignment of the D1 peak to Frenkel defects, which are generally rather stable with temperature [238]. A similar reversible behavior was observed for the two Mn-doped catalysts too. On the other side, for the Ce95Cu5 sample the two spectra recorded at 350 °C overlap (Figure 3.8 D), but the ones registered at RT at the beginning and at the end of the test are quite different (Figure 3.8 B). While the F_{2g} band is unaffected by the thermal cycle, the defect band reveals a spectral change: in detail, the D1 component remains almost unchanged, but the D2 peak moves slightly to higher Raman shift and becomes more intense.

This result points out an unexpected behavior for the Ce95Cu5 catalyst, as previous literature works report either a decrease of the D/F_{2g} ratio due to particle aggregation or a reversibility of the Raman spectra after thermal cycles [207,231,237]. The variation can be quantified by comparing the $D2/F_{2g}$ ratio of the initial and final spectra: this parameter increases of 34% during the test. It can be therefore inferred that there is actually an increase in the number of D2 defects in ceria lattice during heating and that these changes are not completely reversible once returned to RT. The oxygen-rich atmosphere in this test suggests however that the formed species are related to the presence of Cu in high oxidation states, namely Cu^{2+} or even Cu^{3+}, which was detected by XANES and proposed as part of the catalytically active site in CO oxidation by Elias et al. [245].

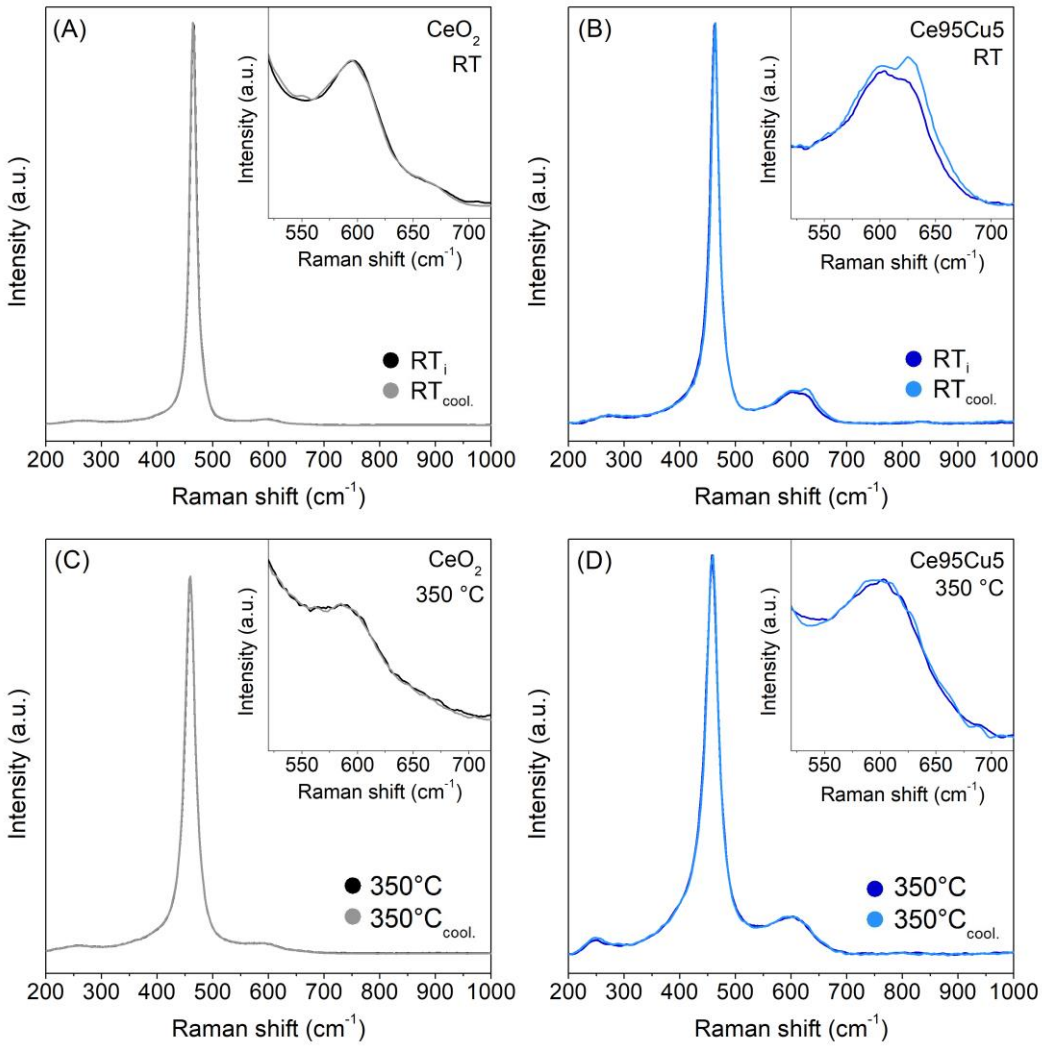

Figure 3.8. Comparisons between the Raman spectra collected on CeO_2 (A) and Ce95Cu5 (B) at RT at the beginning (RT_i) and at the end ($RT_{cool.}$) of the static tests, in which the samples were heated up to 700 °C and then cooled down in a static air atmosphere; the same comparisons are reported also at 350 °C for CeO_2 (C) and Ce95Cu5 (D). All the spectra were normalized to the F_{2g} band. The insets display a magnification of the defect region.

Raman analyses in air flow at high temperature

Once the temperature dependent spectra were acquired in a static atmosphere by allowing the system to reach the thermal equilibrium at each step, the actual conditions used in the catalytic processes were tested. The thus obtained Raman spectra are very similar to those recorded during the static analyses: although in this case the sample was kept in air flow and heated following a temperature ramp, no significant differences could be detected. An additional test was set-up in order to understand if any change involving the defect sites at high temperature could be preserved at the end of the cooling ramp. After recording the spectrum at 700 °C, pure nitrogen was fluxed into the cell. After fifteen minutes a new spectrum was acquired at 700 °C, and no differences due to the change of the atmosphere were detected.

The whole cooling phase was then conducted in nitrogen flow. Once returned to RT, a spectrum was acquired, which can be compared with the RT_i one. In the case of CeO_2 (Figure 3.9 A), only a slight increase of the band width was observed. Such change could be related to the appearance of an extremely weak shoulder due to the formation of Ce^{3+}-associated oxygen vacancies (D3 band), but the very small difference does not allow conclusive explanations. The same broadening was not observed for the Ce95Mn5 and Ce95Cu2.5Mn2.5 samples, whose RT_i and RT_{cool} spectra are almost perfectly overlapped, as happened for the static tests. This suggests that very few new oxygen vacancies are generated at high temperature in the absence of a reductant to be converted; indeed, the absence of oxygen in the atmosphere during the cooling-down should hamper its re-adsorption from the gaseous phase and the refilling of oxygen vacancies generated at high temperature, leading to an irreversible increase of the vacancy related band (D3), which is actually not clearly observed.

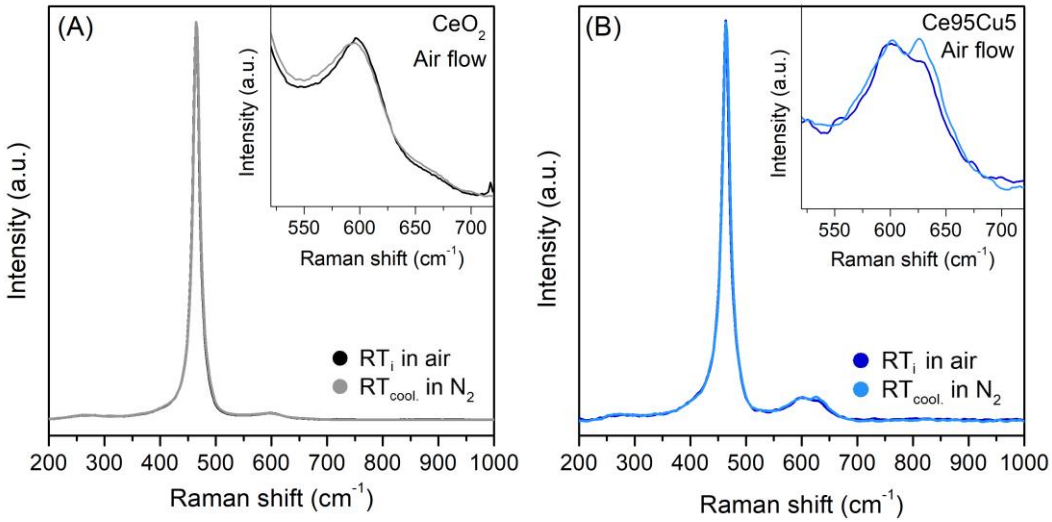

Figure 3.9. Comparison between the Raman spectra collected on CeO_2 (A) and Ce95Cu5 (B) at RT at the beginning (RT_i) and at the end ($RT_{cool.}$) of the analyses in air flow, in which the samples were heated up to 700 °C in air flow and then cooled down in N_2 flow. All the spectra were normalized to the F_{2g} band. The insets display a magnification of the defect region.

Also for the Ce95Cu5 sample, the comparison between the initial and final spectra recorded at RT, shown in Figure 3.9 B, leads to results similar to those previously obtained with the static analysis. Once again, a change in the defect region can be detected, since the intensity of the D2 component increases: the $D2/F_{2g}$ ratio varies from 0.061 at the beginning of the test to 0.083 at the end, with a 35% increase, similar to that observed in the static analysis. The absence of any effect of the nitrogen atmosphere means that the new defect sites are generated during the heating ramp and confirms their assignment to oxidized copper sites. Their formation in the early stages of the heating process is also supported by the perfect overlapping of the 350 °C spectra, recorded during the heating and cooling phases. As the presence of Cu^+ cations is often associated with an oxygen vacancy in the lattice, it could be hypothesized that oxygen vacancy filling occurs during

Cu sites oxidation, and therefore that the D2 component is actually due to a vacancy-free defect site.

The suggested assignment is further supported by an additional heating and cooling ramp in pure nitrogen atmosphere, at the end of which the increase of the D2 component and the overall raise of the D/F_{2g} ratio are negligible, as shown in Figure 3.10. Moreover, exposure of the catalyst to air at RT after this treatment readily led to an increase of the D2 component, pointing out the need of an oxidizing atmosphere to allow the formation of the discussed defect species.

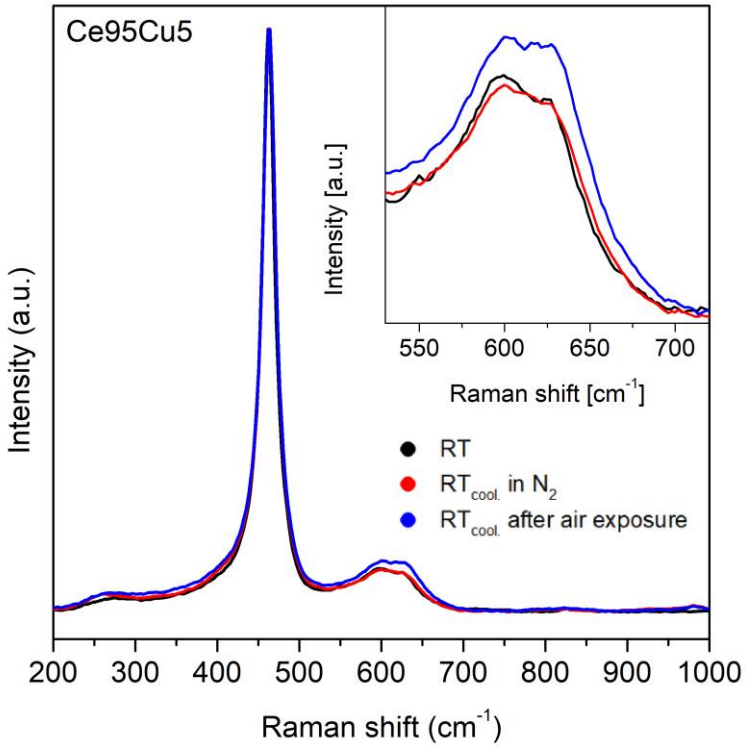

Figure 3.10. Raman spectra collected at RT on a tablet of Ce95Cu5 during an additional test in pure nitrogen atmosphere. After pure nitrogen was fluxed into the cell, the first spectrum (RT_i) was acquired. The temperature was increased with a rate of 3 °C min^{-1} until 700 °C, then the sample was cooled down to RT in N_2 flow and a spectrum was collected ($RT_{cool.}$ in N_2). Finally, air was fluxed into the cell and after 10 min a new spectrum was recorded ($RT_{cool.}$ after air exposure). All the spectra were normalized to the F_{2g} band. The inset shows a magnification of the defect region.

In situ Raman analyses of soot conversion

Figure 3.11 shows the Raman spectra recorded at RT on the four tablets prepared by mixing catalyst and soot in tight contact. When soot is added to the catalyst, in the Raman spectra two large partially overlapping bands appear, centered at about 1350 cm^{-1} and 1600 cm^{-1}, typical of amorphous carbon [246,247]. Besides these, other two minor bands are detected: one is centered at about 800 cm^{-1}, while the second extends in the range 200 – 450 cm^{-1}, partially superimposed to the F_{2g} peak; such features are typical of silica, which is present in Printex-U as a contamination (see Figure 3.12). Despite both the F_{2g} peak and the defects band of the catalyst are still visible, the Raman signal is weak due to

the huge absorption of light by soot particles. The resulting high noise does not allow a reliable interpretation of the shape of the defect bands at RT.

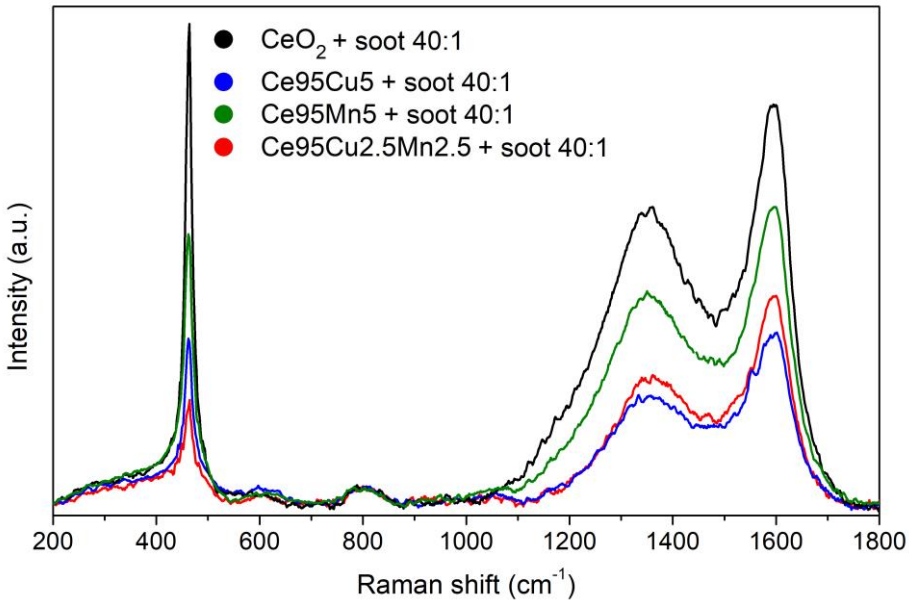

Figure 3.11. Raman spectra collected at RT on the four tablets of mixed catalyst and soot.

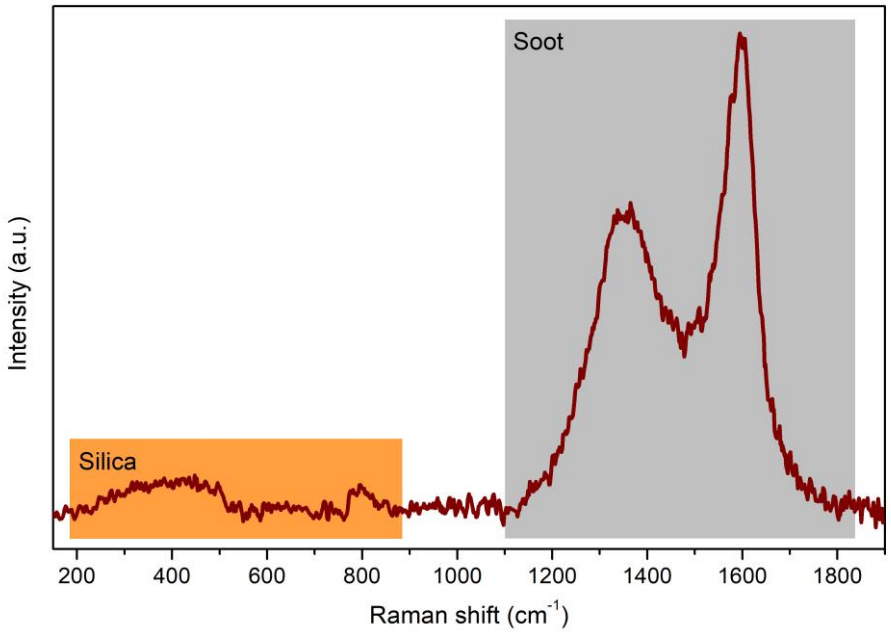

Figure 3.12. Raman spectra collected at RT on a tablet of pure Printex-U soot, in which silica bands are visible.

Figure 3.13 shows the Raman spectra recorded during the in situ tests on the four tablets of catalyst and soot. Generally, at the beginning of the test, all the Raman peaks, including the typical vibrational features of soot, move to lower Raman shift and become larger and less intense as the temperature increases, due to the effect of heating on the vibrational properties of the materials, as detailed

above. At a certain temperature, soot conversion starts and soot related peaks quickly lose intensity; meanwhile all the typical modes of ceria become more intense due to the reduction in light absorption caused by the decrease of the soot content in the tablets. Once soot is totally converted, the peaks of the catalysts begin to lose intensity again.

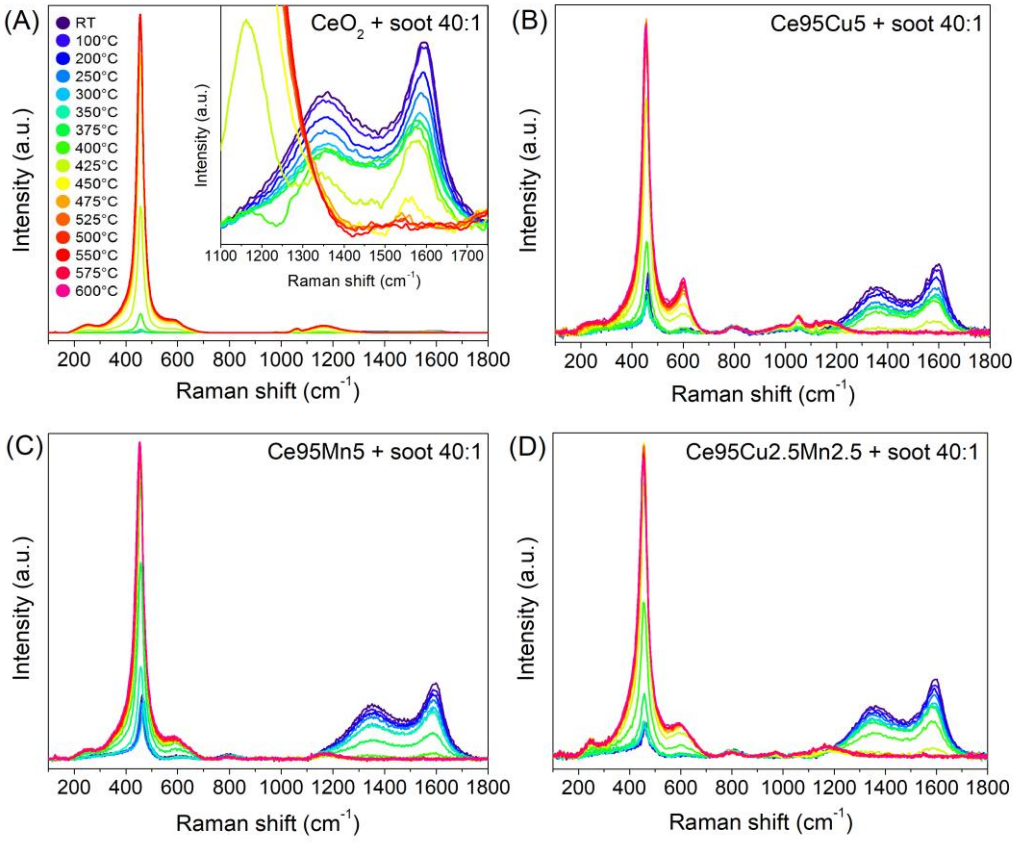

Figure 3.13. In situ Raman spectra recorded at different temperatures during the analyses of soot oxidation on the four tablets containing CeO_2 (A), Ce95Cu5 (B), Ce95Mn5 (C) and Ce95Cu2.5Mn2.5 (D). In the inset the evolution of the soot bands is magnified.

Figure 3.14 reports the result of the same measurements performed on a 40:1 silica-soot tablet in air as a control sample. The complete conversion of soot in air in the absence of the catalyst is attained at temperatures around 750°C, confirming the improved soot oxidation in presence of the catalytic materials. In detail, Ce95Mn5 appears to be the most active catalyst in the series, in agreement with the results of the standard activity tests reported in Figure 3.4. In fact, soot conversion starts at 350 °C and is complete at 425 °C, as observed by the disappearance of the carbon-related Raman bands (Figure 3.13 C). Pure ceria and the Cu-doped samples are characterized by worse performances.

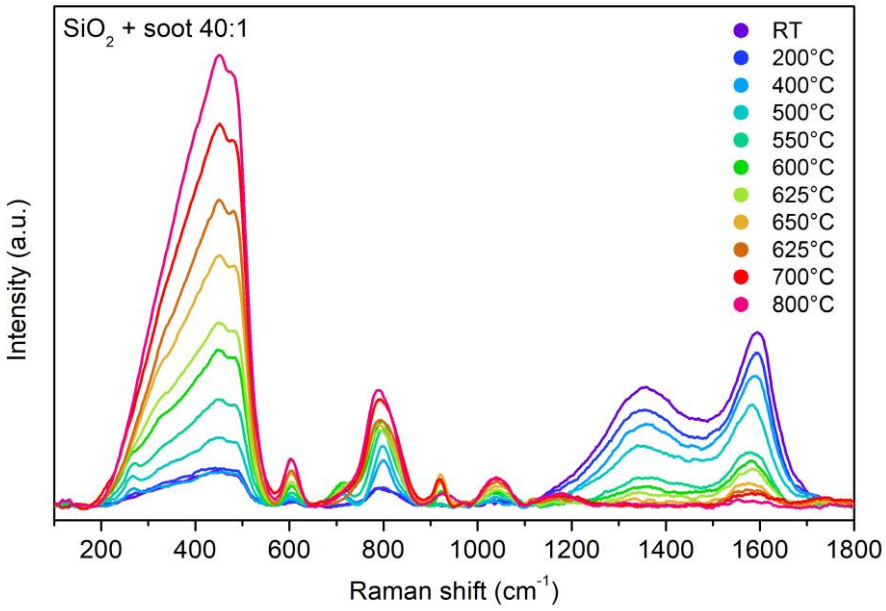

Figure 3.14. Raman spectra collected at different temperatures during the in situ soot oxidation test on a 40:1 silica-soot tablet. Silica features gain intensity when soot is oxidized, similarly to the ceria bands of the soot-catalyst tablets; therefore, the integrated area of silica band from 200 to 550 cm^{-1} was exploited to calculate the Raman based conversion curve for the soot-silica tablet reported in Figure 3.15.

The results can be better analyzed by calculating a conversion curve starting from the Raman spectra. In standard activity tests, the conversion is obtained as the ratio between the amount of CO_2 produced at a certain temperature and the total amount measured during the whole oxidation process by IR absorption. In analogy, the area of the main Raman soot band could be employed for the calculation, but the decrease of its intensity due to the heating complicates the identification of the onset of the catalytic activity. Instead, as shown in Figure 3.15 A, the variation of the F_{2g} band intensity vs. temperature clearly differs in presence of soot and the light off of the reaction can be therefore detected by the deviation from its normal trend. The intensity change covers more than one order of magnitude for all the catalysts, allowing a very good sensitivity, which is also confirmed by the fact that a slight increase of the band intensity is still observed when all the soot Raman features have disappeared. The conversion curves, shown in Figure 3.15 B, are therefore calculated through the equation (3.1), as the ratio between the variation of the integrated area of the F_{2g} band at a certain temperature (T_x) with respect to the catalytic process onset one (T_i) and the total area increase measured at the temperature at which the maximum intensity is reached, before the F_{2g} band starts to decrease again (T_f):

$$\boldsymbol{Soot\ conversion} = \frac{\boldsymbol{A_{F_{2g}}(T_x) - A_{F_{2g}}(T_i)}}{\boldsymbol{A_{F_{2g}}(T_f) - A_{F_{2g}}(T_i)}} \qquad (3.1)$$

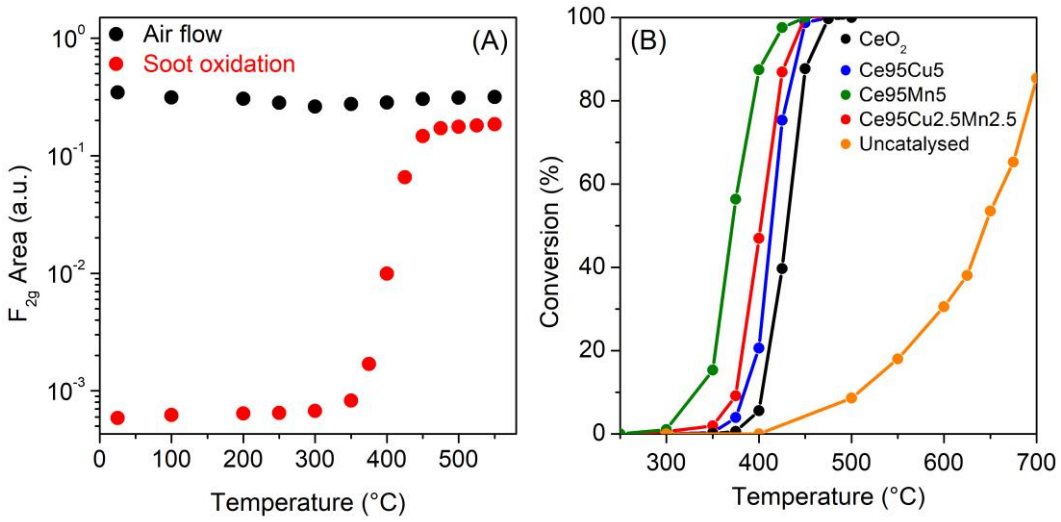

Figure 3.15. Variation of the F_{2g} peak area as a function of temperature during the analysis in air flow and during soot oxidation on the CeO_2 catalyst (A); the area of the F_{2g} band has been normalized to the acquisition parameters and to the area of the main band of the internal Si reference. Soot conversion curves obtained from the Raman spectra collected during the in situ tests over the four catalysts and for the uncatalyzed reaction (B); the latter curve was obtained as detailed in the caption of Figure 3.14.

It should be noted that the Raman curves are shifted toward lower temperatures in comparison to the ones calculated in the catalytic activity tests (reported in Figure 3.4 A). This phenomenon can be partially explained by the lower soot-catalyst ratio employed in the Raman measurements, in order to preserve an acceptable signal to noise ratio. Indeed, Figure 3.16 reports the soot conversion for a 9:1 CeO_2-soot tablet; during this test, an increase of almost 20 °C of the $T_{50\%}$ has been observed, due to the higher soot content.

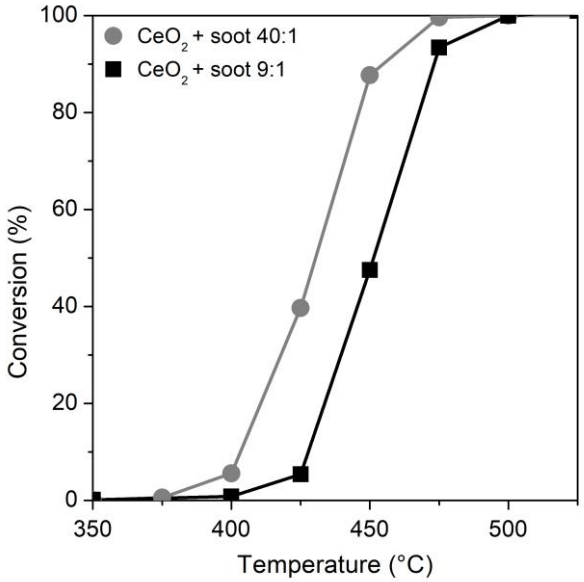

Figure 3.16. Comparison between the conversion curves obtained from the Raman spectra collected during the in situ analyses of soot oxidation on tablets with a 40:1 and 9:1 catalyst-soot ratio.

The Raman conversion curves confirm the high activity of the Ce95Mn5 catalyst, and also the similar lower activities of Ce95Cu5 and Ce95Cu2.5Mn2.5. However, the behavior of CeO_2 is quite different. Indeed, its conversion curve is delayed with respect to the ones of the doped ceria samples. In agreement with this result, soot Raman bands are still observed at higher temperatures compared to the other catalysts (Figure 3.13 A). The repetition of both the standard and Raman tests pointed out the reproducibility of these outcomes, thus showing that a slight variation of the soot concentration in the analyzed laser spot cannot account for this discrepancy.

Actually, in previous studies the effect of the catalyst optical absorption on the penetration depth at specific laser wavelengths and therefore on the observed Raman features has been carefully analyzed [248]. It can be reasonably postulated that such effects can explain the unexpected trend in the Raman conversion. Indeed, the doped catalysts provide similar higher light absorption (i.e. lower penetration depth) at the 514.5 nm excitation wavelength with respect to the pure ceria, as can be noticed in Figure 3.17. As in the set-up of the heating cell air is flowing on the top of the catalyst tablet, a slightly delayed soot oxidation is expected for the deepest layers, which can be only probed in the case of the least absorbing CeO_2 catalyst. The dependence of the results on the absorption features of the sample, which can differ significantly from one material to another, constitutes a limitation of the proposed method, since a quantitative correction taking into account the material absorption coefficient is not easily available. The comparison of Figure 3.15 B and Figure 3.4 A also reveals a swap between the Ce95Cu5 and Ce95Cu2.5Mn2.5 conversion curves calculated from the Raman data, which can also be ascribed to the shorter penetration depth of the exciting laser light into the Ce95Cu2.5Mn2.5 tablet. Indeed, the UV-Vis diffuse reflectance spectra in Figure 3.17 suggest a higher light absorption for the ternary oxide catalyst, confirming that such measurements can provide a good qualitative explanation of the discrepancies observed between the conversion curves obtained by the two procedures. The Raman conversions could better match the standard ones when the method is applied to samples presenting similar absorption at the wavelength of the light source used in Raman spectroscopy or by performing Raman analysis with multiwavelength excitations.

The Raman spectra were then further analyzed in order to understand the observed activity trend in terms of the present defect sites. Indeed, soot combustion is believed to proceed through a Mars-van Krevelen oxygen vacancy-mediated mechanism, similarly to CO oxidation. The two suggested pathways of the reaction involve i) the formation of reactive oxygen O_2^{x-} on reduced Ce^{3+} or reduced substitutional cations associated with the presence of oxygen vacancies, followed by spillover towards the soot particles, or ii) the reduction of the catalyst through the direct transfer of lattice oxygen at the soot-ceria interface, which occurs together with oxygen vacancies formation [136].

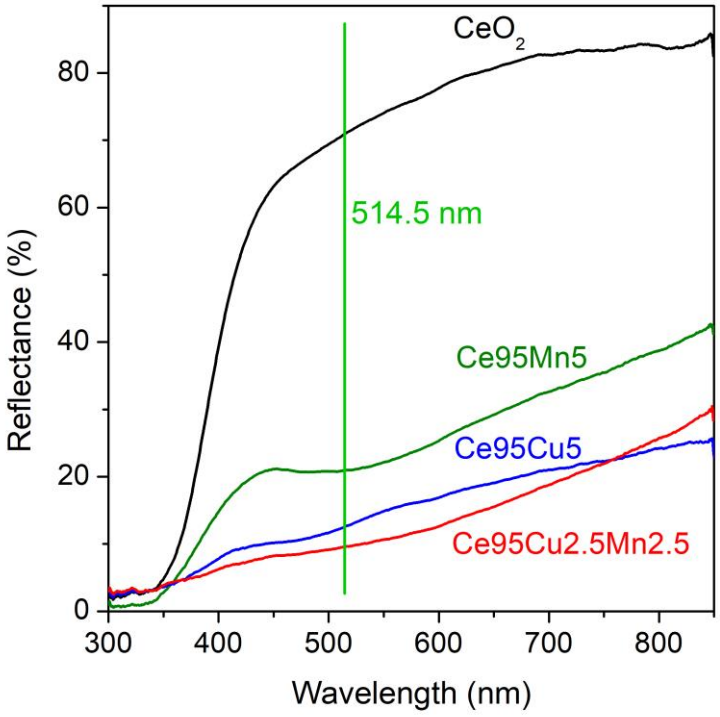

Figure 3.17. Diffuse reflectance UV-Vis-NIR spectra collected on the CeO_2, Ce95Cu5, Ce95Mn and Ce95Cu2.5Mn2.5 catalysts. The green line marks the 514.5 nm laser excitation wavelength employed for the Raman measurements.

All the three defect sites identified by Raman spectroscopy can be fruitfully involved in such mechanisms. D1 Frenkel pairs contribute to oxygen mobility and transfer in the presence of reducing species [249]. D2 defects containing a doping cation foster the weakening of lattice oxygen bonds. Finally, the D3 sites, associated with reduced Ce^{3+} or foreign cations, are representative of the reducibility of the catalyst and can be readily activated to form O_2^{x-}. In particular, the higher $D3/F_{2g}$ ratio for the Cu-containing catalysts suggests a higher reducibility of these samples, which is associated with a lower vacancy formation energy [245], and is confirmed by the best CO oxidation activity [143]. Moreover, a higher soot conversion at low temperature (< 350 °C) was observed in standard combustion tests for these catalysts in comparison to CeO_2 and Ce95Mn5 (Figure 3.4 A), which could be related to the consumption of the already present D3 sites (their involvement in O_2^{x-} species formation and consequent oxidation) in the initial heating stage. However, the lack of a correlation between the D/F_{2g} ratio and the soot combustion activity above $T_{5\%}$ evidences differences between the CO and soot oxidation reactions. Several factors have been cited in the previous literature to explain this phenomenon. First of all, the lack of a dependence of soot conversion on the surface area of the catalyst was noticed and attributed to the importance of soot-catalyst contact points, instead of on the whole available surface area [192]. This trend seems to be confirmed by the set of four catalysts, where no clear dependence on the surface area is present, which was instead previously observed for CO oxidation [143]. In agreement with this hypothesis, the well-defined nanocubic morphology of the undoped ceria has been previously

shown to provide advantages in terms of soot oxidation activity [143]. Such effect seems to be mostly related to the increased number of catalyst-soot contact points with respect to the small polyhedra agglomerates, since the abundance of the highly active (1 0 0) facets was not higher for the CeO_2 and Ce95Mn5 nanocubes compared to the Ce95Cu5 and Ce95Cu2.5Mn2.5 samples [143].

Moreover, it was recently postulated that the presence of a large amount of oxygen vacancies can lead to reactive oxygen species deactivation through their reduction, favoring the formation of new lattice oxygen instead of highly active peroxides and superoxides [191,192]. A simplified scheme of this mechanism is depicted in Figure 3.18. Such phenomenon can be particularly detrimental in the case of soot oxidation, where the regeneration of oxygen vacancy sites is limited by the few contact points with the reductant (soot particles). Based on these hypotheses, it can be suggested that in the case of soot oxidation the presence of a higher content of oxygen vacancies in the Cu-doped catalysts does not allow the regeneration of all the consumed reduced defect sites and therefore the formation of new O_2^{x-} species. The capture of reactive oxygen species by vacancies may compete with soot oxidation, leading to the deactivation of part of the defect sites. Despite their crucial role, no Raman bands attributable to peroxides and superoxides, which are usually detected in the 830-860 cm^{-1} and 1125-1139 cm^{-1} range on ceria based materials [238,250,251], could be observed on the catalysts, nor at RT neither in the first heating phase. It should be noted that their features have been rarely directly observed at RT [251], while highly reducing conditions, such as H_2 atmosphere at elevated temperature followed by cooling in oxygen, are usually required for their stable formation. Instead, they probably only exist as transient species in the here analyzed catalytic process, especially above 250°C, where their Raman signal results strongly attenuated according to the TPD experiments on nanostructured ceria materials performed by Wu et al. [238]. Interestingly, the mechanism of vacancy annihilation by oxygen species proposed by them to explain the desorption of only the 20% of the adsorbed oxygen species recalls the described vacancy-O_2^{x-} reaction, showing that this is actually a significant pathway for ceria catalysts.

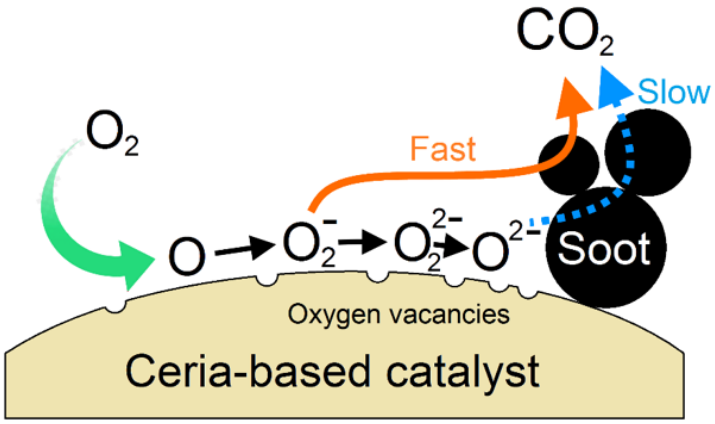

Figure 3.18. Scheme of the reactive O_2^{x-} species deactivation by oxygen vacancies during soot oxidation (adapted from [191] with modifications).

However, an influence of such mechanism on the defect sites could be expected. Figure 3.19 shows the comparison between the RT Raman spectra recorded on the Ce95Cu5 catalyst-soot tablets during the in situ test and those previously obtained on the pure catalyst in air flow at the beginning (Figure 3.19 A) and at the end (Figure 3.19 B) of the tests. The spectra have been normalized to the F_{2g} peak of ceria.

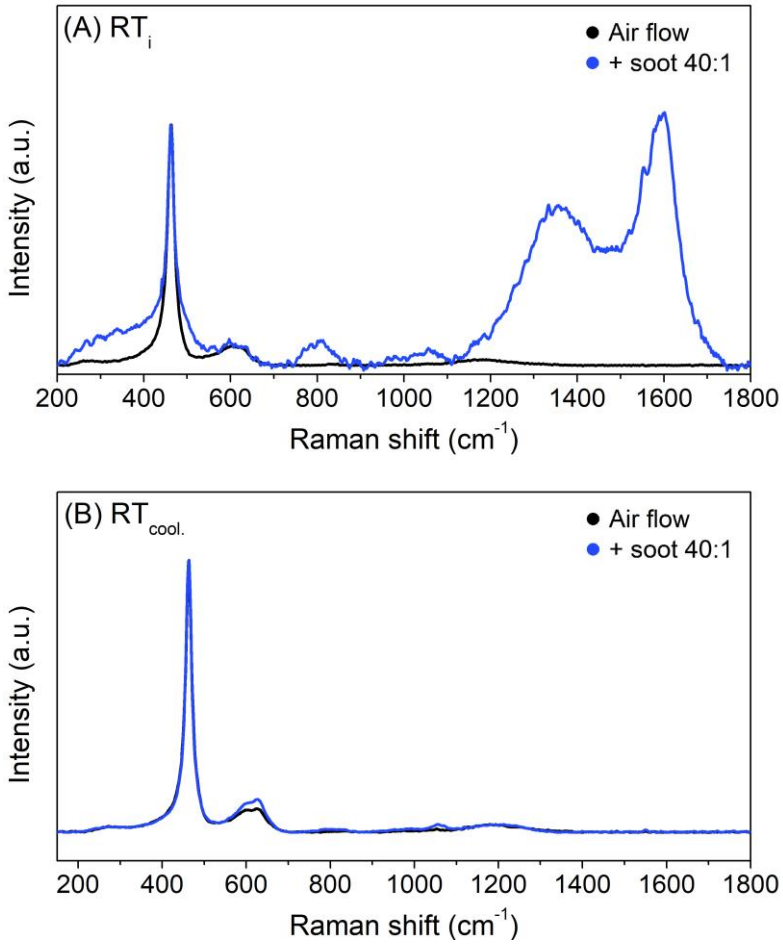

Figure 3.19. Comparison between the RT Raman spectra recorded on the tablets of Ce95Cu5 during the soot oxidation test and the analysis in air flow, at the beginning (A) and at the end (B) of the test. All the spectra were normalized to the F_{2g} band.

Before heating, the spectrum is extremely noisy in the presence of soot, thus a reliable analysis of the D bands is not possible. Instead, at the end of the test, when the shielding effect of soot is not present anymore, the defect band in the spectrum of the tablet is clearly more intense than that of the spectrum recorded on the pure catalyst. The huge increase of the D1 and especially the D2 band of Ce95Cu5 observed after soot conversion may be indicative of the partial conversion of vacancy sites to oxidized sites, supporting the conclusions drawn above. Table 3.5 summarizes the D/F_{2g} ratios calculated for the Ce95Cu5 sample using the spectra recorded at RT at the beginning and at the end of the different carried out tests. The D/F_{2g} ratio increases during each test, but the increment is definitely higher when soot oxidation takes place on the catalyst; this reaction seems to enhance the formation of new defects and to promote structural changes.

Similar comparisons between the $RT_{cool.}$ spectra recorded during the in situ tests and during the analyses in air flow for the other three catalysts are reported in Figure 3.20. A slight increase of the D2 band is observed in the case of Ce95Cu2.5Mn2.5 too, consistently with its low soot oxidation activity, while the curves are almost overlapped for the CeO_2 and Ce95Mn5 samples, showing that if any change in the defect sites occurs during soot conversion, such variation is reversible. It seems therefore that the higher soot oxidation activity of the last two catalysts is not only related to their nanocubic morphology, but also to their ability to avoid O_2^{x-} species deactivation, which can be instead indirectly observed in the Raman spectra of the Cu-containing catalysts through the increase of the D2 component at the end of the tests.

Table 3.5. D/F_{2g} ratios at RT for the Ce95Cu5 sample before and after the different types of test.

Type of test	D/F_{2g}		
	RT_i	$RT_{cool.}$	Variation
Static	0.310	0.357	+ 15.1%
Air flow	0.196	0.228	+ 16.6%
Soot oxidation	0.305	0.449	+ 47.0%

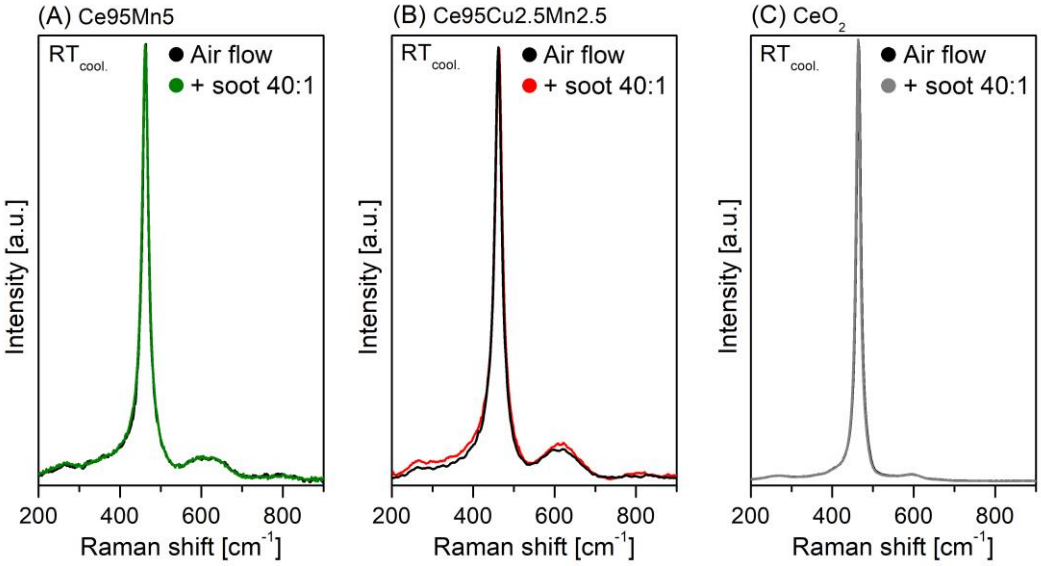

Figure 3.20. Raman spectra collected at RT at the end of the analyses in air flow and of the in situ tests with soot on the Ce95Mn5 (A), Ce95Cu2.5Mn2.5 (B) and CeO_2 (C) samples. All the spectra were normalized to the F_{2g} band.

Thus, pure and Mn-doped ceria, which display a stable defect sites distribution, are characterized by the highest activity in soot oxidation while Ce95Cu5 and partially Ce95Cu2.5Mn2.5 undergo important changes in the defect types during soot combustion. The results indicate that Mn can be profitably added to ceria catalysts, since it improves the physico-chemical properties with beneficial effects on the activity during the soot oxidation.

3.4 Conclusions

In the current chapter, four different ceria-based catalysts prepared via hydrothermal synthesis were studied by in situ Raman spectroscopy to monitor the presence and the evolution of defect sites at high temperature and during the soot oxidation reaction. Cu and Mn doping fostered the formation of both intrinsic and extrinsic defects in the ceria framework, whose concentration was estimated by the Raman band intensity ratio Dn/F_{2g}. In detail, two main Raman components were identified in the defect band: the D1 peak around 600 cm^{-1}, assigned to intrinsic Frenkel anion pairs, and the D2 component around 630 cm^{-1}, ascribed to extrinsic defect sites. The higher reducibility of the Cu-containing catalysts was supported by the detection of an additional weak band around 560 cm^{-1}, due to reduced Ce^{3+} associated with oxygen vacancies.

High temperature cycles in air provided no evidence for new oxygen vacancies formation, while the observed changes were mostly due to the combination of strain and anharmonicity effects and were reversible at RT, except for Ce95Cu5, for which the extrinsic defect component increased its intensity. Tests in different atmospheres suggested the assignment of this D2 band to oxidized Cu-containing sites without oxygen vacancies.

In situ Raman analyses on soot-catalyst tablets allowed to directly observe soot conversion in the range between 350 and 450 °C, depending on the studied catalyst, both from the decrease of carbon Raman bands and from the huge rise in intensity of ceria features due to the gradually reduced absorption of light by soot. A method was proposed to calculate the soot conversion from Raman spectra and the resulting trends were compared to those obtained with standard methods: Ce95Mn5 was confirmed as the best catalyst for soot oxidation, while less agreement was found among the conversion curves of the other samples, due to their different light-absorption features.

The almost reversible behavior of pure and Mn-doped ceria even after soot conversion demonstrated the superior ability of these catalysts to regenerate the most active defect sites. Instead, a huge increase of both $D1/F_{2g}$ and $D2/F_{2g}$ ratios was observed in the case of Ce95Cu5 at the end of the test, which was already evident after the complete conversion of soot; this result is compatible with the deactivation of reactive oxygen species through their reaction with oxygen vacancies. Such an effect is less marked but present also in case of the Ce95Cu2.5Mn2.5 catalyst, suggesting that the formation of oxygen vacancy-free defect sites is promoted during soot oxidation on defective catalysts presenting a huge quantity of oxygen vacancies on their surface. These outcomes provide new insights into the role of the defects in the catalytic combustion of soot, proving that in situ Raman analyses can support the design of more active catalysts.

Chapter 4

New insights on the defect sites evolution during CO oxidation over doped ceria nanocatalysts probed by in situ Raman spectroscopy

The study presented in this chapter was published, with modifications, as [212]:

Sartoretti, E.; Novara, C.; Fontana, M.; Giorgis, F.; Piumetti, M.; Bensaid, S.; Russo, N.; Fino, D. New insights on the defect sites evolution during CO oxidation over doped ceria nanocatalysts probed by in situ Raman spectroscopy. *Appl. Catal. A Gen.* **2020**, *596*, 117517, doi:10.1016/j.apcata.2020.117517.

4.1 Introduction

As previously discussed, mixed oxides have been widely investigated in the field of heterogeneous catalysis in the last decades [252,253]. In particular, cerium oxide has received much attention both as carrier and as oxidation catalyst [88,130], thanks to its high oxygen storage capacity and excellent redox properties [91]. Ceria features depend on several parameters, such as morphology or defect abundance. In fact, different types of point defects can be found in the ceria lattice, e.g. vacancies or interstitials, and their presence can foster the oxygen transport through the solid matrix [135,236]. Oxygen mobility is an important feature for ceria, since CO oxidation and also other reactions are believed to occur via a MvK-type mechanism [88,131,136–138].

In order to improve ceria properties, metal dopants can be introduced into the structure, causing lattice distortion and increasing the number of defect sites; as a result, the material can obtain an improved thermal stability accompanied by

increased reducibility and oxygen mobility, with beneficial effects on the catalytic activity [140,145,160,161]. As also shown in Chapter 3, remarkable results can be obtained with copper and manganese: in fact, these elements possess different possible oxidation states, and the good coupling of their redox cycles to that of cerium allows to obtain more reducible and active materials [162–166]. The doping-induced superficial oxygen vacancies and Ce^{3+} cations can also act as activators for gaseous O_2, whose adsorption on these sites results in the formation of highly-active peroxide or superoxide ions [254]. Furthermore, also the arrangement and distribution of the active sites can affect the final activity [255,256]. Therefore, the cerium reduction-oxidation cycle is directly related to the defect chemistry, and it is promoted on more easily-reducible materials. However, though understanding the nature of the defect sites involved in the catalysis is crucial for the rational design of active materials, the identification of the various lattice defects, of their arrangement and of the associated catalytic mechanisms is still under debate.

In the present chapter, the four hydrothermally-synthesized ceria-based nanocatalysts studied in the previous chapter [143,203] (consisting of pure ceria nanocubes and ceria doped with 5% Cu, 5% Mn, and 2.5% Cu + 2.5% Mn) were used to investigate the role of the defect sites in CO oxidation via Raman spectroscopy. Such reaction was chosen since CO conversion was proved to be directly influenced by the defect abundancy [143,162,243] while the heterogeneous set of catalysts allows to test the behavior of different defects sites. In situ Raman analyses were performed during the CO oxidation, in order to monitor the evolution of the defects and of the surface chemical species from room temperature to the catalytic regime. Moreover, the four materials were subjected to cycles of reduction and subsequent oxidation, isolating the vacancy creation and refilling steps in order to better understand how intrinsic and extrinsic defects on ceria-based catalysts are involved in the CO oxidation.

4.2 Experimental methods

In the present chapter, four different catalysts are considered, which are the same investigated in Chapter 3: the CeO_2 sample is made of pure ceria, while the other samples, named Ce95Cu5, Ce95Mn5 and Ce95Cu2.5Mn2.5, are made of ceria doped with 5% Cu, 5% Mn, and 2.5% Cu together with 2.5% Mn, respectively. All the catalysts were obtained via the hydrothermal procedure described in Chapter 2 and were calcined in air at 550 °C for 4 h [143].

The four catalysts were investigated via TEM and their catalytic activity towards CO oxidation was evaluated. A deep study via ex situ and in situ Raman spectroscopy was then carried out, in order to study the material defectiveness and its evolution during CO oxidation. In situ Raman analyses were carried out on catalyst tablets using the Linkam TS1500 cell housed in the Raman spectrometer.

4.2.1 In situ Raman analyses of the CO oxidation

A constant 45 mL min^{-1} flow of a gas mixture containing 1000 ppm of CO and 10% O_2 in N_2 was sent into the Linkam cell during these analyses, employing Brooks 5850S mass flow controllers. After having acquired a spectrum at RT (RT_i), the cell was heated with a constant rate of 3 °C min^{-1} up to 500 °C, recording spectra at different temperatures. After collecting a spectrum at 500 °C, a 45 mL min^{-1} flow of air (20% O_2 in N_2) was sent into the cell, and after 10 min the cell was cooled down to RT. Finally, a last spectrum was acquired at RT ($RT_{cool.}$).

4.2.2 In situ Raman analyses during reduction-oxidation cycles

A 45 mL min^{-1} flow of pure N_2 was sent into the cell before collecting a spectrum at RT (RT_i). Then the cell was heated up to 400 °C with a rate of 10 °C min^{-1}. After waiting some minutes for the stabilization of the temperature, a first spectrum was collected in N_2 atmosphere. Then, different gaseous mixtures were sent into the cell, changing the gas composition every 40 min. First 1000 ppm of CO in N_2 were flowed, followed by flushing the cell with pure N_2 and finally sending O_2. After flushing the cell with nitrogen again, a second cycle of reduction in CO/N_2 atmosphere, flushing in N_2 and reoxidation in O_2 was repeated. Since the gas requires about 10 min to completely replace the previous atmosphere in the cell, Raman spectra were acquired after 10, 25 and 40 min from each change of the gas composition. Finally, pure N_2 was sent into the cell, which was then cooled down to RT, and a last spectrum was collected at RT ($RT_{cool.}$).

In order to analyze the kinetic of defect evolution on the Ce95Cu5 catalyst, time series were acquired during the first ten minutes after the gas change. Raman spectra were recorded continuously, at the conditions specified previously except for the total acquisition time that was set to 15 s.

4.3 Results and discussion

4.3.1 Catalyst characterization and activity

The four ceria-based materials were extensively characterized with complementary techniques, such as XRD, nitrogen physisorption, FESEM, and XPS [143,203], as reported in the previous chapter. For the sake of convenience, some of the main physico-chemical and textural properties revealed by these analyses are recalled in Table 4.1.

In addition, Transmission Electron Microscopy (TEM) was carried out in order to further investigate the morphology and the structure of the four classes of samples; Figure 4.1 provides an overview of the significant results obtained with this technique.

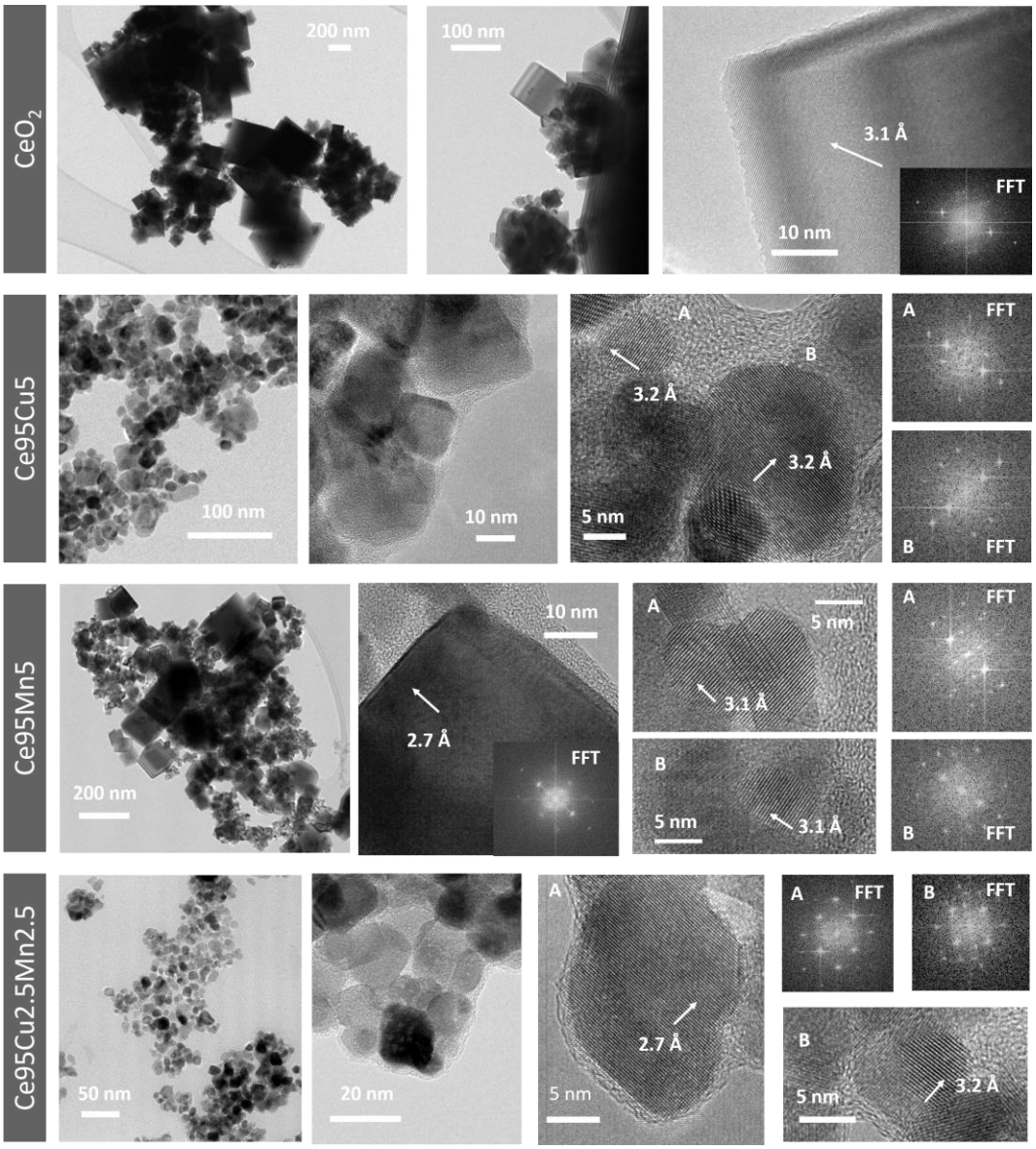

Figure 4.1. TEM characterization of the pristine and doped ceria powders, providing Bright-Field low magnification images and High-Resolution TEM images with corresponding Fast Fourier Transforms (FFT). In HRTEM images, interplanar spacings calculated from FFT are provided [~3.1 Å (1 1 1), ~2.7 Å (2 0 0) family of planes of the CeO_2 structure]. Labels A and B mark the correspondence between the analyzed particle and its FFT.

Concerning the pristine CeO_2 nanostructures, they exhibit the usual nanocubic morphology, with typical lateral size in the range 20 – 500 nm, in accordance with previously reported results [143]. Selected area electron diffraction (SAED) provided in Figure 4.2 confirms that the sole crystalline phase present is CeO_2 (face-centered (F) lattice, *Fm3m* space group [257]). As expected, high-resolution TEM (HRTEM) and subsequent analysis of Fast Fourier Transforms (FFT) of the images suggest that the nanocubes of different size are single crystals, showing interplanar spacings in accordance with CeO_2 structure.

Regarding the doped samples, it is clear by comparison of low-magnification TEM images that the presence of the different nitrate precursors influences the

morphology of the powders. Specifically, the synthesis of Ce95Cu5 and Ce95Cu2.5Mn2.5 provides nanoparticles with diameter values approximately in the 5 – 30 nm range, while Ce95Mn5 exhibits the presence of both nanoparticles (5 – 30 nm) and nanocubes (lateral size 20 – 200 nm). Regarding the crystalline structure, SAED patterns in Figure 4.2 confirm the presence of CeO_2 with no significant distortion of the unit cell and the absence of secondary phases. These results are in accordance with the information obtained by HRTEM, showing that the doped nanostructures are single crystals regardless of the particular morphology, and with the XRD analyses (Figure 3.2). Moreover, the presence of the doping elements in the samples was confirmed by Energy Dispersive X-ray spectroscopy (representative spectra are provided in Figure 4.3).

Table 4.1. Structural and physico-chemical properties of the four samples.

Catalyst	D_C [a] [nm]	a [Å]	SSA [b] [$m^2\ g^{-1}$]	Ce^{3+} [c] [%]	D/F_{2g} [d]
CeO_2	135	5.412	9	21	0.022
Ce95Cu5	34	5.409	46	27	0.256
Ce95Mn5	79	5.409	17	21	0.124
Ce95Cu2.5Mn2.5	23	5.408	52	26	0.225

[a] Average crystallite size (D_C) and lattice constant (a) estimated via XRD
[b] Specific surface area obtained via N_2-physisorption
[c] Superficial Ce^{3+} abundancy evaluated via XPS
[d] D/F_{2g} ratio obtained from the Raman spectra collected at RT

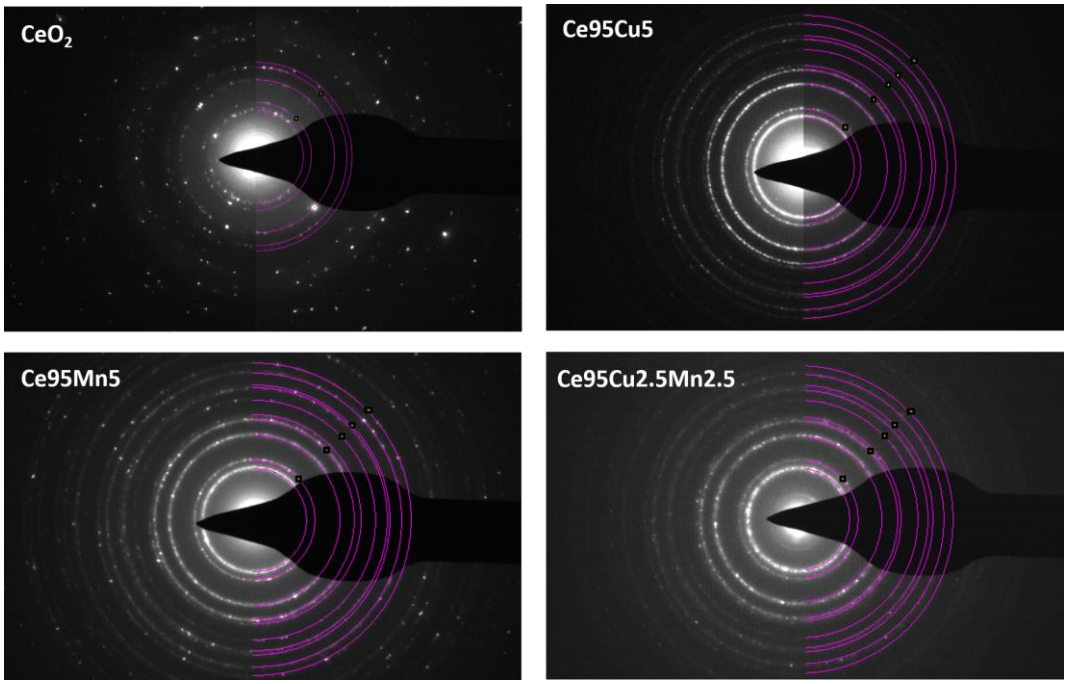

Figure 4.2. Selected area electron diffraction (SAED) patterns of the four samples. The violet lines represent a simulated pattern for ceria crystal structure.

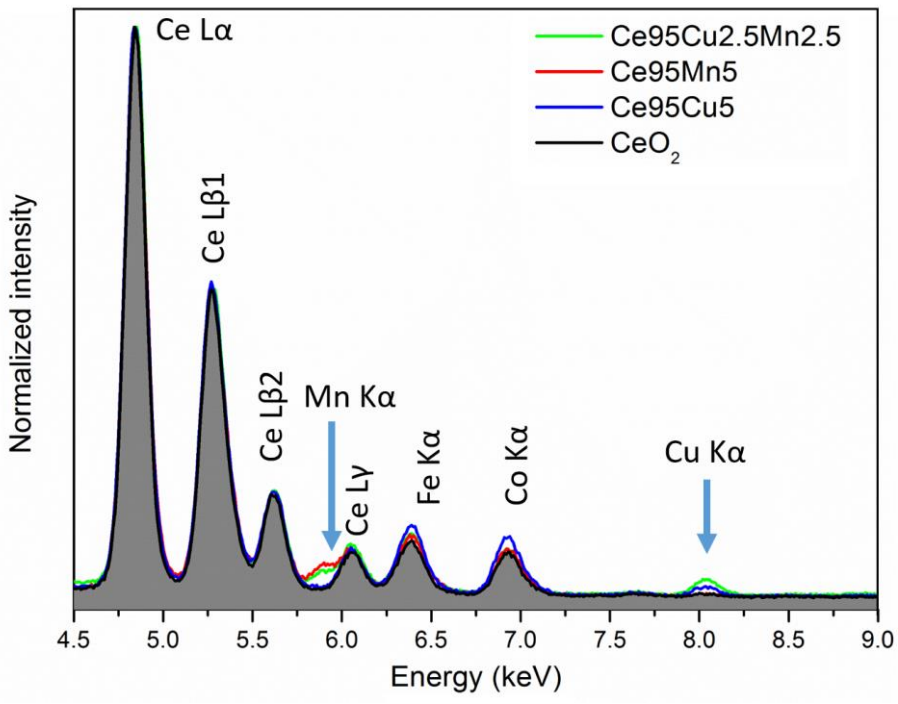

Figure 4.3. Representative EDX spectra for the pristine and doped ceria powders acquired with parallel beam illumination in the transmission electron microscope. Au TEM grids were used for the analysis instead of common Cu grids, in order to avoid the presence of a spurious Cu Kα peak. Fe/Co peaks are due to the pole pieces.

The results of the catalytic activity test of CO oxidation are recalled in Figure 4.4 [143]. The graph shows the CO conversion as a function of the temperature over the four samples, compared to the non-catalytic CO oxidation (yellow curve), promoted only by the temperature. All the catalysts are able to significantly reduce the temperature required for the CO oxidation, but a considerable difference can be noticed between pure and doped ceria in terms of performances. For a quantitative comparison, the specific reaction rate of CO oxidation (r_{CO}) can be considered, namely the rate of CO conversion at a given temperature normalized to the specific surface area of the catalyst. The values calculated at 120 and 150 °C are reported in Table 4.2: while pure CeO_2 showed a low r_{CO}, this parameter was remarkably higher for the three doped materials. In fact, Ce95Mn5 exhibited a specific reactivity ten times higher already at 120 °C, while even better results were obtained with Ce95Cu2.5Mn2.5 and Ce95Cu5. The higher activity of the Cu-doped samples is related to their higher specific surface area and reducibility [143], but it also depends on a higher defect abundancy [203]. Indeed, since the CO oxidation is believed to occur via a MvK-type mechanism on ceria-based materials, oxygen vacancies and lattice defects are directly involved in the catalysis.

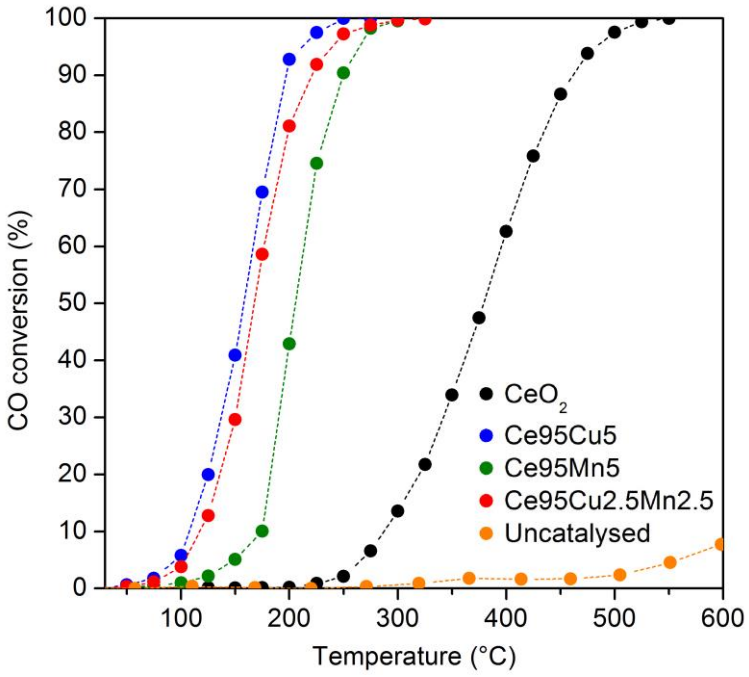

Figure 4.4. CO conversion curves as a function of the temperature, obtained feeding the reactor with a gas mixture containing 1000 ppm of CO and 10% of O_2 in N_2 [143].

Table 4.2. Catalytic properties of the four samples.

Catalyst	r_{CO} at 125 °C [$\mu mol_{CO}\ h^{-1}\ m^{-2}$]	$T_{10\%}$ [°C]	$T_{50\%}$ [°C]	$T_{90\%}$ [°C]
CeO_2	0.17	287	379	462
Ce95Cu5	5.33	107	158	197
Ce95Mn5	1.57	175	206	249
Ce95Cu2.5Mn2.5	3.02	117	168	221

As demonstrated in the previous chapter, Raman spectroscopy is a valuable tool that can be fruitfully employed in the investigation of ceria defectiveness [203,251,258]. Indeed, besides the main F_{2g} peak at 460 – 465 cm^{-1}, ascribed to the symmetric stretching mode of the Ce–O bonds [201,236], a band related to the presence of defects can be observed at higher shift in a typical Raman spectrum of ceria. Usually, a single component can be detected around 595 cm^{-1} on pure ceria: this D1 peak can be linked to the presence of Frenkel-type defects, in which a vacancy is generated by the displacement of an oxygen atom into an interstitial position [201,228,238]. Besides this component, other peaks can appear in the defect region of the spectra recorded on doped ceria, due to the formation of other types of defects: these sites can be considered extrinsic, i.e. induced by the doping, in contrast with the intrinsic Frenkel pairs already present in pure ceria.

When the four samples investigated in this study are concerned, the three doped samples were characterized by the presence of a more intense and broader

defect band in their Raman spectra with respect to pure ceria [203], as expected due to the good dispersion of the dopants in ceria lattice suggested by the absence of segregated secondary phases. Following a well-established method for comparing the defect abundancy of different ceria-based samples in a semi-quantitative way [207,238,243,259], the ratio between the area of the D band and that of the F_{2g} peak (D/F_{2g}) was calculated (see Table 4.1). Although it was previously observed that nanocubes are characterized by an increased D band contribution compared to nanopolyhedra [238], due to the exposure of more reactive (1 0 0) facets, in this case the influence of dopant incorporation in ceria lattice clearly overcomes any shape-related effect. In detail, for the four catalysts the D/F_{2g} ratios calculated at RT followed the trend CeO_2 < Ce95Mn5 < Ce95Cu2.5Mn2.5 < Ce95Cu5, which well correlates with the catalytic activity towards CO oxidation discussed above [203]. As shown by the representative spectra deconvolution of CeO_2 and Ce95Cu5 in Figure 4.5, the higher D/F_{2g} ratio for the doped catalysts is accounted for by an increase of the D1 peak contribution, that indicates a doping-induced rise of the abundancy of Frenkel-type sites, as well as by the appearance of a D2 band, located above 600 cm^{-1}, that can be ascribed to oxidized sites with a dopant cation not containing oxygen vacancies [203,231,260,261]. Finally, a D3 component, located around 550 – 570 cm^{-1}, usually assigned to oxygen vacancies [227,229,235,236], was barely detectable only in the spectra of the two Cu-doped samples. Schematic structures of the three defect types are depicted in Figure 3.6.

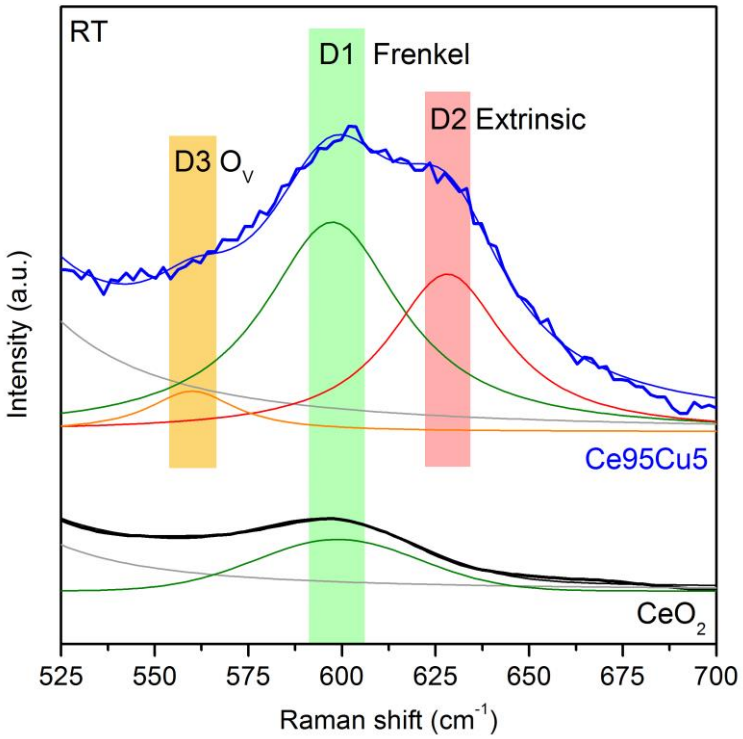

Figure 4.5. Magnification of the defect region of the Raman spectra collected in air at RT on the CeO_2 and Ce95Cu5 samples (see Figure 3.5). The spectra were normalized to the F_{2g} peak intensity and are vertically shifted for clarity reason. The curves obtained by the fitting and deconvolution of the defect band are reported as thin lines.

As a matter of fact, Raman spectroscopy has a great potential in probing the real time evolution of the different defect sites and is expected to provide new details on their involvement in the reaction mechanism; for this reason, in situ Raman analyses were performed studying the catalysts under reactive conditions.

4.3.2 In situ Raman analyses of the CO oxidation reaction

In order to provide new insights into the catalytic role played by the defects, Raman measurements were carried out during the CO oxidation. A mixture of 1000 ppm of CO and 10% of O_2 in N_2 was flowed on the catalyst, then the sample was heated and Raman spectra were collected at different temperatures. No changes were observed at RT upon the exposure of the samples to CO.

Figure 4.6 A reports the Raman spectra acquired on the CeO_2 sample. As previously discussed, the defect band consists in a single D1 peak, as displayed in Figure 4.5, and the evolution of this component during the test is reported in the inset of Figure 4.6 A. As the temperature rose, the peaks in the spectra moved to lower Raman shift and became broader: the red-shift is a consequence of the thermal-induced strain, while the peak broadening is mainly due to anharmonicity effects [231,244]. In agreement with the recent literature for temperature-dependent Raman analyses on ceria catalysts [203], a foreseen growth of the D3 band as a consequence of the reduction of the catalyst could not be identified since its contribution would be masked by these spectral changes. A continuous decrease of the intensity of the bands was also reported previously during heating ramps in air (see Chapter 3 and Figure 3.7 A). Instead, in the case of CO oxidation a clear inversion of the trend was noticed at around 300 °C.

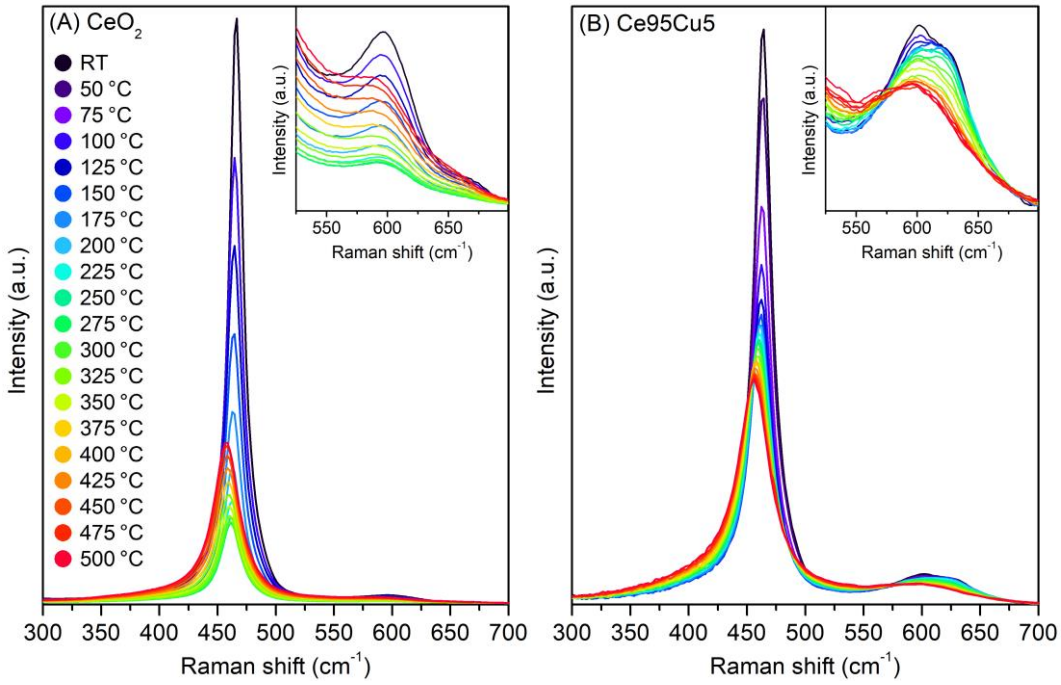

Figure 4.6. Raman spectra collected at different temperatures during CO oxidation (1000 ppm of CO and 10% of O_2 in N_2) on the CeO_2 (A) and Ce95Cu5 (B) samples. In the insets, the defect region is magnified.

To better understand the origin of this unexpected behavior, the main curve parameters of the F_{2g} bands were analyzed as a function of the temperature and compared with the analogous parameters obtained when heating the sample in air (tests presented in Chapter 3). Position and width of the F_{2g} peak changed almost linearly with the temperature in presence of CO, with a very similar trend to that observed performing the analyses in air (see Figure 4.7 A and B). On the other hand, the F_{2g} band showed a sharper intensity decrease in the low temperature range (RT – 250 °C) with respect to the sample heated in air (see Figure 4.7 C), followed by an almost stationary phase (250 – 300 °C) and a net and continuous growth above 300 °C.

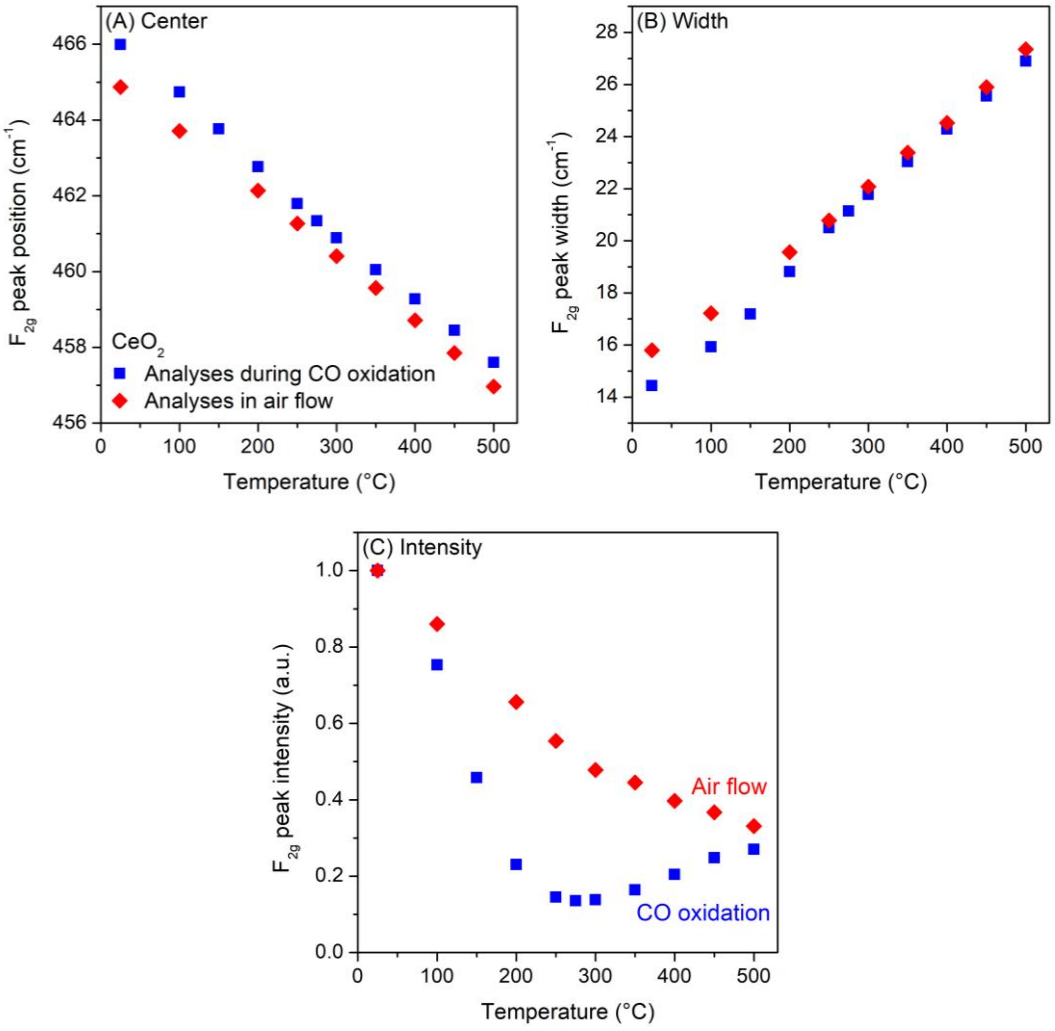

Figure 4.7. Position (A), full width at half maximum (B) and height (C) of the F_{2g} peak as a function of the temperature; the values were obtained from the Raman spectra collected on pure CeO_2 during the in situ analyses of CO oxidation (Figure 4.6 A) and during analyses in air flow (Figure 3.7 A, [203]).

The discussed behavior is consistent with an intensity increase caused by a change of the optical absorption by the catalyst, and thus of the laser beam penetration depth. Indeed, defect formation, topological evolution yielded by structural distortions or other similar effects would imply a modification of the vibrational band shape also involving the width and the spectral position. A

deeper inspection of the spectra revealed that this behavior seems to be connected to that of another band, located around 1500 cm^{-1}; a magnification of this region of the Raman spectra is reported in Figure 4.8 A.

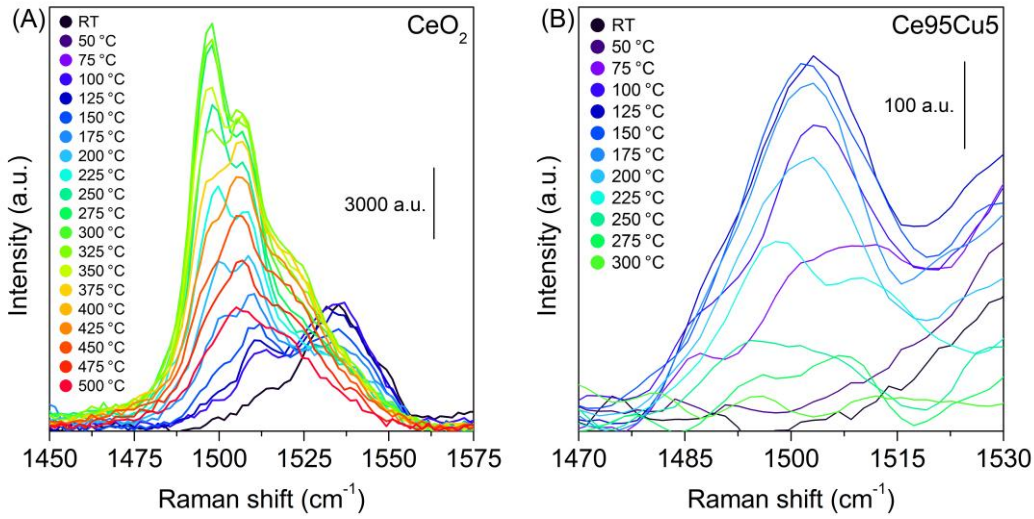

Figure 4.8. Magnifications in the 1450-1575 cm^{-1} range of the Raman spectra collected at different temperatures during the CO oxidation on the CeO_2 (A) and Ce95Cu5 (B) samples.

As displayed in the picture, at RT a low-intensity broad band was detected at 1535 cm^{-1}: this Raman feature can be associated to the presence of some organic contamination on the sample surface, since it disappeared completely during the heating. At the same time, as the temperature rose, a structured band appeared in the Raman spectra; one narrow component, located at 1510 cm^{-1}, could be observed already at 100 °C, then a second peak near 1500 cm^{-1} could be distinguished with respect to the first one starting from 200 °C, and finally a shoulder appeared at around 1525 cm^{-1} above 300 °C. Despite the general decrease in the Raman intensity, this band grew until 300 °C, then its intensity decreased. This suggests the assignment of the multi-component band to carbon-based molecules forming on the nanoparticle surface, which are later desorbed and oxidized by the catalyst at high temperature.

An analogous behavior could be noticed also for a weaker band around 1120 cm^{-1} (see Figure 4.9 A), that appears superimposed to the second order mode of ceria and can be reasonably assigned to the vibrational pattern of the same chemical species. The formation of these compounds does not seem to be related to the presence of previous carbonaceous contamination, since very similar results were obtained when repeating the in situ Raman measurements on a CeO_2 sample pretreated in air at 500 °C for 1 h (see Figure 4.10). Furthermore, Raman spectra collected through faster acquisitions and focusing the spot in different zones of the sample allowed to rule out that laser-induced effects could account for the generation of the observed compounds.

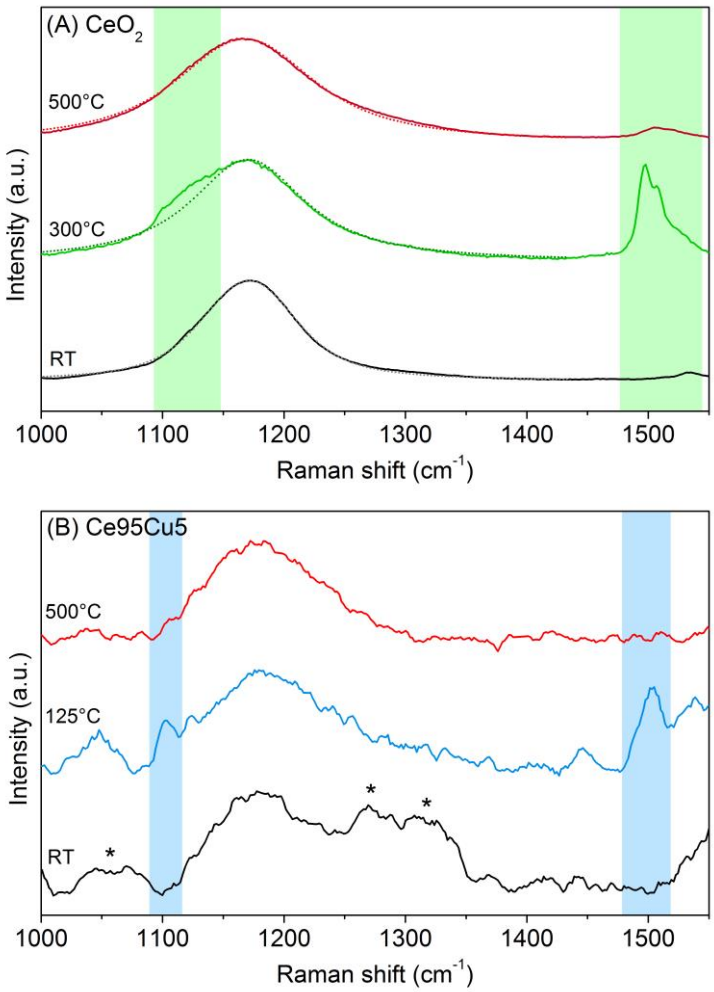

Figure 4.9. Magnification in the 1000 – 1550 cm^{-1} range of the Raman spectra acquired on the CeO_2 (A) and Ce95Cu5 (B) samples during CO oxidation from RT to 500 °C. For each catalyst, the initial (RT) and final (500 °C) spectra are reported, together with an intermediate spectrum recorded at the temperature at which the most intense polyenes-associated bands are visible (located in the regions highlighted with colored bands). The dotted lines in Figure 4.9 A, representing the shape of ceria second order band obtained by deconvolution, were added to assist the identification of the 1120 cm^{-1} band. The asterisks in Figure 4.9 B indicate peaks associated to the presence of contaminants at RT.

Despite the formation of carbonates or formates, resulting from the interaction of CO with ceria, has been previously observed by FTIR spectroscopy during CO conversion [262,263], the typical vibrational modes of such species are not consistent with the Raman fingerprint detected in the in situ analyses here reported. Instead, this pattern closely resembles the Raman spectra of polyenes, which are featured by two main bands related to single and double carbon-carbon bond stretching, respectively [264]. The position of such bands varies with the length of the polyene chain [264,265], possibly explaining the presence of different components. Moreover, the conjugated system of polyenes may be characterized by electronic transitions around 500 nm for specific chain lengths [264], leading to the absorption of part of the excitation/scattered light, causing the decrease of the Raman signal intensity of ceria. Above 300 °C, however, the CeO_2 catalyst starts to be significantly active, as shown in Figure 4.4; the

subsequent growth of the intensity of ceria-related bands could be therefore a consequence of the disappearance of the adsorbed species revealed by the 1500 cm^{-1} and 1120 cm^{-1} bands. It should be noted that the matching between the excitation wavelength and the electronic transition of the analyzed molecules is responsible for a resonance Raman regime which can lead to a strong enhancement of the Raman scattering efficiencies. For this reason, the formation of different hydrocarbons, including the resonant polyenes, can be hypothesized during the first stages of the CO oxidation reaction, as a consequence of a dissociative adsorption of CO on the catalyst surface together with an involvement of the initially present OH groups.

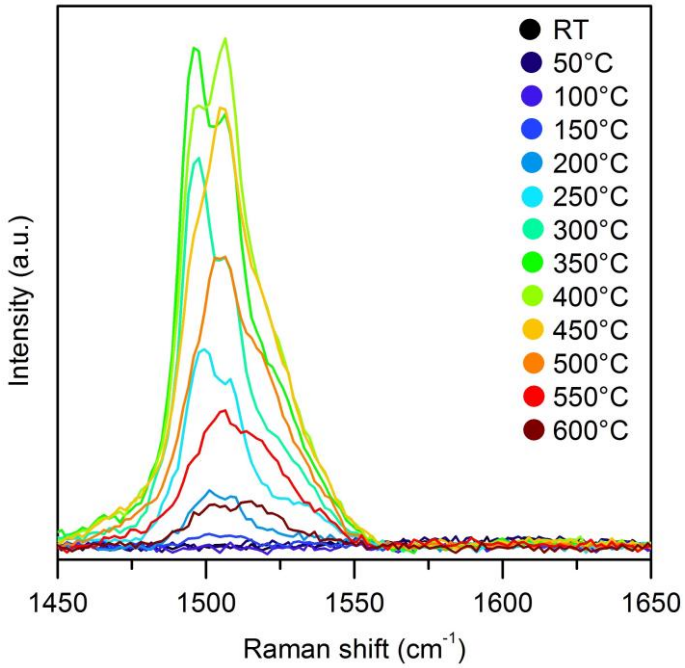

Figure 4.10. Magnification in the 1450-1650 cm^{-1} range of the Raman spectra collected at different temperatures during the CO oxidation on a CeO_2 sample. The catalyst tablet was pretreated at 500 °C for 1 h before starting the analysis, in order to remove any organic contamination. Despite the absence of carbonaceous species at RT (no bands were detected in the 1450-1650 cm^{-1} range), the polyenes-related band located at about 1500 cm^{-1} appears and show a similar behavior to that previously observed.

Figure 4.6 B reports the spectra acquired performing the in situ analysis of CO oxidation on the Ce95Cu5 sample. As previously discussed, three convoluted peaks can be observed in the defect band of this material, as shown in the RT spectrum reported in Figure 4.5; the evolution of this band during the test is magnified in the inset of Figure 4.6 B. Again, it was not possible to distinguish between catalyst reduction and the always present thermally induced red-shift and broadening of the D band components. Figure 4.6 B shows that the spectral intensity decreased monotonically while heating the cell, maintaining the behavior also at high temperature. However, this variation was characterized by two different slopes in different temperature ranges.

The values of the F_{2g} peak position, width and height calculated from the spectra presented in Figure 4.6 B were compared with the analogous parameters obtained heating the same sample in air (tests reported in Chapter 3). In analogy with the results obtained for pure ceria, the changes in position and width were linear and very similar during the two different tests, as shown in Figure 4.11 A and B. Instead, the intensity drop was faster in the early heating phase when flowing CO, as displayed in Figure 4.11 C, then it became slower and constant above 150 °C.

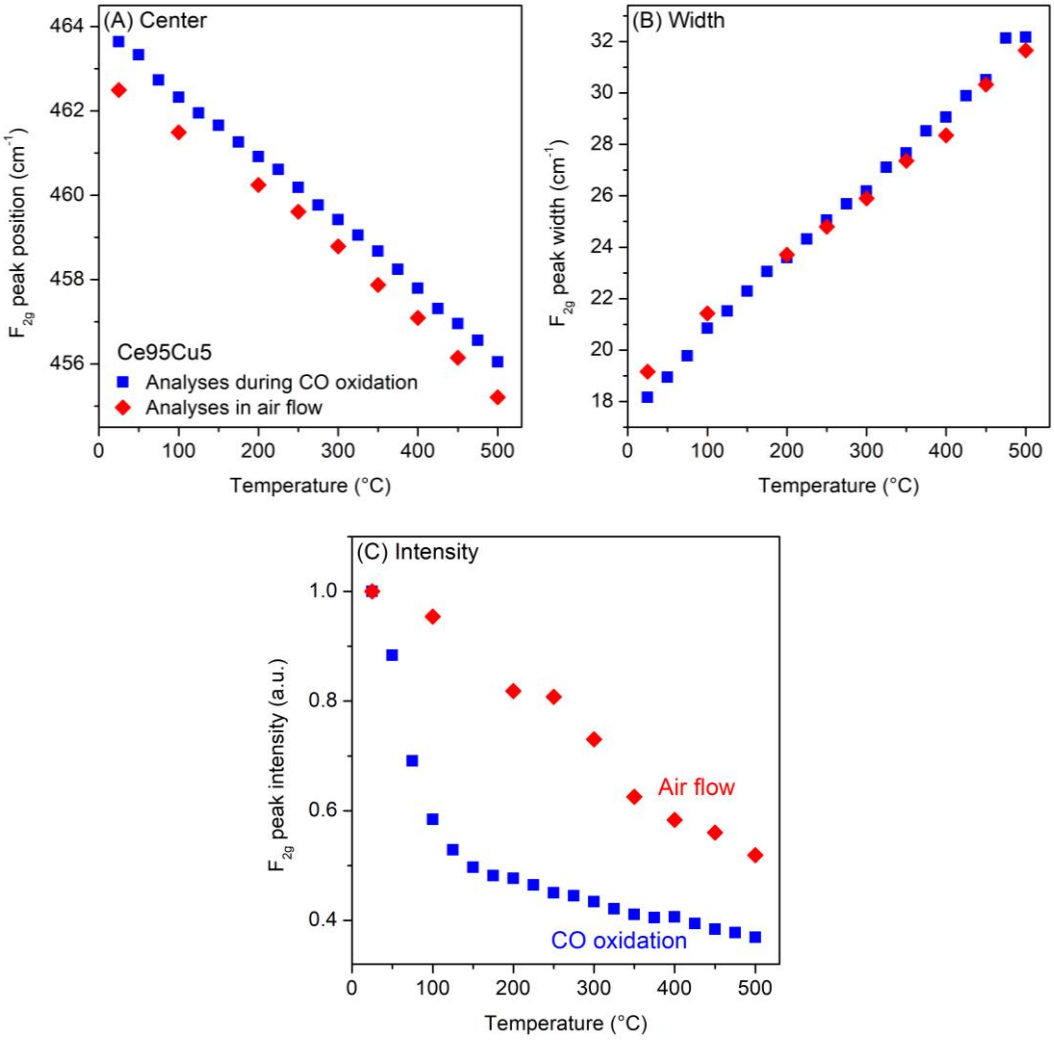

Figure 4.11. Position (A), full width at half maximum (B) and height (C) of the F_{2g} peak as a function of the temperature; the values were obtained from the Raman spectra collected on Ce95Cu5 during the in situ analyses of CO oxidation (Figure 4.6 B) and during analyses in air flow (Figure 3.7 B, [203]).

This behavior is probably associated to that of a band detected at 1500 cm^{-1}, whose magnification is reported in Figure 4.8 B. Despite the spectra collected on Ce95Cu5 are noisier, a distinguishable peak appeared at 75 °C, reached the maximum intensity at 125 °C and then decreased until disappearing above 225 °C. Again, a band around 1120 cm^{-1} followed the same trend with the temperature (see Figure 4.9 B). These bands could be attributed to the formation of polyenes

on the catalyst surface, which could absorb visible light, thus weakening the Raman spectral intensity. Above 125 °C, however, when the catalytic activity of the Ce95Cu5 sample starts to be significant, the adsorbed carbonaceous species are oxidized. The temperature at which the 1500 and 1120 cm^{-1} bands reach their maximum seems thereby to be correlated with the catalytic activity. Since the light off temperature of Cu-doped ceria is lower than that of pure CeO_2, a lower amount of molecules can be expected to form on the surface; as a result, the effect of the decreasing light absorption associated to the conversion of polyenes only partially mitigates the drop of the spectral intensity caused by the heating.

Concerning the spectra collected on the two Mn-doped catalysts (reported in Figure 4.12 A and B), a monotonic decrease of the F_{2g} intensity was observed during the heating, which was however very slight for Ce95Mn5. For both these samples, no clear band was detected at 1500 cm^{-1}. Several reasons can account for its absence, including the higher noise associated with the higher light absorption of the catalysts [203], the formation of shorter/longer polyenes which do not experience a resonant Raman enhancement at 514.5 nm or a minor amount of residual OH species.

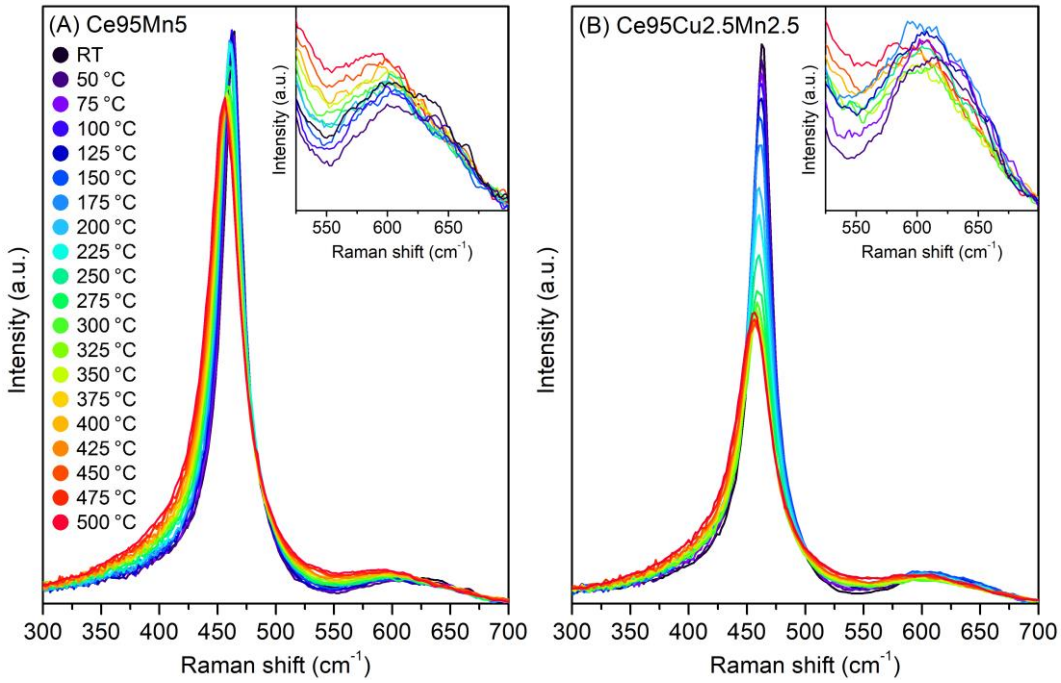

Figure 4.12. Raman spectra collected at different temperatures during CO oxidation (1000 ppm of CO and 10% of O_2 in N_2) on the Ce95Mn5 (A) and Ce95Cu2.5Mn2.5 (B) samples. In the insets, the defect region is magnified (the spectra are shown every 50 °C to reduce the number of overlapping curves).

Raman analysis therefore allowed to identify an unusual reaction pathway, which probably accounts for a minor fraction of the total CO conversion, but supports the existence of CO dissociative adsorption in an O_2-containing atmosphere. A similar disproportionation mechanism on ceria was in fact previously observed only in reducing conditions leading to the growth of soot-like amorphous carbon on the catalyst surface [135,266]. Hence, the presence of

strongly active sites, needed to lower the high energy barrier to the CO bond dissociation [267], can be hypothesized.

After reaching 500 °C, the samples were cooled down to RT in air flow and a spectrum was acquired ($RT_{cool.}$), which can be compared with the one collected at RT at the beginning of the test (RT_i). Comparisons between these two spectra for the four catalysts are reported in Figure 4.13.

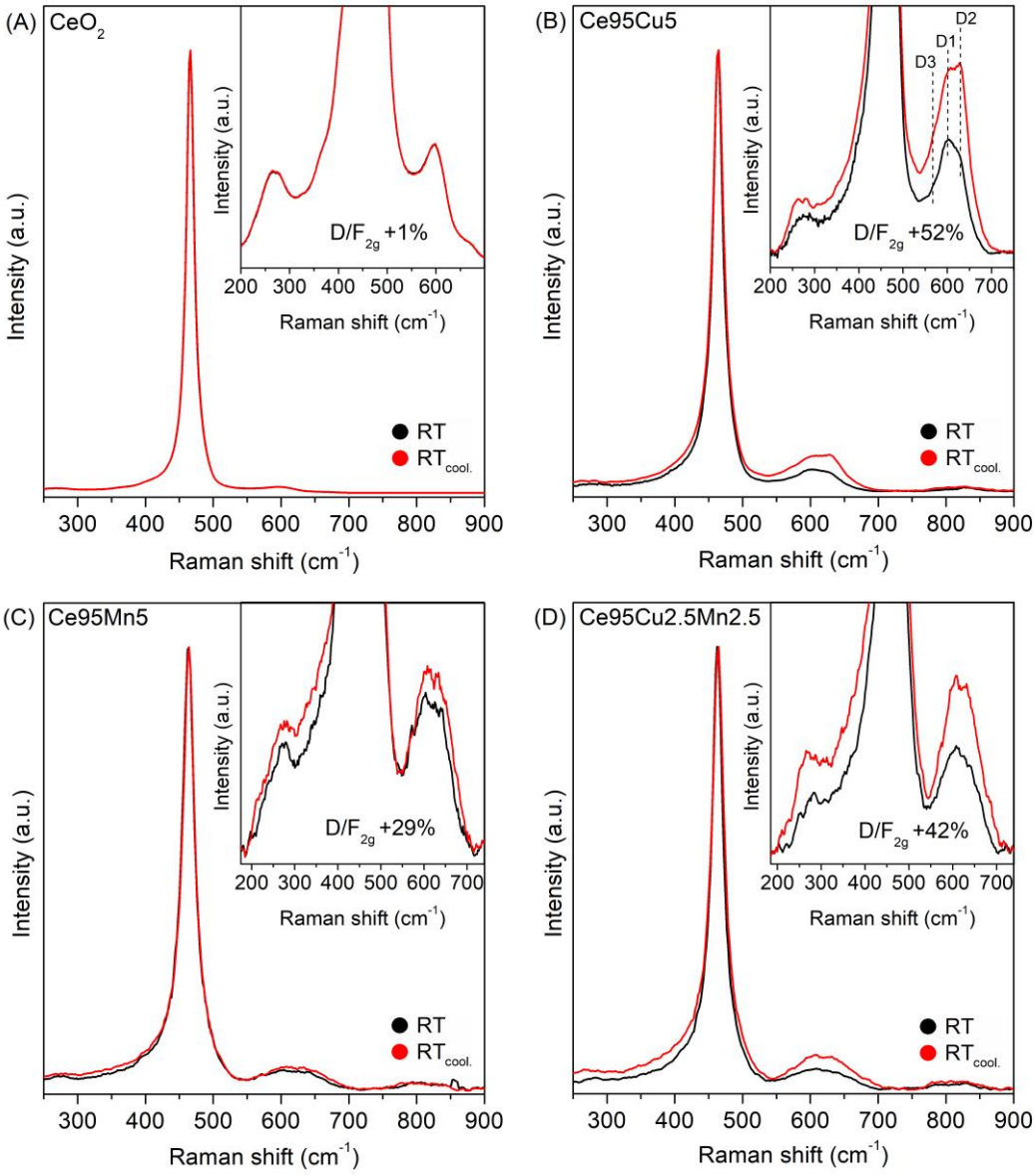

Figure 4.13. Comparisons between the Raman spectra acquired in air at RT at the beginning (RT_i) and at the end ($RT_{cool.}$) of the in situ analyses performed during CO oxidation on the CeO_2 (A), Ce95Cu5 (B), Ce95Mn5 (C) and Ce95Cu2.5Mn2.5 (D) samples. In each inset, a magnification of the defect band is shown, and the increase of the D/F_{2g} ratio after the test is reported. The spectra were normalized to the intensity of the F_{2g} peak.

For pure ceria, the two spectra are almost completely overlapped, and the total reversibility indicates that the CO oxidation does not significantly affect the structure of the catalyst. Instead, for the three doped samples some differences

were detected in the defect region, as displayed in the insets of Figure 4.13. The growth in the intensity of the defect band suggests that new defects were formed in the samples while the reaction occurred. This behavior is quite unusual, since reversibility of the Raman spectra or a decrease of the defect band intensity after thermal cycles have been typically reported in the literature [207,231,237]. However, a raise in the defect band was already noticed in the previous chapter, but only for the Ce95Cu5 sample. Instead, this time an increase in the defectiveness is evident also for Ce95Mn5, though slight, and Ce95Cu2.5Mn2.5. The Ce95Cu5 catalyst exhibited the highest increase in the D/F_{2g} ratio among the tested materials, with a variation of this parameter higher than that previously observed after a thermal cycle in air (+52% instead of +16%) [203]. Also the Ce95Cu2.5Mn2.5 sample underwent a significant increase in the defectiveness, while the variation was less marked for Ce95Mn5. The microstructure of all the doped catalysts is therefore significantly affected by the CO oxidation reaction.

4.3.3 In situ Raman analyses during reduction-oxidation cycles

In order to further investigate the structural changes induced in ceria-based materials by the interaction with CO, Raman analyses were performed exposing the catalysts to cycles of reduction and oxidation, following the schedule reported in Figure 4.14. The samples were heated in pure N_2 until 400 °C, since all the four catalysts are active towards CO oxidation at this temperature. Raman spectra were collected 10, 25 and 40 min after each gas change. After keeping the catalysts in an atmosphere of 1000 ppm of CO in N_2, pure nitrogen was used to flush the cell; afterwards, the samples were reoxidized in O_2. Finally, after cleaning the cell with nitrogen, a second cycle of reduction and oxidation was carried out, to verify if the changes observed in the spectra were reproducible. Unfortunately, the evolution of the surface oxygen species could not be monitored, since no variations were detected in the regions in which the typical bands of peroxide or superoxide ions can be found.

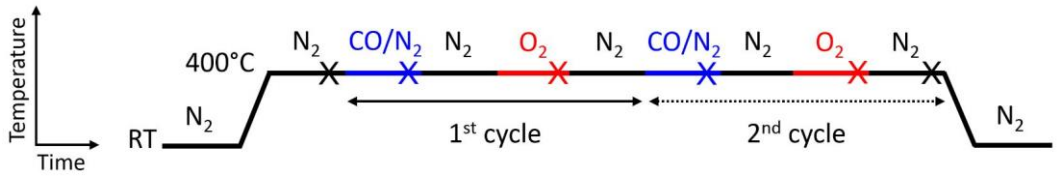

Figure 4.14. Scheme of the sequence adopted for the in situ Raman analyses performed during cycles of reduction and oxidation. The crosses indicate when the spectra reported in Figure 4.15 were collected.

The Raman spectra collected during the cycles on pure CeO_2 after 40 min from each atmosphere change are presented in Figure 4.15 A. In the inset, the defect bands normalized to the F_{2g} peak are magnified. No significant spectral variations were detected when changing the gas composition, confirming the CeO_2 structural stability discussed above.

Conversely, remarkable differences were observed among the spectra acquired on the Ce95Cu5 sample in the different atmospheres, which are displayed in Figure 4.15 B. A drastic decrease in the spectral intensity was observed under reducing conditions; moreover, this event was coupled with a broadening of the F_{2g} peak and a variation of the defect band, as detailed in the inset of Figure 4.15 B (the normalized spectra are reported for a more proper comparison). In fact, after flowing CO in N_2, the defect band acquired a flat shape, due to the rise of a component located around 550 cm^{-1}; however, the absolute intensity change of the different defect bands could not be evaluated due to the simultaneous spectral intensity drop, that could lead to unreliable conclusions.

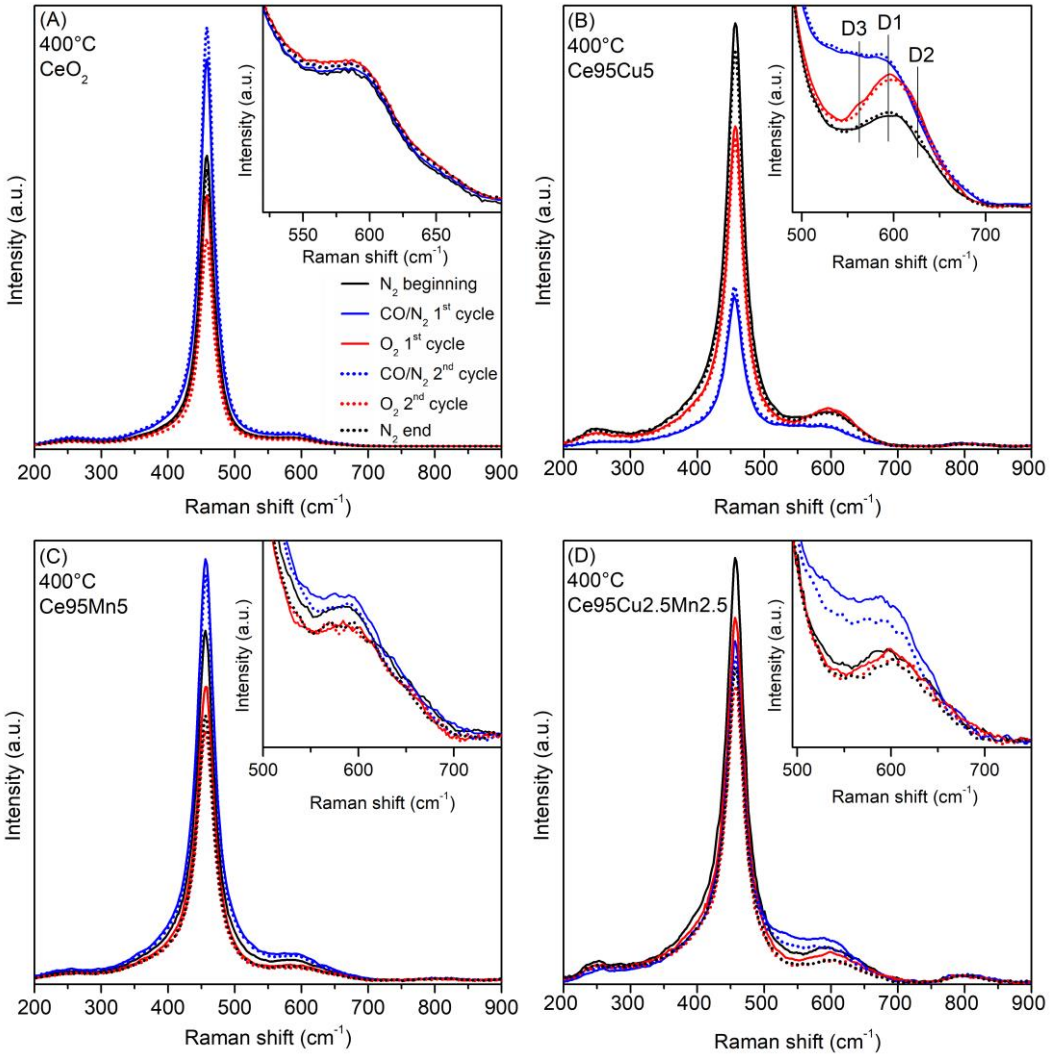

Figure 4.15. Raman spectra acquired during cycles of reduction (1000 ppm of CO in N_2) and oxidation (pure O_2) at 400 °C on the CeO_2 (A), Ce95Cu5 (B), Ce95Mn5 (C) and Ce95Cu2.5Mn2.5 (D) samples. The spectra were collected 40 min after the gas change, in correspondence with the crosses in Figure 4.14. The spectra recorded during the first cycle are represented with solid lines, while the spectra measured during the second cycle are depicted with dotted lines. In each inset, a magnification of the defect region of the spectra normalized to the intensity of the F_{2g} peak is reported.

As anticipated, a D3 peak lying in the 530-560 cm^{-1} spectral region is usually ascribed to the presence of oxygen vacancies, whose formation is associated to the reduction of Ce^{4+} to Ce^{3+} [204,235,236,238]. A similar effect was already observed by Agarwal et al. [201] and Wu et al. [238] when collecting UV Raman spectra on ceria nanorods after flowing highly concentrated CO (33% in He) at 350°C and hydrogen, respectively. Moreover, Andriopoulou et al. reported a flattening of the Raman defect band of rare-earth doped ceria-zirconia in reducing conditions [231]. Actually, Agarwal et al. also noticed the contemporary formation of carbonates and formates adsorbed on the catalyst surface by FTIR spectroscopy, but only a minor part of the newly-generated defects was ascribed to the presence of these carbonaceous species [201]. Furthermore, they suggested that the broad band at 550 cm^{-1} could result from the contribution of different components: besides simple oxygen vacancies, other types of defects may form during CO exposure, e.g. interstitial sites and Schottky disorders; at the same time, vacancy clustering may occur, resulting in the formation of dimers or trimers which are likely to give rise to Raman signals slightly different from that of the isolated defects.

A similar explanation can be given also for the Ce95Cu5 sample analyzed in this study, which appears to be more reducible than nanostructured pure ceria: the appearance of a broad D3 band can indicate the formation of new defectiveness at quite low CO concentrations, and the induced lattice strain can account for the F_{2g} broadening and for the dramatic intensity drop in the spectrum [240]. Indeed, the deposition of carbon at the catalyst surface, that could cause an increased absorption and thus a reduced Raman intensity, was not observed, probably due to the quite high temperature compared to the light off of Ce95Cu5 (see Figure 4.16). However, a partial recovery of the spectral intensity was obtained sending O_2 into the cell; at the same time, the intense and broad D3 band observed in CO atmosphere completely vanished when the sample was reoxidized, while a growth of the D1 and D2 peaks was noticed. This suggests that the refill of the oxygen vacancies can occur at 400 °C in pure oxygen atmosphere, and it is concomitant with the formation of new Frenkel pairs and extrinsic oxidized defect sites. The results obtained performing the second cycle of reduction and oxidation were almost the same; furthermore, the spectrum acquired in N_2 at the end of the test is very similar to that collected at the beginning in the same atmosphere, both considering the spectral intensity and the D band. Therefore, eventual irreversible structural changes induced by reduction or oxidation cannot be noticed at 400 °C.

Figure 4.15 C displays the spectra collected on the Ce95Mn5 sample. The spectra acquired in the different atmospheres present only minor variations in the D band, which is slightly more intense and is probably featured by the appearance of a weak D3 component in reducing conditions; when O_2 is flowed, instead, the defect band becomes a little less intense than that of the spectrum measured in nitrogen at the beginning: this variation suggests that all the oxygen vacancies previously created in reducing atmosphere can be completely refilled, while not all of the initial Frenkel and extrinsic D2 defects are restored during the reoxidation phase. The D band growth is less marked during the second exposure

to CO, showing that the reduction is more difficult after the first cycle; moreover, the final spectrum in nitrogen is similar to those recorded in O_2. The non-complete reversibility of the behavior of this catalyst could be associated to the formation of carbonates or formates at the surface, that may reduce the activity during the second cycle [262]. However, due to the low sensitivity of Raman spectroscopy towards C-O bonds and to the low concentration of CO, carbonate and formate groups were not detected in the spectra.

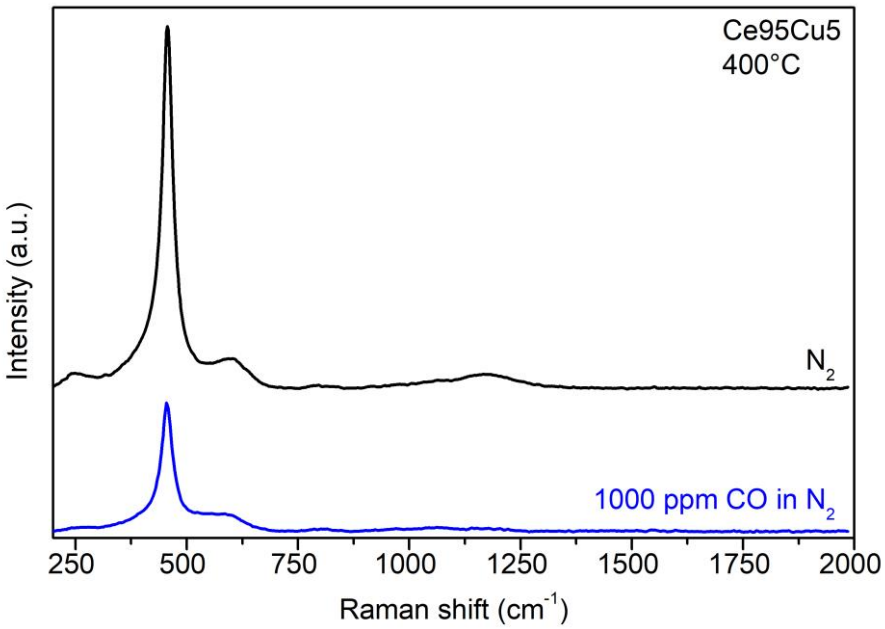

Figure 4.16. Raman spectra acquired on the Ce95Cu5 sample at 400 °C in two different atmospheres during the cycles of reduction and oxidation. When the sample is exposed to 1000 ppm of CO in N_2, the spectral intensity drops but no bands related to the formation of soot-like species can be detected.

An intermediate behavior was noticed for the Ce95Cu2.5Mn2.5 sample, whose spectra are reported in Figure 4.15 D. In reducing conditions, a remarkable rise in the D band can be noticed, especially around 550 cm^{-1}, as happened for Ce95Cu5. Moreover, a red-shift and a broadening of the F_{2g} peak were detected, coupled with a decrease in the spectral intensity. All these effects can be due to the generation of new defect sites during CO exposure. However, similarly to the Ce95Mn5 sample, Ce95Cu2.5Mn2.5 spectra acquired in nitrogen and oxygen during the second cycle are very similar, while a less marked rise in the D band was noticed during the second reduction; furthermore, the changes observed in this phase occurred gradually, as pointed out in Figure 4.17, while all the spectral changes were already complete 10 minutes after the gas change for the other samples. These results suggest that the newly-formed oxygen vacancies can be easily refilled by O_2; however, the behavior of the material is not totally reversible, since after a complete oxidation the formation of D3 defects in reducing atmosphere seems to be partially hindered.

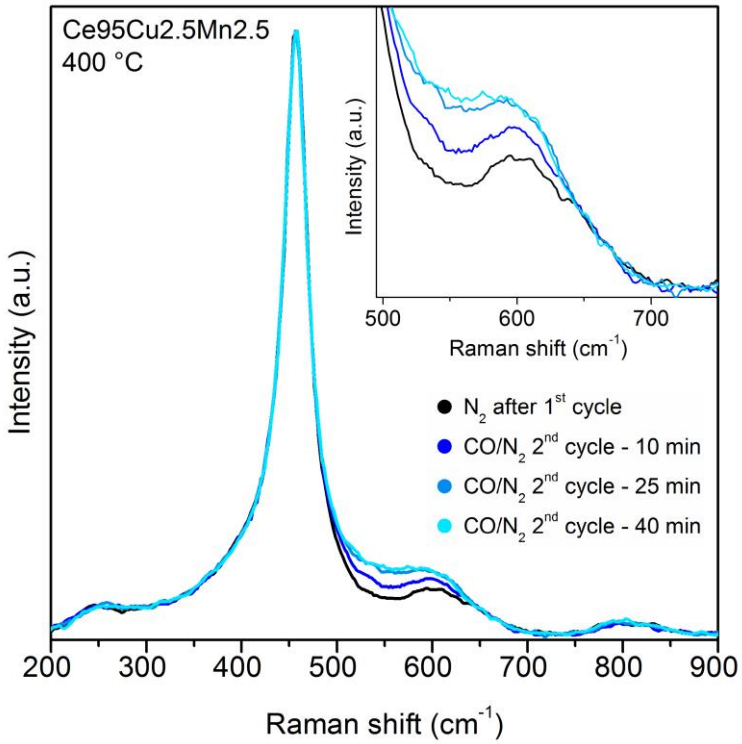

Figure 4.17. Raman spectra acquired on the Ce95Cu2.5Mn2.5 sample during the reducing phase of the 2nd cycle of reduction and oxidation. The spectra were collected at 400 °C immediately before and 10, 25 and 40 min after the gas change from N_2 to the 1000 ppm CO/N_2 mixture. All the spectra were normalized to the intensity of the F_{2g} peak. In the inset a magnification of the defect band is shown.

After the cycles of reduction and oxidation at 400°C, Raman measurements were carried out on the different samples cooled to RT; the collected spectra ($RT_{cool.}$) are reported in Figure 4.18, together with those acquired in the same conditions before the test (RT_i).

An almost total reversibility was confirmed for pure CeO_2, since only negligible differences can be noticed between the spectra in Figure 4.18 A. Also the Ce95Mn5 sample exhibited only minor variations, limited to a slight displacement of the defect band towards higher Raman shift, probably induced by the oxidation. Conversely, a remarkable growth of the D band after the test was observed for the two Cu-doped samples. Actually, the ternary oxide experienced an intermediate increase in the D/F_{2g} ratio, similar to that previously observed after the CO oxidation. The Ce95Cu5 catalyst, instead, underwent a higher rise in the D band after the cycles of reduction and oxidation, as displayed in the inset of Figure 4.18 B. The exposure of this sample to different atmospheres seems thereby to produce significant changes in the microstructure, fostering the increase of the defectiveness.

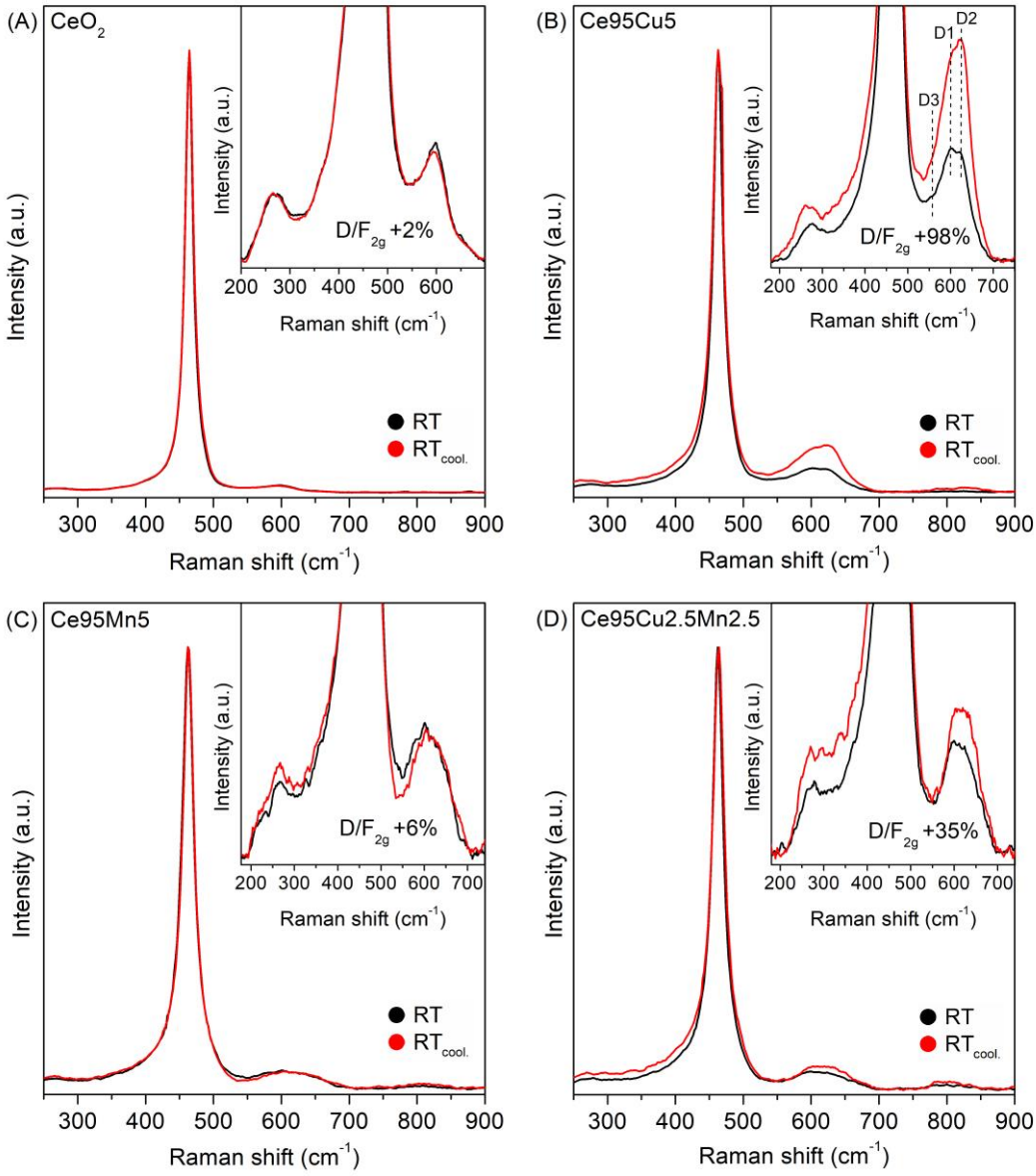

Figure 4.18. Comparisons between the Raman spectra acquired in air at RT at the beginning (RT_i) and at the end ($RT_{cool.}$) of the in situ analyses performed during cycles of reduction and oxidation on the CeO_2 (A), Ce95Cu5 (B), Ce95Mn5 (C) and Ce95Cu2.5Mn2.5 (D) samples. In each inset, a magnification of the defect band is shown, and the increase of the D/F_{2g} ratio after the test is reported. The spectra were normalized to the intensity of the F_{2g} peak.

A correlation can be found between the behavior of the four materials during the Raman analyses and their catalytic activity. Actually, the Ce95Cu5 sample, which was found to be the most reducible and performing catalyst, exhibited the most remarkable increase in the D3 band in reducing conditions, in addition to the highest increase in the D/F_{2g} ratio after the test. Minor changes were detected in the spectra collected on the Ce95Mn5 sample, which in fact showed a less interesting catalytic performance. For the ternary oxide, an intermediate behavior between those of the Cu- and Mn-doped samples corresponded to an intermediate activity. Finally, no significant changes were detected in the spectra recorded on pure CeO_2, which in fact resulted to be the least active material. These results

confirm the key role of the catalyst reducibility in case of the CO oxidation reaction; this property can be evaluated through the extent of the intensity increase and of the formation rate of the D3 band at high temperature, but is interestingly related to a rise of the non-reduced defect sites at RT. Thanks to the quick rearrangement of the structure in Ce95Cu5, evidenced by marked spectral changes, this catalyst is the most suitable one to further deepen the understanding of this phenomenon. Therefore, time-resolved Raman analyses were carried out on the Ce95Cu5 sample during the first 10 minutes of reaction, studying the effect of CO concentration on the structural disorder.

Two cycles of reduction and oxidation were repeated, using 1000 and 2000 ppm of CO in N_2 as reducing mixture. For what concerns the Raman spectra collected at 400 °C after 40 minutes from each gas change, the results appear similar at the two CO concentrations (see Figure 4.15 B at 1000 ppm and Figure 4.19 at 2000 ppm).

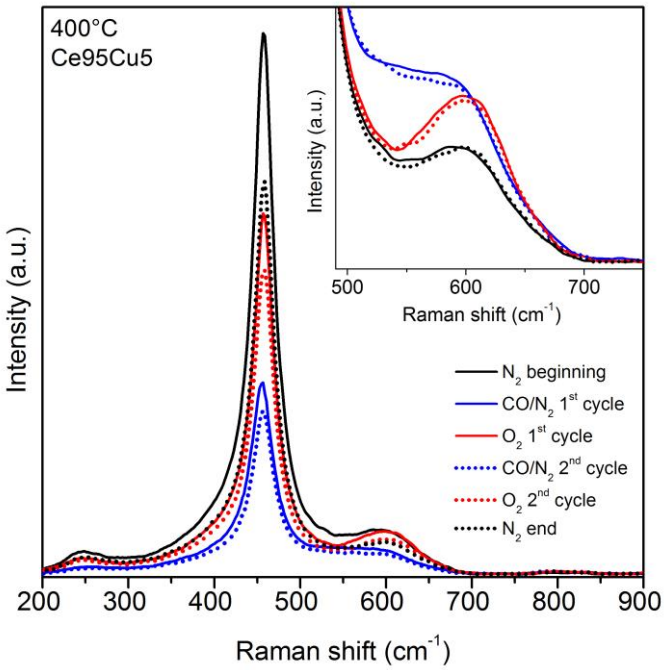

Figure 4.19. Raman spectra acquired on the Ce95Cu5 sample at 400 °C during cycles of reduction and oxidation, in which 2000 ppm of CO in N_2 was used as reducing mixture. The spectra were collected 40 min after the gas change. In the inset the spectra normalized to the intensity of the F_{2g} peak are reported and a magnification of the defect band is shown.

Nevertheless, some differences could be noticed when the evolution of the spectra was monitored during the gas change from pure N_2 to the CO/N_2 mixture, through the continuous acquisition of Raman spectra during the first 10 minutes of reaction. As it can be appreciated from the time series collected at 1000 and 2000 ppm of CO (Figure 4.20 A and B, respectively) the increase of the contribution of the D3 component occurred in the first minutes of exposure to CO and was associated with a marked intensity drop and with a broadening of the F_{2g} peak. For this reason, a comparison based on the calculation of the D/F_{2g} ratio may not

be reliable: in fact, as previously discussed, the changes in the F_{2g} peak induced by the appearance of new defects could lead to misinterpretation in the microstructural analysis. However, since the D3 defects form in reducing conditions, while the D2 peak is related to oxidized sites, the D3/D2 ratio could provide an indication of the reduction state of the sample. The evolution of the spectrum after sending CO in the cell can be thereby followed by tracking this parameter, whose trend is compared at 1000 and 2000 ppm of CO in Figure 4.20 C. The calculated curves show an almost linear increase of the D3/D2 ratio after flowing the gas, which reaches a stable value after around 200 s only at the higher CO concentration. An incipient plateau is reached also at 1000 ppm, but at later times, after more than 25 minutes. In the presence of a higher CO concentration the changes occurred earlier, confirming an increased reaction rate; on the other hand, the mean values of the D3/D2 ratio at saturation only showed minor changes, rising from 1.37 to 1.40.

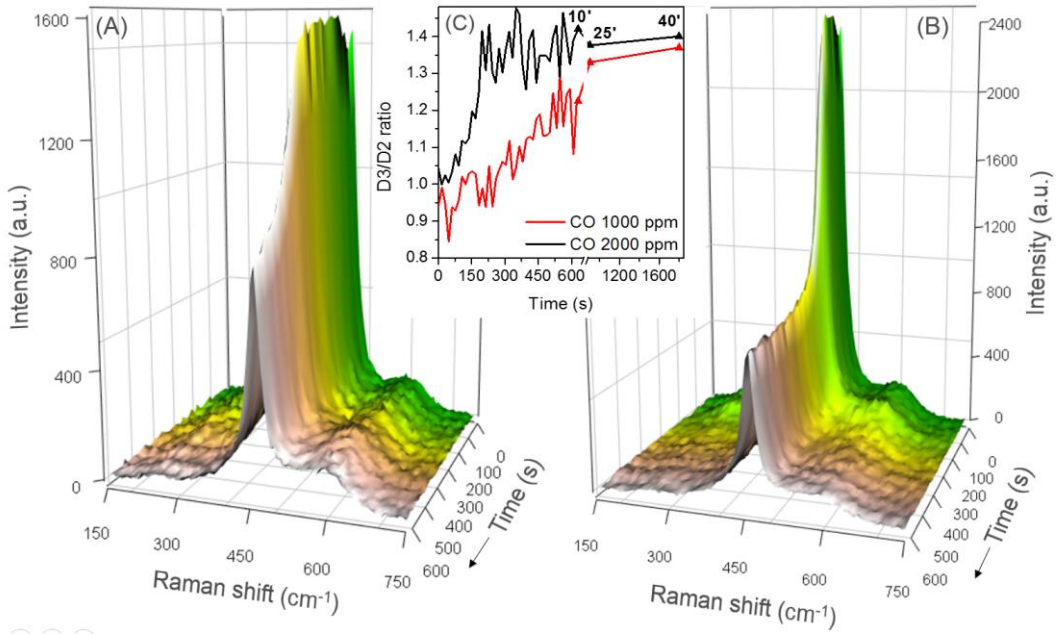

Figure 4.20. Time evolution of the Raman spectra collected on the Ce95Cu5 catalyst at 400°C after switching the gas flow from pure N_2 to a mixture of 1000 (A) or 2000 (B) ppm of CO in N_2. In the inset (C) the trend of the D3/D2 intensity ratio is reported.

This result points out the dependence of the spectrum on the CO concentration: a higher quantity of CO in the gas only slightly affects the amount of vacancies generated at the equilibrium, but it enhances their formation rate. However, the development of oxygen vacancies associated to reduced cations seems to be a consequence of the catalytic conversion of CO, rather than the activation mechanism. This outcome is also consistent with the absence of a strong D3 component during the conversion of CO in air, which suggests that the oxidation step of the catalytic cycle (vacancy refilling) is faster than the reduction one (vacancy formation) in line with the findings of Kopelent et al. [268]. Actually, the absence of O_2 in the atmosphere allows to capture the release of

lattice oxygen, which seems to form stable vacancies only in oxygen poor conditions.

In order to verify if the D3 defects generated at 400 °C could be stable at RT, a final test was carried out on the Ce95Cu5 sample: the catalyst was heated up to 400 °C, then a cycle of reduction in 1000 ppm of CO in N_2 followed by oxidation in O_2 was performed; afterwards, the CO/N_2 mixture was sent into the cell and after 40 min the sample was cooled to RT in this atmosphere; finally, the catalyst was exposed to O_2. The spectra collected at RT before and after this test are reported in Figure 4.21, together with a scheme of the test schedule.

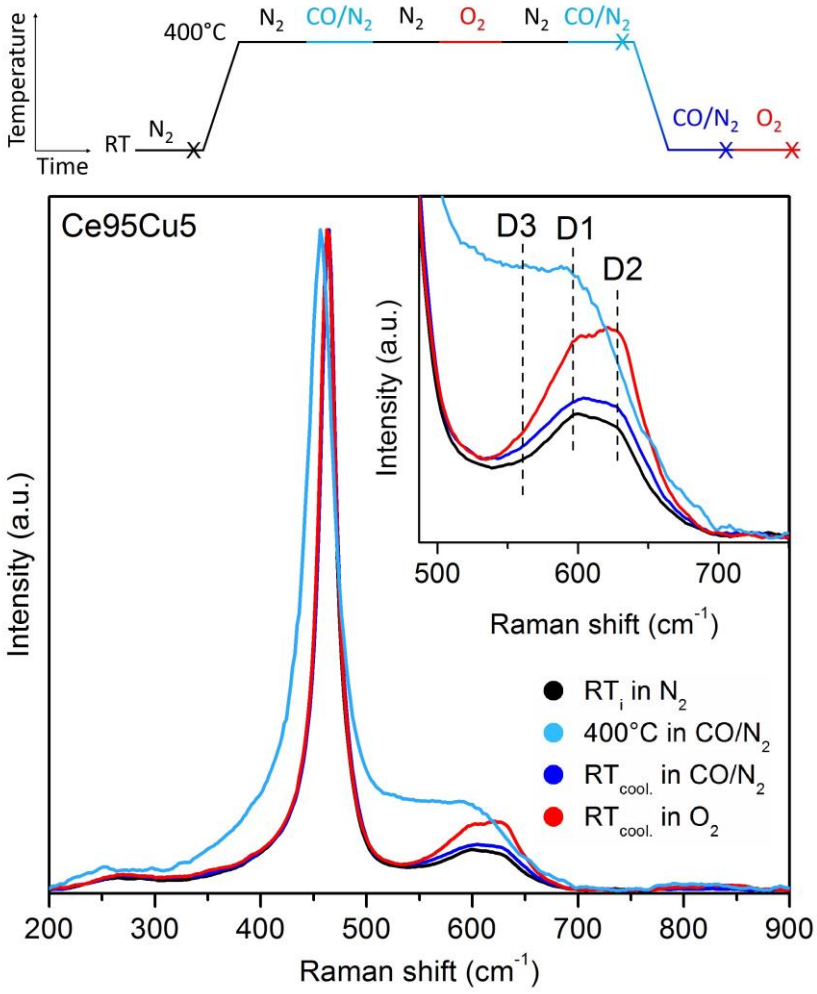

Figure 4.21. Raman spectra acquired during the in situ analyses performed on the Ce95Cu5 sample during cycles of reduction and oxidation: at the beginning of the test (RT_i), at 400°C after 40 minutes in 1000 ppm of CO in N_2, at the end of the test ($RT_{cool.}$) in 1000 ppm of CO in N_2 and after the exposure to oxygen. In the inset, a magnification of the defect band is shown. The spectra were normalized to the intensity of the F_{2g} peak. The scheme above the picture briefly resumes how the test was performed and the crosses indicate when the spectra shown in the figure were collected.

The intense D3 band observed at 400 °C almost completely disappeared during the cooling phase, before exposing the sample to oxygen. However, the D band, which preserved its original shape, was more intense after the test (+15%) suggesting that a moderate quantity of new D1 and D2 defects was generated

during the cycle. Finally, in oxidizing conditions, a remarkable increase of the D band was observed (+81%): this confirms that the D1 and D2 defects predominantly form in presence of oxygen; moreover, these changes were emphasized when the structure of the material had been previously affected by the exposure to CO.

These last results raise questions about the precursors of the additional D1 and D2 sites, which cannot be only created through a direct oxygen vacancy refilling mechanism. Indeed, neither the disappearance of the D3 band nor the rise of the D2 band are associated to a corresponding increase or decrease of another defect component, as could be expected. A possible explanation could derive from the clustering of oxygen vacancies under reducing conditions, which could be associated to the formation of reduced sites consisting both in Cu clusters at the catalyst surface and Ce^{3+} cations. In this case, a scheme illustrating the behavior of the oxygen vacancies during the tests is depicted in Figure 4.22.

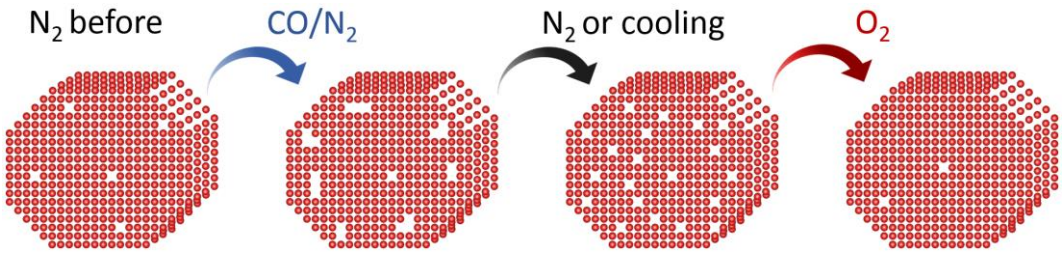

Figure 4.22. Simplified scheme illustrating the evolution of oxygen vacancies during the different tests performed on the Ce95Cu5 catalyst; the red spheres represent the oxygen ions in the ceria lattice, while the cations are not shown for the sake of clarity.

Multiple vacancy clusters, whose existence has been hypothesized and proved by different authors [201,255,269–271], could provide the broad and unresolved D3 band and better explain the huge decrease of the intensity of the F_{2g} mode as a consequence of a greater disruption of the structural order [271]. Moreover, the presence of small copper clusters was previously proposed by Elias et al. [245] according to their in situ XANES (X-ray absorption near-edge spectroscopy) and EXAFS (extended X-ray absorption fine structure) measurements performed on 10% Cu doped ceria catalysts in CO atmosphere. Such metallic copper sites exhibited a reversible behavior upon reoxidation, as also detected in a different study by in situ XRD analyses that evidenced the cyclic appearance of metallic Cu reflections during H_2/O_2 alternating exposure of Cu-containing ceria [272]. A similar reversible clustering mechanism was described also for Pd-containing perovskite [273]. However, in the present study, the reversibility is already detected by lowering the temperature and therefore by decreasing the conversion rate of CO. Such behavior can be consistent with the reorganization of surface vacancy clusters due to the diffusion of bulk oxygen to the surface when the rate of CO oxidation is decreased and the reaction finally stops. Nevertheless, isolated oxygen vacancies can still be present and can readily be refilled by molecular oxygen dissociation upon reoxidation of the sample. This process can reasonably lead to the formation of new D2 and D1 defects and can explain why the catalysts

which did not undergo analogous structural modifications during CO oxidation showed a smaller or negligible increase of these components at the end of the reaction. The reason behind such dissimilar behavior during and after CO conversion may eventually be found in the different redox properties of the dopants (Cu ions features the highest reducibility in the set) and their consequent different tendency to form aggregated reduced sites in conjunction with the formation of oxygen vacancies in the ceria lattice.

4.4 Conclusions

In the present chapter, the CO oxidation reaction was studied by in situ Raman spectroscopy on four nanostructured ceria-based materials in order to investigate the relationship between their catalytic activity and defectiveness.

A higher defect density, evaluated through the calculation of the D/F_{2g} Raman band ratio, and new extrinsic defect sites were detected in the doped samples at RT, consistently with the good dispersion of the dopant cations in ceria matrix suggested by TEM. In situ Raman analyses during the CO oxidation allowed then to monitor structural evolution in operando conditions. While the changes in the defect band were limited and possibly masked by temperature effects, the spectra acquired during these tests evidenced the formation of polyene-like chains on the surface of the CeO_2 and Ce95Cu5 catalysts before their activation towards CO oxidation. Such results may be an evidence of the existence of CO disproportionation (i.e. of dissociative adsorption) also in oxidizing conditions at low temperature. Comparing the Raman spectra recorded at RT before and after CO oxidation, reversibility was observed only for pure CeO_2. Instead, the doped samples exhibited a rise of the D band, which was especially marked for the two Cu-doped materials.

The interaction between the catalysts and CO at the origin of these changes was further investigated by in situ Raman analyses during cycles of reduction (CO in N_2) and oxidation (pure O_2) at 400 °C. Pure ceria confirmed its higher stability, while the Ce95Cu5 sample exhibited remarkable variations: a broad band around 550 cm^{-1} (D3) appeared in reducing conditions, pointing out the formation of oxygen vacancies in the lattice, that were quickly refilled when flowing O_2, together with an increase of the high Raman shift defect bands (D1 and D2).

While D3 defects could be observed in the high temperature Raman spectra, it was not possible to preserve them at RT, even without switching to oxidant atmospheres; these last results suggest that the very broad features of the D3 defects are more likely related to vacancy clusters. When CO oxidation ceases as a consequence of the temperature decrease, these clusters are readily reorganized in isolated vacancies, which can be the precursors of the oxidized D1 and D2 defect sites appearing in oxygen.

The two Mn-doped samples were characterized by a less marked growth of the D3 band during the exposure to CO. Interestingly, a correlation between the D3 intensity and formation rate in reducing conditions and the catalytic activity was found, suggesting that the D3 sites are formed as a consequence of the

catalytic oxidation, as also supported by the observed dependence on the CO concentration. Moreover, the greater reducibility was associated to a stronger increase of the Frenkel sites and oxidized defects components (D1 and D2) once returned to RT, consistently with the involvement of the defect sites in a more pronounced structural rearrangement, fostered by the presence of easily reducible dopants.

Although further investigations are required in order to extend the results to other types of ceria-based materials, the tests carried out in different atmospheres allowed to unveil some interesting mechanisms which contribute to defining the catalyst reducibility and reactivity, leading to outcomes which are worth considering in the framework of designing performing catalysts.

Chapter 5

Nanostructured equimolar ceria-praseodymia for total oxidations in low-O_2 conditions

The study presented in this chapter was published, with modifications, as [274]:

Sartoretti, E.; Martini, F.; Piumetti, M.; Bensaid, S.; Russo, N.; Fino, D. Nanostructured Equimolar Ceria-Praseodymia for Total Oxidations in Low-O_2 Conditions. *Catalysts* **2020**, *10*, 1–16, doi:10.3390/catal10020165.

5.1 Introduction

In the recent years, several strategies have been implemented by automotive manufacturers in order to comply with the CO_2 emission targets imposed by many nations (e.g. 95 g/km in the European Union) [65]. Diesel engines provide a good efficiency, but they require a complex after-treatment apparatus [79] and they have encountered a decline in popularity in the last years; hence, many efforts have been devoted to improving the overall fuel economy of gasoline engines. Among the different solutions developed, the Gasoline Direct Injection (GDI) technology presents several advantages with respect to Port Fuel Injection (PFI), since a GDI engine can work with higher efficiency and lower fuel consumption [66]. However, the reduced degree of mixing in the combustion chamber entails the production of a greater range and quantity of noxious combustion by-products in the fuel-rich regions of the flame, e.g. unburned hydrocarbons and carbonaceous particulate matter (soot) [66,67,125,275]. Since the actual regulations strictly limit not only the mass but also the number of solid particles that can be emitted, GDI vehicles have been equipped with a Gasoline Particulate Filter (GPF) in order to keep the emissions within the limits [65,68,275]. The

structure and operating principle of a GPF are similar to that of a Diesel Particulate Filter (DPF), but the regeneration phase is more critical due to the lack of oxygen. In fact, while the O_2 concentration is usually around 10% in diesel exhaust, it is lower than 5% in stratified-charge GDI engines and it is barely measurable in homogeneous-charge GDI engines, due to the stoichiometric air-to-fuel ratio employed [127].

In order to lower the temperature and time required for the GPF regeneration, as well as the associated fuel consumption, a catalytic coating can be placed on the filter walls with the purpose of promoting soot oxidation. To this end, ceria-based catalysts have been widely investigated, thanks to the interesting physico-chemical properties and redox cycle typical of these materials [129,136,178]. In fact, the high ceria OSC can be exploited to oxidize different pollutants (e.g. CO or soot). Moreover, ceria nanoparticles with tailored shape can be obtained by tuning the synthesis conditions [207]. The morphology plays a key role in defining ceria activity, because it affects not only the specific surface area and exposed crystal planes, but also the type and quantity of solid-solid contact points in the case of soot oxidation [115,145,184,207], as discussed in Chapter 1.

Ceria properties can be further tuned by inserting certain dopant ions into its crystal structure, in order to improve the activity and stability of the catalytic system. Among the rare earth elements studied as dopants, promising results in terms of soot oxidation activity have been obtained with Pr [188,199]. In particular, nanostructured equimolar ceria-praseodymia was even able to outperform a supported Pt-based catalyst [160,276]. Although this material has been thoroughly investigated under different conditions, a complete study in low oxygen availability is required to evaluate its application in a GPF.

In this chapter, a nanostructured equimolar ceria-praseodymia catalyst was prepared via hydrothermal synthesis and characterized with several techniques in order to evaluate its textural, morphological and physico-chemical properties. The catalytic activity was explored considering different reactions, namely CO oxidation, ethylene and propylene total oxidation and soot combustion. The tests were performed keeping an O_2 concentration of 1%, a value representative of a GDI engine exhaust [275], and the performances in oxygen-deficient and oxygen-rich conditions were compared. Finally, a kinetic study of the soot oxidation reaction was carried out, estimating the oxygen reaction order.

5.2 Experimental methods

In the present chapter, an equimolar Ce-Pr oxide (Ce50Pr50) was prepared via hydrothermal synthesis and calcined in air at 650 °C for 4 h. The catalyst was studied using different characterization techniques, to identify its main physico-chemical and morphological properties; in detail, XRD, N_2-physisorption, FESEM, XPS and temperature programmed analyses were performed. The catalytic activity towards the oxidation of CO, VOCs and soot was evaluated as well. All the experimental methods used for catalyst preparation, characterization and testing were described in Chapter 2.

5.3 Results and discussion

5.3.1 Catalyst characterization

The synthesized material was investigated using different complementary techniques, in order to unveil its physico-chemical and textural properties. Figure 5.1 displays the powder XRD diffractogram of the Ce50Pr50 catalyst, compared with that of pure ceria prepared using the same synthesis procedure. The mixed oxide exhibits the typical pattern of the fluorite crystalline structure of ceria, marked by the presence of the (1 1 1), (2 0 0), (2 2 0), (3 1 1) and (2 2 2) planes [145,155,160,161,207]. This similarity indicates that Pr ions are well incorporated into the ceria lattice, which is confirmed by the absence of additional peaks attributable to segregated oxides. However, the peaks in the XRD pattern of the Ce50Pr50 catalyst are slightly shifted towards lower angles with respect to those of pure ceria, especially at low 2Θ values. Moreover, the lattice parameter a calculated using the Nelson-Riley extrapolation function is lower for the mixed oxide (5.408 Å) with respect to CeO_2 (5.412 Å), suggesting that Ce^{4+} ions in ceria are mainly replaced by Pr^{4+} ions, which have a slightly smaller ionic radius [222].

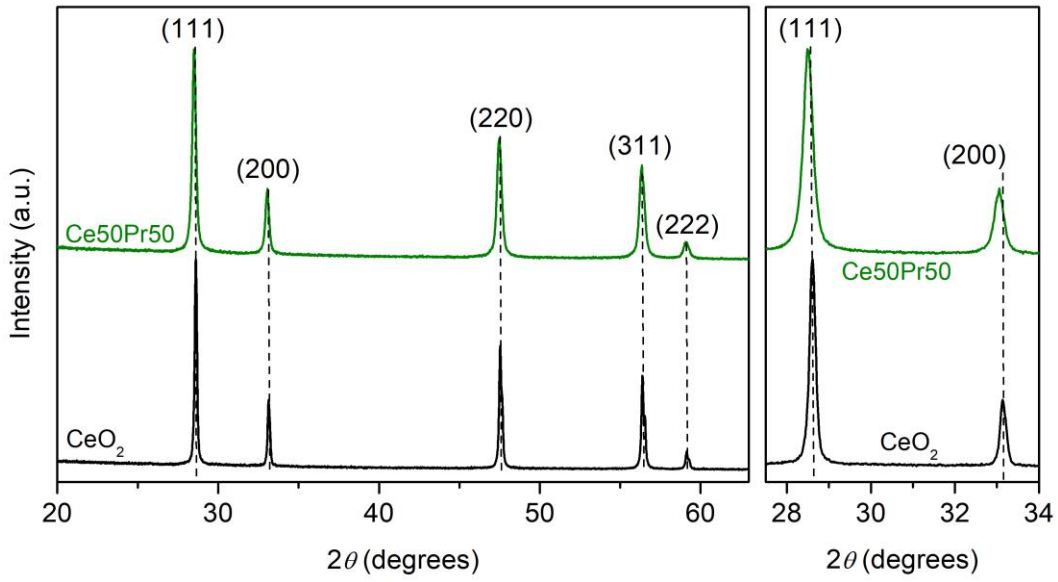

Figure 5.1. XRD diffractograms of the Ce50Pr50 catalyst and of pure ceria, with an enlargement of the first two peaks in the right panel to better show the shift in position.

The (2 0 0)/(1 1 1) and (2 2 0)/(1 1 1) peak intensity ratios were calculated, and the values obtained were 0.32 and 0.63, respectively. Both these parameters are higher than those observed on pure ceria samples prepared in analogous conditions (being 0.30 and 0.51, respectively [207]), and especially the (2 2 0)/(1 1 1) ratio shows a remarkable increase. This result suggests that Pr addition can affect the crystal growth during the synthesis, inducing an increase in the relative abundancy of the (1 1 0) planes. Furthermore, praseodymium addition was found to also influence the final dimension of the particles. Indeed, the average crystallite size was estimated using Scherrer's equation, and the value

obtained for the Ce50Pr50 catalyst (42 nm) was significantly lower than that observed for pure ceria nanoparticles (139 nm).

The specific surface area of the Ce50Pr50 sample was calculated via nitrogen physisorption, using the BET method. A value of 13 m^2 g^{-1} was found, slightly higher than that of pure CeO_2 (7 m^2 g^{-1}), in agreement with the smaller size of the ceria-praseodymia crystallites pointed out by the XRD results.

Figure 5.2 reports some FESEM micrographs of the Ce50Pr50 catalyst, in which two different types of nanostructures can be noticed. Both nanopolyhedra and nanorods are present in the sample, instead of the nanocubes previously observed in pure ceria prepared using analogous synthesis conditions [207]. This confirms that Pr addition directly affects the ripening process, promoting the growth of (1 1 0) crystal planes and thus favoring edge truncation and elongation of the particles. EDX analyses were performed focusing the spot on different points of the sample. The average composition of the mixed oxide resulted to be very close to the nominal one, with 49.4% of cerium and 50.6% of praseodymium. Furthermore, EDX mapping, whose results are reported in Figure 5.3, showed that the two elements are evenly distributed in the space, confirming the good homogeneity of the Ce50Pr50 sample.

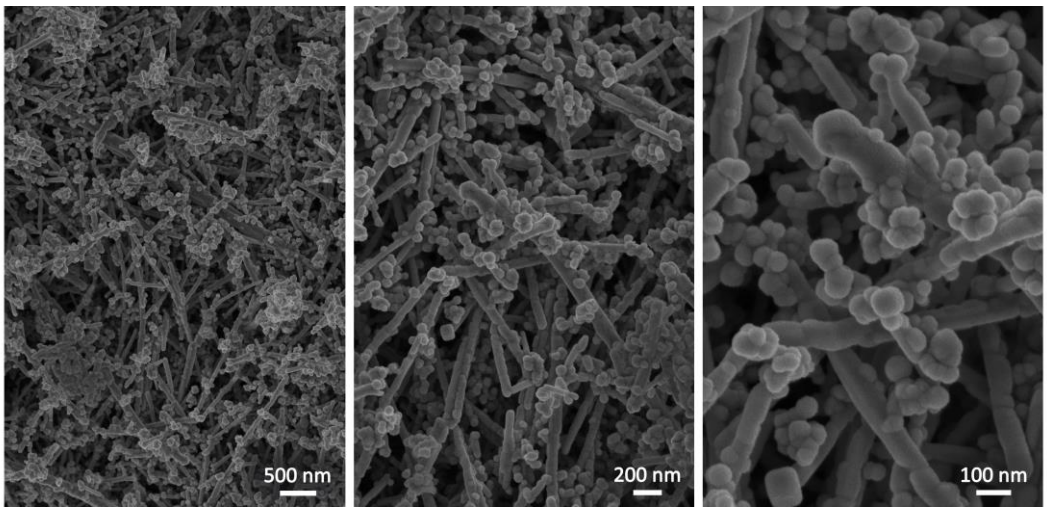

Figure 5.2. FESEM images of the Ce50Pr50 catalyst.

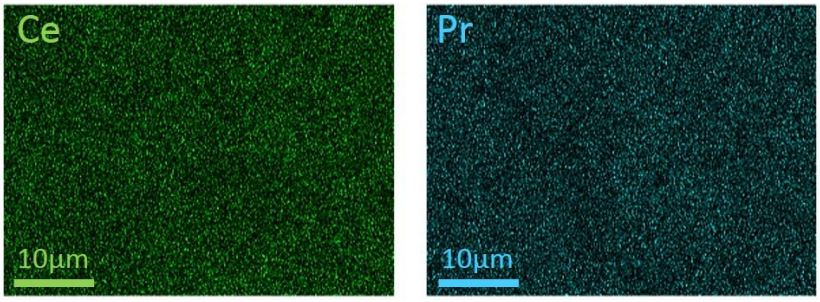

Figure 5.3. EDX maps of the Ce50Pr50 catalyst showing the distribution of Ce and Pr atoms.

The oxygen species at the surface of the sample were investigated analyzing the O 1*s* XP spectrum shown in Figure 5.4, in which two distinct peaks can be observed. The intense peak centered at 528.1 eV can be ascribed to lattice oxygen (the so-called "O_β") [186,277] and it is slightly shifted towards lower binding energy as a consequence of Pr addition [160]. The peak at higher binding energy (530.9 eV) is instead assigned to the various "O_α" capping oxygen species chemisorbed on the surface, e.g. hydroxyl (OH^-), carbonate (CO_3^{2-}), peroxide (O_2^{2-}) or superoxide (O^{2-}) ions [142,223]. The relative abundance of the O_α species, calculated from the area of the deconvolved peaks and reported in Table 5.1, resulted to be significantly high. A great quantity of chemisorbed oxygen can foster oxygen mobility and spillover at the catalyst surface, with beneficial effects during the oxidation reactions [145]; in particular, reactive oxygen species play a key role in the soot oxidation, in which a direct interaction between the two solid phases is limited by the few contact points.

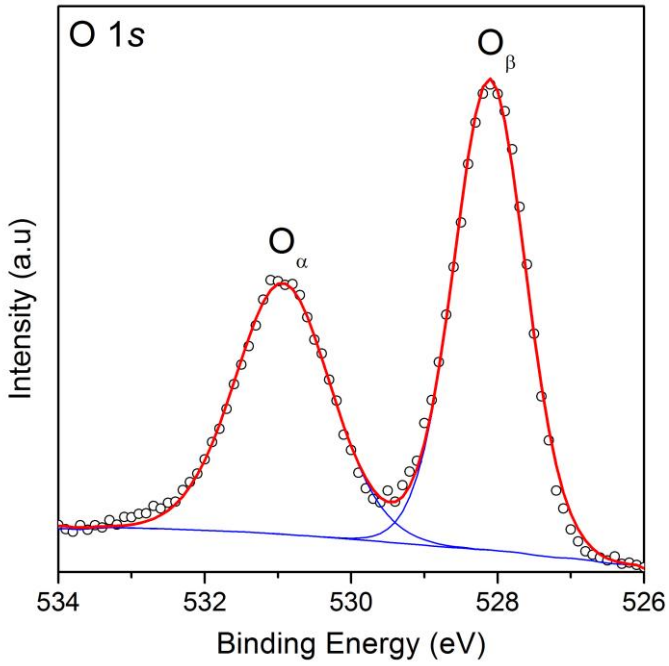

Figure 5.4. Deconvoluted XP spectrum of the Ce50Pr50 catalyst in the O 1*s* core level region.

Table 5.1. Relative abundances of different species at the surface of the Ce50Pr50 catalyst derived from the deconvolution of the XP spectra.

Catalyst	O_α	O_β	Ce^{3+}	Ce^{4+}	Pr^{3+}	Pr^{4+}
Ce50Pr50	41.6 %	58.4 %	19.3 %	80.7 %	63.8 %	36.2 %

Figure 5.5 A depicts the Ce 3*d* core level region of the XP spectrum. Five "u" and five "v" peaks were identified, related to $3d_{3/2}$ and $3d_{5/2}$ states, respectively. The v°, v', u° and u' peaks were ascribed to Ce^{3+} ions, while the other six peaks were assigned to the 4+ oxidation state [278,279]. A similar deconvolution was

performed on the Pr 3*d* XP spectrum, in the 968 – 923 eV region (Figure 5.5 B), ascribing four peaks (herein denoted as a°, a', b° and b') to Pr^{3+} ions and other six peaks to the 4+ oxidation state [280]. The relative abundance of the Ce and Pr cations was estimated after the deconvolution, and the calculated values are resumed in Table 5.1. Although Pr addition was proved to increase the Ce^{3+} quantity [160,281], cerium maintains 4+ as primary valence. Instead, most of the Pr cations are in the lower oxidation states, confirming the higher reducibility of this element and suggesting a strong presence of oxygen vacancies at the catalyst surface.

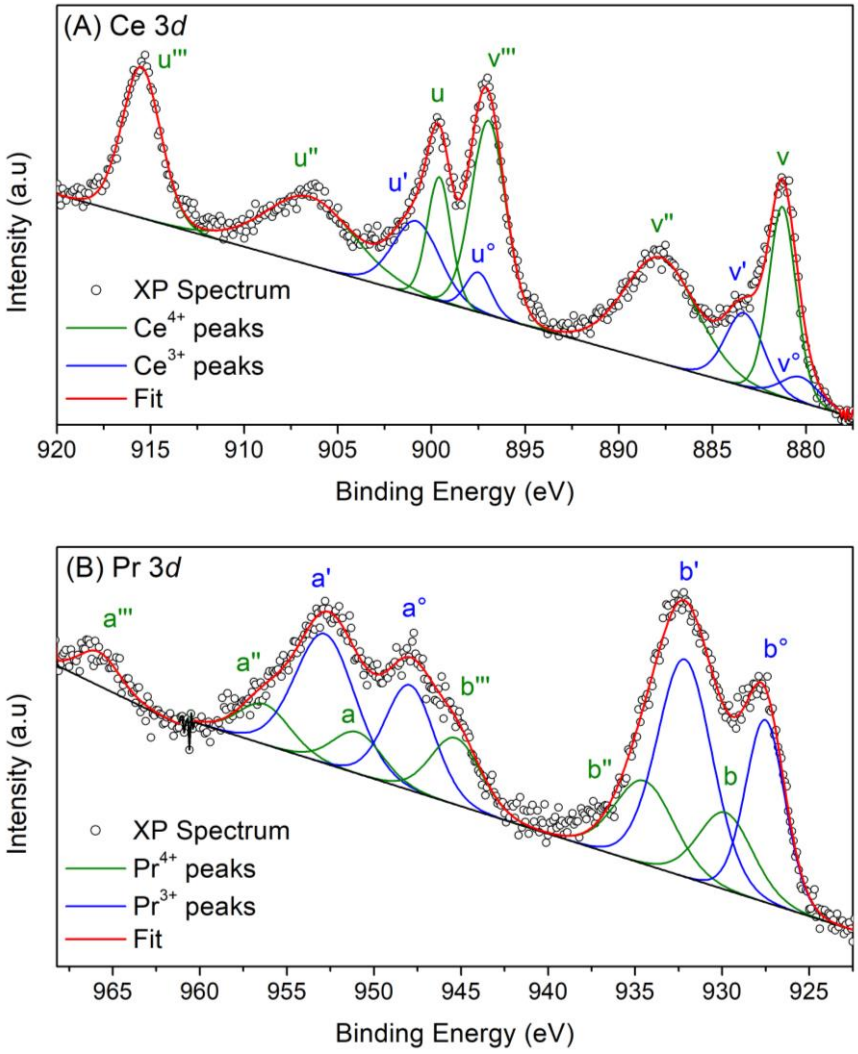

Figure 5.5. Deconvolved XP spectra of the Ce50Pr50 catalyst in the Ce 3*d* (A) and Pr 3*d* (B) core levels regions.

In order to better investigate the reducibility of the catalyst, different types of temperature programmed reduction were performed. The H_2-TPR profiles of pure and 50% Pr doped ceria are reported in Figure 5.6 A. The reduction of pure ceria occurs in two steps: a lower temperature peak centered at about 600 °C is associated to the surface reduction, while a band located above 700 °C is related to the slow release of bulk β-oxygen at very high temperature [282,283]. For the Ce50Pr50 sample, a single intense peak was observed during the H_2-TPR,

pointing out that Ce and Pr ions are simultaneously reduced from a 4+ to a 3+ valence state. The position of this asymmetric component, centered around 460 °C, suggests that Pr addition significantly increases the ceria reducibility; in fact, the incorporation of Pr ions can weaken the Ce-O bond, thus fostering the oxygen release from both the surface and the bulk.

The results of the CO-TPR are reported in Figure 5.6 B. In this case, the CO_2 concentration at the outlet was monitored, as this species is the result of the reaction between the CO and the oxygen released from the catalyst lattice. While reduction peaks were barely visible for pure ceria nanocubes, here a peak around 550 °C can be clearly observed for the Ce50Pr50 catalyst, as a result of its higher reducibility and OSC (the operating conditions adopted in this work differ from the ones of the CO-TPR reported in [199], and therefore the peak locates at a different temperature).

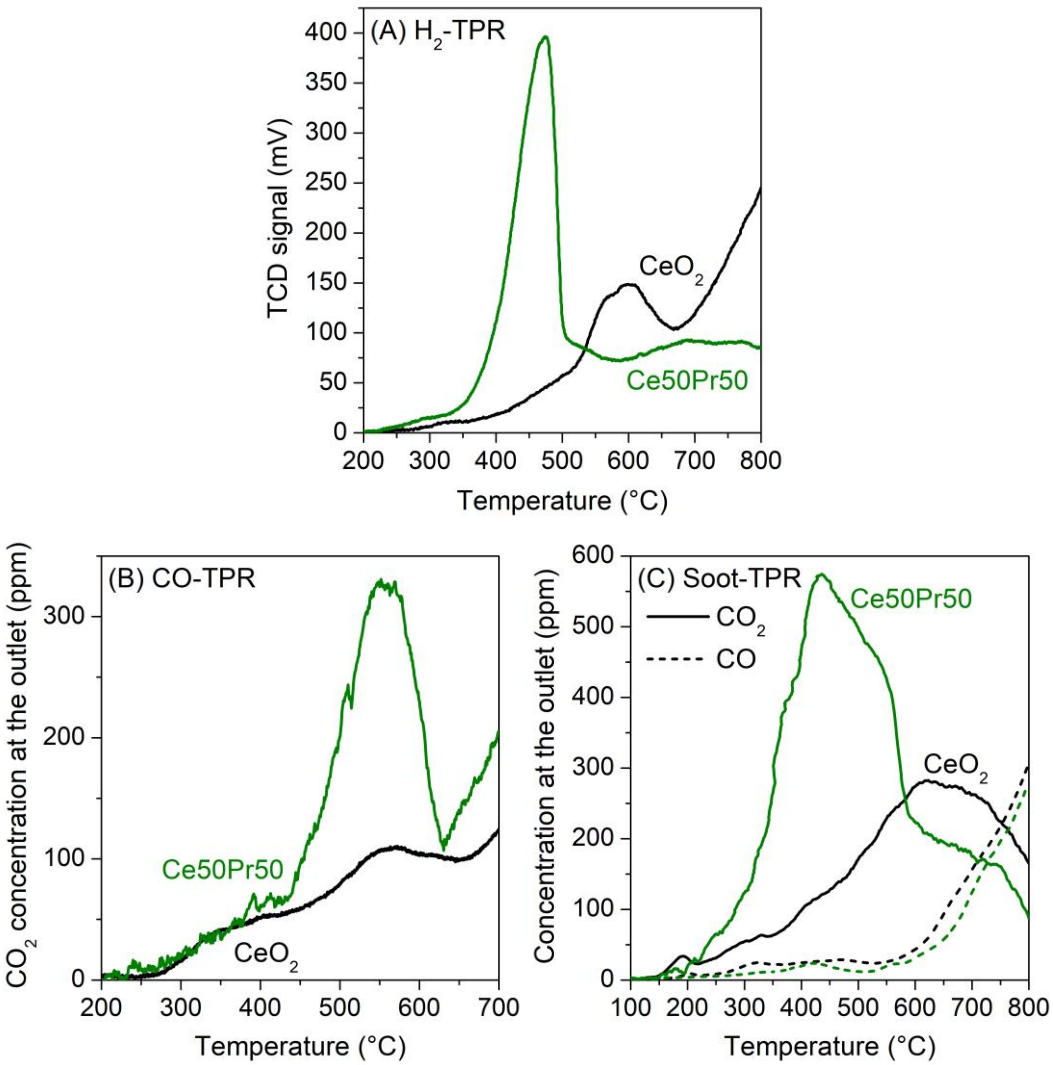

Figure 5.6. Results of the temperature programmed reduction analyses performed on the Ce50Pr50 catalyst and on pure CeO_2: H_2-TPR (A), CO-TPR (B) and soot-TPR (C).

Furthermore, soot-TPR analysis was performed, heating a bed of catalyst and soot in tight contact (i.e. mixed in a ball mill) in absence of gas-phase oxygen. The concentration profiles of the CO and CO_2 produced when the soot is oxidized by pure and Pr-doped ceria are displayed in Figure 5.6 C. Observing the plot, two reaction steps can be identified: at low temperature (200 – 600 °C), when the surface oxygen species are still abundant, the catalyst reduction produces mainly CO_2 and almost no CO, pointing out the good selectivity of Ce50Pr50; however, at high temperature (above 600 °C) more CO starts to be generated, since most of the available oxygen of the catalyst has already been consumed. The mixed oxide is able to release a higher quantity of oxygen, especially at low temperature.

5.3.2 Catalytic activity

The catalytic activity of nanostructured Ce50Pr50 was investigated by performing different oxidation reactions over the catalyst powder. The CO conversion, soot combustion and VOCs total oxidation were tested in low oxygen concentration (1%), in order to simulate the conditions of a GPF.

CO oxidation

The oxidizing capability of the Ce50Pr50 catalyst was firstly evaluated through CO oxidation tests and compared to that of pure ceria. The results obtained, in terms of CO converted to CO_2 as a function of the temperature, are reported in Figure 5.7. In the absence of a catalyst, the thermal conversion of CO starts to be significant only above 500 °C, and it is still lower than 10% at 600 °C. Anyway, this reaction can be activated at much lower temperature by pure CeO_2, and the Ce50Pr50 mixed oxide shows even better catalytic performances. For a quantitative evaluation, the $T_{50\%}$ can be considered, namely the temperature at which 50% of the incoming CO is oxidized. The Ce50Pr50 sample was able to reach such conversion at only 359 °C in high oxygen excess, exhibiting a specific reaction rate of the CO oxidation of 47 $\mu mol_{CO}\ h^{-1}\ m^{-2}$ at this temperature, while the $T_{50\%}$ of pure CeO_2 was 413 °C. Nanostructured ceria-praseodymia is therefore more efficient towards CO abatement with respect to pure ceria [135,160,261] and to Pr-doped ceria synthesized with different techniques [161,284].

The great activity of the Ce50Pr50 catalyst seems to be preserved even when the oxygen availability in the gas phase is limited: indeed, the conversion curve obtained in low-oxygen conditions is quite similar to that measured when feeding the reactor with 10% of oxygen, and the $T_{50\%}$ is just 20 °C higher (see Table 5.2). This interesting performance can be ascribed to the redox properties and high reducibility previously discussed. In fact, since CO oxidation occurs via a MvK-type mechanism over ceria-based catalysts [136], the ability to easily release surface oxygen species accessible to CO molecules plays a key role in defining the catalytic activity. Moreover, also the decrease of the particle size induced by Pr addition has a beneficial effect on the reaction, since the quantity of active sites available to the gaseous reagents is directly related to the specific surface area.

Also pure ceria exhibited a limited shift of the CO conversion curve towards higher temperatures at low-oxygen conditions, presenting a $T_{50\%}$ of 437 °C.

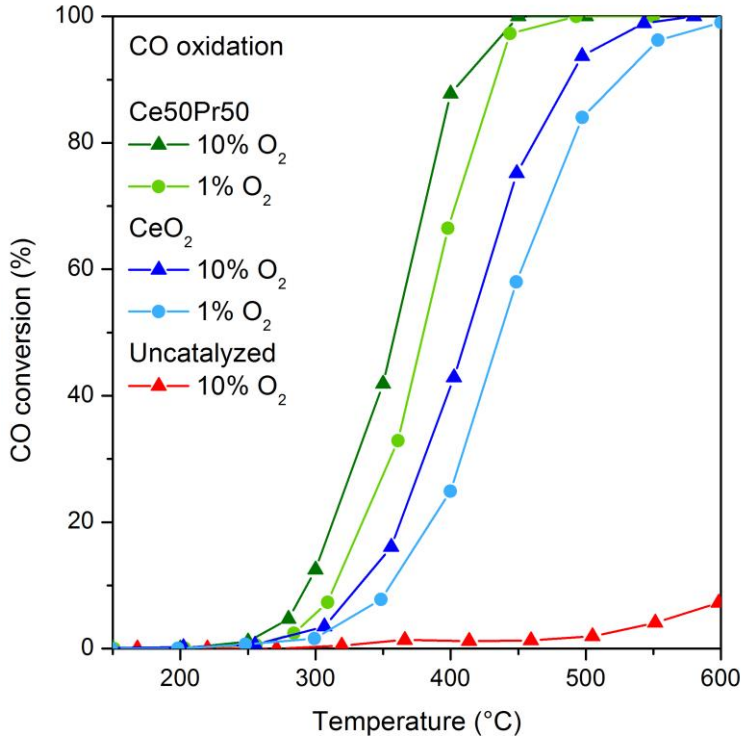

Figure 5.7. CO to CO_2 conversion as a function of the temperature, obtained testing pure CeO_2 and the Ce50Pr50 catalyst in different oxygen conditions.

Table 5.2. Comparison of the parameters obtained from the different catalytic tests performed in low-oxygen conditions (1% O_2) over the Ce50Pr50 catalyst and pure CeO_2. The temperatures at which 10, 50 and 90% of conversion were reached are reported.

Reaction	Catalyst	$T_{10\%}$ [°C]	$T_{50\%}$ [°C]	$T_{90\%}$ [°C]
CO oxidation	CeO_2	355	437	525
	Ce50Pr50	314	380	433
Ethylene oxidation	CeO_2	450	532	615
	Ce50Pr50	173	211	252
Propylene oxidation	CeO_2	370	475	543
	Ce50Pr50	255	327	389
Soot oxidation (tight contact)	CeO_2 [285]	431	485	527
	Ce50Pr50	414	462	517

VOCs oxidation

In order to investigate the oxidizing activity of pure and Pr-doped ceria towards VOCs, ethylene and propylene were chosen as probe molecules. In fact, these two species are among the unburned hydrocarbons which can be found in the exhaust gas emitted by gasoline cars, since they can partially slip away from the three-way catalyst at certain operative conditions [13]. The abatement of these compounds is of high importance due to the fact that some of them are toxic for human health [14,15,252] and they can also foster the photochemical generation of secondary pollutants, such as ozone [17]. Since ceria-based oxides can be used as catalysts [162,286,287] or noble metals supports [277,288,289] for VOCs oxidation, CeO_2 and Ce50Pr50 are expected to affect these kinds of reactions.

The catalytic tests were carried out at two different concentrations of oxygen, in order to evaluate the effect of this parameter. The conversion curves resulting from the ethylene and propylene oxidation tests are reported in Figure 5.8. Both CeO_2 and Ce50Pr50 were able to catalyze the two oxidation reactions, since the temperatures required for the conversion were considerably lower in the presence of these catalysts with respect to the uncatalyzed tests. However, the mixed oxide showed a remarkably higher activity, as pointed out by the catalytic parameters resumed in Table 5.2.

In the case of ethylene, pure ceria was more sensitive to the O_2 quantity, showing a lower conversion in oxygen shortage, as displayed in Figure 5.8 A. Instead, the oxygen concentration induced only minimal changes on the conversion curve of Ce50Pr50: in fact, the light-off temperature was slightly lower when oxygen was in high excess, as could be expected, but then the 50% of conversion was reached at about 215 °C regardless of the O_2 abundancy. At high temperatures, competitive adsorption between ethylene and oxygen might possibly explain the higher catalytic activity observed at low oxygen concentration (1%): indeed, the higher conversion of ethylene could be due to its higher degree of adsorption on the catalyst with respect to the conditions at high oxygen content (10%).

Conversely, oxygen availability seems to remarkably affect the Ce50Pr50 performances in the case of propylene oxidation, as can be observed in Figure 5.8 B. In detail, when 10% of oxygen was fed to the reactor, the Ce50Pr50 catalyst exhibited a considerable activity, with a $T_{50\%}$ of 205 °C; under 1% of O_2, instead, the 50% of conversion was reached at 327 °C, indicating that Ce50Pr50 is less active in oxygen shortage conditions, although it is still able to significantly promote the propylene oxidation. On the contrary, the role of oxygen seems to be much less relevant for pure CeO_2, whose $T_{50\%}$ only slightly increased from 462 °C to 475 °C when reducing the oxygen concentration.

Furthermore, the Ce50Pr50 catalyst was also capable of affecting the selectivity to CO_2 during the VOCs oxidation. In fact, the uncatalyzed reaction produces 25% of CO in the case of ethylene and 17% in the case of propylene oxidation (average values measured in the 300 – 500 °C range). When Ce50Pr50 is employed, instead, the CO formation is totally negligible in the case of ethylene

(CO_2 selectivity is always almost 100%) and it is marginal also when propylene is used, with a CO_2 selectivity ranging from 97% at 250 °C to values over 99% above 350 °C.

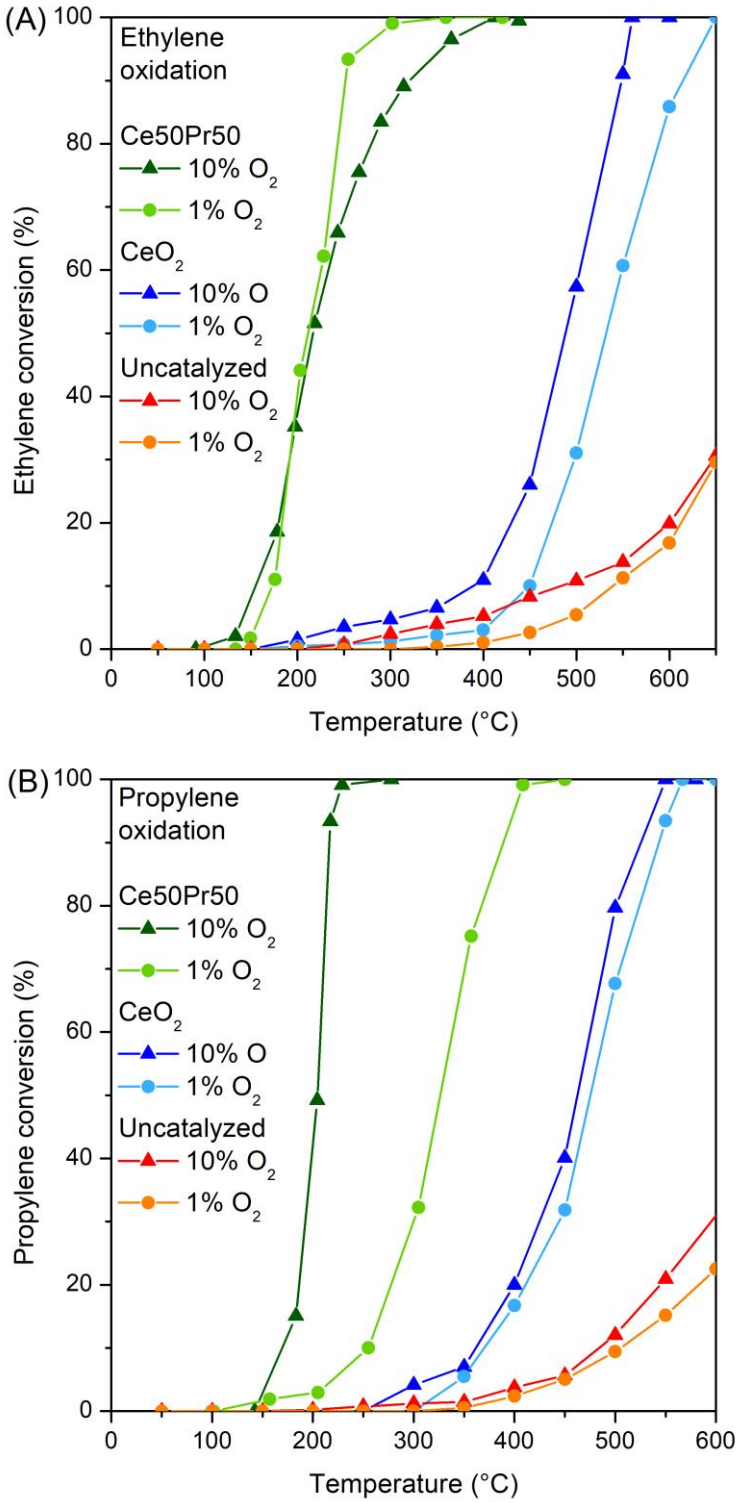

Figure 5.8. Ethylene (A) and propylene (B) conversion curves as a function of the temperature, obtained testing pure CeO_2 and the Ce50Pr50 catalyst in different oxygen conditions.

Soot oxidation

Afterwards, the activity of Ce50Pr50 towards the oxidation of particulate matter was evaluated. Actually, this heterogeneous reaction involves two solid phases, and is therefore strongly dependent on the quality of the contact at the interface, i.e. the force with which the two solids are brought together and the compatibility of their surface features [177,185,207,290,291]. For this reason, the catalytic activity was probed in two different conditions: loose contact (LC), which is more representative of the real situation in a GPF, was achieved by gently mixing the two powders with a spatula, while tight contact (TC), which can provide further information about the intrinsic activity, was reached via ball milling. Synthetic Printex-U carbon black was used as carbonaceous particulate, since it represents a suitable substitute for GDI soot [292], and 1% of O_2 was fed to the reactor.

The results of the soot oxidation tests are reported in Figure 5.9 and Figure 5.10. As expected, better performances were observed at the higher degree of contact, but in both the cases the catalyst was able to significantly reduce the temperature required for the soot conversion. Indeed, while 50% of the soot initially present was oxidized only at 652 °C without a catalyst, the same conversion was reached more than 100 °C earlier with Ce50Pr50: in detail, the $T_{50\%}$ was 510 °C in LC and 465 °C in TC. These values are comparable to those obtained at higher oxygen concentrations [160]. Instead, non-doped ceria exhibited a lower activity in oxygen shortage, since a higher $T_{50\%}$ (485 °C) was obtained when soot oxidation was performed in TC on this catalyst [285] (see Table 5.2).

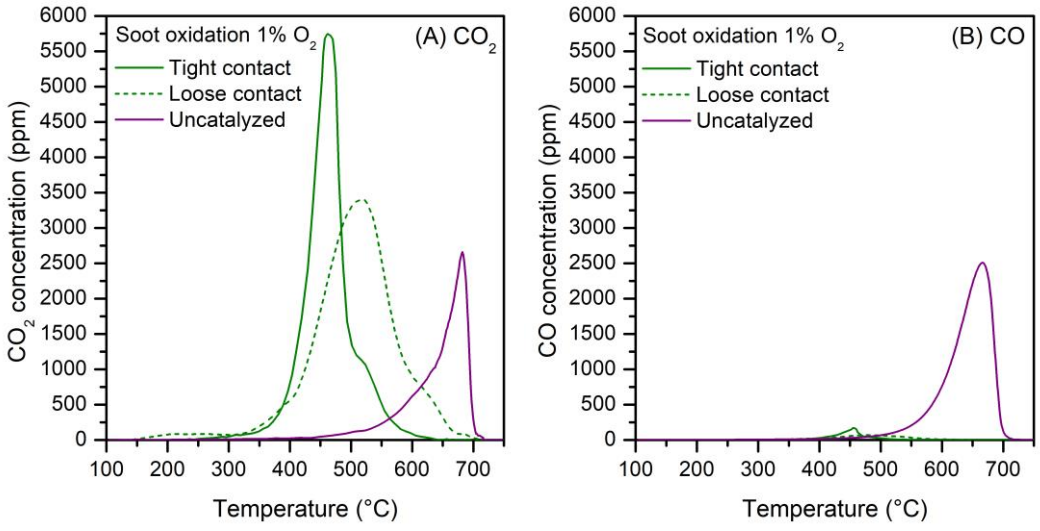

Figure 5.9. CO_2 (A) and CO (B) concentration at the outlet as a function of the temperature during the soot oxidation tests performed over the Ce50Pr50 catalyst in low-O_2 conditions.

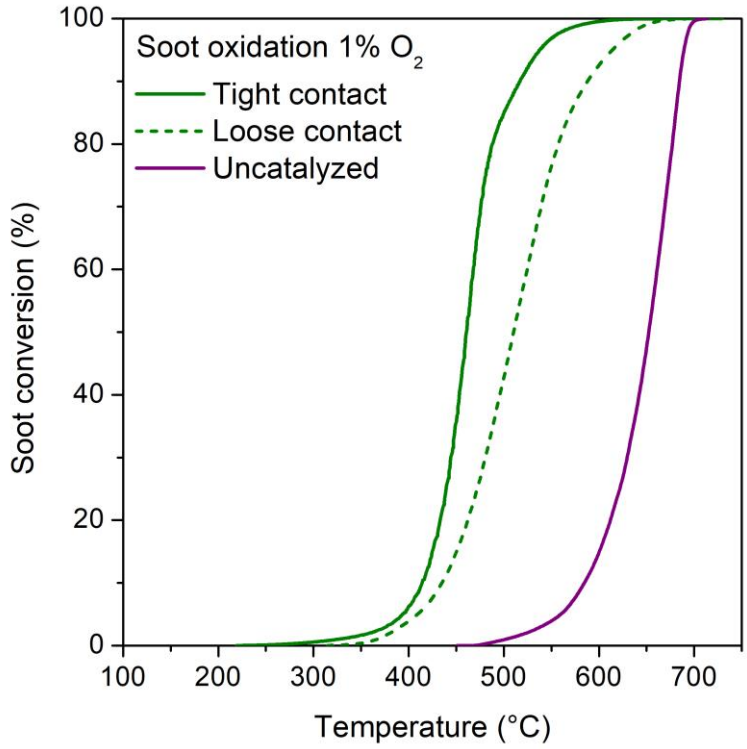

Figure 5.10. Soot conversion as a function of the temperature during the soot oxidation tests performed over the Ce50Pr50 catalyst in low-O_2 conditions.

The Ce50Pr50 catalyst seems therefore able to effectively interact with the gas-phase O_2, even when the concentration of the latter is as low as 1%. As a result, this material was capable of preserving the selectivity towards CO_2 despite the low oxygen availability: indeed, when the soot combustion was performed in the absence of a catalyst, the carbon was converted mainly to CO, as the CO to CO_2 reaction step was hindered by the lack of gas-phase oxygen; instead, in the presence of Ce50Pr50, the CO_2 selectivity exceeded 96.5% in TC and reached 98% in LC.

Finally, kinetic studies were carried out in order to further analyze how the oxygen concentration affects the soot oxidation reaction when it is promoted by Ce50Pr50. The oxygen partial pressure in the gaseous mixture can be expected to affect the reaction rate, and it will therefore feature in the rate equation with a certain reaction order. Kastrinaki et al. [293] described the isothermal oxidation of soot on ceria-based catalysts using a multi-population first-order model: different oxidation rate constants were employed for different soot populations, which were distinguished by their contact conditions with the catalyst. Hence, the macroscopic oxidation process results from several parallel microscopic processes and can be modelled as follows:

$$-\frac{dm}{dt} = \sum_{n} k_i \cdot m_i(t) \cdot [O_2]^{\beta} \tag{5.1}$$

with solutions of the type

$$\boldsymbol{m(t) = \sum_{n} m_{i,0} \cdot e^{-t/\tau_i}} \tag{5.2}$$

with

$$\boldsymbol{\frac{1}{\tau_i} = k_i \cdot [O_2]^{\beta_i}} \tag{5.3}$$

where m is the total soot mass, m_i is the soot mass of the i-th population, k_i is the rate constant for the oxidation in the contact conditions of the i-th population, β_i is the reaction order of oxygen for the i-th population and the subscript 0 indicates the initial soot mass. In tight contact, the contact conditions between the soot and the catalyst can be assumed homogeneous throughout the sample: the sum could therefore be reduced to a single term, and the macroscopic oxidation process can be effectively described by a monoexponential-type model:

$$\boldsymbol{-\frac{dm}{dt} = k_{TC} \cdot m \cdot [O_2]^{\beta}} \tag{5.4}$$

with a solution of the type:

$$\boldsymbol{m(t) = m_0 \cdot e^{-t/\tau_{TC}}} \tag{5.5}$$

The reaction order of oxygen can then be evaluated by carrying out isothermal oxidations at different oxygen partial pressures and by extracting the characteristic reaction times τ from monoexponential fittings of the soot conversion curves. In fact, extracting the logarithm from both members of equation (5.3) provides the following equation:

$$\boldsymbol{log(1/\tau_{TC}) = log(k_{TC}) + \beta\, log([O_2])} \tag{5.6}$$

The thus obtained τ values can be plotted against the respective values of the oxygen fraction in the gaseous mixture in a double logarithmic plot. A linear regression of the experimental points will provide a line whose slope is the reaction order of oxygen and whose intercept is the rate constant for tight contact conditions.

This kind of kinetic evaluation was carried out by performing isothermal soot oxidation at 450 °C at three different O_2 concentrations, namely 1%, 5% and 10%; the results of these tests are presented in Figure 5.11. The soot oxidation curves in Figure 5.11 A point out the detrimental effect of the lack of oxygen, since a reduction of its abundance results in a lower reaction rate, as could be expected. After fitting these profiles with a monoexponential function in order to obtain the τ values, the plot in Figure 5.11 B was realized, following equation (5.6), and a

linear regression of the points was performed. The resulting reaction order for oxygen (β) is very close to 1, in agreement with the results of Neeft et al. [294] and Darcy et al. [295] regarding the non-catalytic oxidation of Printex-U soot. Nevertheless, despite this direct dependence of the reaction rate on the oxygen concentration, the Ce50Pr50 catalyst showed promising performances towards soot combustion even in oxygen shortage conditions, thanks to its high intrinsic activity.

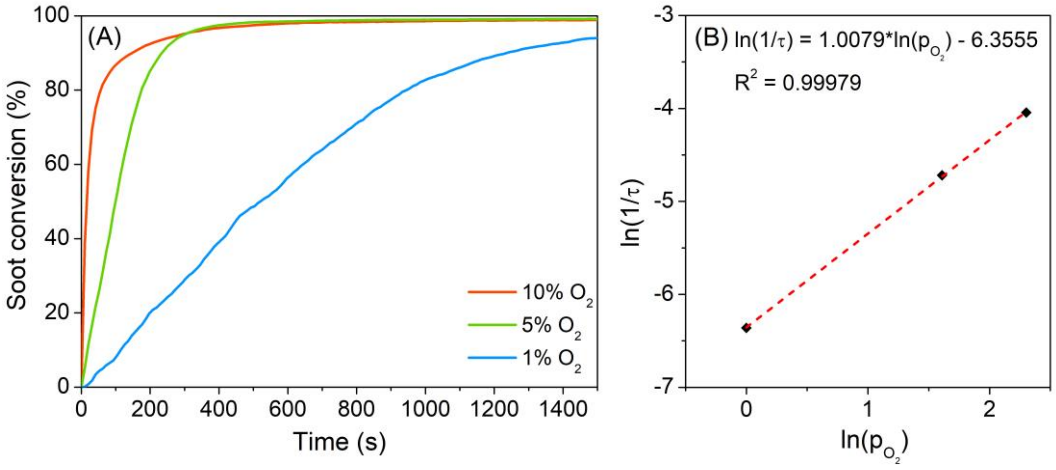

Figure 5.11. Soot conversion profiles as a function of time during the isothermal soot oxidation tests performed over the Ce50Pr50 catalyst in different O_2 conditions (A). Linear regression of the experimental data (B), as described in equation (5.6).

5.4 Conclusions

In this work, a nanostructured equimolar ceria-praseodymia catalyst has been investigated in order to study its behavior and catalytic activity in low-oxygen conditions. Although Pr ions were well incorporated into the ceria lattice, forming a single phase, the doping caused important structural and morphological changes. Indeed, praseodymium addition affected the crystal growth during the synthesis, resulting in the formation of two different kinds of nanoparticles. Furthermore, Pr weakened the cerium-oxygen bond, allowing to obtain a highly reducible material. Thanks to these properties, the catalyst exhibited a promising activity towards different oxidation reactions, especially in the case of soot combustion. Moreover, its performances only slightly worsened when the oxygen concentration in the inlet gaseous mixture was abated from 10% to 1%. The CO_2 selectivity was very high both in VOCs and soot oxidation, and it was fully preserved in oxygen shortage. These results point out the beneficial effects of coupling the Pr^{4+} - Pr^{3+} redox cycle to that of cerium: indeed, the thus-obtained material is capable of fruitfully delivering active oxygen species to particulate matter and gaseous pollutants. Therefore, equimolar ceria-praseodymia could be suitably employed in catalyzed GPFs, in which a high catalytic activity is required to comply with the emission abatement targets in low oxygen availability.

Chapter 6

Ceria-based nanocatalysts doped with La and Nd: investigations into structural/chemical properties and catalytic activity for CO, NO and soot oxidation

The study presented in this chapter has been submitted for publication, with some modifications.

6.1 Introduction

As largely discussed so far in this thesis, ceria-based materials are among the most suitable catalysts for promoting soot oxidation in coated particulate filters, thanks to their excellent redox properties and high oxygen storage capacity. Furthermore, different types of nanostructured ceria particles can be prepared and a well-defined morphology can bring significant benefits: indeed, ceria reactivity depends on the exposed crystal facets [135,136,259] and the shape of the nanoparticles also affect the quality and the number of catalyst-soot contact points, which are crucial aspects in the case of soot oxidation [151,185].

Two main soot oxidation pathways have been identified in the case of ceria-based materials. In detail, a MvK-like mechanism can occur at the catalyst-soot interface, involving the direct oxidation of soot by lattice oxygen coming from the catalyst; the thus-created oxygen vacancies are then refilled by gaseous O_2 [135,136]. Besides, reactive oxygen species such as O_2^- or O^- ions forming at the catalyst surface can be delivered to soot particles through spillover [186,296]. Furthermore, also the NO_x present in Diesel exhausts can take part in the

reactions, by adsorbing at the catalyst surface or by directly oxidizing soot [169,178,197,199].

The physico-chemical and structural properties governing the catalytic activity of ceria-based materials can be further improved by doping [178]. Excellent performances for soot oxidation have been recently obtained with Pr-doped ceria [178,276], especially in the case of nanostructured equimolar mixtures like that presented in the previous chapter [160,199]. However, the catalytic properties of analogous doped ceria nanoparticles with well-defined morphology but containing other lanthanides have been poorly investigated.

In the present chapter, six ceria-based oxides containing different quantities of La or Nd (10, 25 or 50%) were prepared via hydrothermal synthesis and evaluated as oxidizing catalysts. These mixed materials were deeply investigated with various characterization techniques and compared with pure oxides, in order to study the effects of doping on the structure, morphology, defectiveness, surface acidity and chemical/redox properties. The influence of these features on the catalytic activity towards soot oxidation was discussed, taking into account also the CO and NO oxidation capability. In detail, soot oxidation tests were carried out in different conditions, probing two degrees of contact between catalyst and soot and evaluating the catalyst stability upon thermal aging and in presence of water. Finally, NO_x-assisted soot oxidation was investigated, assessing the catalytic performances and suggesting the reaction mechanisms involved.

6.2 Experimental methods

Six ceria-based materials containing different quantities (i.e. 10%, 25% or 50% atomic) of lanthanum or neodymium were prepared via hydrothermal synthesis and calcined in air at 650 °C for 4 h. The samples were named CeXXReYY, where Re is the doping rare earth (La or Nd) while XX and YY are the atomic percentages of Ce and of the doping element, respectively. For the sake of comparison, pure CeO_2, La_2O_3 and Nd_2O_3 oxides were also synthesized, following an analogous procedure. The experimental methods used for the materials preparation, as well as for characterization and testing, were described in Chapter 2.

The catalysts were investigated using different characterization techniques, in order to identify their main structural and physico-chemical properties; in detail, XRD, N_2-physisorption, FESEM, EDX, Raman spectroscopy, XPS and temperature programmed analyses (H_2-TPR, O_2/NH_3/CO_2-TPD) were performed.

The catalytic activity towards the oxidation of CO, NO and soot was evaluated as well. In particular, soot oxidation was probed in two different conditions, namely in tight and loose contact between catalyst and soot. In order to evaluate the catalyst stability, soot oxidation was repeated after aging the samples at 700 °C for 8 h in an oven. Moreover, the effect of water was assessed by performing soot oxidation tests in loose contact feeding the reactor with a mixture of 10% of O_2 and 10% of H_2O in N_2, prepared using a Bronkhorst CEM evaporator.

NO_x-assisted soot oxidation tests were also performed. In this case, the catalytic bed was prepared and pre-treated as described in Chapter 2. Successively, a mixture containing 550 ppm of NO and 10% of O_2 in N_2 was sent to the by-pass line and then to the reactor. After the gas analyzer signals had stabilized, the temperature was increased from 50 up to 700 °C with a 5 °C min^{-1} ramp.

6.3 Results and discussion

6.3.1 Catalyst characterization

Structural and textural properties

The powder XRD diffractograms of the six materials are reported in Figure 6.1, together with those of pure CeO_2, La_2O_3 and Nd_2O_3. Pure ceria exhibits a pattern with eight peaks, typical of fluorite crystal structure [155,256,272,297]. Doped ceria is characterized by analogous diffractograms, but with some differences that become more evident increasing the dopant loading. In fact, the XRD patterns of the doped samples present a progressive shift towards lower angles with respect to that of pure ceria, as displayed in the insets of Figure 6.1. Moreover, only Ce90Nd10 is characterized by symmetric peaks, while all the other catalysts show a shoulder on the left side of each reflection, or even two distinct sets of peaks in the case of the Ce50La50 and Ce50Nd50 equimolar mixtures.

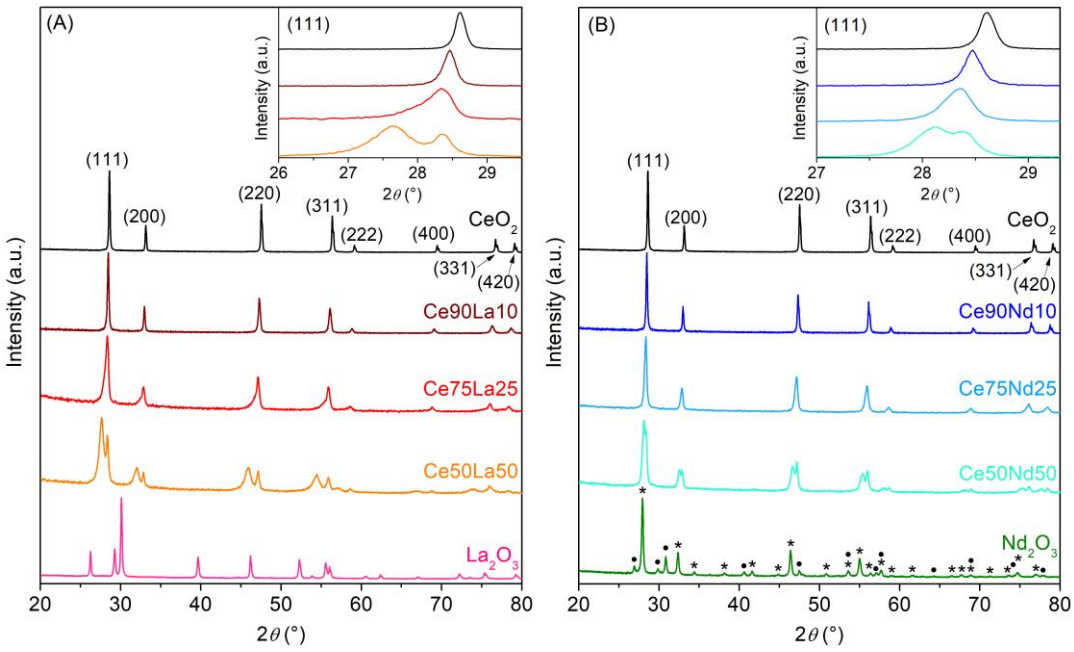

Figure 6.1. XRD diffractograms of the La-doped (A) and Nd-doped (B) ceria-based catalysts. As a comparison, also the patterns of the pure oxides (CeO_2, La_2O_3 and Nd_2O_3, prepared following the same synthesis procedure) are reported. For the biphasic Nd_2O_3, the peaks of the cubic (✳) and hexagonal (●) crystal structures are distinguished. In the insets, the (111) peak of the fluorite lattice is magnified.

However, this behavior does not seem related to La or Nd segregation. In fact, the typical peaks of the La_2O_3 hexagonal structure [298,299] are completely absent in the patterns of La-doped ceria, as evident from Figure 6.1 A, suggesting that La ions are well-incorporated in the ceria lattice also at high La loading. Nd seems to form a solid solution with ceria too, although this time the presence of small crystals of segregated Nd_2O_3 cannot be completely ruled out: indeed, neodymium oxide can form two different phases, with cubic and hexagonal structures [300,301], and the main peaks of the former crystal unit are partially overlapped to those of ceria, as displayed in Figure 6.1 B.

Nevertheless, the presence of particles with different compositions can be expected in the doped catalyst powder. The appearance of two sets of XRD peaks might therefore signal a bimodal distribution of the crystals [221], pointing out the existence of two main phases in the mixed oxides with two slightly different cubic structures. The first phase, characterized by higher-angle peaks, could be richer in cerium, since it has a smaller elementary unit and is more abundant in the slightly doped samples. The other phase, giving rise to lower-angle peaks, could present a more reduced structure rich in trivalent cations, since it has a larger crystal unit and becomes dominant as the dopant loading is increased.

For all the catalysts, the lattice constant (a) and the average crystallite size (D_c) of each detected phase were calculated and the values are reported in Table 6.1. The variation of the lattice constant as a function of doping is also detailed in Figure 6.2. The unit cell size of the dopant-enriched reduced structures increases almost linearly with the dopant content. Also the unit cell of the cerium-enriched oxidized structures undergoes an enlargement at increasing dopant loading, but a plateau is reached in this case. Lattice expansion, which is especially remarkable in the case of La doping, is the result of the insertion of La^{3+} and Nd^{3+} ions in ceria structure: indeed, the ionic radii of these species (1.16 and 1.109 Å, respectively) are larger than that of the Ce^{4+} ions they replace (0.97 Å) [222]. A higher abundance of Ce^{3+} in doped ceria could contribute to this effect as well. The progressive expansion of the crystal unit cells can explain the gradual shift observed in the XRD patterns of the doped samples (insets of Figure 6.1) [302]. Concerning the average crystallite size, it is always higher for the identified Ce-rich phase (right peaks); moreover, it becomes lower for both the phases as the dopant loading is increased: this means that the doping affects the particle growth during the synthesis, hindering the formation of big crystals [188].

La and Nd doping influenced the specific surface area of the catalysts too, as shown by the values in Table 6.1. In fact, the dopant addition caused an increase in surface area, in agreement with the smaller size of the crystallites. This effect is more marked for the Ce-La mixed oxides, which are indeed characterized by lower D_c values. As a result, the Ce75La25 and Ce50La50 samples exhibit the highest specific surface area. Also the pore volume of the six samples changes, but with different trends: this parameter increases with La addition, while it decreases when Nd is incorporated in ceria. However, all the catalysts present a quite low pore volume, limited to that of the interparticle voids, as expected for non-porous powders. The doping causes also a drop in the average pore diameter,

especially in the Ce-La mixed oxides, which is likely the result of the smaller particle size.

Table 6.1. Structural properties of the catalysts.

Catalyst	XRD peaks considered	a [Å]	D_C [a] [nm]	SSA [b] [m^2 g^{-1}]	V_p [b] [cm^3 g^{-1}]	D_p [b] [nm]	D/F_{2g} [c]
CeO_2	-	5.412	144	7	0.054	30	0.03
Ce90La10	Left peaks	5.447	42	9	0.037	16	0.16
	Right peaks	5.438	103				
Ce75La25	Left peaks	5.495	12	14	0.041	12	0.31
	Right peaks	5.455	38				
Ce50La50	Left peaks	5.592	11	18	0.047	10	0.88
	Right peaks	5.458	36				
Ce90Nd10	-	5.431	109	10	0.075	27	0.18
Ce75Nd25	Left peaks	5.466	36	13	0.066	20	0.45
	Right peaks	5.447	66				
Ce50Nd50	Left peaks	5.506	20	12	0.038	12	1.44
	Right peaks	5.451	58				

[a] Lattice constant (a) and average crystallite size (D_C) estimated via XRD

[b] Specific surface area (SSA), total pore volume (V_p) and average pore diameter (D_p) obtained via N_2-physisorption

[c] D/F_{2g} ratio calculated through Raman spectra deconvolution

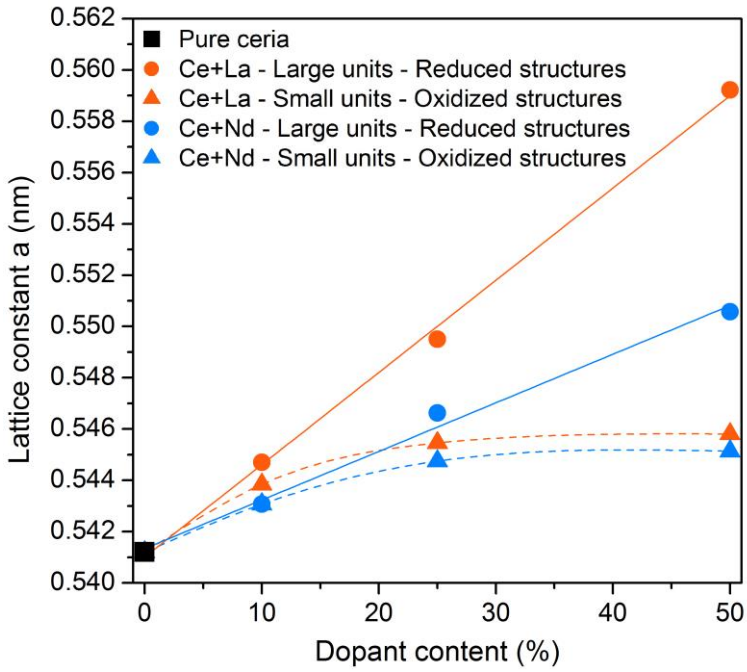

Figure 6.2. Variation of the lattice constant (*a*) as a function of doping for the two different types of crystal units identified in ceria doped with La and Nd.

The morphology of the prepared catalysts was investigated via electron microscopy. As previously described in the literature [207,212], the synthesis route here employed allows to obtain pure ceria in the form of well-defined cubic nanoparticles, with size ranging from 50 to 400 nm (Figure 6.3 G). However, the morphology changes upon doping, as shown by the FESEM micrographs of the mixed oxides displayed in Figure 6.3 A-F. Actually, only Ce90Nd10 preserves a purely nanocubic structure similar to that of CeO_2, albeit characterized by smaller particles in the 50 – 300 nm range. Also the other five catalysts exhibit nanocubic shapes, with reduced particle dimensions as the dopant concentration increases, but rod-like structures can be noticed besides. The elongated particles become more abundant with increasing dopant loading and they even constitute the prevalent morphological species in the two equimolar oxides.

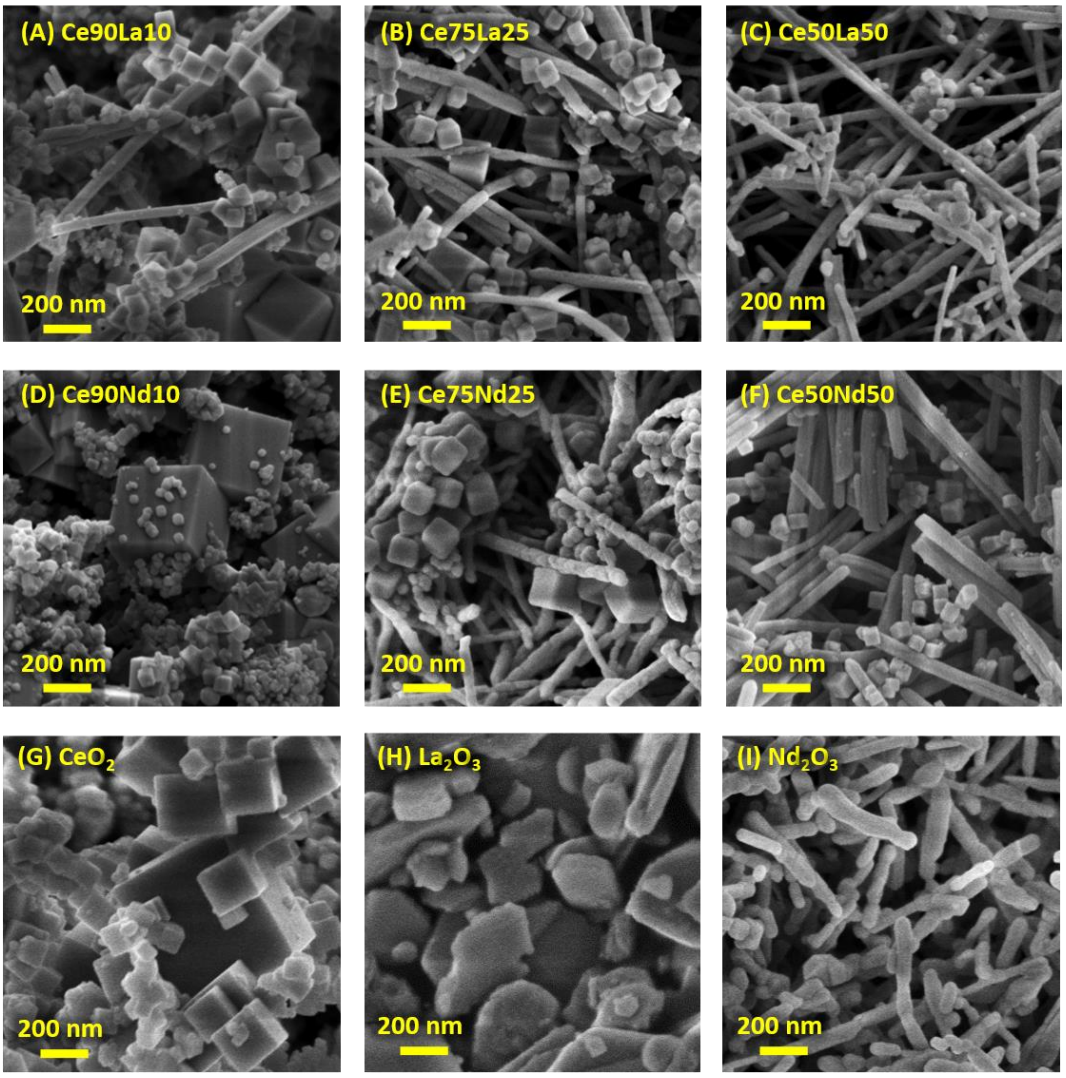

Figure 6.3. FESEM micrographs of the Ce90La10 (A), Ce75La25 (B), Ce50La50 (C), Ce90Nd10 (D), Ce75Nd25 (E) and Ce50Nd50 (F) catalysts, compared with pure CeO_2 (G), La_2O_3 (H) and Nd_2O_3 (I).

The incorporation of La and Nd in ceria structure has therefore two main effects on the particle ripening process: the dopant ions hinder the crystal growth, fostering the formation of smaller nanocubes, and at the same time favor the elongation of the particles. Furthermore, the two crystalline phases detected by XRD could correspond to the two different shapes: the cubes likely consist of Ce-rich bigger crystals with smaller and less distorted unit cells, while the rods might contain a higher quantity of dopant ions and be formed by several small crystals with larger and more deformed unit cells. Anyway, the morphology of the mixed oxides is different from that of the La_2O_3 and Nd_2O_3 irregular particles (shown in Figure 6.3 H and I, respectively), consistently with the absence of segregated pure oxides.

EDX analysis was performed focusing the spot on different points of the sample. The thus obtained average dopant concentration in the bulk of the mixed oxides is reported in Table 6.2 and all the values result to be very close to the nominal ones. Furthermore, an EDX map was collected on the Ce50La50 sample (shown in Figure 6.4) and similar uniform signals were obtained for Ce and La. However, because of the limited resolution of this technique, an even distribution of the two elements can be assumed only at micrometric level. In order to further investigate the compositional differences between cubes and rods, a linear map was acquired on the Ce50La50 sample and the results are reported in Figure 6.5. A line crossing a group of nanocubes amidst fibers was chosen and on the central agglomeration of cubic nanoparticles a more intense O signal and a lower La signal were recorded, while Ce signal only slightly increased compared to that of the surrounding region. Hence, these results support the attribution of a Ce-richer and more oxidized structure to the nanocubes.

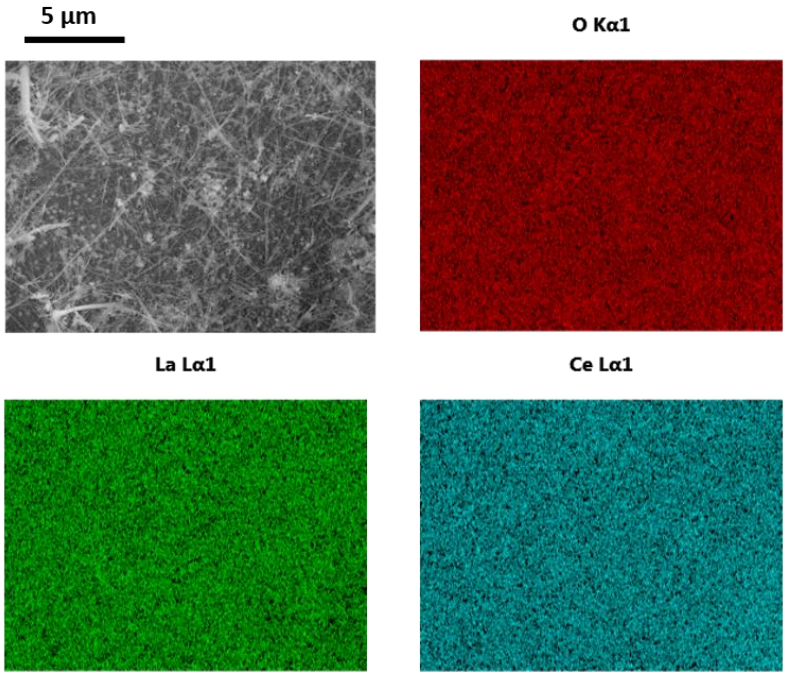

Figure 6.4. EXD map acquired on the Ce50La50 sample.

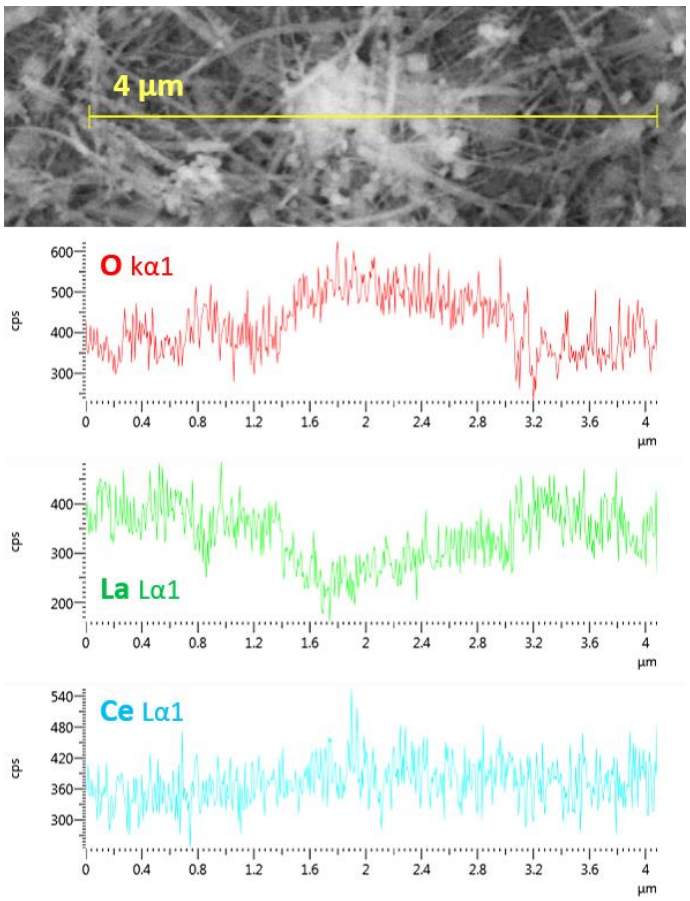

Figure 6.5. EXD analysis carried out on the Ce50La50 sample by acquiring EDX spectra on the yellow line depicted in the upper figure. In the graphs, the intensity profiles of the EDX peaks of the three elements along the line are plotted.

Raman spectroscopy was used to analyze the effects induced by doping on the microstructure and defectiveness of the catalysts. The Raman spectra of the ceria-based samples are reported in Figure 6.6. The spectra are featured by an intense vibrational mode located at 465 cm^{-1} for pure ceria, that is ascribed to the symmetric stretching of the CeO_8 unit in the fluorite structure (F_{2g} mode); besides, a weaker band around 600 cm^{-1} arises in the presence of defects (D band) [201,203]. The addition of different amounts of dopants clearly affects both the main bands. In detail, the F_{2g} mode significantly shifts towards lower wavenumber, due to the expansion of the unit cell upon the incorporation of larger cations and to the generation of new defects. At the same time, the structure distortion accounts for an asymmetric broadening of the F_{2g} peak, as previously reported for rare earth doped ceria [257]. All the described effects become more evident by increasing the dopant concentration. As expected, no splitting of the main band is detected despite the mixture consists of two different families of nanostructures (rods and cubes), as they retain the same crystalline phase. Nevertheless, the very broad linewidth of the F_{2g} peak at high dopant concentration is consistent with a heterogeneous distribution of dopants and defect sites in the two nanoshapes.

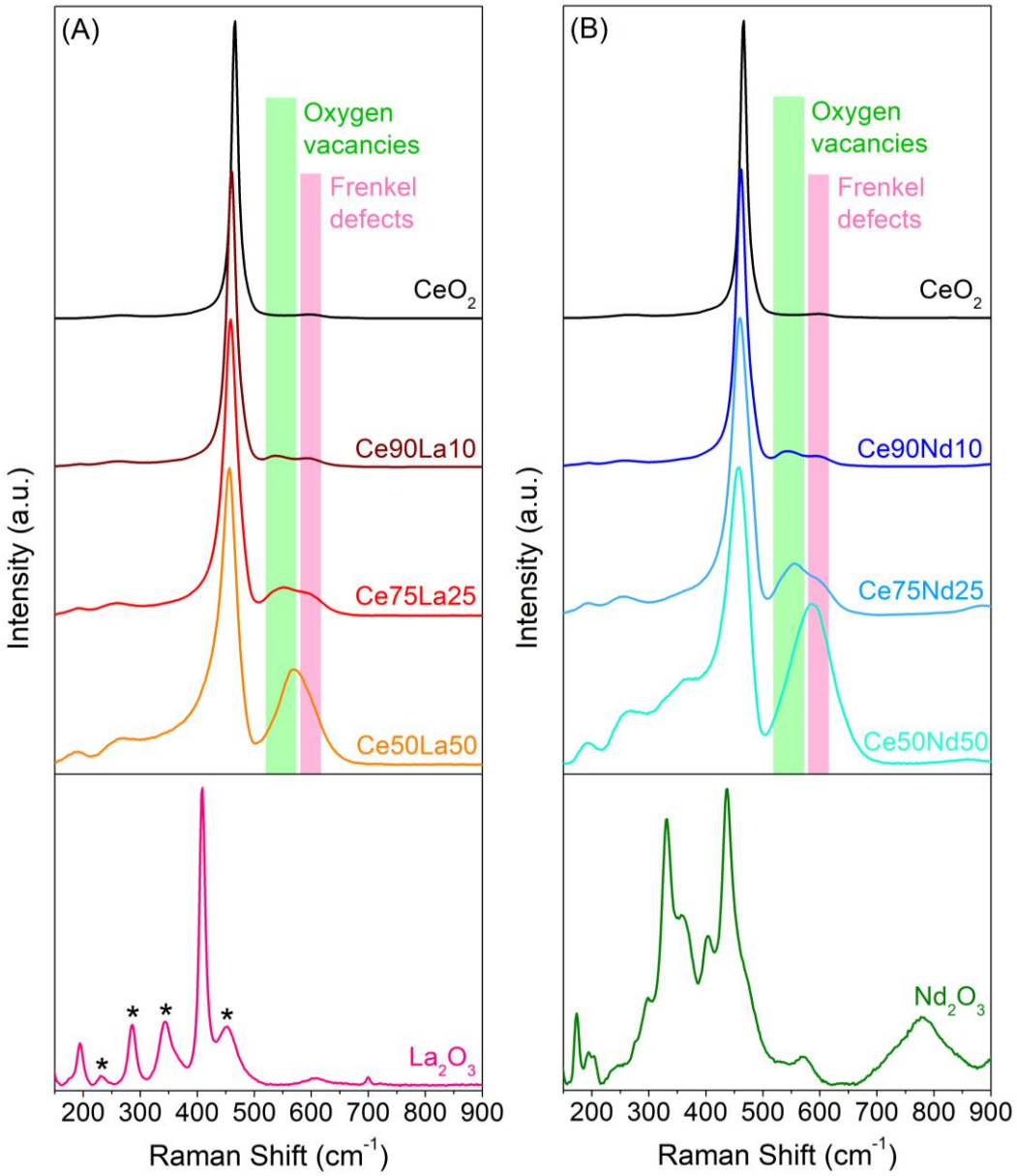

Figure 6.6. Raman spectra collected at room temperature on the La-doped (A) and Nd-doped (B) ceria-based samples compared to pure CeO_2, La_2O_3 and Nd_2O_3.

Concerning the defect band, it consists of a single peak for the pure ceria, that was previously assigned to Frenkel anion pairs, i.e. oxygen vacancies generated by the displacement of a lattice oxide ion into an interstitial site [201,228,238]. In the presence of the rare earth dopants, the defect-induced Raman band appears broader and more intense compared to pure ceria, witnessing an increased defect density. In the case of a moderate La/Nd substitution (10%) two components can be clearly distinguished. The first one, located around 540 cm^{-1}, has been assigned to oxygen vacancies associated to the reduction of Ce^{4+} to Ce^{3+} or to the incorporation of trivalent dopants [227,229,234,236]; consistently, this peak is very intense in the case of Nd^{3+} and La^{3+} doped ceria. The second component occurs at 596 cm^{-1}, at a Raman shift roughly corresponding to the one observed for intrinsic Frenkel anion pairs, whose amount however increases in the presence of dopants [203]. Interestingly, these two peaks become less resolved at 25%

doping and completely convoluted in the case of the equimolar samples. This behavior can be tentatively explained by the generation of several defect sites of the same type in different or distorted lattice environments, increasing the linewidth of the two bands until they cannot be resolved anymore. A reduction of the concentration of intrinsic oxygen-containing defects when Ce^{4+} is increasingly replaced by the 3+ dopant cations can also be hypothesized.

The areas of the whole defect-induced band and the main F_{2g} peak were determined by spectral deconvolution to calculate the D/F_{2g} ratio, which is indicative of the defect density of the catalysts [143,243,303]. In detail, six curves were needed to fit the 200 – 750 cm^{-1} range, as proposed in [304], with two Lorentzian profiles used for the deconvolution of both the D and F_{2g} bands. The values of D/F_{2g} ratio are reported in Table 6.1 and evidence a significant increase of the defectiveness and oxygen deficiency of the catalysts upon rising the dopant concentration.

Moreover, the comparison of the Raman spectra of the doped catalysts with the ones of the pure La and Nd oxides shown in Figure 6.6 further confirms the absence of significant dopant segregation already inferred by XRD analysis, or anyway possible clusterizations within nanometric domains are beyond the sensitivity of these techniques. Indeed, the main bands of the two rare earth oxides, which are in agreement with the previously reported vibrational pattern of hexagonal (195 and 409 cm^{-1}) La_2O_3 [305] and mixed hexagonal (190 and 436 cm^{-1}) [305] and cubic (331 cm^{-1}) [306] Nd_2O_3, are not observed in the Raman spectra of the doped ceria samples, even at 50% Nd or La concentration, evidencing a good incorporation of the dopants in ceria lattice. Moreover, the weak Raman modes marked with an asterisk in the spectrum of the pure La_2O_3 match very well the vibrational pattern of the lanthanum oxide synthesized by Cui et al. [307] and are also absent in the spectra of the doped catalysts.

Surface oxidation state and reducibility

The surface chemical properties of the different materials were studied via XPS. The composition of the outermost atomic layers of the mixed catalysts, in terms of dopant concentration, is reported in Table 6.2. At low doping, significant compositional differences were observed between bulk and surface. In fact, a higher-than-expected lanthanum content was detected at the surface of Ce90La10 and Ce75La25, while the Ce90Nd10 sample mainly accommodates Nd in the bulk. Instead, the other materials are more uniform, although a slight cerium prevalence can be observed at the surface of the two equimolar oxides.

Table 6.2. Composition of the six catalysts and relative abundance of the surface species obtained via XPS.

Catalyst	Dopant content [a] [% at.]			Oxygen species [%]		Cerium species [%]	
	Nominal	Bulk [b]	Surface	O_α	O_β	Ce^{3+}	Ce^{4+}
CeO_2	-	-	-	31.8	68.3	22.0	78.0
Ce90La10	10	9.9	24.4	51.8	48.2	31.6	68.4
Ce75La25	25	26.0	35.8	47.3	52.7	28.0	72.0
Ce50La50	50	50.0	42.4	61.7	38.3	25.4	74.6
Ce90Nd10	10	10.1	5.3	32.5	67.5	23.2	76.8
Ce75Nd25	25	24.1	26.2	38.7	61.3	22.7	77.3
Ce50Nd50	50	49.8	45.6	51.7	48.3	21.2	78.8

[a] Dopant content is expressed in atomic percentage of La or Nd with respect to the total amount of cations

[b] Dopant content in the bulk measured via EDX

The O *1s* XP spectra displayed in Figure 6.7 A can provide information about the surface oxygen species of the six catalysts. As can be noticed in the picture, two distinct peaks are generally observed. The lower binding energy peak, centered at 528.4 – 528.8 eV, can be ascribed to lattice oxygen (O_β), i.e. O^{2-} ions bounded to cerium [161,186,187,243,278,308,309]. In the mixed oxides, this component is slightly shifted towards lower binding energy with respect to pure ceria, as a consequence of the doping. A similar effect was previously observed also in other ceria-based materials [161,187]. The second peak at about 531.2 eV is instead associated to the presence of different capping oxygen species (O_α), such as hydroxyls (OH^-), carbonates (CO_3^{2-}) and also highly reactive peroxide (O_2^{2-}) or superoxide (O_2^-) ions [186,243,308,309]. These species can foster oxygen spillover at the surface and take part in the catalysis, hence their increase may be related to a higher soot oxidation activity [161]. A third low-intensity component located at 533.8 eV was detected in the Ce90La10 spectrum and it can result from the presence of adventitious species such as adsorbed water, formates or carbonates [261,310,311]. The relative abundance of the O_α and O_β species is reported in Table 6.2. All the mixed oxides exhibited a larger quantity of capping oxygen species compared with pure ceria. Moreover, the O_α abundance generally rises with increasing dopant loading and it is higher in the La-containing samples.

Figure 6.7 B displays the high-resolution XP spectra of the Ce *3d* core level. According to the literature, two sets of features can be identified: five "v" peaks correspond to Ce $3d_{5/2}$ level, while five "u" peaks are related to the Ce $3d_{3/2}$ state. Among them, four peaks (v°, v', u° and u') can be assigned to Ce^{3+} ions, while the remaining six peaks can be ascribed to the 4+ oxidation state [186,261,274,278,312,313]. The Ce^{3+} abundance can thus be estimated through

peak deconvolution and the obtained values are reported in Table 6.2. The La-doped catalysts are characterized by a relative quantity of Ce^{3+} significantly higher than that of pure CeO_2. Conversely, Nd addition does not affect so much this property. However, the Ce^{3+} relative abundance decreases at increasing dopant content for both La and Nd. Therefore, a mild doping promotes the formation of Ce^{3+} ions, but the latter species become less favored as the dopant content further increases.

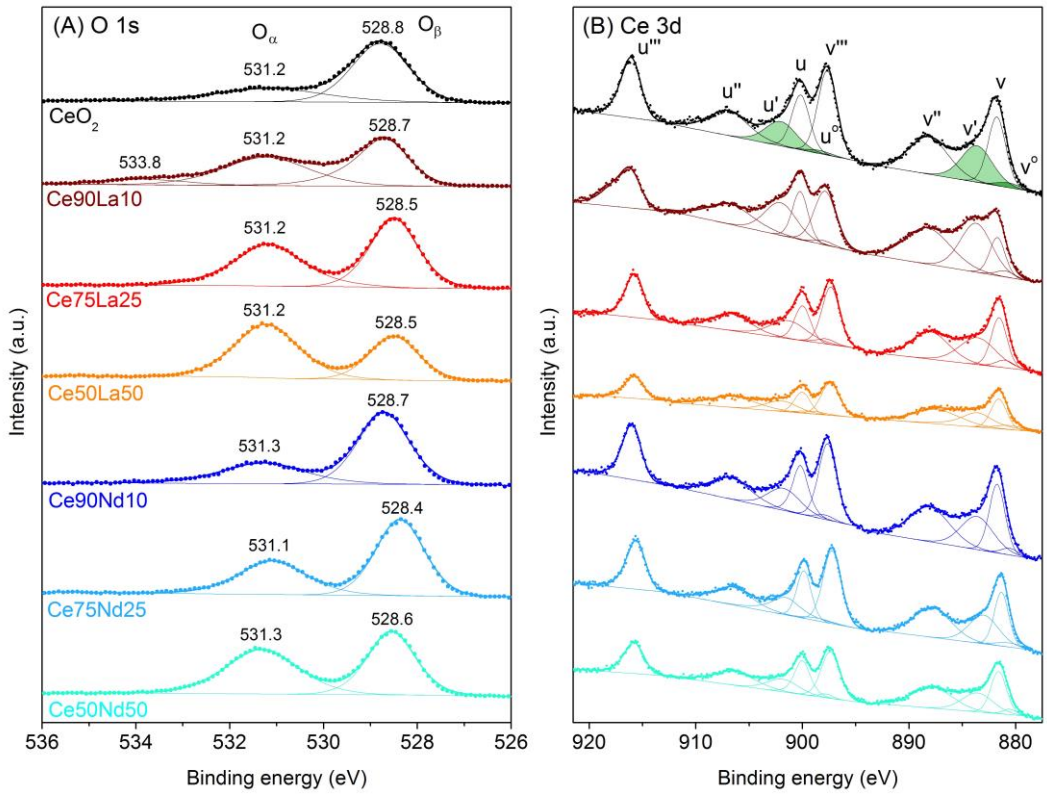

Figure 6.7. Deconvolved XP spectra of the six catalysts in the O 1s (A) and Ce 3d (B) core levels.

In Figure 6.8 the La *3d* and Nd *3d* XP spectra of the doped catalysts are compared with the ones of pure La_2O_3 and Nd_2O_3. Lanthanum oxide exhibits two main peaks related to the La $3d_{5/2}$ and La $3d_{3/2}$ levels, which are located at 834.9 and 851.7 eV, respectively, in agreement with previous literature [314,315]. The spin-orbit splitting of 16.8 is characteristic of the La_2O_3 phase [316,317]. Other two satellite peaks and two La LMM Auger signals are visible as well [314]. The XP spectra of La-doped ceria feature two additional peaks at about 832.6 and 849.5 eV, which could be due to the La incorporation in ceria lattice or to La bonded to OH or other O_α species [318]. Also Nd_2O_3 exhibits two main and two satellite peaks in the XP spectrum [319,320]. The main peaks are located at 982.5 and 1005 eV for the Nd $3d_{5/2}$ and $3d_{3/2}$ states, respectively, and the spin-orbit splitting of 22.5 eV is typical of this oxide [317]. An additional peak at high binding energy has been ascribed to an O KLL signal [319,320]. Also the three Nd-doped catalysts are characterized by similar XP spectra, with the Nd 3d peaks slightly shifted towards lower binding energy.

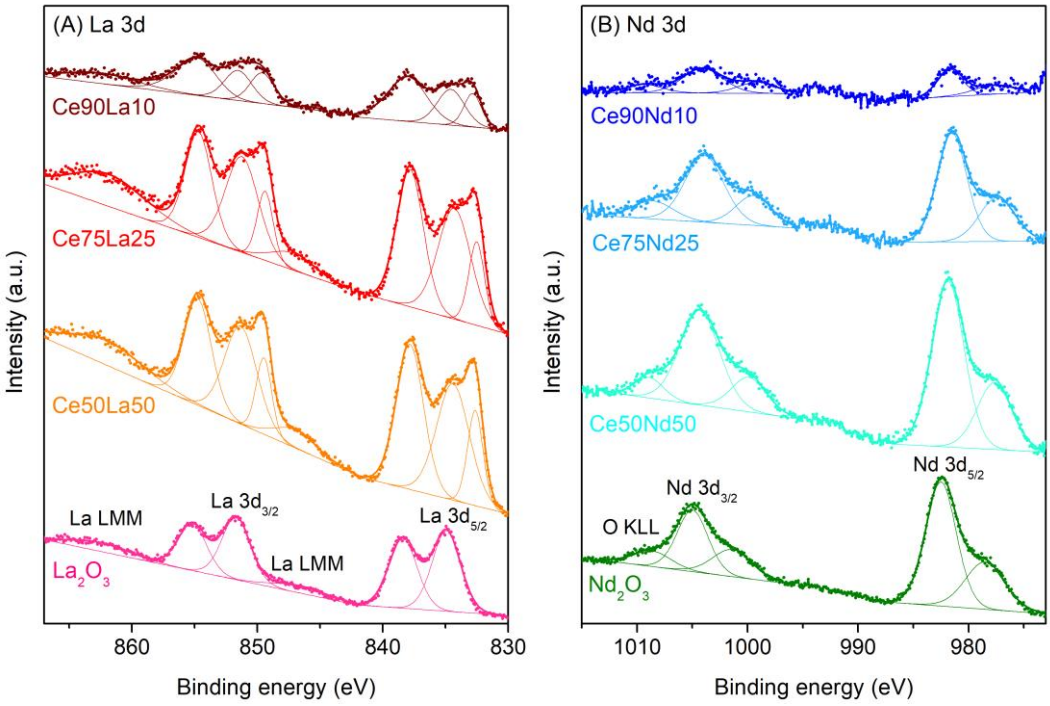

Figure 6.8. Deconvolved XP spectra of the six catalysts in the La 3d (A) and Nd 3d (B) core levels.

The reducibility of the catalysts was examined through H_2-TPR and the obtained curves are shown in Figure 6.9 A and B. The profile of pure ceria features two peaks since its reduction occurs in two steps. The lower temperature peak located around 600 °C is related to the reduction of superficial Ce^{4+} ions, while the larger band above 700 °C is the result of the progressive release of lattice oxygen from the bulk at very high temperature [155,282,321]. Also the doped catalysts are characterized by similar curves, but with surface reduction peaks slightly anticipated at lower temperatures. The only exception is represented by Ce50Nd50, which also exhibited an intense peak between 600 and 700 °C, suggesting that a significant part of the subsurface of this sample may be reduced almost simultaneously with the surface.

Generally, the incorporation of dopant ions in the ceria lattice can weaken the cerium-oxygen bonds and induce the formation of oxygen vacancies, fostering oxygen mobility and thus promoting the reducibility of the mixed oxides [143,188,302,322]. However, for the considered set of catalysts the beneficial effects of doping seem to be limited to the slight anticipation of the surface reduction at lower temperature. Instead, the quantity of oxygen released was not positively affected by La or Nd addition, as pointed out by the values of H_2 consumption during TPR reported in Table 6.3. In detail, the specific consumption of hydrogen related to surface reduction generally decreased when adding La or Nd; only the Ce50Nd50 showed a higher consumption of H_2 at low temperature with respect to pure ceria, due to an improved subsurface reduction. However, the global H_2 consumption at the end of TPR gradually decreased at increasing dopant loading and was minimum for the two equimolar oxides. This trend is likely due to the absence of a redox cycle of La or Nd, whose addition is therefore related to

a lower quantity of oxygen which can be extracted by hydrogen [174], consistently with the higher oxygen deficiency revealed by Raman spectroscopy. However, if the H_2 consumption is normalized to the amount of ceria in the mixed oxide, it is maximum for the two equimolar mixtures and minimum for 10% doped ceria.

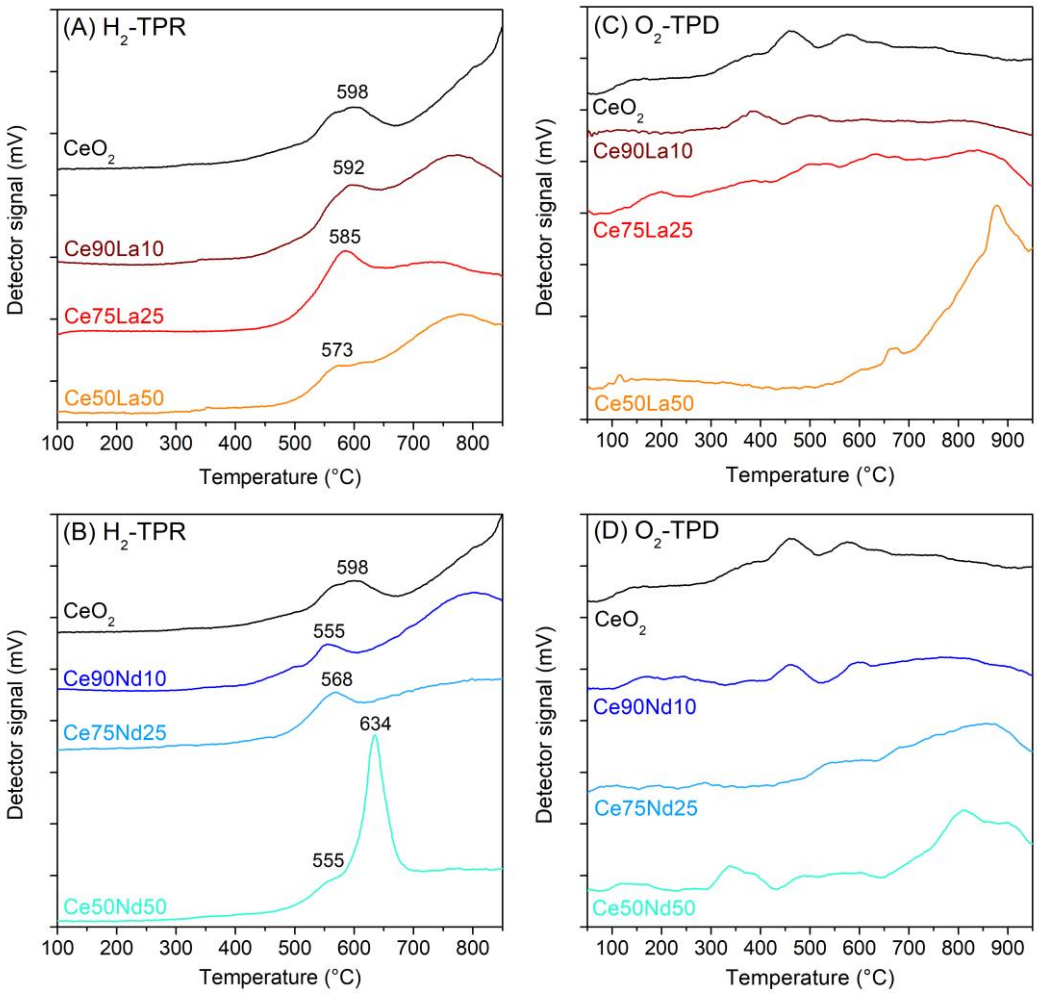

Figure 6.9. H_2-TPR (A, B) and O_2-TPD (C, D) profiles of the La-doped and Nd-doped samples compared with pure ceria.

The oxygen release was further investigated through O_2-TPD, whose results are reported in Figure 6.9 C and D. In this case, the oxygen transfer and the related TCD signal are much lower than those recorded during H_2-TPR, since oxygen desorption is promoted only by the temperature. Lowly doped samples exhibited profiles similar to that of pure ceria, characterized by the presence of some minor desorption peaks in the 300 – 600 °C temperature range [323]. High loading of La or Nd was instead associated to an increase in the quantity of oxygen desorbed above 600 °C. This behavior is likely due to the smaller crystals and higher surface area typical of the highly doped oxides. In particular, an intense peak at high temperature can be observed in the case of Ce50La50, which may be related to the remarkably high abundance of O_α species at the surface of this sample, as found out via XPS.

Table 6.3. Specific consumption of hydrogen during H_2-TPR.

Catalyst	Superficial H_2 consumption [mmol g^{-1}]	Total H_2 consumption [mmol $g_{catalyst}^{-1}$]	[mmol g_{ceria}^{-1}]
CeO_2	0.441	1.77	1.77
Ce90La10	0.442	1.17	1.30
Ce75La25	0.431	1.19	1.59
Ce50La50	0.341	1.03	2.06
Ce90Nd10	0.380	1.25	1.39
Ce75Nd25	0.397	1.18	1.57
Ce50Nd50	0.637	0.98	1.96

Acid-base properties of the surface

Besides reducibility and oxygen availability, also the acid-base properties of the surface are of interest since they affect the strength of interaction between the catalyst and various gaseous reactive species. The oxidizing activity is hence linked to the material acidity [324,325]. For this reason, the acid and basic sites of the mixed oxides were investigated via NH_3-TPD and CO_2-TPD, respectively; the desorption profiles obtained are displayed in Figure 6.10.

Concerning NH_3-TPD, pure ceria is characterized by an almost flat line, which suggests the absence of significant quantities of acid sites; this is consistent with the mainly basic nature attributed to this oxide [326,327]. Similarly, some doped samples show flat profiles too, as can be seen in Figure 6.10 A and B. Instead, quite intense ammonia desorption bands between 250 and 500 °C can be clearly observed for Ce50La50 and Ce75Nd25, signaling the presence of acid sites with a medium strength at the catalyst surface [328,329]. These sites are stronger and more abundant for the Ce-La equimolar oxide. A less intense band attributable to quite strong acid sites could be detected also for the Ce75La25 sample.

In line with previous studies [161,330,331], also the quantity of basic sites was affected by La and Nd doping, as evinced by CO_2-TPD. In fact, the profiles in Figure 6.10 C and D point out the presence of a considerable amount of weak sites in the lowly doped samples, revealed by the desorption peaks at low temperature, while these sites are much less in pure ceria and in the two equimolar mixtures. However, the latter samples are characterized by significant CO_2 desorption above 300 °C. Actually, CO_2 adsorption on metal oxides can occur on sites with various strength, e.g. superficial OH, O^{2-} or cations, resulting in the formation of different carbonaceous species such as hydrogen carbonates, mono/bi/poly-dentate carbonates or metal carboxylates [326,332]. The peak located at about 150 °C, which is remarkably intense for the Ce75La25, Ce90Nd10 and Ce75Nd25 samples, has been ascribed to the decomposition of monodentate carbonates. The

large band around 400 – 500 °C could instead signal the presence of quite stable bidentate and polydentate carbonates on the Ce50La50 catalyst [326].

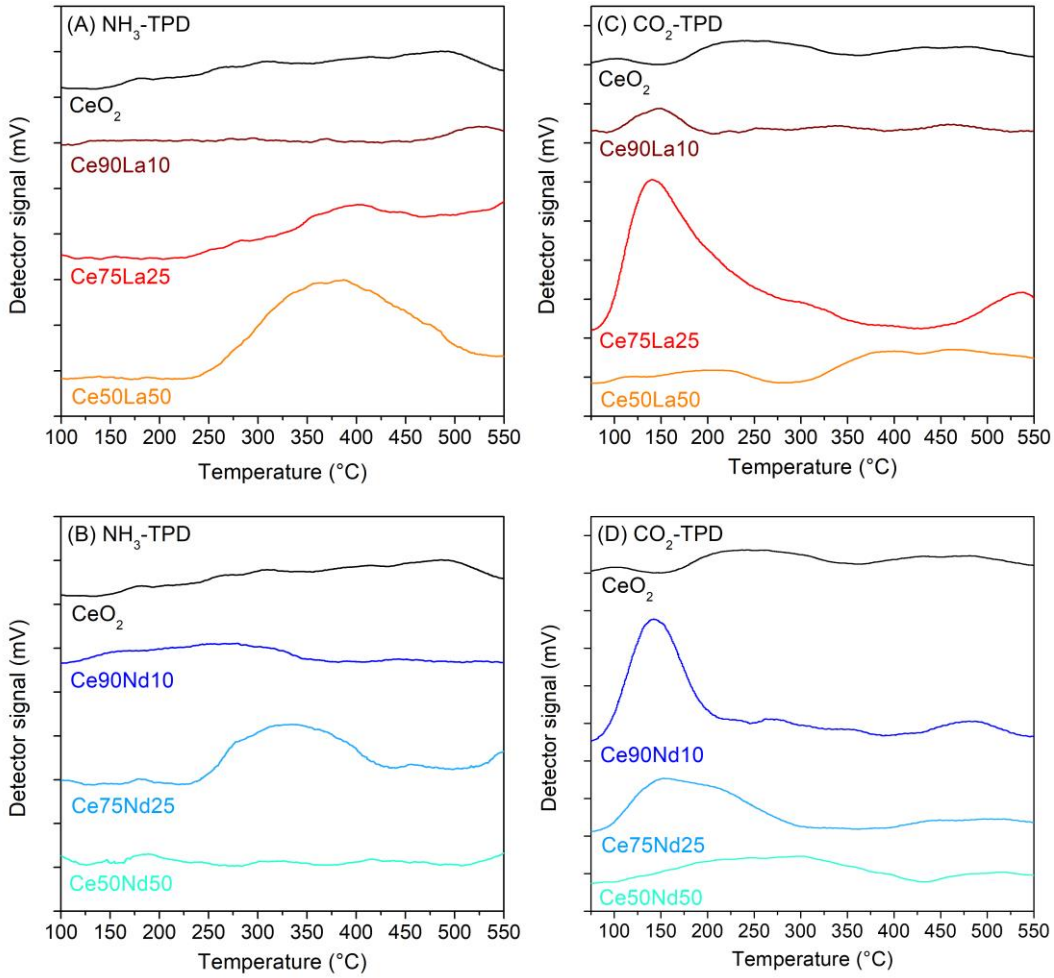

Figure 6.10. NH_3-TPD (A, B) and CO_2-TPD (C, D) profiles of the La-doped and Nd-doped samples compared with pure ceria.

6.3.2 Catalytic activity

The catalytic activity of the prepared materials was investigated considering three reactions which play a key role in the field of automotive aftertreatment, namely CO, NO and soot oxidation.

CO oxidation

The catalytic activity towards CO oxidation was assessed in isothermal mode, considering a sequence of steady states at different temperatures; in this way, possible adsorption or desorption phenomena do not affect the analysis. The profiles of CO conversion as a function of the temperature are presented in Figure 6.11, while the temperatures at which 10%, 50% and 90% ($T_{10\%}$, $T_{50\%}$ and $T_{90\%}$, respectively) of CO conversion were reached are reported in Table 6.4.

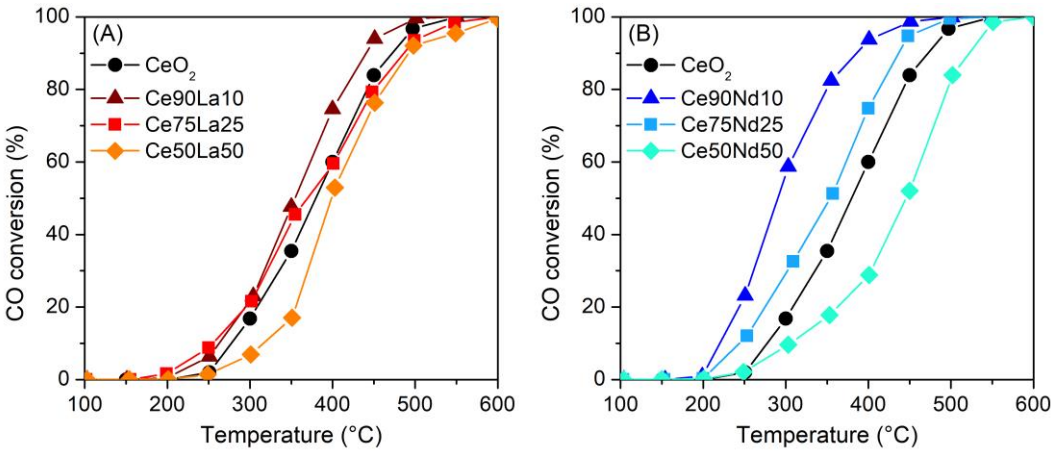

Figure 6.11. Evolution of the CO conversion as a function of the temperature during the CO oxidation tests performed on the La-doped (A) and Nd-doped (B) samples.

Table 6.4. Summary of the results obtained from the catalytic tests of CO oxidation.

Catalyst	$T_{10\%}$ [°C]	$T_{50\%}$ [°C]	$T_{90\%}$ [°C]	r_{CO} at 250 °C [$\mu mol_{CO}\ h^{-1}\ m^{-2}$]
CeO_2	277	380	472	3.50
Ce90La10	263	354	441	8.58
Ce75La25	255	370	486	7.71
Ce50La50	316	399	492	0.95
Ce90Nd10	220	290	386	28.4
Ce75Nd25	244	354	437	10.8
Ce50Nd50	305	446	522	2.15

Moderate doping allows to fairly improve the CO oxidation activity with respect to pure ceria: in fact, the $T_{50\%}$ reduces by ca. 25 and 90 °C upon the introduction of 10% of La and Nd, respectively. This variation can be ascribed to the formation of a proper quantity of defect sites, associated with Ce-O bonds weakening. However, further increases of the dopant quantity result in a gradual worsening of the catalytic performances, with the Ce-La and Ce-Nd equimolar oxides presenting a $T_{50\%}$ about 20 and 65 °C higher than that of pure ceria. Consistently, also the values of the specific reaction rate of CO oxidation (r_{CO}), reported in Table 6.4, point out a reverse trend between dopant loading and catalytic activity.

Such an effect may be linked to the greater presence of strong basic sites in highly doped ceria, as revealed by CO_2-TPD: CO and CO_2 might indeed accumulate on these sites, forming stable carbonate-like species which can hamper the adsorption of further CO molecules at the catalyst surface, thus retarding CO conversion [161,330]. The transformation of carbonates into

physisorbed CO_2 has also been recognized as the rate determining step (RDS) in MvK-mediated CO oxidation over rare earth-doped ceria (111) facets [333]; stronger basic sites can be therefore expected to increase the RDS energy barrier, detrimentally affecting the CO oxidation rate. Furthermore, excessive ceria dilution likely contribute to the observed activity decay: in fact, since the 3+ dopant ions cannot be oxidized, an over-reduced material presenting a lower density of MvK active sites is obtained upon high dopant loading, consistently with the Raman and H_2-TPR results. For these reasons, higher surface area and defect abundance do not seem to always improve the catalytic activity in the case of CO oxidation over rare earth-doped ceria.

NO oxidation

NO oxidation tests were carried out in isothermal mode too, in order to avoid possible adsorption or desorption phenomena. The results are reported in Figure 6.12, which displays the profiles of the NO_2 fraction in the NO_x mixture downstream the reactor as a function of the temperature.

Pure ceria starts promoting NO to NO_2 oxidation above 350 °C and reaches the maximum conversion around 450 °C, then the NO_2 fraction gradually decreases following the thermodynamic equilibrium existing between NO and NO_2 [153,160,199]. Despite the higher surface area, the doped samples were characterized by catalytic performances more or less similar to those of CeO_2. Actually, Ce90La10 exhibited a lower light-off temperature and a slightly higher maximum conversion at 450 °C. However, a further increase of the La loading caused a progressive drop of the catalytic activity for NO oxidation. The three Nd-doped oxides showed instead similar profiles, and only Ce75Nd25 was able to slightly outperform pure ceria in terms of maximum conversion. Therefore, La and Nd addition does not seem to significantly promote NO oxidation, probably because of the limited effects of doping on the catalyst reducibility.

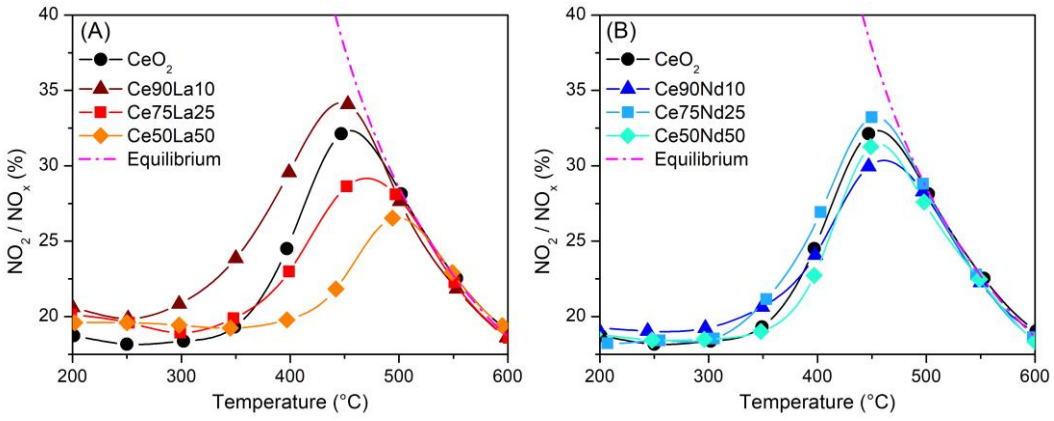

Figure 6.12. Evolution of the NO_2/NO_x fraction in the outlet as a function of the temperature during the NO oxidation tests performed on the La-doped (A) and Nd-doped (B) samples.

Soot oxidation

The catalytic activity towards soot oxidation was carefully evaluated by performing tests in various conditions. Two different degrees of contact between the catalyst and soot powders were probed and the effects of the presence of NO_x and water were also examined. The $T_{10\%}$, $T_{50\%}$ and $T_{90\%}$ measured during the different tests will be used for comparison purposes.

First of all, soot oxidation was carried out in tight contact, i.e. mixing soot and catalyst via ball milling; thereby, numerous contact points between the two solid powders were created and so the catalytic performances were mainly determined by the intrinsic activity of the materials. The profiles of the CO and CO_2 produced during these tests are displayed in Figure 6.13 while the conversion curves are reported in Figure 6.14 A and D. As can be seen from the latter pictures and from the specific reaction rates (r_{soot}) reported in Table 6.5, the catalytic activity varies following this trend: Ce90Nd10 < CeO_2 < Ce50Nd50 < Ce90La10 < Ce75La25 < Ce75Nd25 < Ce50La50. Although Ce90Nd10 seems slightly less active than pure CeO_2, La and Nd doping generally promotes soot oxidation. In detail, two promising materials can be distinguished from the other ones. Ce75Nd25 is the most performing sample in the Nd-doped set and it was able to lower the reaction light-off temperature by 40 °C with respect to pure ceria. However, the Ce50La50 equimolar mixture exhibited the highest catalytic activity, remarkably outperforming all the other oxides. This sample was indeed able to convert more than half of the soot initially present below 400 °C.

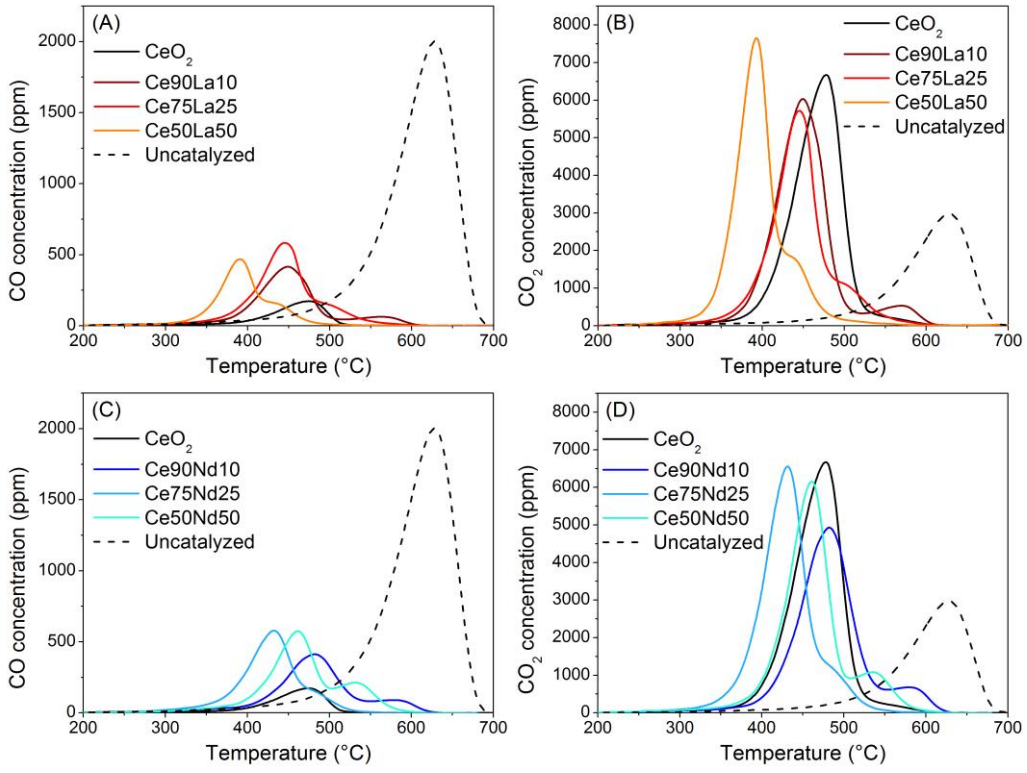

Figure 6.13. CO (A, C) and CO_2 (B, D) concentration at the outlet as a function of the temperature during the soot oxidation tests performed in tight contact conditions on La-doped (A, B) and Nd-doped (C, D) ceria.

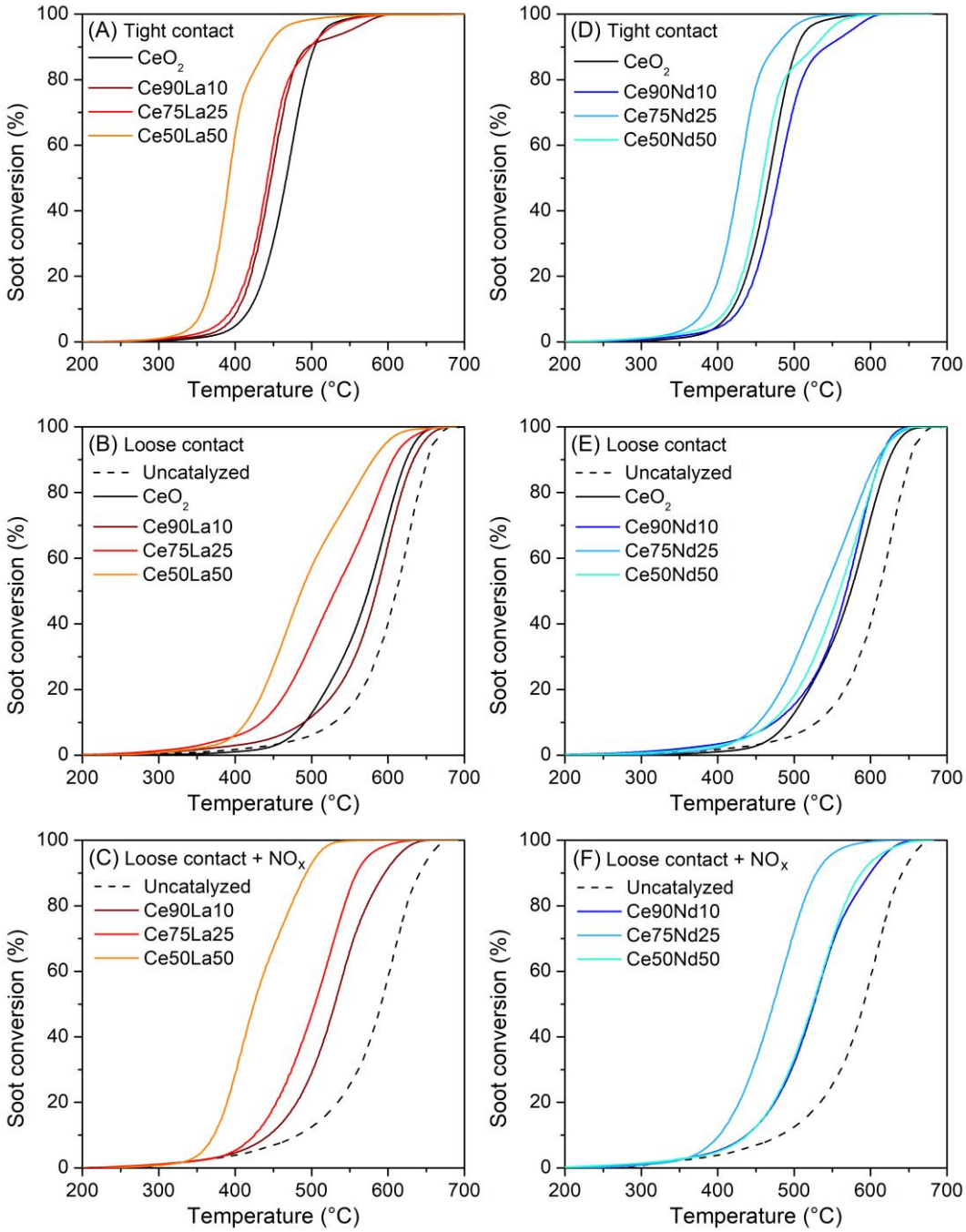

Figure 6.14. Conversion curves as a function of the temperature resulting from the different soot oxidation tests performed on La-doped (A, B, C) and Nd-doped (D, E, F) ceria. NO_x-free soot oxidation was performed in tight (A, D) and loose (B, E) contact, while NO_x-assisted soot oxidation was carried out in loose contact (C, F).

A correlation can be found between the catalytic activity and the surface acidity: indeed, it is worth noting that the three most active catalysts are the ones presenting more acid sites at their surface, as previously pointed out by NH_3-TPD. Actually, the presence of strong acid sites can foster the formation of carbon radical intermediates, thanks to the electronic interactions at the interface between soot and catalyst particles [168,334]. The thus formed highly reactive species can be easily oxidized by oxygen coming from both the gas bulk or the catalyst lattice

and this mechanism likely contributes to an effective conversion of soot at lower temperature.

Table 6.5. Summary of the results obtained from the catalytic tests of standard soot oxidation (10% O_2 in N_2) performed in different conditions (loose or tight contact).

Catalyst	Soot oxidation						
	Loose contact			Tight contact			
	$T_{10\%}$ [°C]	$T_{50\%}$ [°C]	$T_{90\%}$ [°C]	$T_{10\%}$ [°C]	$T_{50\%}$ [°C]	$T_{90\%}$ [°C]	r_{soot} at 375 °C [$mmol_{soot}$ h^{-1} g^{-1}]
CeO_2	491	574	624	419	467	504	1.31
Ce90La10	490	585	633	404	447	496	2.63
Ce75La25	434	531	606	395	442	499	3.58
Ce50La50	414	487	580	358	392	443	30.3
Ce90Nd10	474	568	612	428	479	542	1.07
Ce75Nd25	453	539	609	384	428	475	6.95
Ce50Nd50	470	559	613	412	458	526	1.95

Moreover, also the selectivity towards CO_2 was assessed and the values obtained are reported in Figure 6.15. Ce50La50 resulted to be the most selective mixed oxide, although its CO_2 selectivity was slightly lower than that of pure ceria; Ce50Nd50 was instead the least selective. The higher CO production observed for the doped materials is likely related to the negative effects of La and Nd addition on ceria catalytic activity towards CO oxidation. It is however worth noting that all the samples presented a much higher CO_2 selectivity with respect to the uncatalyzed case, in which it was only 61.4%.

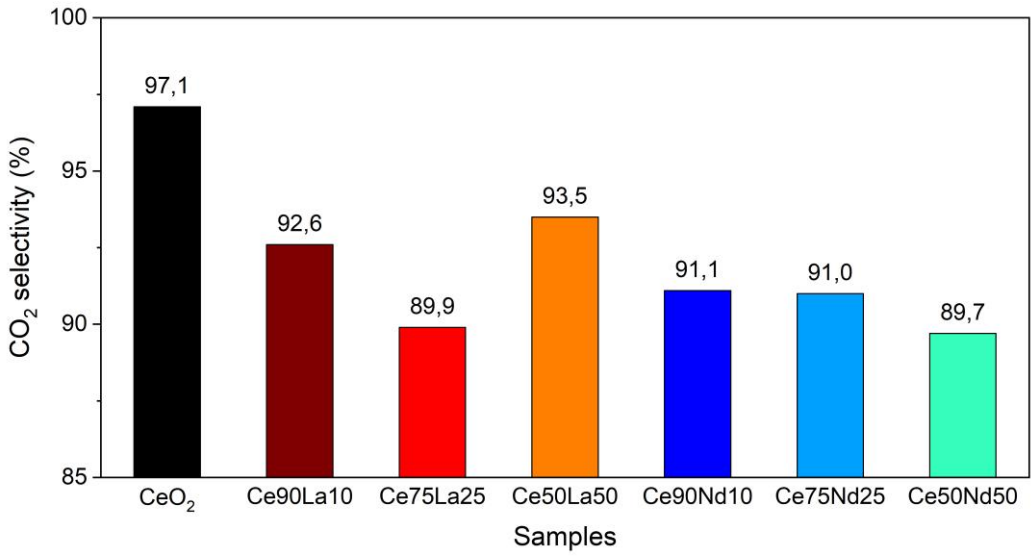

Figure 6.15. CO_2 selectivity of the different catalysts during the soot oxidation tests performed in tight contact conditions, derived from the profiles displayed in Figure 6.13.

Figure 6.14 B and E display the results of the soot oxidation tests carried out in loose contact, while direct comparisons between the performances in tight and loose contact are reported for each sample in Figure 6.16. As expected, in loose contact all the conversion curves are shifted towards higher temperatures. Actually, in this case the transfer of active oxygen species from the catalyst to the soot particles is hindered by the lower amount of contact points [177,185,188]. Furthermore, a wider range of temperature is required for the complete oxidation, since different fractions of soot with different intensities of contact with the catalyst coexist in the solid mixture [293,335]. If the $T_{50\%}$ are considered (Table 6.5), the catalytic activity in loose contact follows the trend: Ce90La10 < CeO_2 < Ce90Nd10 < Ce50Nd50 < Ce75Nd25 < Ce75La25 < Ce50La50. Pure ceria and the lowly-doped samples are again characterized by similar performances, while a higher dopant loading is associated with a better activity, especially in the case of the Ce-La mixed oxides. La doping also caused a progressive increase of the specific reaction rate, whose values calculated at 400 °C are reported in Table 6.6. Instead, Ce75Nd25 was again the most active among the Nd-doped samples.

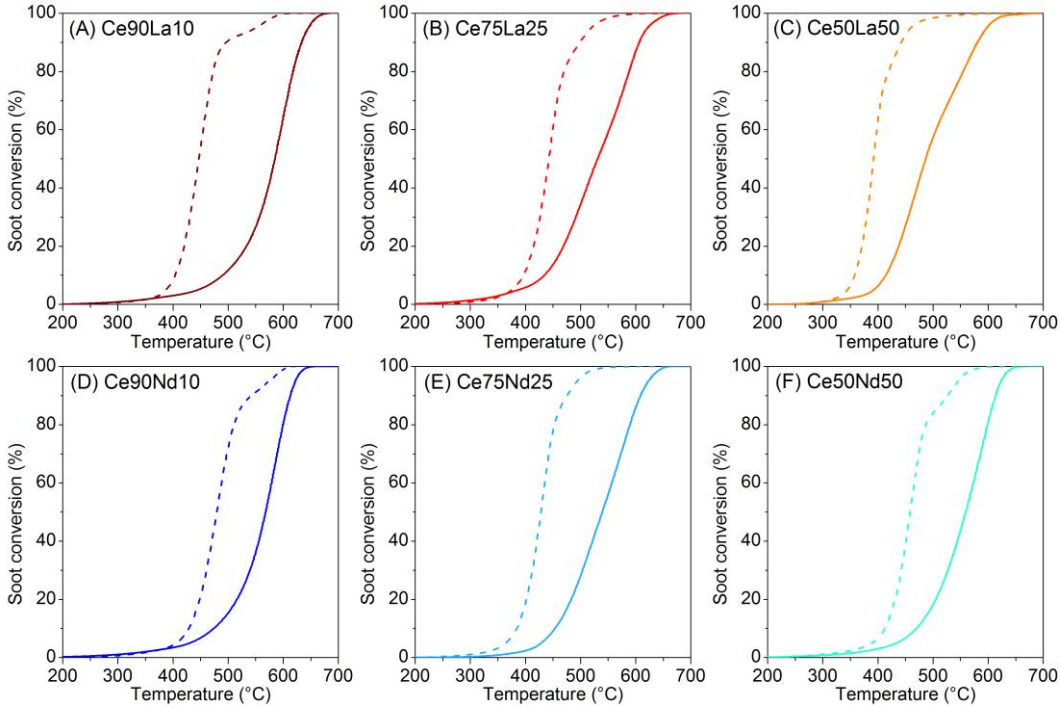

Figure 6.16. Conversion curves as a function of the temperature resulting from the soot oxidation tests performed on the six samples in tight (dashed lines) and loose (straight lines) contact conditions.

These results could be correlated with the different morphologies, since the catalysts presenting more fibers are also characterized by a higher ability in oxidizing soot, in accordance with previous studies [151,188,297]. In fact, a network of rods and fibers can suitably accommodate soot particles maximizing the number of contact points [151]. Moreover, the decrease of the temperature required for soot combustion is related to the reduction of the particle size upon doping, as displayed in Figure 6.17. The Ce50La50 sample is the most performing

catalyst also in loose contact: thanks to its high intrinsic activity and its fibrous structure, this equimolar oxide was indeed able to reduce the temperature required for ceria-catalyzed soot oxidation by about 80 °C, with a $T_{50\%}$ of 487 °C. Of course, also the greater abundance of capping oxygen species and acid sites at the surface and the higher specific surface area contribute to the excellent catalytic properties of this material.

Table 6.6. Specific reaction rates of soot oxidation (r_{soot}) during the catalytic tests performed in loose contact in the absence (10% O_2 in N_2) and in the presence (550 ppm NO + 10% O_2 in N_2) of NO_x.

Catalyst	r_{soot} at 400 °C [$\mu mol_{soot}\ h^{-1}\ m^{-2}$]	
	Loose contact	Loose contact + NO_x
CeO_2	67.8	-
Ce90La10	71.5	241
Ce75La25	86.9	156
Ce50La50	230	858
Ce90Nd10	74.2	85.1
Ce75Nd25	81.4	392
Ce50Nd50	69.1	137

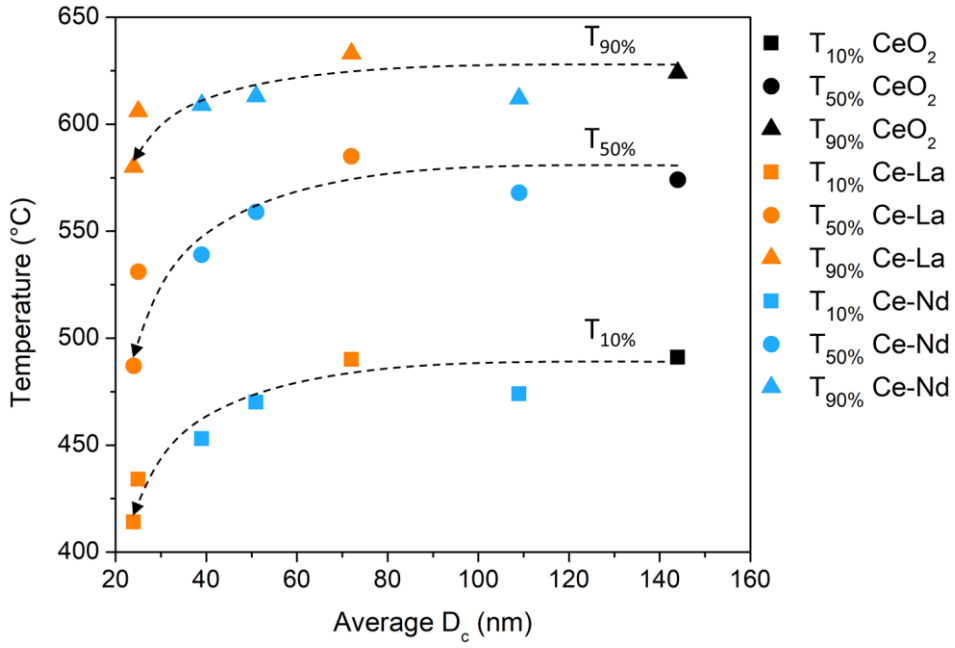

Figure 6.17. Variation of the catalytic performances as a function of the average crystallite size of the samples during soot oxidation in loose contact.

Tests repeated after aging the Ce50La50 and Ce75Nd25 catalysts at 700°C for 8 h resulted in very similar conversion curves (as shown in Figure 6.18), indicating that these active samples are highly stable too.

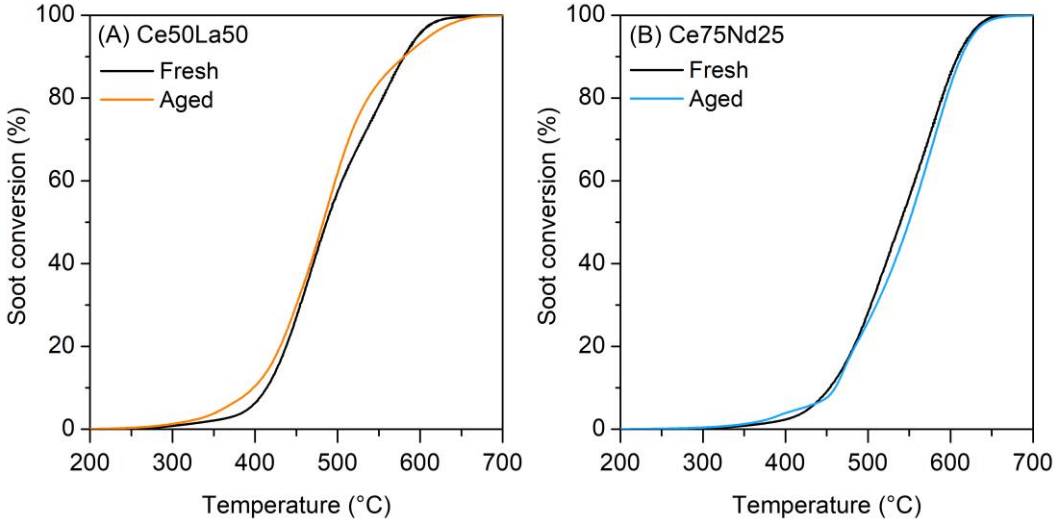

Figure 6.18. Conversion curves as a function of the temperature resulting from the soot oxidation tests performed in loose contact on fresh and aged Ce50La50 (A) and Ce75Nd25 (B).

Moreover, also the effect of water on the soot oxidation performances of these materials was evaluated, since a high quantity of this species is usually present in the engine exhaust. As can be seen in Figure 6.19 and Table 6.7, the addition of 10% H_2O in the reactant gas phase beneficially affects loose contact soot oxidation, lowering the T_{50} by more than 40 °C. Such a promoting effect, previously observed for other ceria-based materials [171,195], is probably the result of different phenomena. Actually, surface hydroxylation can improve oxygen mobility while a wet soot-catalyst interface can account for a more effective oxygen transfer [336,337]. Moreover, Park et al. have recently found out via isotopic experiments and DFT studies that water can behave as an active oxygen source for soot oxidation [171]; in fact, H_2O can easily adsorb and dissociate over Ce-based oxides, forming reactive OH species which can significantly increase the reaction rate.

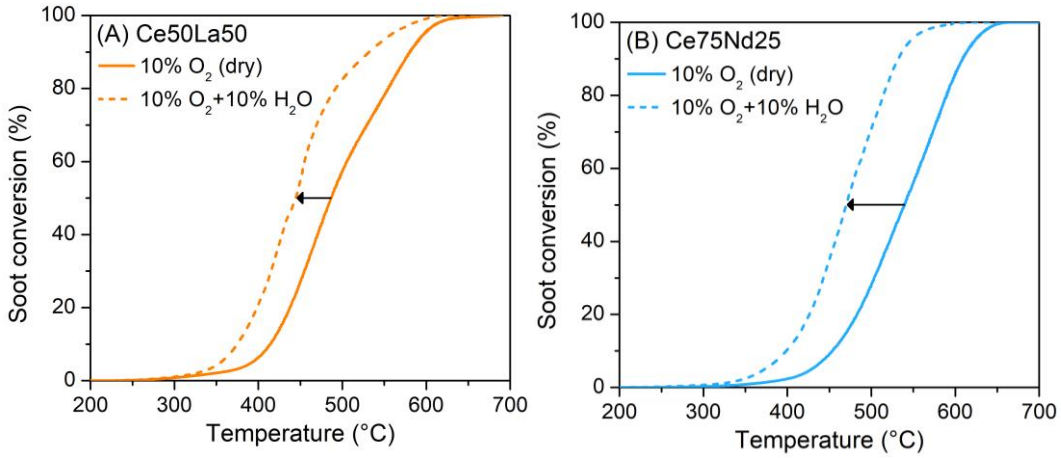

Figure 6.19. Effect of water on the catalytic performances of the Ce50La50 (A) and Ce75Nd25 (B) samples during soot oxidation in loose contact.

Table 6.7. Summary of the results obtained from the catalytic tests of soot oxidation performed in different contact conditions (loose or tight contact) in the presence of NO_x (550 ppm NO + 10% O_2 in N_2) or water (10% H_2O + 10% O_2 in N_2).

Catalyst	In the presence of NO_x						In the presence of H_2O		
	Loose contact			Tight contact			Loose contact		
	$T_{10\%}$ (°C)	$T_{50\%}$ (°C)	$T_{90\%}$ (°C)	$T_{10\%}$ (°C)	$T_{50\%}$ (°C)	$T_{90\%}$ (°C)	$T_{10\%}$ (°C)	$T_{50\%}$ (°C)	$T_{90\%}$ (°C)
Ce90La10	444	531	596	-	-	-	-	-	-
Ce75La25	425	505	559	-	-	-	-	-	-
Ce50La50	372	424	493	366	407	461	375	444	532
Ce90Nd10	438	526	600	-	-	-	-	-	-
Ce75Nd25	402	472	529	398	452	503	398	470	532
Ce50Nd50	439	524	588	-	-	-	-	-	-

For the sake of completeness, the catalytic properties of La- and Nd-doped ceria can be compared with those of other nanostructured ceria-based mixed oxides containing different doping elements, synthesized and tested in analogous conditions in previous studies [143,145,188,281]. Such a comparison can be found in Figure 6.20, which reports the $T_{50\%}$ measured during soot oxidation in tight and loose contact as a function of dopant loading for ceria doped with different lanthanides (La, Nd or Pr) and transition metals (Zr, Cu or Mn). As can be seen, Zr and Pr allow to obtain better results at low doping; nevertheless, La has a progressive beneficial effect on ceria activity and it is the most effective dopant at high loading. In the end, equimolar ceria-lanthana results to be the most performing catalyst among the considered set of ceria-based materials, thanks to its optimal morphology and surface properties.

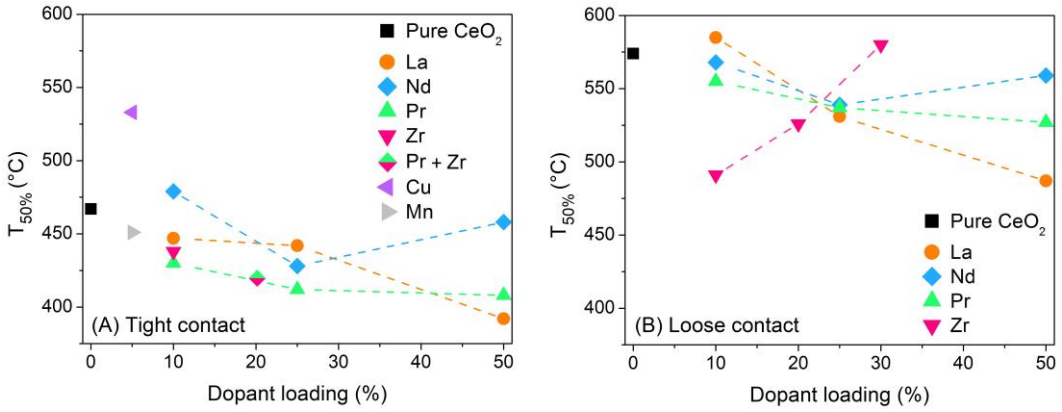

Figure 6.20. Catalytic performances (in terms of $T_{50\%}$) as a function of dopant loading during soot oxidation performed in tight (A) and loose (B) contact. The La- and Nd-doped samples are compared to other nanostructured ceria-based oxides obtained via hydrothermal procedure and tested in analogous conditions, but containing Pr [188,281], Zr [145], Cu [143] and Mn [143].

NO_x-assisted soot oxidation

The soot oxidation tests in loose contact were repeated in the presence of NO_x and the conversion profiles are displayed in Figure 6.14 C and F. A direct comparison between the results obtained in the presence and in the absence of NO_x is instead reported in Figure 6.21. The NO fed to the reactor can be partly converted to NO_2 by the catalyst; the latter species is a stronger oxidant than O_2, therefore able to promote soot combustion [153,197,200]. In fact, the performances of all the samples benefited from NO addition, as all the conversion curves are shifted towards lower temperature when soot oxidation is assisted by NO_x. In this case, the trend of catalytic activity is the following: Ce50La50 > Ce75Nd25 > Ce75La25 > Ce50Nd50 ≈ Ce90Nd10 ≈ Ce90La10 (Table 6.7). A slightly different trend can be observed considering the specific reaction rates reported in Table 6.6. In any case, Ce50La50 and Ce75Nd25 confirm to be the most active samples for soot oxidation.

The investigation of the catalytic mechanisms promoted by mixed oxides during NO_x-assisted soot oxidation is a rather tough operation; indeed, several different reactions, giving rise to a complex network of interconnected pathways, are expected to take place at the same time [153,160,169,199,200,338,339]. Actually, many oxygen species can be involved in soot combustion, such as gaseous O_2, lattice oxygen ions with a MvK-like behavior or reactive oxygen species at the catalysts surface [129,186,192,203,296,340]. Furthermore, also NO_x can take part in catalytic soot oxidation and two main mechanisms have been identified. An indirect pathway involves NO oxidation over the catalyst, producing NO_2 molecules which then attack soot from the gas phase [169,197]; at the end, NO is obtained again and the whole cycle may be repeated [198,199]. Besides, soot oxidation can also occur via a direct pathway involving the NO_x adsorbed on the catalyst: in fact, nitrites or nitrates at the solid surface can decompose in the proximity of soot particles, generating active species able to

attack soot directly from the solid phase [199,200]. The significance of each mechanism depends on various factors, such as the chemical properties of the catalyst or the operative conditions. For instance, the indirect mechanism has been recognized as the predominant one when noble metals such as Pt are employed [160,198]. However, metal oxides are usually less active towards NO oxidation and so their catalytic performances may be related to the activation and promotion of other pathways. For example, a direct mechanism involving the adsorbed nitrates has been recently proposed for nanostructured equimolar ceria-praseodymia [199].

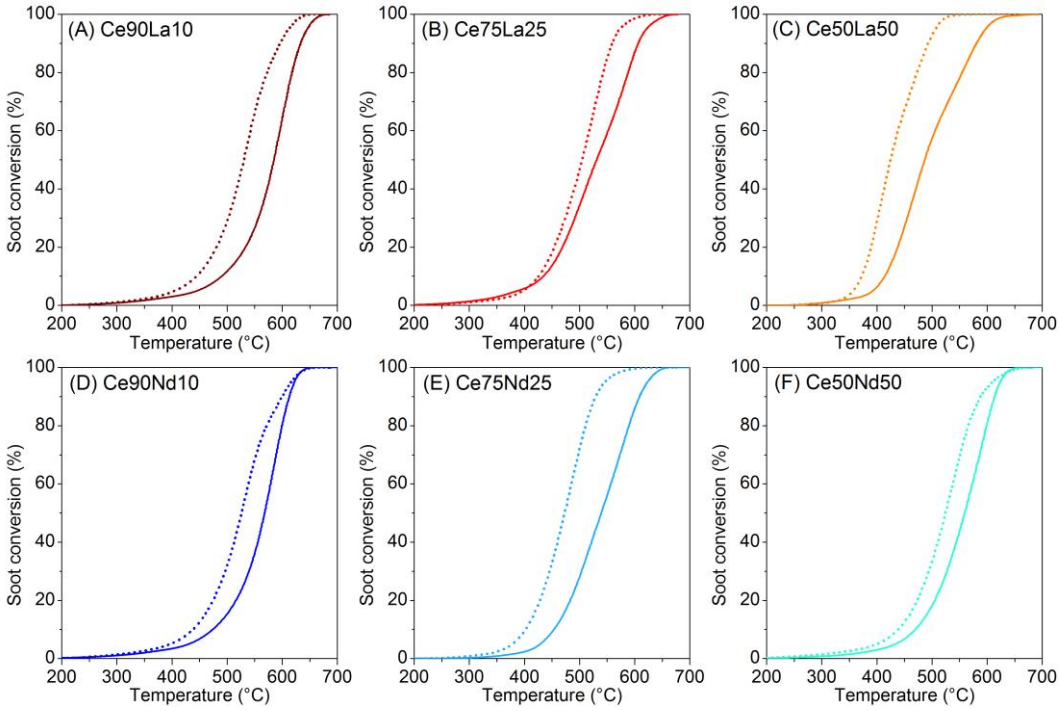

Figure 6.21. Conversion curves as a function of the temperature resulting from the soot oxidation tests performed on the six samples in loose contact in the absence (straight lines) and in the presence (dotted lines) of NO_x.

In order to shed some light on the catalytic mechanisms favored by La- and Nd-doped ceria and to verify if the adsorbed NO_x play a direct role in the catalysis, NO_x-assisted soot oxidation was also performed in tight contact. The thus obtained conversion curves can be compared with those previously provided by all the other soot oxidation tests; such a comparison is reported in Figure 6.22 for the two most active samples, i.e. Ce50La50 and Ce75Nd25. As can be seen from the picture, the equimolar Ce-La mixture was always characterized by superior performances. Anyway, both the catalysts exhibited analogous changes when the conditions were varied. In details, NO_x addition had a remarkable promoting action on soot combustion in loose contact, while its effect was slightly detrimental in tight contact, as pointed out by the arrows in Figure 6.22.

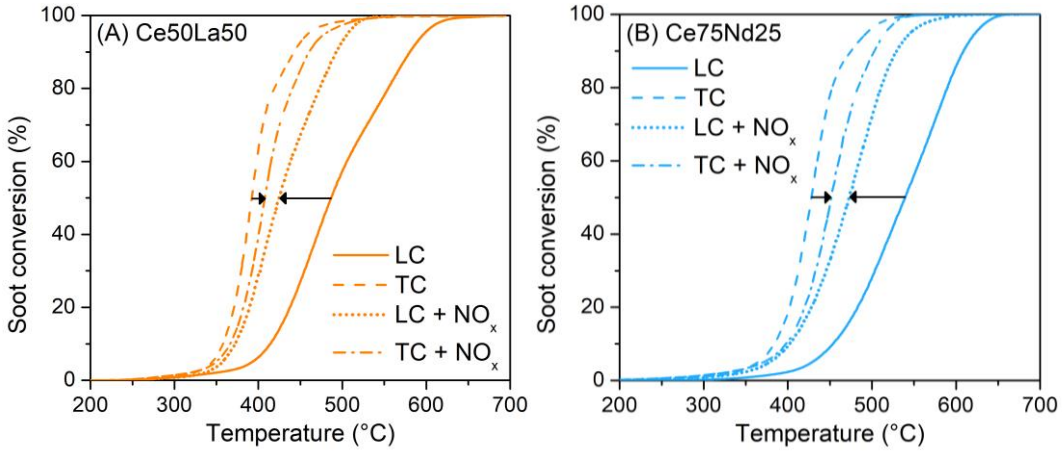

Figure 6.22. Conversion curves as a function of the temperature resulting from the different types of soot oxidation tests performed on the Ce50La50 (A) and Ce75Nd25 (B) samples in loose contact (LC) or tight contact (TC) in the absence or in the presence of NO_x. The arrows highlight the effects of NO_x addition on soot conversion.

An explanation for this behavior should take into account all the mechanisms presented above. Consistently, a simplified scheme describing some of the possible phenomena involved is depicted in Figure 6.23. Actually, in loose contact the low number of contact points is a kinetic limitation, since the transfer of active oxygen species can take place only in those regions of the catalyst surface which are close to soot particles (Figure 6.23 A). In this situation, the presence of NO is beneficial: indeed, it can be converted to NO_2 which can then move through the gas phase and reach soot regardless of the degree of contact (Figure 6.23 C). Conversely, in tight contact the reaction kinetics is controlled by the intrinsic activity of the species involved in soot oxidation. Reactive oxygen species, which are believed to be more powerful oxidizers than NO_2 [153,200], are far available thanks to the intimate contact conditions (Figure 6.23 B). In this context, the presence of NO_x can lower the activity of the catalyst, since adsorbed nitrites or nitrates may replace the highly active oxygen species at the surface and hamper their re-formation (Figure 6.23 D). In fact, since soot oxidation in tight contact starts at a lower temperature (below 400 °C), adsorbed NO_x may be quite stable in these conditions [341], thus lowering the overall reaction rate; moreover, also the presence of quite strong basic sites, as those detected at the Ce50La50 surface, may account for enhanced nitrates stability. This behavior is quite different from that exhibited by other ceria-based materials, such as equimolar ceria-praseodymia, in which adsorbed nitrates were found to play a crucial active role in soot oxidation [199]. The chemical properties of the catalyst governing the interactions with gaseous or adsorbed NO_x, such as surface acidity and basicity, eventually account for these differences.

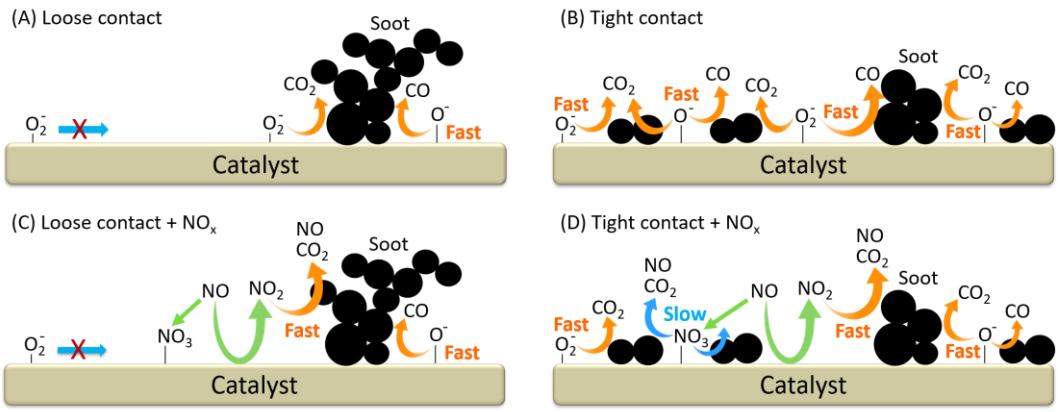

Figure 6.23. Scheme reporting some of the possible reaction pathways occurring at the surface of the Ce-La and Ce-Nd catalysts during soot oxidation in the absence (A, B) or in the presence (C, D) of NO_x in loose (A, C) or tight (B, D) contact.

6.4 Conclusions

In this work, six ceria-based catalysts for soot oxidation were prepared by hydrothermal synthesis and carefully compared. La and Nd doping significantly affects the structural, physico-chemical and catalytic properties of ceria. These elements can be well-incorporated in ceria lattice, obtaining a fibrous morphology associated not only to a higher surface area but also to a better soot-catalyst contact. The Ce-O bonds are weakened in the mixed oxides, but this effect is counterbalanced by a lower quantity of available oxygen: in fact, a high La^{3+} or Nd^{3+} loading is associated to a huge increase of the catalyst defectiveness and of the concentration of oxygen vacancies, resulting in a less reducible oxygen-deficient material.

As a consequence, while moderate doping (10%) improves the CO oxidation activity, a further replacement of Ce with La or Nd leads to a progressive worsening of the catalytic performances, despite a greater surface area and defect abundance. However, also the formation of new basic sites upon doping hinders CO conversion. Analogously, the mixed oxides exhibit an activity for NO oxidation quite similar to that of pure CeO_2, without significant benefits from La and Nd addition. Conversely, soot oxidation is promoted by doping, especially in the case of the Ce75Nd25 and Ce50La50 samples.

In particular, the Ce-La equimolar mixture exhibited excellent catalytic properties, outperforming also analogous ceria-based oxides investigated in previous studies. This sample was indeed able to start soot combustion in loose contact below 400 °C in the presence of NO_x, despite its quite poor activity towards NO oxidation. Moreover, it resulted very stable after thermal aging and benefited from the presence of water in the gas stream. These outstanding performances can be ascribed to the greater surface area and improved morphology, as well as to the high intrinsic activity and to the large amount of active oxygen species and acid sites at the surface of this sample. A direct involvement of adsorbed nitrates in catalytic soot oxidation, as previously

described for analogous Ce-Pr nanostructures, was actually ruled out for Ce50La50; in fact, NO_x mainly passively adsorb on this sample, replacing active oxygen species and thereby detrimentally affecting the activity in tight contact; the quite low temperature required for soot combustion in these conditions and the presence of fairly strong superficial basic sites may eventually account for the excessive stability of the adsorbed NO_x.

In the end, equimolar ceria-lanthana is a really promising catalyst for soot oxidation and should be taken into account for future developments.

Chapter 7

Conclusions and future perspectives

In this thesis, ceria-based nanostructured catalysts doped with different elements were studied. The effects of doping were investigated, searching for the relations between the structural/chemical properties of the mixed oxides and their catalytic activity towards the oxidation of automotive pollutants.

Both transition metals and rare earths could be well incorporated in ceria fluorite structure, forming solid solutions. Hence, structural distortion, morphological alterations and formation of defects were observed upon doping. These changes were generally associated with improved activity, but different results were obtained depending on the dopant type and quantity and on the reaction considered. In fact, CO oxidation and soot combustion are very dissimilar reactions and are therefore affected by different parameters.

This is evident in the case of Cu- and Mn-doped ceria: while the first oxide featured the best activity for CO oxidation thanks to its large surface area and high defectiveness, the latter sample was much more active for soot oxidation, and this may be related to the different morphology. However, further information was acquired by monitoring the defect sites evolution during the reactions via in situ Raman spectroscopy. The increase of vacancy-free sites exhibited by the Cu-doped samples after soot oxidation suggested that a high concentration of oxygen vacancies may foster the deactivation of the reactive oxygen species at the catalyst surface, thus hindering oxygen spillover, that is one of the main oxidation mechanisms in case of a poor catalyst-pollutant contact. Hence, an intermediate quantity of oxygen vacancies like that exhibited by Mn-doped ceria is optimal for promoting soot oxidation.

Cu-doped ceria revealed to have a more reducible and mobile structure also during CO oxidation. Indeed, Raman analyses performed during cycles of reduction and oxidation suggested that oxygen vacancy clusters can form in reducing atmosphere. Interestingly, these clusters could reorganize not only in the presence of O_2 but also in inert atmosphere or upon a temperature decrease, as a consequence of the bulk oxygen migration; isolated vacancies were formed in this

way, which could then evolve into Frenkel and extrinsic oxidized dopant-containing sites when exposed to oxygen.

Also doping with rare earths was considered, with the aim of developing nanostructured catalysts for soot oxidation. The addition of Pr, La or Nd affected the ripening process during the synthesis, fostering the production of smaller nanocubes amongst rod-like particles. Equimolar ceria-praseodymia exhibited a greater reducibility with respect to pure CeO_2, thanks to the Pr^{4+} – Pr^{3+} redox cycle. Being able to easily release active oxygen also in lack of gaseous O_2, this material could be a suitable candidate for catalyzing soot oxidation in GPFs. Instead, the incorporation of non-reducible La and Nd ions detrimentally affected the reducibility as well as the catalytic activity for CO and NO oxidation. Conversely, soot oxidation generally benefited from La and Nd addition, even though the mixed oxides presented a high quantity of oxygen vacancies. However, due to the non-reducibility of these dopants, the associated vacancies are likely less reactive than those of Cu-doped ceria and are not involved in active oxygen consumption.

The Ce-La equimolar oxide exhibited an outstanding soot oxidation activity in all the tested conditions, and it was even able to outperform ceria-praseodymia. Besides the optimal morphology and surface acidity, also the presence of highly reactive capping oxygen species at the surface of ceria-lanthana can account for the excellent activity of this catalyst. Consistently, the presence of NO_x worsened soot oxidation activity in tight contact, due to the replacement of reactive oxygen by more stable adsorbed nitrates.

The results presented in this thesis provide new insights into the mechanisms responsible for the performances of ceria-based materials. However, they also raise new questions about the reasons behind the defect evolution observed. Additional efforts should be therefore devoted to understanding which kinds of interactions between ceria and the dopant ions define the oxygen vacancies reactivity. The best outcomes could probably be obtained by coupling theoretical simulations with advanced in operando analyses. Unveiling the nature of these hidden behaviors will point the way towards the rational design of superior ceria-based catalysts.

References

1. *Air quality in Europe 2019*; Copenhagen, **2019**.
2. *The European environment - state and outlook 2020*; Copenhagen, **2020**.
3. Vallero, D.A. *Fundamentals of Air Pollution - Fifth edition*; Academic Press, **2014**.
4. Mallik, C. Anthropogenic sources of air pollution. In *Air Pollution: Sources, Impacts and Controls*; CABI, **2019**; pp. 6–25.
5. Squizzato, S.; Masiol, M.; Agostini, C.; Visin, F.; Formenton, G.; Harrison, R.M.; Rampazzo, G. Factors, origin and sources affecting PM1 concentrations and composition at an urban background site. *Atmos. Res.* **2016**, *180*, 262–273, doi:10.1016/j.atmosres.2016.06.002.
6. Arti, C.; Manisha, G.; Anuradha, S. Megacities of developing countries. In *Air pollution: sources, impacts and controls*; CABI, **2019**; pp. 151–164.
7. Pan, L.; Yao, E.; Yang, Y. Impact analysis of traffic-related air pollution based on real-time traffic and basic meteorological information. *J. Environ. Manage.* **2016**, *183*, 510–520, doi:10.1016/j.jenvman.2016.09.010.
8. Sher, E. *Handbook of Air Pollution From Internal Combustion Engines*; **1998**; ISBN 9780126398557.
9. Raub, J.A.; Mathieu-Nolf, M.; Hampson, N.B.; Thom, S.R. Carbon monoxide poisoning - A public health perspective. *Toxicology* **2000**, *145*, 1–14, doi:10.1016/S0300-483X(99)00217-6.
10. Rose, J.J.; Wang, L.; Xu, Q.; McTiernan, C.F.; Shiva, S.; Tejero, J.; Gladwin, M.T. Carbon monoxide poisoning: Pathogenesis, management, and future directions of therapy. *Am. J. Respir. Crit. Care Med.* **2017**, *195*, 596–606, doi:10.1164/rccm.201606-1275CI.
11. Chen, R.; Pan, G.; Zhang, Y.; Xu, Q.; Zeng, G.; Xu, X.; Chen, B.; Kan, H. Ambient carbon monoxide and daily mortality in three Chinese cities: The China Air Pollution and Health Effects Study (CAPES). *Sci. Total Environ.* **2011**, *409*, 4923–4928, doi:10.1016/j.scitotenv.2011.08.029.
12. Cheng, W.K.; Hamrin, D.; Heywood, J.B.; Hochgreb, S.; Min, K.; Norris, M. An overview of hydrocarbon emissions mechanisms in spark-ignition engines. *SAE Tech. Pap.* **1993**, doi:10.4271/932708.
13. Schmitz, T.; Hassel, D.; Weber, F.J. Determination of VOC-components in the exhaust of gasoline and diesel passenger cars. *Atmos. Environ.* **2000**, *34*, 4639–4647, doi:10.1016/S1352-2310(00)00303-4.
14. Kampa, M.; Castanas, E. Human health effects of air pollution. *Environ. Pollut.* **2008**, *151*, 362–367, doi:10.1016/j.envpol.2007.06.012.
15. Pappas, G.P.; Herbert, R.J.; Henderson, W.; Koenig, J.; Stover, B.; Barnhart, S. The respiratory effects of volatile organic compounds. *Int. J. Occup. Environ. Health* **2000**, *6*, 1–8, doi:10.1179/oeh.2000.6.1.1.
16. Li, X.; Yang, Y.; Xu, X.; Xu, C.; Hong, J. Air pollution from polycyclic aromatic hydrocarbons generated by human activities and their health effects in China. *J. Clean. Prod.* **2016**, *112*, 1360–1367, doi:10.1016/j.jclepro.2015.05.077.
17. Shao, M.; Zhang, Y.; Zeng, L.; Tang, X.; Zhang, J.; Zhong, L.; Wang, B. Ground-level ozone in the Pearl River Delta and the roles of VOC and NO_x

in its production. *J. Environ. Manage.* **2009**, *90*, 512–518, doi:10.1016/j.jenvman.2007.12.008.
18. Masum, B.M.; Masjuki, H.H.; Kalam, M.A.; Rizwanul Fattah, I.M.; M Palash, S.; Abedin, M.J. Effect of ethanol-gasoline blend on NO_x emission in SI engine. *Renew. Sustain. Energy Rev.* **2013**, *24*, 209–222, doi:10.1016/j.rser.2013.03.046.
19. Kee, R.J.; Coltrin, M.E.; Glarborg, P. *Chemically Reacting Flow: Theory and Practice*; Wiley-Interscience, **2003**;
20. Lerdau, M.T.; Munger, J.W.; Jacob, D.J. The NO_2 Flux Conundrum. *Science (80-.).* **2000**, *289*, 2291–2293, doi:10.1126/science.289.5488.2291.
21. Hine, C.H.; Meyers, F.H.; Wright, R.W. Pulmonary Changes in Animals Exposed To Nitrogen Dioxide. *Toxicol. Appl. Pharmacol.* **1970**, *16*, 201–213, doi:https://doi.org/10.1016/0041-008X(70)90177-8.
22. Conti, S.; Harari, S.; Caminati, A.; Zanobetti, A.; Schwartz, J.D.; Bertazzi, P.A.; Cesana, G.; Madotto, F. The association between air pollution and the incidence of idiopathic pulmonary fibrosis in Northern Italy. *Eur. Respir. J.* **2018**, *51*, doi:10.1183/13993003.00397-2017.
23. Carugno, M.; Consonni, D.; Randi, G.; Catelan, D.; Grisotto, L.; Bertazzi, P.A.; Biggeri, A.; Baccini, M. Air pollution exposure, cause-specific deaths and hospitalizations in a highly polluted italian region. *Environ. Res.* **2016**, *147*, 415–424, doi:10.1016/j.envres.2016.03.003.
24. Chen, R.; Samoli, E.; Wong, C.M.; Huang, W.; Wang, Z.; Chen, B.; Kan, H. Associations between short-term exposure to nitrogen dioxide and mortality in 17 Chinese cities: The China Air Pollution and Health Effects Study (CAPES). *Environ. Int.* **2012**, *45*, 32–38, doi:10.1016/j.envint.2012.04.008.
25. Ritz, B.; Lee, P.C.; Hansen, J.; Lassen, C.F.; Ketzel, M.; Sørensen, M.; Raaschou-Nielsen, O. Traffic-related air pollution and parkinson's disease in Denmark: A case–control study. *Environ. Health Perspect.* **2016**, *124*, 351–356, doi:10.1289/ehp.1409313.
26. Latza, U.; Gerdes, S.; Baur, X. Effects of nitrogen dioxide on human health: Systematic review of experimental and epidemiological studies conducted between 2002 and 2006. *Int. J. Hyg. Environ. Health* **2009**, *212*, 271–287, doi:10.1016/j.ijheh.2008.06.003.
27. Chen, R.; Huang, W.; Wong, C.M.; Wang, Z.; Quoc Thach, T.; Chen, B.; Kan, H. Short-term exposure to sulfur dioxide and daily mortality in 17 Chinese cities: The China air pollution and health effects study (CAPES). *Environ. Res.* **2012**, *118*, 101–106, doi:10.1016/j.envres.2012.07.003.
28. Clarke, A.G.; Radojevic, M. Oxidation of SO_2 in rainwater and its role in acid rain chemistry. *Atmos. Environ.* **1987**, *21*, 1115–1123, doi:10.1016/0004-6981(87)90238-1.
29. Xu, L.; Wang, C.; Chang, H.; Wu, Q.; Zhang, T.; Li, J. New Insight into SO_2 Poisoning and Regeneration of CeO_2-WO_3/TiO_2 and V_2O_5-WO_3/TiO_2 Catalysts for Low-Temperature NH_3-SCR. *Environ. Sci. Technol.* **2018**, *52*, 7064–7071, doi:10.1021/acs.est.8b01990.
30. Zhang, L.; Wang, D.; Liu, Y.; Kamasamudram, K.; Li, J.; Epling, W. SO_2 poisoning impact on the NH_3-SCR reaction over a commercial Cu-SAPO-34 SCR catalyst. *Appl. Catal. B Environ.* **2014**, *156–157*, 371–377, doi:10.1016/j.apcatb.2014.03.030.
31. Tikhomirov, K.; Kröcher, O.; Elsener, M.; Wokaun, A. MnO_x-CeO_2 mixed oxides for the low-temperature oxidation of diesel soot. *Appl. Catal. B*

Environ. **2006**, *64*, 72–78, doi:10.1016/j.apcatb.2005.11.003.
32. Allansson, R.; Maloney, C.A.; Walker, A.P.; Warren, J.P. Sulphate Production Over The CRT$^{(TM)}$: What Fuel Sulphur Level Is Required To Enable The EU 4 And EU 5 PM Standards To Be Met? *SAE Trans.* **2000**, *109*, 1254–1258.
33. van Setten, B.A.A.L.; Makkee, M.; Moulijn, J.A. Science and technology of catalytic diesel particulate filters. *Catal. Rev.* **2001**, *43*, 489–564, doi:10.1081/CR-120001810.
34. Sun, Y.; Zhuang, G.; Wang, Y.; Han, L.; Guo, J.; Dan, M.; Zhang, W.; Wang, Z.; Hao, Z. The air-borne particulate pollution in Beijing - Concentration, composition, distribution and sources. *Atmos. Environ.* **2004**, *38*, 5991–6004, doi:10.1016/j.atmosenv.2004.07.009.
35. Guan, B.; Zhan, R.; Lin, H.; Huang, Z. Review of the state-of-the-art of exhaust particulate filter technology in internal combustion engines. *J. Environ. Manage.* **2015**, *154*, 225–258, doi:10.1016/j.jenvman.2015.02.027.
36. Ljungman, P.L.S.; Andersson, N.; Stockfelt, L.; Andersson, E.M.; Sommar, J.N.; Eneroth, K.; Gidhagen, L.; Johansson, C.; Lager, A.; Leander, K.; et al. Long-term exposure to particulate air pollution, black carbon, and their source components in relation to ischemic heart disease and stroke. *Environ. Health Perspect.* **2019**, *127*, 1–11, doi:10.1289/EHP4757.
37. Croft, D.P.; Zhang, W.; Lin, S.; Thurston, S.W.; Hopke, P.K.; Masiol, M.; Squizzato, S.; van Wijngaarden, E.; Utell, M.J.; Rich, D.Q. The association between respiratory infection and air pollution in the setting of air quality policy and economic change. *Ann. Am. Thorac. Soc.* **2019**, *16*, 321–330, doi:10.1513/AnnalsATS.201810-691OC.
38. Yorifuji, T.; Kashima, S. Air pollution: Another cause of lung cancer. *Lancet Oncol.* **2013**, *14*, 788–789.
39. Raaschou-Nielsen, O.; Andersen, Z.J.; Beelen, R.; Samoli, E.; Stafoggia, M.; Weinmayr, G.; Hoffmann, B.; Fischer, P.; Nieuwenhuijsen, M.J.; Brunekreef, B.; et al. Air pollution and lung cancer incidence in 17 European cohorts: Prospective analyses from the European Study of Cohorts for Air Pollution Effects (ESCAPE). *Lancet Oncol.* **2013**, *14*, 813–822, doi:10.1016/S1470-2045(13)70279-1.
40. Valavanidis, A.; Fiotakis, K.; Vlachogianni, T. Airborne particulate matter and human health: Toxicological assessment and importance of size and composition of particles for oxidative damage and carcinogenic mechanisms. *J. Environ. Sci. Heal. - Part C Environ. Carcinog. Ecotoxicol. Rev.* **2008**, *26*, 339–362, doi:10.1080/10590500802494538.
41. Englert, N. Fine particles and human health - A review of epidemiological studies. *Toxicol. Lett.* **2004**, *149*, 235–242, doi:10.1016/j.toxlet.2003.12.035.
42. Pardo, M.; Porat, Z.; Rudich, A.; Schauer, J.J.; Rudich, Y. Repeated exposures to roadside particulate matter extracts suppresses pulmonary defense mechanisms, resulting in lipid and protein oxidative damage. *Environ. Pollut.* **2016**, *210*, 227–237, doi:10.1016/j.envpol.2015.12.009.
43. Coker, E.S.; Cavalli, L.; Fabrizi, E.; Guastella, G.; Lippo, E.; Parisi, M.L.; Pontarollo, N.; Rizzati, M.; Varacca, A.; Vergalli, S. The Effects of Air Pollution on COVID-19 Related Mortality in Northern Italy. *Environ. Resour. Econ.* **2020**, doi:10.1007/s10640-020-00486-1.
44. Conticini, E.; Frediani, B.; Caro, D. Can atmospheric pollution be

considered a co-factor in extremely high level of SARS-CoV-2 lethality in Northern Italy? *Environ. Pollut.* **2020**, *261*, 114465, doi:10.1016/j.envpol.2020.114465.
45. Eggleton, T. *A Short Introduction to Climate Change*; Cambridge University Press: Port Melbourne, **2013**; ISBN 9781107618763.
46. Anderson, T.R.; Hawkins, E.; Jones, P.D. CO_2, the greenhouse effect and global warming: from the pioneering work of Arrhenius and Callendar to today's Earth System Models. *Endeavour* **2016**, *40*, 178–187, doi:10.1016/j.endeavour.2016.07.002.
47. Hashimoto, K. Global Temperature and Atmospheric Carbon Dioxide Concentration. In *Global Carbon Dioxide Recycling: For Global Sustainable Development by Renewable Energy*; Springer Singapore: Singapore, **2019**; pp. 5–17 ISBN 978-981-13-8584-1.
48. Olivier, J.G.J.; Peters, J.A.H.W. *Trends in Global CO_2 and Total Greenhouse Gas Emissions*; **2020**;
49. The Keeling Curve | A daily record of atmospheric carbon dioxide from Scripps Institution of Oceanography at UC San Diego Available online: https://scripps.ucsd.edu/programs/keelingcurve/ (accessed on Aug 24, **2020**).
50. Hashimoto, K. The Greenhouse Effect and Global Warming. In *Global Carbon Dioxide Recycling: For Global Sustainable Development by Renewable Energy*; Springer Singapore: Singapore, **2019**; pp. 19–23 ISBN 978-981-13-8584-1.
51. Vargo, L.J.; Anderson, B.M.; Dadić, R.; Horgan, H.J.; Mackintosh, A.N.; King, A.D.; Lorrey, A.M. Anthropogenic warming forces extreme annual glacier mass loss. *Nat. Clim. Chang.* **2020**, doi:10.1038/s41558-020-0849-2.
52. May, C. Rising groundwater and sea-level rise. *Nat. Clim. Chang.* **2020**, doi:10.1038/s41558-020-0886-x.
53. Johnson, G.C.; Lyman, J.M. Warming trends increasingly dominate global ocean. *Nat. Clim. Chang.* **2020**, *10*, 757–761, doi:10.1038/s41558-020-0822-0.
54. Taufik, M.; Torfs, P.J.J.F.; Uijlenhoet, R.; Jones, P.D.; Murdiyarso, D.; Van Lanen, H.A.J. Amplification of wildfire area burnt by hydrological drought in the humid tropics. *Nat. Clim. Chang.* **2017**, *7*, 428–431, doi:10.1038/nclimate3280.
55. Huang, J.; Yu, H.; Guan, X.; Wang, G.; Guo, R. Accelerated dryland expansion under climate change. *Nat. Clim. Chang.* **2016**, *6*, 166–171, doi:10.1038/nclimate2837.
56. Prein, A.F.; Heymsfield, A.J. Increased melting level height impacts surface precipitation phase and intensity. *Nat. Clim. Chang.* **2020**, *10*, 771–776, doi:10.1038/s41558-020-0825-x.
57. Turner, C. *Climate Change and Biodiversity*; Scientific e-Resources, **2018**; ISBN 9781839472480.
58. Feeley, K.J.; Bravo-Avila, C.; Fadrique, B.; Perez, T.M.; Zuleta, D. Climate-driven changes in the composition of New World plant communities. *Nat. Clim. Chang.* **2020**, doi:10.1038/s41558-020-0873-2.
59. Aleixo, I.; Norris, D.; Hemerik, L.; Barbosa, A.; Prata, E.; Costa, F.; Poorter, L. Amazonian rainforest tree mortality driven by climate and functional traits. *Nat. Clim. Chang.* **2019**, *9*, 384–388, doi:10.1038/s41558-019-0458-0.

60. Pecl, G.T.; Araújo, M.B.; Bell, J.D.; Blanchard, J.; Bonebrake, T.C.; Chen, I.C.; Clark, T.D.; Colwell, R.K.; Danielsen, F.; Evengård, B.; et al. Biodiversity redistribution under climate change: Impacts on ecosystems and human well-being. *Science.* **2017**, *355*, doi:10.1126/science.aai9214.
61. Chen, K.; Horton, R.M.; Bader, D.A.; Lesk, C.; Jiang, L.; Jones, B.; Zhou, L.; Chen, X.; Bi, J.; Kinney, P.L. Impact of climate change on heat-related mortality in Jiangsu Province, China. *Environ. Pollut.* **2017**, *224*, 317–325, doi:10.1016/j.envpol.2017.02.011.
62. Gasparrini, A.; Guo, Y.; Sera, F.; Vicedo-Cabrera, A.M.; Huber, V.; Tong, S.; de Sousa Zanotti Stagliorio Coelho, M.; Nascimento Saldiva, P.H.; Lavigne, E.; Matus Correa, P.; et al. Projections of temperature-related excess mortality under climate change scenarios. *Lancet Planet. Heal.* **2017**, *1*, e360–e367, doi:10.1016/S2542-5196(17)30156-0.
63. Bennett, J.E.; Blangiardo, M.; Fecht, D.; Elliott, P.; Ezzati, M. Vulnerability to the mortality effects of warm temperature in the districts of England and Wales. *Nat. Clim. Chang.* **2014**, *4*, 269–273, doi:10.1038/nclimate2123.
64. Silva, R.A.; West, J.J.; Lamarque, J.F.; Shindell, D.T.; Collins, W.J.; Faluvegi, G.; Folberth, G.A.; Horowitz, L.W.; Nagashima, T.; Naik, V.; et al. Future global mortality from changes in air pollution attributable to climate change. *Nat. Clim. Chang.* **2017**, *7*, 647–651, doi:10.1038/nclimate3354.
65. Hooftman, N.; Messagie, M.; Van Mierlo, J.; Coosemans, T. A review of the European passenger car regulations – Real driving emissions vs local air quality. *Renew. Sustain. Energy Rev.* **2018**, *86*, 1–21, doi:10.1016/j.rser.2018.01.012.
66. Johnson, T.; Joshi, A. Review of Vehicle Engine Efficiency and Emissions. *SAE Int. J. Engines* **2018**, *11*, 1307–1330, doi:10.4271/2018-01-0329.
67. Johnson, T. Vehicular Emissions in Review. *SAE Int. J. Engines* **2016**, *9*, 1258–1275, doi:10.4271/2016-01-0919.
68. Giechaskiel, B.; Joshi, A.; Ntziachristos, L.; Dilara, P. European Regulatory Framework and Particulate Matter Emissions of Gasoline Light-Duty Vehicles: A Review. *Catalysts* **2019**, *9*, 586, doi:10.3390/catal9070586.
69. Frigessi di Rattalma, M. *The Dieselgate: a Legal Perspective*; Springer International Publishing, **2017**; ISBN 9783319483238.
70. Grange, S.K.; Grange, S.K.; Farren, N.J.; Vaughan, A.R.; Davison, J.; Carslaw, D.C. Post-Dieselgate: Evidence of NO_x Emission Reductions Using On-Road Remote Sensing. *Environ. Sci. Technol. Lett.* **2020**, *7*, 382–387, doi:10.1021/acs.estlett.0c00188.
71. Tsiakmakis, S.; Fontaras, G.; Ciuffo, B.; Samaras, Z. A simulation-based methodology for quantifying European passenger car fleet CO_2 emissions. *Appl. Energy* **2017**, *199*, 447–465, doi:10.1016/j.apenergy.2017.04.045.
72. Pajdowski, P.; Woodburn, J.; Bielaczyc, P.; Puchalka, B. Development of RDE/ISC test methodology in light of Euro 6d/VI emissions limits. *Combust. Engines* **2019**, *178*, 274–282, doi:10.19206/CE-2019-348.
73. Söderena, P.; Laurikko, J.; Kuikka, K.; Tilli, A.; Kousa, A.; Väkevä, O.; Venho, A.; Haaparanta, S.; Nuottimäki, J.; Lehto, K.; et al. *Euro 6 Diesel Passenger Cars' Emissions Field Tests : Project Final Report*; VTT Technical Research Centre of Finland, **2019**.
74. Giechaskiel, B.; Lähde, T.; Schwelberger, M.; Kleinbach, T.; Roske, H.;

Teti, E.; van den Bos, T.; Neils, P.; Delacroix, C.; Jakobsson, T.; et al. Particle number measurements directly from the tailpipe for type approval of heavy-duty engines. *Appl. Sci.* **2019**, *9*, doi:10.3390/app9204418.
75. Reducing CO_2 emissions from passenger cars. Available online: https://ec.europa.eu/clima/policies/transport/vehicles/cars_en (accessed on Aug 24, **2020**).
76. Monitoring of CO_2 emissions from passenger cars – Regulation (EU) 2019/631 Available online: https://www.eea.europa.eu/data-and-maps/data/co2-cars-emission-18 (accessed on Aug 24, **2020**).
77. CO_2 emission performance standards for cars and vans (2020 onwards) Available online: https://ec.europa.eu/clima/policies/transport/vehicles/regulation_en (accessed on Aug 24, **2020**).
78. Joshi, A. Review of Vehicle Engine Efficiency and Emissions. In Proceedings of the SAE Technical Papers; SAE International, **2020**; Vol. 2020-April.
79. Sapio, F.; Millo, F.; Fino, D.; Monteverde, A.; Sartoretti, E.; Bianco, A.; Postrioti, L.; Tarabocchia, A.; Buitoni, G.; Brizi, G. Experimental and Numerical Analysis of Latest Generation Diesel Aftertreatment Systems. *SAE Tech. Pap. Ser.* **2019**, *1*, doi:10.4271/2019-24-0142.
80. Heck, R.M.; Farrauto, R.J.; Gulati, S.T. *Catalytic air pollution control: commercial technology*; John Wiley, **2009**; ISBN 0470275030; 9780470275030.
81. Farrauto, R.J.; Heck, R.M. Catalytic converters: State of the art and perspectives. *Catal. Today* **1999**, *51*, 351–360, doi:10.1016/S0920-5861(99)00024-3.
82. Chen, Y.; Deng, J.; Fan, J.; Jiao, Y.; Wang, J.; Chen, Y. Key role of NO + C_3H_8 reaction for the elimination of NO in automobile exhaust by three-way catalyst. *Environ. Sci. Pollut. Res.* **2019**, *26*, 26071–26081, doi:10.1007/s11356-019-05834-3.
83. Wunsch, R.; Schön, C.; Frey, M.; Tran, D.; Proske, S.; Wandrey, T.; Kalogirou, M.; Schäffner, J. Detailed experimental investigation of the NO_x reaction pathways of three-way catalysts with focus on intermediate reactions of NH_3 and N_2O. *Appl. Catal. B Environ.* **2020**, *272*, doi:10.1016/j.apcatb.2020.118937.
84. Sabatini, S.; Gelmini, S.; Hoffman, M.A.; Onori, S. Design and experimental validation of a physics-based oxygen storage — thermal model for three way catalyst including aging. *Control Eng. Pract.* **2017**, *68*, 89–101, doi:10.1016/j.conengprac.2017.07.007.
85. Choung, J.W.; Lee, S.M.; Kim, S.J.; Lee, D.H.; Kwon, K. Smart engine control strategy for the fuel efficiency improvement via understanding the unique behavior of TWC. In Proceedings of the SAE Technical Papers; SAE International, **2019**; Vol. 2019-March.
86. Rood, S.; Eslava, S.; Manigrasso, A.; Bannister, C. Recent advances in gasoline three-way catalyst formulation: A review. *Proc. Inst. Mech. Eng. Part D J. Automob. Eng.* **2020**, *234*, 936–949, doi:10.1177/0954407019859822.
87. Aneggi, E.; de Leitenburg, C.; Boaro, M.; Fornasiero, P.; Trovarelli, A. *Catalytic applications of cerium dioxide*; Elsevier Inc., **2020**; ISBN 9780128156612.
88. Trovarelli, A.; Fornasiero, P. *Catalysis by Ceria and Related Materials*;

Catalytic Science Series; Imperial Ccollege Press, **2013**; Vol. 12; ISBN 978-1-84816-963-0.
89. Ozawa, M.; Takahashi-Morita, M.; Kobayashi, K.; Haneda, M. Core-shell type ceria zirconia support for platinum and rhodium three way catalysts. *Catal. Today* **2017**, *281*, 482–489, doi:10.1016/j.cattod.2016.06.029.
90. Danielis, M.; Colussi, S.; Leitenburg, C. De; Llorca, J.; Trovarelli, A. Outstanding Methane Oxidation Performance of Palladium-Embedded Ceria Catalysts Prepared by a One-Step Dry Ball-Milling Method. *Angew. Chemie - Int. Ed.* **2018**, *57*, 10212–10216, doi:10.1002/anie.201805929.
91. Mullins, D.R. The surface chemistry of cerium oxide. *Surf. Sci. Rep.* **2015**, *70*, 42–85, doi:10.1016/j.surfrep.2014.12.001.
92. Kim, C.H.; Schmid, M.; Schmieg, S.J.; Tan, J.; Li, W. The effect of Pt-Pd ratio on oxidation catalysts under simulated diesel exhaust. *SAE 2011 World Congr. Exhib.* **2011**, doi:10.4271/2011-01-1134.
93. Hazlett, M.J.; Epling, W.S. Heterogeneous catalyst design: Zoned and layered catalysts in diesel vehicle aftertreatment monolith reactors. *Can. J. Chem. Eng.* **2019**, *97*, 188–206, doi:10.1002/cjce.23293.
94. Tang, W.; Lu, X.; Liu, F.; Du, S.; Weng, J.; Hoang, S.; Wang, S.; Nam, C.Y.; Gao, P.X. Ceria-based nanoflake arrays integrated on 3D cordierite honeycombs for efficient low-temperature diesel oxidation catalyst. *Appl. Catal. B Environ.* **2019**, *245*, 623–634, doi:10.1016/j.apcatb.2019.01.028.
95. Al-Harbi, M.; Hayes, R.; Votsmeier, M.; Epling, W.S. Competitive NO, CO and hydrocarbon oxidation reactions over a diesel oxidation catalyst. *Can. J. Chem. Eng.* **2012**, *90*, 1527–1538, doi:10.1002/cjce.20659.
96. Luján, J.M.; Climent, H.; García-Cuevas, L.M.; Moratal, A. Pollutant emissions and diesel oxidation catalyst performance at low ambient temperatures in transient load conditions. *Appl. Therm. Eng.* **2018**, *129*, 1527–1537, doi:10.1016/j.applthermaleng.2017.10.138.
97. Kanno, Y.; Hihara, T.; Watanabe, T.; Katoh, K.; Nagata, M. Low sulfate generation diesel oxidation catalyst. *SAE Tech. Pap.* **2004**, doi:10.4271/2004-01-1427.
98. Banno, Y.; Tanaka, Y.; Hihara, T.; Nagata, M. Pre-filter diesel oxidation catalyst development for DOC-CSF system. *SAE Tech. Pap.* **2004**, doi:10.4271/2004-01-1430.
99. Sampara, C.S.; Bissett, E.J.; Assanis, D. Hydrocarbon storage modeling for diesel oxidation catalysts. *Chem. Eng. Sci.* **2008**, *63*, 5179–5192, doi:10.1016/j.ces.2008.06.021.
100. Millo, F.; Vezza, D. Characterization of a new advanced diesel oxidation catalyst with low temperature NO_x storage capability for LD diesel. *SAE Tech. Pap.* **2012**, doi:10.4271/2012-01-0373.
101. Nova, I.; Lietti, L.; Forzatti, P. Mechanistic aspects of the reduction of stored NO_x over Pt-Ba/Al_2O_3 lean NO_x trap systems. *Catal. Today* **2008**, *136*, 128–135, doi:10.1016/j.cattod.2008.01.006.
102. Kumar, A.; Harold, M.P.; Balakotaiah, V. Isotopic studies of NO_X storage and reduction on Pt/BaO/Al2O3 catalyst using temporal analysis of products. *J. Catal.* **2010**, *270*, 214–223, doi:10.1016/j.jcat.2009.12.018.
103. Li, J.; Currier, N.; Yezerets, A.; Chen, H.-Y.; Hess, H.; Mulla, S. Impact of Rh Oxidation State on NO_x Reduction Performance of Multi-Component Lean NO_x Trap (LNT) Catalyst. *SAE Int. J. Engines* **2016**, *9*, 1615–1622, doi:10.2307/26284926.
104. Nova, I.; Lietti, L.; Castoldi, L.; Tronconi, E.; Forzatti, P. New insights in

the NO_x reduction mechanism with H_2 over Pt-Ba/γ-Al_2O_3 lean NO_x trap catalysts under near-isothermal conditions. *J. Catal.* **2006**, *239*, 244–254, doi:10.1016/j.jcat.2006.01.013.
105. Nova, I.; Castoldi, L.; Lietti, L.; Tronconi, E.; Forzatti, P.; Prinetto, F.; Ghiotti, G. NO_x adsorption study over Pt-Ba/alumina catalysts: FT-IR and pulse experiments. *J. Catal.* **2004**, *222*, 377–388, doi:10.1016/j.jcat.2003.11.013.
106. Medhekar, V.; Balakotaiah, V.; Harold, M.P. TAP study of NO_x storage and reduction on Pt/Al_2O_3 and Pt/Ba/Al_2O_3. *Catal. Today* **2007**, *121*, 226–236, doi:10.1016/j.cattod.2006.08.063.
107. Václavík, M.; Kočí, P.; Novák, V.; Thompsett, D. NO_x conversion and selectivity in multi-layer and sequential DOC-LNT automotive exhaust catalysts: Influence of internal transport. *Chem. Eng. J.* **2017**, *329*, 128–134, doi:10.1016/j.cej.2017.05.129.
108. Li, M.; Easterling, V.G.; Harold, M.P. Towards optimal operation of sequential NO_x storage and reduction and selective catalytic reduction. *Appl. Catal. B Environ.* **2016**, *184*, 364–380, doi:10.1016/j.apcatb.2015.11.029.
109. Damma, D.; Ettireddy, P.R.; Reddy, B.M.; Smirniotis, P.G. *A review of low temperature NH_3-SCR for removal of NO_x*; **2019**; Vol. 9; ISBN 1513556347.
110. Jung, Y.; Shin, Y.J.; Pyo, Y.D.; Cho, C.P.; Jang, J.; Kim, G. NO_x and N_2O emissions over a Urea-SCR system containing both V_2O_5-WO_3/TiO_2 and Cu-zeolite catalysts in a diesel engine. *Chem. Eng. J.* **2017**, *326*, 853–862, doi:10.1016/j.cej.2017.06.020.
111. Wang, A.; Wang, Y.; Walter, E.D.; Washton, N.M.; Guo, Y.; Lu, G.; Peden, C.H.F.; Gao, F. NH_3-SCR on Cu, Fe and Cu + Fe exchanged beta and SSZ-13 catalysts: Hydrothermal aging and propylene poisoning effects. *Catal. Today* **2019**, *320*, 91–99, doi:10.1016/j.cattod.2017.09.061.
112. Metkar, P.S.; Harold, M.P.; Balakotaiah, V. Selective catalytic reduction of NO_x on combined Fe- and Cu-zeolite monolithic catalysts: Sequential and dual layer configurations. *Appl. Catal. B Environ.* **2012**, *111–112*, 67–80, doi:10.1016/j.apcatb.2011.09.019.
113. Maunula, T. NO_x Reduction with the Combinations on LNT and SCR in Diesel Applications. *SAE Int. J. Mater. Manuf.* **2014**, *7*, 195–206.
114. Fino, D. Diesel emission control: Catalytic filters for particulate removal. *Sci. Technol. Adv. Mater.* **2007**, *8*, 93–100, doi:10.1016/j.stam.2006.11.012.
115. Fino, D.; Bensaid, S.; Piumetti, M.; Russo, N. A review on the catalytic combustion of soot in Diesel particulate filters for automotive applications: From powder catalysts to structured reactors. *Appl. Catal. A Gen.* **2016**, *509*, 75–96, doi:10.1016/j.apcata.2015.10.016.
116. Ootake, M.; Kondou, T.; Ikeda, M.; Daigo, M.; Nakano, M.; Yokoyama, J.; Miura, M. Development of diesel engine system with DPF for the European market. *SAE Tech. Pap.* **2007**, *2007*, doi:10.4271/2007-01-1061.
117. Koltsakis, G.C.; Katsaounis, D.K.; Markomanolakis, I.A.; Samaras, Z.C.; Naumann, D.; Saberi, S.; Böhm, A. Metal foam substrate for DOC and DPF applications. In Proceedings of the SAE Technical Papers; **2007**.
118. Konstandopoulos, A.G.; Metallinou, R. Parametric Representation of the Entire Pressure Drop Evolution during Particulate Filter Loading. In Proceedings of the SAE Technical Papers; SAE International, **2020**; Vol.

2020-April.
119. Neyertz, C.A.; Banús, E.D.; Miró, E.E.; Querini, C.A. Potassium-promoted $Ce_{0.65}Zr_{0.35}O_2$ monolithic catalysts for diesel soot combustion. *Chem. Eng. J.* **2014**, *248*, 394–405, doi:10.1016/j.cej.2014.03.048.
120. Beatrice, C.; Iorio, S. Di; Guido, C.; Napolitano, P. Detailed characterization of particulate emissions of an automotive catalyzed DPF using actual regeneration strategies. *Exp. Therm. Fluid Sci.* **2012**, *39*, 45–53, doi:10.1016/j.expthermflusci.2012.01.005.
121. Lückert, P.; Arndt, S.; Duvinage, F.; Kemmner, M.; Binz, R.; Storz, O.; Reusch, M.; Braun, T.; Ellwanger, S. The New Mercedes-Benz 4-Cylinder Diesel Engine OM654 – The Innovative Base Engine of the New Diesel Generation. *Aachen Colloq.* **2015**, 867–892.
122. Lörch, H.; Weiß, U.; Pamio, G.; Bauer, R.; Schütte, T.; Kahrstedt, J.; Düsterdiek, T.; Kösters, M. The New EU6 R4 and V6 TDI Engines from Volkswagen and Audi Integration of SCR Functionality in a Close-Coupled Diesel Particulate Filter. *22nd Aachen Colloq. Automob. Engine Technol.* **2013**, 1293–1312.
123. Czerwinski, J.; Zimmerli, Y.; Mayer, A.; D'Urbano, G.; Zürcher, D. Emission Reduction with Diesel Particle Filter with SCR Coating (SDPF). *Emiss. Control Sci. Technol.* **2015**, *1*, 152–166, doi:10.1007/s40825-015-0018-7.
124. Marchitti, F.; Nova, I.; Tronconi, E. Experimental study of the interaction between soot combustion and NH_3-SCR reactivity over a Cu-Zeolite SDPF catalyst. *Catal. Today* **2016**, *267*, 110–118, doi:10.1016/j.cattod.2016.01.027.
125. Raza, M.; Chen, L.; Leach, F.; Ding, S. A Review of particulate number (PN) emissions from gasoline direct injection (gdi) engines and their control techniques. *Energies* **2018**, *11*, doi:10.3390/en11061417.
126. Saito, C.; Nakatani, T.; Miyairi, Y.; Yuuki, K.; Makino, M.; Kurachi, H.; Heuss, W.; Kuki, T.; Furuta, Y.; Kattouah, P.; et al. New particulate filter concept to reduce particle number emissions. *SAE 2011 World Congr. Exhib.* **2011**, doi:10.4271/2011-01-0814.
127. Chincholkar, S.P.; Suryawanshi, J.G. Gasoline Direct Injection: An Efficient Technology. *Energy Procedia* **2016**, *90*, 666–672, doi:10.1016/j.egypro.2016.11.235.
128. Aneggi, E.; Trovarelli, A. Potential of Ceria-Zirconia-Based Materials in Carbon Soot Oxidation for Gasoline Particulate Filters. *Catalysts* **2020**, *10*, 768, doi:10.3390/catal10070768.
129. Gao, Y.; Duan, A.; Liu, S.; Wu, X.; Liu, W.; Li, M.; Chen, S.; Wang, X.; Weng, D. Study of $Ag/Ce_xNd_{1-x}O_2$ nanocubes as soot oxidation catalysts for gasoline particulate filters: Balancing catalyst activity and stability by Nd doping. *Appl. Catal. B Environ.* **2017**, *203*, 116–126, doi:10.1016/j.apcatb.2016.10.006.
130. Montini, T.; Melchionna, M.; Monai, M.; Fornasiero, P. Fundamentals and Catalytic Applications of CeO_2-Based Materials. *Chem. Rev.* **2016**, *116*, 5987–6041, doi:10.1021/acs.chemrev.5b00603.
131. Royer, S.; Duprez, D. Catalytic Oxidation of Carbon Monoxide over Transition Metal Oxides. *ChemCatChem* **2011**, *3*, 24–65, doi:10.1002/cctc.201000378.
132. Baxter, R.J.; Hu, P. Insight into why the Langmuir-Hinshelwood mechanism is generally preferred. *J. Chem. Phys.* **2002**, *116*, 4379–4381,

doi:10.1063/1.1458938.
133. Dann, E.K.; Gibson, E.K.; Catlow, C.R.A.; Celorrio, V.; Collier, P.; Eralp, T.; Amboage, M.; Hardacre, C.; Stere, C.; Kroner, A.; et al. Combined spatially resolved operando spectroscopy: New insights into kinetic oscillations of CO oxidation on Pd/Γ-Al_2O_3. *J. Catal.* **2019**, *373*, 201–208, doi:10.1016/j.jcat.2019.03.037.
134. Liu, B.; Li, W.; Song, W.; Liu, J. Carbonate-mediated Mars-van Krevelen mechanism for CO oxidation on cobalt-doped ceria catalysts: Facet-dependence and coordination-dependence. *Phys. Chem. Chem. Phys.* **2018**, *20*, 16045–16059, doi:10.1039/c8cp01694a.
135. Wu, Z.; Li, M.; Overbury, S.H. On the structure dependence of CO oxidation over CeO_2 nanocrystals with well-defined surface planes. *J. Catal.* **2012**, *285*, 61–73, doi:10.1016/j.jcat.2011.09.011.
136. Trovarelli, A.; Llorca, J. Ceria Catalysts at Nanoscale: How Do Crystal Shapes Shape Catalysis? *ACS Catal.* **2017**, *7*, 4716–4735.
137. Spezzati, G.; Benavidez, A.D.; DeLaRiva, A.T.; Su, Y.; Hofmann, J.P.; Asahina, S.; Olivier, E.J.; Neethling, J.H.; Miller, J.T.; Datye, A.K.; et al. CO oxidation by Pd supported on CeO_2 (100) and CeO_2 (111) facets. *Appl. Catal. B Environ.* **2019**, *243*, 36–46, doi:10.1016/j.apcatb.2018.10.015.
138. Sun, Y.; Li, C.; Djerdj, I.; Khalid, O.; Cop, P.; Sann, J.; Weber, T.; Werner, S.; Turke, K.; Guo, Y.; et al. Oxygen storage capacity versus catalytic activity of ceria-zirconia solid solutions in CO and HCl oxidation. *Catal. Sci. Technol.* **2019**, *9*, 2163–2172, doi:10.1039/c9cy00222g.
139. Bulgakov, N.N.; Sadykov, V.A.; Lunin, V. V.; Kemnitz, E. Lattice defects and oxygen absorption/migration in ceria/ceria-zirconia solid solutions: Analysis by semiempirical interacting bonds method. *React. Kinet. Catal. Lett.* **2002**, *76*, 103–110, doi:10.1023/A:1015621613212.
140. Trovarelli, A. Structural and Oxygen Storage/Release Properties of CeO_2-Based Solid Solutions. *Comments Inorg. Chem.* **1999**, *20*, 263–284, doi:10.1080/02603599908021446.
141. Ganduglia-Pirovano, M.V.; Hofmann, A.; Sauer, J. Oxygen vacancies in transition metal and rare earth oxides: Current state of understanding and remaining challenges. *Surf. Sci. Rep.* **2007**, *62*, 219–270, doi:10.1016/j.surfrep.2007.03.002.
142. Bensaid, S.; Piumetti, M.; Novara, C.; Giorgis, F.; Chiodoni, A.; Russo, N.; Fino, D. Catalytic Oxidation of CO and Soot over Ce-Zr-Pr Mixed Oxides Synthesized in a Multi-Inlet Vortex Reactor: Effect of Structural Defects on the Catalytic Activity. *Nanoscale Res. Lett.* **2016**, *11*, 1–14, doi:10.1186/s11671-016-1713-1.
143. Dosa, M.; Piumetti, M.; Bensaid, S.; Andana, T.; Novara, C.; Giorgis, F.; Fino, D.; Russo, N. Novel Mn–Cu-Containing CeO_2 Nanopolyhedra for the Oxidation of CO and Diesel Soot: Effect of Dopants on the Nanostructure and Catalytic Activity. *Catal. Letters* **2018**, *148*, 298–311, doi:10.1007/s10562-017-2226-y.
144. Zhou, K.; Wang, X.; Sun, X.; Peng, Q.; Li, Y. Enhanced catalytic activity of ceria nanorods from well-defined reactive crystal planes. *J. Catal.* **2005**, *229*, 206–212, doi:10.1016/j.jcat.2004.11.004.
145. Piumetti, M.; Bensaid, S.; Russo, N.; Fino, D. Investigations into nanostructured ceria-zirconia catalysts for soot combustion. *Appl. Catal. B Environ.* **2016**, *180*, 271–282, doi:10.1016/j.apcatb.2015.06.018.
146. Piumetti, M.; Bensaid, S.; Russo, N.; Fino, D. Nanostructured ceria-based

catalysts for soot combustion: Investigations on the surface sensitivity. *Appl. Catal. B Environ.* **2015**, *165*, 742–751, doi:10.1016/j.apcatb.2014.10.062.
147. Guo, M.; Yin, W.; Zhao, F.; Wang, Q.; Hu, C. Nanostructured Ceria-Praseodymium and Ceria-Terbium Mixed Oxides: Relationship Between Structural Change and Catalytic Activity Towards CO Oxidation. *J. Nanosci. Nanotechnol.* **2019**, *19*, 5999–6005, doi:10.1166/jnn.2019.16542.
148. Romero-Núñez, A.; Díaz, G. High oxygen storage capacity and enhanced catalytic performance of $NiO/Ni_xCe_{1-x}O_{2-\delta}$ nanorods: synergy between Ni-doping and 1D morphology. *RSC Adv.* **2015**, *5*, 54571–54579, doi:10.1039/c5ra04259c.
149. Singhania, N.; Anumol, E.A.; Ravishankar, N.; Madras, G. Influence of CeO_2 morphology on the catalytic activity of CeO_2-Pt hybrids for CO oxidation. *Dalt. Trans.* **2013**, *42*, 15343–15354, doi:10.1039/c3dt51364e.
150. Muñoz, F.F.; Acuña, L.M.; Albornoz, C.A.; Leyva, A.G.; Baker, R.T.; Fuentes, R.O. Redox properties of nanostructured lanthanide-doped ceria spheres prepared by microwave assisted hydrothermal homogeneous co-precipitation. *Nanoscale* **2015**, *7*, 271–281, doi:10.1039/c4nr05630b.
151. Bensaid, S.; Russo, N.; Fino, D. CeO_2 catalysts with fibrous morphology for soot oxidation: The importance of the soot-catalyst contact conditions. *Catal. Today* **2013**, *216*, 57–63, doi:10.1016/j.cattod.2013.05.006.
152. Miceli, P.; Bensaid, S.; Russo, N.; Fino, D. Effect of the morphological and surface properties of CeO_2-based catalysts on the soot oxidation activity. *Chem. Eng. J.* **2015**, *278*, 190–198, doi:10.1016/j.cej.2014.10.055.
153. Alcalde-Santiago, V.; Davó-Quiñonero, A.; Lozano-Castelló, D.; Bueno-López, A. On the soot combustion mechanism using 3DOM ceria catalysts. *Appl. Catal. B Environ.* **2018**, *234*, 187–197, doi:10.1016/j.apcatb.2018.04.023.
154. Nolan, M.; Parker, S.C.; Watson, G.W. The electronic structure of oxygen vacancy defects at the low index surfaces of ceria. *Surf. Sci.* **2005**, *595*, 223–232, doi:10.1016/j.susc.2005.08.015.
155. Aneggi, E.; Wiater, D.; De Leitenburg, C.; Llorca, J.; Trovarelli, A. Shape-dependent activity of ceria in soot combustion. *ACS Catal.* **2014**, *4*, 172–181, doi:10.1021/cs400850r.
156. Pan, C.J.; Tsai, M.C.; Su, W.N.; Rick, J.; Akalework, N.G.; Agegnehu, A.K.; Cheng, S.Y.; Hwang, B.J. Tuning/exploiting Strong Metal-Support Interaction (SMSI) in Heterogeneous Catalysis. *J. Taiwan Inst. Chem. Eng.* **2017**, *74*, 154–186, doi:10.1016/j.jtice.2017.02.012.
157. Zhu Chen, J.; Talpade, A.; Canning, G.A.; Probus, P.R.; Ribeiro, F.H.; Datye, A.K.; Miller, J.T. Strong metal-support interaction (SMSI) of Pt/CeO_2 and its effect on propane dehydrogenation. *Catal. Today* **2020**, 1–6, doi:10.1016/j.cattod.2020.06.075.
158. Happel, M.; Mysliveček, J.; Johánek, V.; Dvořák, F.; Stetsovych, O.; Lykhach, Y.; Matolín, V.; Libuda, J. Adsorption sites, metal-support interactions, and oxygen spillover identified by vibrational spectroscopy of adsorbed CO: A model study on Pt/ceria catalysts. *J. Catal.* **2012**, *289*, 118–126, doi:10.1016/j.jcat.2012.01.022.
159. Danielis, M.; Colussi, S.; De Leitenburg, C.; Soler, L.; Llorca, J.; Trovarelli, A. The effect of milling parameters on the mechanochemical synthesis of $Pd\text{-}CeO_2$ methane oxidation catalysts. *Catal. Sci. Technol.* **2019**, *9*, 4232–4238, doi:10.1039/c9cy01098j.

160. Andana, T.; Piumetti, M.; Bensaid, S.; Veyre, L.; Thieuleux, C.; Russo, N.; Fino, D.; Quadrelli, E.A.; Pirone, R. Nanostructured equimolar ceria-praseodymia for NO_x-assisted soot oxidation: Insight into Pr dominance over Pt nanoparticles and metal–support interaction. *Appl. Catal. B Environ.* **2018**, *226*, 147–161, doi:10.1016/j.apcatb.2017.12.048.
161. Mukherjee, D.; Rao, B.G.; Reddy, B.M. CO and soot oxidation activity of doped ceria: Influence of dopants. *Appl. Catal. B Environ.* **2016**, *197*, 105–115, doi:10.1016/j.apcatb.2016.03.042.
162. Piumetti, M.; Bensaid, S.; Andana, T.; Russo, N.; Pirone, R.; Fino, D. Cerium-copper oxides prepared by solution combustion synthesis for total oxidation reactions: From powder catalysts to structured reactors. *Appl. Catal. B Environ.* **2017**, *205*, 455–468, doi:10.1016/j.apcatb.2016.12.054.
163. Gao, Y.; Wu, X.; Liu, S.; Weng, D.; Ran, R. MnO_x–CeO_2 mixed oxides for diesel soot oxidation: a review. *Catal. Surv. from Asia* **2018**, *22*, 230–240, doi:10.1007/s10563-018-9255-4.
164. Kappis, K.; Papadopoulos, C.; Papavasiliou, J.; Vakros, J.; Georgiou, Y.; Deligiannakis, Y.; Avgouropoulos, G. Tuning the catalytic properties of copper-promoted nanoceria via a hydrothermal method. *Catalysts* **2019**, *9*, doi:10.3390/catal9020138.
165. Venkataswamy, P.; Jampaiah, D.; Mukherjee, D.; Aniz, C.U.; Reddy, B.M. Mn-doped Ceria Solid Solutions for CO Oxidation at Lower Temperatures. *Catal. Letters* **2016**, *146*, 2105–2118, doi:10.1007/s10562-016-1811-9.
166. Zhao, F.; Li, S.; Wu, X.; Yue, R.; Li, W.; Chen, Y. Synergetic effect over flame-made manganese doped CuO-CeO_2 nanocatalyst for enhanced CO oxidation performance. *RSC Adv.* **2019**, *9*, 2343–2352, doi:10.1039/c8ra09626k.
167. Konsolakis, M.; Sgourakis, M.; Carabineiro, S.A.C. Surface and redox properties of cobalt-ceria binary oxides: On the effect of Co content and pretreatment conditions. *Appl. Surf. Sci.* **2015**, *341*, 48–54, doi:10.1016/j.apsusc.2015.02.188.
168. Sudarsanam, P.; Hillary, B.; Amin, M.H.; Rockstroh, N.; Bentrup, U.; Brückner, A.; Bhargava, S.K. Heterostructured Copper-Ceria and Iron-Ceria Nanorods: Role of Morphology, Redox, and Acid Properties in Catalytic Diesel Soot Combustion. *Langmuir* **2018**, *34*, 2663–2673, doi:10.1021/acs.langmuir.7b03998.
169. Shen, Q.; Lu, G.; Du, C.; Guo, Y.; Wang, Y.; Guo, Y.; Gong, X. Role and reduction of NO_x in the catalytic combustion of soot over iron-ceria mixed oxide catalyst. *Chem. Eng. J.* **2013**, *218*, 164–172, doi:10.1016/j.cej.2012.12.010.
170. Devaiah, D.; Reddy, L.H.; Park, S.E.; Reddy, B.M. Ceria–zirconia mixed oxides: Synthetic methods and applications. *Catal. Rev. - Sci. Eng.* **2018**, *60*, 177–277, doi:10.1080/01614940.2017.1415058.
171. Park, C.S.; Lee, M.W.; Lee, J.H.; Jeong, E.J.; Lee, S.H.; Choung, J.W.; Kim, C.H.; Ham, H.C.; Lee, K.Y. Promoting effect of H_2O over macroporous Ce-Zr catalysts in soot oxidation. *Mol. Catal.* **2019**, *474*, 110416, doi:10.1016/j.mcat.2019.110416.
172. Aneggi, E.; De Leitenburg, C.; Llorca, J.; Trovarelli, A. Higher activity of Diesel soot oxidation over polycrystalline ceria and ceria-zirconia solid solutions from more reactive surface planes. *Catal. Today* **2012**, *197*, 119–126, doi:10.1016/j.cattod.2012.07.030.
173. Liu, S.; Wu, X.; Weng, D.; Ran, R. Ceria-based catalysts for soot

oxidation: A review. *J. Rare Earths* **2015**, *33*, 567–590, doi:10.1016/S1002-0721(14)60457-9.
174. Li, P.; Chen, X.; Li, Y.; Schwank, J.W. A review on oxygen storage capacity of CeO_2-based materials: Influence factors, measurement techniques, and applications in reactions related to catalytic automotive emissions control. *Catal. Today* **2019**, *327*, 90–115, doi:10.1016/j.cattod.2018.05.059.
175. Kim, H.J.; Jang, M.G.; Shin, D.; Han, J.W. Design of Ceria Catalysts for Low-Temperature CO Oxidation. *ChemCatChem* **2020**, *12*, 11–26, doi:10.1002/cctc.201901787.
176. Kim, K.; Han, J.W. Mechanistic study for enhanced CO oxidation activity on (Mn,Fe) co-doped CeO_2(111). *Catal. Today* **2017**, *293–294*, 82–88, doi:10.1016/j.cattod.2016.11.046.
177. Di Sarli, V.; Landi, G.; Lisi, L.; Saliva, A.; Di Benedetto, A. Catalytic diesel particulate filters with highly dispersed ceria: Effect of the soot-catalyst contact on the regeneration performance. *Appl. Catal. B Environ.* **2016**, *197*, 116–124, doi:10.1016/j.apcatb.2016.01.073.
178. Bueno-López, A. Diesel soot combustion ceria catalysts. *Appl. Catal. B Environ.* **2014**, *146*, 1–11, doi:10.1016/j.apcatb.2013.02.033.
179. Aneggi, E.; de Leitenburg, C.; Dolcetti, G.; Trovarelli, A. Diesel soot combustion activity of ceria promoted with alkali metals. *Catal. Today* **2008**, *136*, 3–10, doi:10.1016/j.cattod.2008.01.002.
180. Weng, D.; Li, J.; Wu, X.; Lin, F. Promotional effect of potassium on soot oxidation activity and SO_2-poisoning resistance of Cu/CeO_2 catalyst. *Catal. Commun.* **2008**, *9*, 1898–1901, doi:10.1016/j.catcom.2008.03.010.
181. Neyertz, C.A.; Miró, E.E.; Querini, C.A. K/CeO_2 catalysts supported on cordierite monoliths: Diesel soot combustion study. *Chem. Eng. J.* **2012**, *181–182*, 93–102, doi:10.1016/j.cej.2011.11.010.
182. Blanchard, G.; Seguelong, T.; Michelin, J.; Schuerholz, S.; Terres, F. Ceria-based fuel-borne catalysts for series diesel particulate filter regeneration. *SAE Tech. Pap.* **2003**, doi:10.4271/2003-01-0378.
183. Lacarriere, A.; Seguelong, T.; Spivey, D.; Das, A. The Fuel-Borne Catalyst Approach: A Cost-Effective and Robust Solution to Address the Requirements of BS-VI for Diesel Vehicles. *SAE Tech. Pap.* **2017**, *2017-Janua*, doi:10.4271/2017-26-0127.
184. Miceli, P.; Bensaid, S.; Russo, N.; Fino, D. CeO_2-based catalysts with engineered morphologies for soot oxidation to enhance soot-catalyst contact. *Nanoscale Res. Lett.* **2014**, *9*, 1–10, doi:10.1186/1556-276X-9-254.
185. Piumetti, M.; van der Linden, B.; Makkee, M.; Miceli, P.; Fino, D.; Russo, N.; Bensaid, S. Contact dynamics for a solid-solid reaction mediated by gas-phase oxygen: Study on the soot oxidation over ceria-based catalysts. *Appl. Catal. B Environ.* **2016**, *199*, 96–107, doi:10.1016/j.apcatb.2016.06.006.
186. Soler, L.; Casanovas, A.; Escudero, C.; Pérez-Dieste, V.; Aneggi, E.; Trovarelli, A.; Llorca, J. Ambient pressure photoemission spectroscopy reveals the mechanism of carbon soot oxidation in ceria-based catalysts. *ChemCatChem* **2016**, *8*, 2748–2751, doi:10.1002/cctc.201600615.
187. Andana, T.; Piumetti, M.; Bensaid, S.; Russo, N.; Fino, D.; Pirone, R. CO and Soot Oxidation over Ce-Zr-Pr Oxide Catalysts. *Nanoscale Res. Lett.* **2016**, *11*, 1–9, doi:10.1186/s11671-016-1494-6.

188. Andana, T.; Piumetti, M.; Bensaid, S.; Russo, N.; Fino, D.; Pirone, R. Nanostructured ceria-praseodymia catalysts for diesel soot combustion. *Appl. Catal. B Environ.* **2016**, *197*, 125–137, doi:10.1016/j.apcatb.2015.12.030.
189. He, H.; Lin, X.; Li, S.; Wu, Z.; Gao, J.; Wu, J.; Wen, W.; Ye, D.; Fu, M. The key surface species and oxygen vacancies in MnO_x(0.4)-CeO_2 toward repeated soot oxidation. *Appl. Catal. B Environ.* **2018**, *223*, 134–142, doi:10.1016/j.apcatb.2017.08.084.
190. Lin, X.; Li, S.; He, H.; Wu, Z.; Wu, J.; Chen, L.; Ye, D.; Fu, M. Evolution of oxygen vacancies in MnO_x-CeO_2 mixed oxides for soot oxidation. *Appl. Catal. B Environ.* **2018**, *223*, 91–102, doi:10.1016/j.apcatb.2017.06.071.
191. Liu, S.; Wu, X.; Tang, J.; Cui, P.; Jiang, X.; Chang, C.; Liu, W.; Gao, Y.; Li, M.; Weng, D. An exploration of soot oxidation over CeO_2-ZrO_2 nanocubes: Do more surface oxygen vacancies benefit the reaction? *Catal. Today* **2017**, *281*, 454–459, doi:10.1016/j.cattod.2016.05.036.
192. Liu, S.; Wu, X.; Liu, W.; Chen, W.; Ran, R.; Li, M.; Weng, D. Soot oxidation over CeO_2 and Ag/CeO_2: Factors determining the catalyst activity and stability during reaction. *J. Catal.* **2016**, *337*, 188–198, doi:10.1016/j.jcat.2016.01.019.
193. Hernández-Giménez, A.M.; Lozano-Castelló, D.; Bueno-López, A. Effect of CO_2, H_2O and SO_2 in the ceria-catalyzed combustion of soot under simulated diesel exhaust conditions. *Appl. Catal. B Environ.* **2014**, *148–149*, 406–414, doi:10.1016/j.apcatb.2013.11.029.
194. Aneggi, E.; Llorca, J.; de Leitenburg, C.; Dolcetti, G.; Trovarelli, A. Soot combustion over silver-supported catalysts. *Appl. Catal. B Environ.* **2009**, *91*, 489–498, doi:10.1016/j.apcatb.2009.06.019.
195. Xu, J.; Lu, G.; Guo, Y.; Guo, Y.; Gong, X.Q. A highly effective catalyst of Co-CeO_2 for the oxidation of diesel soot: The excellent NO oxidation activity and NO_x storage capacity. *Appl. Catal. A Gen.* **2017**, *535*, 1–8, doi:10.1016/j.apcata.2017.02.005.
196. Gao, Y.; Wu, X.; Liu, S.; Weng, D.; Ran, R. Effect of water vapor on sulfur poisoning of MnO_X-CeO_2/Al_2O_3 catalyst for diesel soot oxidation. *RSC Adv.* **2016**, *6*, 57033–57040, doi:10.1039/c6ra09241a.
197. Atribak, I.; Azambre, B.; Bueno López, A.; García-García, A. Effect of NO_x adsorption/desorption over ceria-zirconia catalysts on the catalytic combustion of model soot. *Appl. Catal. B Environ.* **2009**, *92*, 126–137, doi:10.1016/j.apcatb.2009.07.015.
198. Azambre, B.; Collura, S.; Darcy, P.; Trichard, J.M.; Da Costa, P.; García-García, A.; Bueno-López, A. Effects of a Pt/$Ce_{0.68}Zr_{0.32}O_2$ catalyst and NO_2 on the kinetics of diesel soot oxidation from thermogravimetric analyses. *Fuel Process. Technol.* **2011**, *92*, 363–371, doi:10.1016/j.fuproc.2010.09.029.
199. Andana, T.; Piumetti, M.; Bensaid, S.; Russo, N.; Fino, D. Heterogeneous mechanism of NO_x-assisted soot oxidation in the passive regeneration of a bench-scale diesel particulate filter catalyzed with nanostructured equimolar ceria-praseodymia. *Appl. Catal. A, Gen.* **2019**, *583*, 117136, doi:10.1016/j.apcata.2019.117136.
200. Zhang, H.; Yuan, S.; Wang, J.L.; Gong, M.C.; Chen, Y. Effects of contact model and NO_x on soot oxidation activity over Pt/MnO_x-CeO_2 and the reaction mechanisms. *Chem. Eng. J.* **2017**, *327*, 1066–1076, doi:10.1016/j.cej.2017.06.013.

201. Agarwal, S.; Zhu, X.; Hensen, E.J.M.; Lefferts, L.; Mojet, B.L. Defect chemistry of ceria nanorods. *J. Phys. Chem. C* **2014**, *118*, 4131–4142, doi:10.1021/jp409989y.
202. Sullivan, J.A.; Dulgheru, P.; Atribak, I.; Bueno-López, A.; García-García, A. Attempts at an in situ Raman study of ceria/zirconia catalysts in PM combustion. *Appl. Catal. B Environ.* **2011**, *108–109*, 134–139, doi:10.1016/j.apcatb.2011.08.018.
203. Sartoretti, E.; Novara, C.; Giorgis, F.; Piumetti, M.; Bensaid, S.; Russo, N.; Fino, D. In situ Raman analyses of the soot oxidation reaction over nanostructured ceria-based catalysts. *Sci. Rep.* **2019**, *9*, 3875, doi:10.1038/s41598-019-39105-5.
204. Schilling, C.; Hess, C. Real-Time Observation of the Defect Dynamics in Working Au/CeO_2 Catalysts by Combined Operando Raman/UV-Vis Spectroscopy. *J. Phys. Chem. C* **2018**, *122*, 2909–2917, doi:10.1021/acs.jpcc.8b00027.
205. Perkowitz, S. *Optical Characterization of Semiconductors: Infrared, Raman, and Photoluminescence Spectroscopy*; Academic Press, **1993**; ISBN 0125507704.
206. Taylor, P.; Loudon, R. *The Raman effect in crystals*; **1964**; ISBN 0001873640010.
207. Piumetti, M.; Bensaid, S.; Andana, T.; Dosa, M.; Novara, C.; Giorgis, F.; Russo, N.; Fino, D. Nanostructured Ceria-Based Materials: Effect of the Hydrothermal Synthesis Conditions on the Structural Properties and Catalytic Activity. *Catalysts* **2017**, *7*, 174, doi:10.3390/catal7060174.
208. Mai, H.X.; Sun, L.D.; Zhang, Y.W.; Si, R.; Feng, W.; Zhang, H.P.; Liu, H.C.; Yan, C.H. Shape-selective synthesis and oxygen storage behavior of ceria nanopolyhedra, nanorods, and nanocubes. *J. Phys. Chem. B* **2005**, *109*, 24380–24385, doi:10.1021/jp055584b.
209. Uvarov, V.; Popov, I. Metrological characterization of X-ray diffraction methods for determination of crystallite size in nano-scale materials. *Mater. Charact.* **2007**, *58*, 883–891, doi:10.1016/j.matchar.2006.09.002.
210. Naderi, M. Surface Area: Brunauer-Emmett-Teller (BET). In *Progress in Filtration and Separation*; Elsevier Ltd, **2015**; pp. 585–608 ISBN 9780123983077.
211. Barrett, E.P.; Joyner, L.G.; Halenda, P.P. The determination of pore volume and area distributions in porous substances. I. Computations from nitrogen isotherms. *J. Am. Chem. Soc.* **1951**, *73*, 373–380.
212. Sartoretti, E.; Novara, C.; Fontana, M.; Giorgis, F.; Piumetti, M.; Bensaid, S.; Russo, N.; Fino, D. New insights on the defect sites evolution during CO oxidation over doped ceria nanocatalysts probed by in situ Raman spectroscopy. *Appl. Catal. A Gen.* **2020**, *596*, 117517, doi:10.1016/j.apcata.2020.117517.
213. Trovarelli, A.; de Leitenburg, C.; Boaro, M.; Dolcetti, G. The utilization of ceria in industrial catalysis. *Catal. Today* **1999**, *50*, 353–367, doi:10.1016/S0920-5861(98)00515-X.
214. Andana, T.; Piumetti, M.; Bensaid, S.; Veyre, L.; Thieuleux, C.; Russo, N.; Fino, D.; Quadrelli, E.A.; Pirone, R. Ceria-supported small Pt and Pt_3Sn nanoparticles for NO_x-assisted soot oxidation. *Appl. Catal. B Environ.* **2017**, *209*, 295–310, doi:10.1016/j.apcatb.2017.03.010.
215. Piumetti, M.; Andana, T.; Bensaid, S.; Russo, N.; Fino, D.; Pirone, R. Study on the CO Oxidation over Ceria-Based Nanocatalysts. *Nanoscale*

Res. Lett. **2016**, *11*, 165, doi:10.1186/s11671-016-1375-z.
216. Salzberg, H.W. *Thomas,Jm - Introduction to Principles of Heterogeneous Catalysis*; Academic Press, **1967**; Vol. 114; ISBN 0013-4651.
217. Sahoo, T.R.; Armandi, M.; Arletti, R.; Piumetti, M.; Bensaid, S.; Manzoli, M.; Panda, S.R.; Bonelli, B. Pure and Fe-doped CeO_2 nanoparticles obtained by microwave assisted combustion synthesis: Physico-chemical properties ruling their catalytic activity towards CO oxidation and soot combustion. *Appl. Catal. B Environ.* **2017**, *211*, 31–45, doi:10.1016/j.apcatb.2017.04.032.
218. Gamarra, D.; Munuera, G.; Hungría, A.B.; Fernández-García, M.; Conesa, J.C.; Midgley, P.A.; Wang, X.Q.; Hanson, J.C.; Rodríguez, J.A.; Martínez-Arias, A. Structure-activity relationship in nanostructured copper-ceria-based preferential CO oxidation catalysts. *J. Phys. Chem. C* **2007**, *111*, 11026–11038, doi:10.1021/jp072243k.
219. Rao, K.N.; Venkataswamy, P.; Reddy, B.M. Structural characterization and catalytic evaluation of supported copper-ceria catalysts for soot oxidation. *Ind. Eng. Chem. Res.* **2011**, *50*, 11960–11969, doi:10.1021/ie201474p.
220. Mai, H.X.; Sun, L.D.; Zhang, Y.W.; Si, R.; Feng, W.; Zhang, H.P.; Liu, H.C.; Yan, C.H. Shape-selective synthesis and oxygen storage behavior of ceria nanopolyhedra, nanorods, and nanocubes. *J. Phys. Chem. B* **2005**, *109*, 24380–24385, doi:10.1021/jp055584b.
221. Agarwal, S.; Lefferts, L.; Mojet, B.L.; Ligthart, D.A.J.M.; Hensen, E.J.M.; Mitchell, D.R.G.; Erasmus, W.J.; Anderson, B.G.; Olivier, E.J.; Neethling, J.H.; et al. Exposed surfaces on shape-controlled ceria nanoparticles revealed through AC-TEM and water-gas shift reactivity. *ChemSusChem* **2013**, *6*, 1898–1906, doi:10.1002/cssc.201300651.
222. Shannon, R.D. Revised effective ionic radii and systematic studies of interatomic distances in halides and chalcogenides. *Acta Crystallogr. Sect. A* **1976**, *32*, 751–767, doi:10.1107/S0567739476001551.
223. Chen, D.; He, D.; Lu, J.; Zhong, L.; Liu, F.; Liu, J.; Yu, J.; Wan, G.; He, S.; Luo, Y. Investigation of the role of surface lattice oxygen and bulk lattice oxygen migration of cerium-based oxygen carriers: XPS and designed H_2-TPR characterization. *Appl. Catal. B Environ.* **2017**, *218*, 249–259, doi:10.1016/j.apcatb.2017.06.053.
224. Piumetti, M.; Bensaid, S.; Fino, D.; Russo, N. Nanostructured ceria-zirconia catalysts for CO oxidation: Study on surface properties and reactivity. *Appl. Catal. B Environ.* **2016**, *197*, 35–46, doi:10.1016/j.apcatb.2016.02.023.
225. Hu, Z.; Liu, X.; Meng, D.; Guo, Y.; Guo, Y.; Lu, G. Effect of Ceria Crystal Plane on the Physicochemical and Catalytic Properties of Pd/Ceria for CO and Propane Oxidation. *ACS Catal.* **2016**, *6*, 2265–2279, doi:10.1021/acscatal.5b02617.
226. Nakajima, A.; Yoshihara, A.; Ishigame, M. Defect-induced Raman spectra in doped CeO_2. *Phys. Rev. B* **1994**, *50*, 13297.
227. Vinodkumar, T.; Rao, B.G.; Reddy, B.M. Influence of isovalent and aliovalent dopants on the reactivity of cerium oxide for catalytic applications. *Catal. Today* **2015**, *253*, 57–64, doi:10.1016/j.cattod.2015.01.044.
228. Lee, Y.; He, G.; Akey, A.J.; Si, R.; Flytzani-Stephanopoulos, M.; Herman, I.P. Raman analysis of mode softening in nanoparticle $CeO_{2-\delta}$ and Au-$CeO_{2-\delta}$ during CO oxidation. *J. Am. Chem. Soc.* **2011**, *133*, 12952–12955,

doi:10.1021/ja204479j.
229. Acharya, S.A.; Gaikwad, V.M.; D'Souza, S.W.; Barman, S.R. Gd/Sm dopant-modified oxidation state and defect generation in nano-ceria. *Solid State Ionics* **2014**, *260*, 21–29, doi:10.1016/j.ssi.2014.03.008.
230. Li, L.; Chen, F.; Lu, J.-Q.; Luo, M.-F. Study of defect sites in $Ce_{1-x}M_xO_{2-\delta}$ (x = 0.2) solid solutions using Raman spectroscopy. *J. Phys. Chem. A* **2011**, *115*, 7972–7, doi:10.1021/jp203921m.
231. Andriopoulou, C.; Trimpalis, A.; Petallidou, K.C.; Sgoura, A.; Efstathiou, A.M.; Boghosian, S. Structural and Redox Properties of $Ce_{1-x}Zr_xO_{2-\delta}$ and $Ce_{0.8}Zr_{0.15}RE_{0.05}O_{2-\delta}$ (RE: La, Nd, Pr, Y) Solids Studied by High Temperature in Situ Raman Spectroscopy. *J. Phys. Chem. C* **2017**, *121*, 7931–7943, doi:10.1021/acs.jpcc.7b00515.
232. Pu, Z.-Y.; Liu, X.-S.; Jia, A.-P.; Xie, Y.-L.; Lu, J.-Q.; Luo, M.-F. Enhanced Activity for CO Oxidation over Pr- and Cu-Doped CeO_2 Catalysts: Effect of Oxygen Vacancies. *J. Phys. Chem. C* **2008**, *112*, 15045–15051, doi:10.1021/jp805389k.
233. Agarwal, S.; Lefferts, L.; Mojet, B.L. Ceria Nanocatalysts: Shape Dependent Reactivity and Formation of OH. *ChemCatChem* **2013**, *5*, 479–489, doi:10.1002/cctc.201200491.
234. Paunović, N.; Dohčević-Mitrović, Z.; Scurtu, R.; Aškrabić, S.; Prekajski, M.; Matović, B.; Popović, Z. V. Suppression of inherent ferromagnetism in Pr-doped CeO_2 nanocrystals. *Nanoscale* **2012**, *4*, 5469, doi:10.1039/c2nr30799e.
235. Taniguchi, T.; Watanabe, T.; Sugiyama, N.; Subramani, A.K.; Wagata, H.; Matsushita, N.; Yoshimura, M. Identifying defects in ceria-based nanocrystals by UV resonance Raman spectroscopy. *J. Phys. Chem. C* **2009**, *113*, 19789–19793, doi:10.1021/jp9049457.
236. Filtschew, A.; Hofmann, K.; Hess, C. Ceria and Its Defect Structure: New Insights from a Combined Spectroscopic Approach. *J. Phys. Chem. C* **2016**, *120*, 6694–6703, doi:10.1021/acs.jpcc.6b00959.
237. Spanier, J.E.; Robinson, R.D.; Zhang, F.; Chan, S.-W.; Herman, I.P. Size-dependent properties of CeO_{2-y} nanoparticles as studied by Raman scattering. *Phys. Rev. B* **2001**, *64*, 245407, doi:10.1103/PhysRevB.64.245407.
238. Wu, Z.; Li, M.; Howe, J.; Meyer, H.M.; Overbury, S.H. Probing defect sites on CeO_2 nanocrystals with well-defined surface planes by raman spectroscopy and O_2 adsorption. *Langmuir* **2010**, *26*, 16595–16606, doi:10.1021/la101723w.
239. Chen, S.; Li, L.; Hu, W.; Huang, X.; Li, Q.; Xu, Y.; Zuo, Y.; Li, G. Anchoring High-Concentration Oxygen Vacancies at Interfaces of CeO_{2-x}/Cu toward Enhanced Activity for Preferential CO Oxidation. *ACS Appl. Mater. Interfaces* **2015**, *7*, 22999–23007, doi:10.1021/acsami.5b06302.
240. McBride, J.R.; Hass, K.C.; Poindexter, B.D.; Weber, W.H. Raman and x-ray studies of $Ce_{1-x}RE_xO_{2-y}$, where RE=La, Pr, Nd, Eu, Gd, and Tb. *J. Appl. Phys.* **1994**, *76*, 2435–2441, doi:10.1063/1.357593.
241. Konsolakis, M. The role of Copper–Ceria interactions in catalysis science: Recent theoretical and experimental advances. *Appl. Catal. B Environ.* **2016**, *198*, 49–66, doi:10.1016/j.apcatb.2016.05.037.
242. Li, Y.; Wei, Z.; Gao, F.; Kovarik, L.; Baylon, R.A.L.; Peden, C.H.F.; Wang, Y. Effect of Oxygen Defects on the Catalytic Performance of VO_x

/CeO_2 Catalysts for Oxidative Dehydrogenation of Methanol. *ACS Catal.* **2015**, *5*, 3006–3012, doi:10.1021/cs502084g.
243. Lykaki, M.; Pachatouridou, E.; Carabineiro, S.A.C.; Iliopoulou, E.; Andriopoulou, C.; Kallithrakas-Kontos, N.; Boghosian, S.; Konsolakis, M. Ceria nanoparticles shape effects on the structural defects and surface chemistry: Implications in CO oxidation by Cu/CeO_2 catalysts. *Appl. Catal. B Environ.* **2018**, *230*, 18–28, doi:10.1016/j.apcatb.2018.02.035.
244. Da Silva, A.N.; Pinto, R.C.F.; Freire, P.T.C.; Junior, J.A.L.; Oliveira, A.C.; Filho, J.M. Temperature and high pressure effects on the structural features of catalytic nanocomposites oxides by Raman spectroscopy. *Spectrochim. Acta - Part A Mol. Biomol. Spectrosc.* **2015**, *138*, 763–773, doi:10.1016/j.saa.2014.11.081.
245. Elias, J.S.; Stoerzinger, K.A.; Hong, W.T.; Risch, M.; Giordano, L.; Mansour, A.N.; Shao-Horn, Y. In situ spectroscopy and mechanistic insights into CO oxidation on transition-metal-substituted ceria nanoparticles. *ACS Catal.* **2017**, *7*, 6843–6857, doi:10.1021/acscatal.7b01600.
246. Sadezky, A.; Muckenhuber, H.; Grothe, H.; Niessner, R.; Pöschl, U. Raman microspectroscopy of soot and related carbonaceous materials: Spectral analysis and structural information. *Carbon N. Y.* **2005**, *43*, 1731–1742, doi:10.1016/j.carbon.2005.02.018.
247. Saffaripour, M.; Tay, L.L.; Thomson, K.A.; Smallwood, G.J.; Brem, B.T.; Durdina, L.; Johnson, M. Raman spectroscopy and TEM characterization of solid particulate matter emitted from soot generators and aircraft turbine engines. *Aerosol Sci. Technol.* **2017**, *51*, 518–531, doi:10.1080/02786826.2016.1274368.
248. Guo, M.; Lu, J.; Wu, Y.; Wang, Y.; Luo, M. UV and visible Raman studies of oxygen vacancies in rare-earth-doped ceria. *Langmuir* **2011**, *27*, 3872–3877, doi:10.1021/la200292f.
249. Mamontov, E.; Egami, T.; Pennsyl, V.; Brezny, R.; Koranne, M.; Grace, W.R.; Grace, C.; Da, V.; Tyagi, S. Lattice Defects and Oxygen Storage Capacity of Nanocrystalline Ceria and Ceria-Zirconia. *J. Phys. Chem. B* **2000**, *104*, 11110–11116, doi:10.1021/jp0023011.
250. Pushkarev, V. V.; Kovalchuk, V.I.; D'Itri, J.L. Probing Defect Sites on the CeO_2 Surface with Dioxygen. *J. Phys. Chem. B* **2004**, *108*, 5341–5348, doi:10.1021/jp0311254.
251. Lohrenscheit, M.; Hess, C. Direct Evidence for the Participation of Oxygen Vacancies in the Oxidation of Carbon Monoxide over Ceria-Supported Gold Catalysts by using Operando Raman Spectroscopy. *ChemCatChem* **2016**, *8*, 523–526, doi:10.1002/cctc.201501129.
252. Zhang, Z.; Jiang, Z.; Shangguan, W. Low-temperature catalysis for VOCs removal in technology and application: A state-of-the-art review. *Catal. Today* **2016**, *264*, 270–278, doi:10.1016/j.cattod.2015.10.040.
253. Osgood, H.; Devaguptapu, S. V.; Xu, H.; Cho, J.; Wu, G. Transition metal (Fe, Co, Ni, and Mn) oxides for oxygen reduction and evolution bifunctional catalysts in alkaline media. *Nano Today* **2016**, *11*, 601–625, doi:10.1016/J.NANTOD.2016.09.001.
254. Zhao, Y.; Teng, B.T.; Wen, X.D.; Zhao, Y.; Chen, Q.P.; Zhao, L.H.; Luo, M.F. Superoxide and peroxide species on CeO_2(111), and their oxidation roles. *J. Phys. Chem. C* **2012**, *116*, 15986–15991, doi:10.1021/jp3016326.
255. Wang, L.; Yu, Y.; He, H.; Zhang, Y.; Qin, X.; Wang, B. Oxygen vacancy

clusters essential for the catalytic activity of CeO_2 nanocubes for o-xylene oxidation. *Sci. Rep.* **2017**, *7*, 1–11, doi:10.1038/s41598-017-13178-6.
256. Papadopoulos, C.; Kappis, K.; Papavasiliou, J.; Vakros, J.; Kuśmierz, M.; Gac, W.; Georgiou, Y.; Deligiannakis, Y.; Avgouropoulos, G. Copper-promoted ceria catalysts for CO oxidation reaction. *Catal. Today* **2019**, 1–7, doi:10.1016/j.cattod.2019.06.078.
257. Artini, C.; Pani, M.; Carnasciali, M.M.; Buscaglia, M.T.; Plaisier, J.R.; Costa, G.A. Structural features of Sm- and Gd-doped ceria studied by synchrotron X-ray diffraction and μ-Raman spectroscopy. *Inorg. Chem.* **2015**, *54*, 4126–4137, doi:10.1021/acs.inorgchem.5b00395.
258. Silva, I.D.C.; Sigoli, F.A.; Mazali, I.O. Reversible Oxygen Vacancy Generation on Pure CeO_2 Nanorods Evaluated by in Situ Raman Spectroscopy. *J. Phys. Chem. C* **2017**, *121*, 12928–12935, doi:10.1021/acs.jpcc.7b03155.
259. Agarwal, S.; Zhu, X.; Hensen, E.J.M.; Mojet, B.L.; Lefferts, L. Surface-Dependence of Defect Chemistry of Nanostructured Ceria. *J. Phys. Chem. C* **2015**, *119*, 12423–12433, doi:10.1021/acs.jpcc.5b02389.
260. Li, L.; Chen, F.; Lu, J.-Q.; Luo, M.-F. Study of defect sites in $Ce_{1-x}M_xO_{2-\delta}$ (x = 0.2) solid solutions using Raman spectroscopy. *J. Phys. Chem. A* **2011**, *115*, 7972–7, doi:10.1021/jp203921m.
261. Polychronopoulou, K.; Zedan, A.F.; AlKetbi, M.; Stephen, S.; Ather, M.; Katsiotis, M.S.; Arvanitidis, J.; Christofilos, D.; Isakovic, A.F.; AlHassan, S. Tailoring the efficiency of an active catalyst for CO abatement through oxidation reaction: The case study of samarium-doped ceria. *J. Environ. Chem. Eng.* **2018**, *6*, 266–280, doi:10.1016/j.jece.2017.12.001.
262. Zhu, H.; Chen, Y.; Wang, Z.; Liu, W.; Wang, L. Catalytic oxidation of CO over mesoporous copper-doped ceria catalysts via a facile CTAB-assisted synthesis. *RCS Adv.* **2018**, 14888–14897, doi:10.1039/c8ra02327a.
263. Bera, P.; Lo, A.; Horne, A.; Martı, A. Comparative in Situ DRIFTS-MS Study of 12 CO- and 13 CO-TPR on CuO/CeO_2 Catalyst. **2009**, 10689–10695.
264. Schaffer, H.E.; Chance, R.R.; Silbey, R.J.; Knoll, K.; Schrock, R.R. Conjugation length dependence of Raman scattering in a series of linear polyenes: Implications for polyacetylene. *J. Chem. Phys.* **1991**, *94*, 4161–4170, doi:10.1063/1.460649.
265. Fernandes, R.F.; Maia, L.F.; Couri, M.R.C.; Costa, L.A.S.; De Oliveira, L.F.C. Raman spectroscopy as a tool in differentiating conjugated polyenes from synthetic and natural sources. *Spectrochim. Acta - Part A Mol. Biomol. Spectrosc.* **2015**, *134*, 434–441, doi:10.1016/j.saa.2014.06.022.
266. Swanson, M.; Pushkarev, V. V.; Kovalchuk, V.I.; D 'itri, J.L.; D'itri, J.L. The dynamic surface chemistry during the interaction of CO with ceria captured by Raman spectroscopy. *Catal. Letters* **2007**, *116*, 41–45, doi:10.1007/s10562-007-9087-8.
267. Böller, B.; Durner, K.M.; Wintterlin, J. The active sites of a working Fischer–Tropsch catalyst revealed by operando scanning tunnelling microscopy. *Nat. Catal.* **2019**, doi:10.1038/s41929-019-0360-1.
268. Kopelent, R.; Van Bokhoven, J.A.; Szlachetko, J.; Edebeli, J.; Paun, C.; Nachtegaal, M.; Safonova, O. V. Catalytically Active and Spectator Ce^{3+} in Ceria-Supported Metal Catalysts. *Angew. Chemie - Int. Ed.* **2015**, *54*, 8728–8731, doi:10.1002/anie.201503022.
269. Xiangwen, L.; Kebin, Z.; Lei, W.; Baoyi, W.; Yadong, L. Oxygen vacancy

clusters promoting reducibility and activity of ceria nanorods. *J. Am. Chem. Soc.* **2009**, *131*, 3140–3141.
270. Wang, H.; Luo, S.; Zhang, M.; Liu, W.; Wu, X.; Liu, S. Roles of oxygen vacancy and O_x^- in oxidation reactions over CeO_2 and Ag/CeO_2 nanorod model catalysts. *J. Catal.* **2018**, *368*, 365–378, doi:10.1016/j.jcat.2018.10.018.
271. Pal, S.; Gogurla, N.; Das, A.; Singha, S.S.; Kumar, P.; Kanjilal, D.; Singha, A.; Chattopadhyay, S.; Jana, D.; Sarkar, A. Clustered vacancies in ZnO: Chemical aspects and consequences on physical properties. *J. Phys. D. Appl. Phys.* **2018**, *51*, doi:10.1088/1361-6463/aaa992.
272. Kappis, K.; Papavasiliou, J. Influence of the Hydrothermal Parameters on the Physicochemical Characteristics of Cu−Ce Oxide Nanostructures. *ChemCatChem* **2019**, *11*, 4765–4776, doi:10.1002/cctc.201901108.
273. Li, J.; Singh, U.G.; Bennett, J.W.; Page, K.; Weaver, J.C.; Zhang, J.; Proffen, T.; Rappe, A.M.; Scott, S.; Seshadri, R. $BaCe_{1-x}Pd_xO_{3-\delta}$ ($0 \leq x \leq 0.1$): Redox Controlled Ingress and Egress of Palladium in a Perovskite. *Chem. Mater.* **2007**, *19*, 1418–1426.
274. Sartoretti, E.; Martini, F.; Piumetti, M.; Bensaid, S.; Russo, N.; Fino, D. Nanostructured Equimolar Ceria-Praseodymia for Total Oxidations in Low-O_2 Conditions. *Catalysts* **2020**, *10*, 1–16, doi:10.3390/catal10020165.
275. Ramos, M.J.M.G.; Wallace, J.S. Fuel Effects on Particulate Matter Emissions Variability from a Gasoline Direct Injection Engine. *SAE Tech. Pap. Ser.* **2018**, 1–17, doi:10.4271/2018-01-0355.Abstract.
276. Guillén-Hurtado, N.; García-García, A.; Bueno-López, A. Active oxygen by Ce-Pr mixed oxide nanoparticles outperform diesel soot combustion Pt catalysts. *Appl. Catal. B Environ.* **2015**, *174–175*, 60–66, doi:10.1016/j.apcatb.2015.02.036.
277. Konsolakis, M.; Carabineiro, S.A.C.; Marnellos, G.E.; Asad, M.F.; Soares, O.S.G.P.; Pereira, M.F.R.; Órfão, J.J.M.; Figueiredo, J.L. Volatile organic compounds abatement over copper-based catalysts: Effect of support. *Inorganica Chim. Acta* **2017**, *455*, 473–482, doi:10.1016/j.ica.2016.07.059.
278. Pappacena, A.; Rancan, M.; Armelao, L.; Llorca, J.; Ge, W.; Ye, B.; Lucotti, A.; Trovarelli, A.; Boaro, M. New Insights into the Dynamics That Control the Activity of Ceria-Zirconia Solid Solutions in Thermochemical Water Splitting Cycles. *J. Phys. Chem. C* **2017**, *121*, 17746–17755, doi:10.1021/acs.jpcc.7b06043.
279. Husak, T.; Hernández, S.; Gionco, C.; Tolod, K.R.; Russo, N.; Muñoz-Tabares, J.A.; Giamello, E.; Castellino, M.; Paganini, M.C. Insights Into the Sunlight-Driven Water Oxidation by Ce and Er-Doped ZrO_2. *Front. Chem.* **2018**, *6*, doi:10.3389/fchem.2018.00368.
280. Poggio-Fraccari, E.; Baronetti, G.; Mariño, F. Pr^{3+} surface fraction in CePr mixed oxides determined by XPS analysis. *J. Electron Spectros. Relat. Phenomena* **2018**, *222*, 1–4, doi:10.1016/j.elspec.2017.11.003.
281. Piumetti, M.; Andana, T.; Bensaid, S.; Fino, D.; Russo, N.; Pirone, R. Ceria-based nanomaterials as catalysts for CO oxidation and soot combustion: Effect of Zr-Pr doping and structural properties on the catalytic activity. *AIChE J.* **2017**, *63*, 216–225, doi:10.1002/aic.15548.
282. Jin, J.; Li, C.; Tsang, C.W.; Xu, B.; Liang, C. Catalytic combustion of methane over Pd/Ce-Zr oxides washcoated monolithic catalysts under oxygen lean conditions. *RSC Adv.* **2015**, *5*, 102147–102156, doi:10.1039/c5ra13223a.

283. Tong, X.; Luo, T.; Meng, X.; Wu, H.; Li, J.; Liu, X.; Ji, X.; Wang, J.; Chen, C.; Zhan, Z. Shape-Dependent Activity of Ceria for Hydrogen Electro-Oxidation in Reduced-Temperature Solid Oxide Fuel Cells. *Small* **2015**, *11*, 5581–5588, doi:10.1002/smll.201501930.
284. Reddy, B.M.; Thrimurthulu, G.; Katta, L. Design of efficient $Ce_xM_{1-x}O_{2-\delta}$ (M = Zr, Hf, Tb and Pr) nanosized model solid solutions for CO oxidation. *Catal. Letters* **2011**, *141*, 572–581, doi:10.1007/s10562-010-0484-z.
285. Dosa, M.; Piumetti, M.; Bensaid, S.; Russo, N.; Fino, D. Novel Mn–Cu-Containing CeO_2 Nanopolyhedra for the Oxidation of CO and Diesel Soot (Part II): Effect of Oxygen Concentration on the Catalytic Activity. *Catal. Letters* **2019**, *149*, 107–118, doi:10.1007/s10562-018-2591-1.
286. Dziembaj, R.; Molenda, M.; Chmielarz, L.; Zaitz, M.M.; Piwowarska, Z.; Rafalska-ŁAsocha, A. Optimization of Cu doped ceria nanoparticles as catalysts for low-temperature methanol and ethylene total oxidation. *Catal. Today* **2011**, *169*, 112–117, doi:10.1016/j.cattod.2010.11.061.
287. Liotta, L.F.; Ousmane, M.; Di Carlo, G.; Pantaleo, G.; Deganello, G.; Marcì, G.; Retailleau, L.; Giroir-Fendler, A. Total oxidation of propene at low temperature over Co_3O_4-CeO_2 mixed oxides: Role of surface oxygen vacancies and bulk oxygen mobility in the catalytic activity. *Appl. Catal. A Gen.* **2008**, *347*, 81–88, doi:10.1016/j.apcata.2008.05.038.
288. Dole, H.A.E.; Baranova, E.A. Ethylene Oxidation in an Oxygen-Deficient Environment: Why Ceria is an Active Support? *ChemCatChem* **2016**, *8*, 1977–1986, doi:10.1002/cctc.201600142.
289. Lang, W.; Harold, M.P. Rate Inhibition and Enhancement on Ceria-Promoted Pd Monolith Catalysts: Oxidation of Acetylene, Ethylene, and Propylene and Their Mixtures. *Ind. Eng. Chem. Res.* **2019**, *58*, 6350–6363, doi:10.1021/acs.iecr.9b00978.
290. Di Sarli, V.; Di Benedetto, A. Combined effects of soot load and catalyst activity on the regeneration dynamics of catalytic diesel particulate filters. *AIChE J.* **2018**, *64*, 1714–1722, doi:10.1002/aic.16047.
291. Di Sarli, V.; Landi, G.; Lisi, L.; Di Benedetto, A. Ceria-coated diesel particulate filters for continuous regeneration. *AIChE J.* **2017**, *63*, 3442–3449, doi:10.1002/aic.15688.
292. Boger, T.; Rose, D.; Nicolin, P.; Gunasekaran, N.; Glasson, T. Oxidation of Soot (Printex® U) in Particulate Filters Operated on Gasoline Engines. *Emiss. Control Sci. Technol.* **2015**, *1*, 49–63, doi:10.1007/s40825-015-0011-1.
293. Kastrinaki, G.; Lorentzou, S.; Konstandopoulos, A.G. Soot Oxidation Kinetics of Different Ceria Nanoparticle Catalysts. *Emiss. Control Sci. Technol.* **2015**, *1*, 247–253, doi:10.1007/s40825-015-0021-z.
294. Neeft, J.P.A.; Nijhuis, T.X.; Smakman, E.; Makkee, M.; Moulijn, J.A. Kinetics of the oxidation of diesel soot. *Fuel* **1997**, *76*, 1129–1136, doi:10.1016/S0016-2361(97)00119-1.
295. Darcy, P.; Da Costa, P.; Mellottée, H.; Trichard, J.M.; Djéga-Mariadassou, G. Kinetics of catalyzed and non-catalyzed oxidation of soot from a diesel engine. *Catal. Today* **2007**, *119*, 252–256, doi:10.1016/j.cattod.2006.08.056.
296. Wang, H.; Jin, B.; Wang, H.; Ma, N.; Liu, W.; Weng, D.; Wu, X.; Liu, S. Study of Ag promoted Fe_2O_3@CeO_2 as superior soot oxidation catalysts: The role of Fe_2O_3 crystal plane and tandem oxygen delivery. *Appl. Catal. B Environ.* **2018**, *237*, 251–262, doi:10.1016/j.apcatb.2018.05.093.

297. Zhang, W.; Niu, X.; Chen, L.; Yuan, F.; Zhu, Y. Soot Combustion over Nanostructured Ceria with Different Morphologies. *Sci. Rep.* **2016**, *6*, 1–10, doi:10.1038/srep29062.
298. Umar, A.; Ibrahim, A.A.; Kumar, R.; Almas, T.; Sandal, P.; Al-Assiri, M.S.; Mahnashi, M.H.; AlFarhan, B.Z.; Baskoutas, S. Fern shaped La_2O_3 nanostructures as potential scaffold for efficient hydroquinone chemical sensing application. *Ceram. Int.* **2020**, *46*, 5141–5148, doi:10.1016/j.ceramint.2019.10.258.
299. Li, Y.; Liu, J.; He, D. Catalytic synthesis of glycerol carbonate from biomass-based glycerol and dimethyl carbonate over Li-La_2O_3 catalysts. *Appl. Catal. A Gen.* **2018**, *564*, 234–242, doi:10.1016/j.apcata.2018.07.032.
300. Huang, B.; Huang, C.; Chen, J.; Sun, X. Size-controlled synthesis and morphology evolution of Nd_2O_3 nano-powders using ionic liquid surfactant templates. *J. Alloys Compd.* **2017**, *712*, 164–171, doi:10.1016/j.jallcom.2017.04.009.
301. Lok, R.; Budak, E.; Yilmaz, E. Structural characterization and electrical properties of Nd_2O_3 by sol–gel method. *J. Mater. Sci. Mater. Electron.* **2020**, *31*, 3111–3118, doi:10.1007/s10854-020-02857-2.
302. Fernandez-garcia, S.; Jiang, L.; Tinoco, M.; Hungria, A.B.; Han, J.; Blanco, G.; Calvino, J.J.; Chen, X. Enhanced Hydroxyl Radical Scavenging Activity by Doping Lanthanum in Ceria Nanocubes. **2016**, doi:10.1021/acs.jpcc.5b09495.
303. Madhuri, C.; Venkataramana, K.; Nurhayati, A.; Reddy, C.V. Effect of La^{3+} and Pr^{3+} co-doping on structural, thermal and electrical properties of ceria ceramics as solid electrolytes for IT-SOFC applications. *Curr. Appl. Phys.* **2018**, *18*, 1134–1142, doi:10.1016/j.cap.2018.06.013.
304. Schmitt, R.; Nenning, A.; Kraynis, O.; Korobko, R.; Frenkel, A.I.; Lubomirsky, I.; Haile, S.M.; Rupp, J.L.M. A review of defect structure and chemistry in ceria and its solid solutions. *Chem. Soc. Rev.* **2020**, *49*, 554–592, doi:10.1039/c9cs00588a.
305. Boldish, S.I.; White, W.B. Vibrational spectra of crystals with the A-type rare earth oxide structure-I. La_2O_3 and Nd_2O_3. *Spectrochim. Acta Part A Mol. Spectrosc.* **1979**, *35*, 1235–1242, doi:10.1016/0584-8539(79)80204-4.
306. Ubaldini, A.; Carnasciali, M.M. Raman characterisation of powder of cubic RE_2O_3 (RE = Nd, Gd, Dy, Tm, and Lu), Sc_2O_3 and Y_2O_3. *J. Alloys Compd.* **2008**, *454*, 374–378, doi:10.1016/j.jallcom.2006.12.067.
307. Cui, J.; Hope, G.A. Raman and Fluorescence Spectroscopy of CeO_2, Er_2O_3, Nd_2O_3, Tm_2O_3, Yb_2O_3, La_2O_3, and Tb_4O_7. *J. Spectrosc.* **2015**, *2015*, 1–8, doi:10.1155/2015/940172.
308. Wei, Y.; Liu, J.; Zhao, Z.; Duan, A.; Jiang, G.; Xu, C.; Gao, J.; He, H.; Wang, X. Three-dimensionally ordered macroporous $Ce_{0.8}Zr_{0.2}O_2$-supported gold nanoparticles: Synthesis with controllable size and super-catalytic performance for soot oxidation. *Energy Environ. Sci.* **2011**, *4*, 2959–2970, doi:10.1039/c0ee00813c.
309. Yao, P.; He, J.; Jiang, X.; Jiao, Y.; Wang, J.; Chen, Y. Factors determining gasoline soot abatement over CeO_2–ZrO_2-MnO_x catalysts under low oxygen concentration condition. *J. Energy Inst.* **2020**, *93*, 774–783, doi:10.1016/j.joei.2019.05.005.
310. Fingerle, M.; Tengeler, S.; Calvet, W.; Mayer, T.; Jaegermann, W. Water Interaction with Sputter-Deposited Nickel Oxide on n-Si Photoanode: Cryo Photoelectron Spectroscopy on Adsorbed Water in the Frozen Electrolyte

Approach. *J. Electrochem. Soc.* **2018**, *165*, H3148–H3153, doi:10.1149/2.0191804jes.
311. Senanayake, S.D.; Stacchiola, D.; Evans, J.; Estrella, M.; Barrio, L.; Pérez, M.; Hrbek, J.; Rodriguez, J.A. Probing the reaction intermediates for the water – gas shift over inverse CeO_x/Au (1 1 1) catalysts. *J. Catal.* **2010**, *271*, 392–400, doi:10.1016/j.jcat.2010.02.024.
312. Barth, C.; Laffon, C.; Olbrich, R.; Ranguis, A.; Parent, P.; Reichling, M. A perfectly stoichiometric and flat CeO_2(111) surface on a bulk-like ceria film. *Sci. Rep.* **2016**, *6*, 2–7, doi:10.1038/srep21165.
313. Sakpal, T.; Lefferts, L. Structure-dependent activity of CeO_2 supported Ru catalysts for CO_2 methanation. *J. Catal.* **2018**, *367*, 171–180, doi:10.1016/j.jcat.2018.08.027.
314. Sunding, M.F.; Hadidi, K.; Diplas, S.; Løvvik, O.M.; Norby, T.E.; Gunnæs, A.E. XPS characterisation of in situ treated lanthanum oxide and hydroxide using tailored charge referencing and peak fitting procedures. *J. Electron Spectros. Relat. Phenomena* **2011**, *184*, 399–409, doi:10.1016/j.elspec.2011.04.002.
315. Yang, C.; Fan, H.; Qiu, S.; Xi, Y.; Fu, Y. Microstructure and dielectric properties of La_2O_3 films prepared by ion beam assistant electron-beam evaporation. *J. Non. Cryst. Solids* **2009**, *355*, 33–37, doi:10.1016/j.jnoncrysol.2008.09.029.
316. Uma, M.; Balaram, N.; Sekhar Reddy, P.R.; Janardhanam, V.; Rajagopal Reddy, V.; Yun, H.J.; Lee, S.N.; Choi, C.J. Structural, Chemical and Electrical Properties of Au/La_2O_3/n-GaN MIS Junction with a High-k Lanthanum Oxide Insulating Layer. *J. Electron. Mater.* **2019**, *48*, 4217–4225, doi:10.1007/s11664-019-07193-8.
317. Moulder, J.F.; Stickle, W.F.; Sobol, P.E.; Bomben, K.D. *Handbook of X-ray Photoelectron Spectroscopy*; Perkin-Elmer Corporation: Eden Prairie, Minnesota (USA), **1992**;
318. Gao, G.; Yang, L.; Dai, B.; Xia, F.; Yang, Z.; Guo, S.; Wang, P.; Geng, F.; Han, J.; Zhu, J. Investigation of the effect of annealing temperature on optical properties of lanthanum-oxide thin films prepared by sol-gel method. *Surf. Coatings Technol.* **2019**, *365*, 164–172, doi:10.1016/j.surfcoat.2018.07.001.
319. Talik, E.; Kruczek, M.; Sakowska, H.; Ujma, Z.; Gała, M.; Neumann, M. XPS characterisation of neodymium gallate wafers. *J. Alloys Compd.* **2004**, *377*, 259–267, doi:10.1016/j.jallcom.2004.01.037.
320. Ying, M.; Hou, J.; Xie, W.; Xu, Y.; Shen, S.; Pan, H.; Du, M. Synthesis, semiconductor characteristics and gas-sensing selectivity for cerium-doped neodymium vanadate nanorods. *Sensors Actuators, B Chem.* **2018**, *260*, 125–133, doi:10.1016/j.snb.2017.12.192.
321. Grabchenko, M. V.; Mamontov, G. V.; Zaikovskii, V.I.; La Parola, V.; Liotta, L.F.; Vodyankina, O. V. The role of metal–support interaction in Ag/CeO_2 catalysts for CO and soot oxidation. *Appl. Catal. B Environ.* **2020**, *260*, 118148, doi:10.1016/j.apcatb.2019.118148.
322. Hernández, W.Y.; Laguna, O.H.; Centeno, M.A.; Odriozola, J.A. Structural and catalytic properties of lanthanide (La, Eu, Gd) doped ceria. *J. Solid State Chem.* **2011**, *184*, 3014–3020, doi:10.1016/j.jssc.2011.09.018.
323. Gaillard, F. Characterisation of Pt/ceria catalysts by one-pass TPD analysis. **2004**, *95*, 23–29.
324. Zhang, C.; Huang, H.; Li, G.; Wang, L.; Song, L.; Li, X. Zeolitic acidity as

a promoter for the catalytic oxidation of toluene over MnO_x/HZSM-5 catalysts. *Catal. Today* **2019**, *327*, 374–381, doi:10.1016/j.cattod.2018.03.019.
325. Piumetti, M.; Bonelli, B.; Massiani, P.; Dzwigaj, S.; Rossetti, I.; Casale, S.; Gaberova, L.; Armandi, M.; Garrone, E. Effect of vanadium dispersion and support properties on the catalytic activity of V-SBA-15 and V-MCF mesoporous materials prepared by direct synthesis. *Catal. Today* **2011**, *176*, 458–464, doi:10.1016/j.cattod.2010.10.066.
326. Azambre, B.; Zenboury, L.; Weber, J. V.; Burg, P. Surface characterization of acidic ceria-zirconia prepared by direct sulfation. *Appl. Surf. Sci.* **2010**, *256*, 4570–4581, doi:10.1016/j.apsusc.2010.02.049.
327. Wu, Z.; Mann, A.K.P.; Li, M.; Overbury, S.H. Spectroscopic investigation of surface dependent acid base property of ceria nanoshapes. *J. Phys. Chem. C* **2015**, *119*, 7340–7350, doi:10.1021/acs.jpcc.5b00859.
328. Hosseinpour, N.; Khodadadi, A.A.; Mortazavi, Y.; Bazyari, A. Nano-ceria-zirconia promoter effects on enhanced coke combustion and oxidation of CO formed in regeneration of silica-alumina coked during cracking of triisopropylbenzene. *Appl. Catal. A Gen.* **2009**, *353*, 271–281, doi:10.1016/j.apcata.2008.10.051.
329. Nair, R.R.; Arulraj, J.; Sunaja Devi, K.R. Ceria doped titania nano particles: Synthesis and photocatalytic activity. *Mater. Today Proc.* **2016**, *3*, 1643–1649, doi:10.1016/j.matpr.2016.04.054.
330. Sudarsanam, P.; Mallesham, B.; Reddy, P.S.; Großmann, D.; Grünert, W.; Reddy, B.M. Nano-Au/CeO_2 catalysts for CO oxidation: Influence of dopants (Fe, La and Zr) on the physicochemical properties and catalytic activity. *Appl. Catal. B Environ.* **2014**, *144*, 900–908, doi:10.1016/j.apcatb.2013.08.035.
331. Katta, L.; Sudarsanam, P.; Mallesham, B.; Reddy, B.M. Preparation of silica supported ceria-lanthana solid solutions useful for synthesis of 4-methylpent-1-ene and dehydroacetic acid. *Catal. Sci. Technol.* **2012**, *2*, 995–1004, doi:10.1039/c2cy00551d.
332. Binet, C.; Daturi, M.; Lavalley, J.C. IR study of polycrystalline ceria properties in oxidised and reduced states. *Catal. Today* **1999**, *50*, 207–225, doi:10.1016/S0920-5861(98)00504-5.
333. Kim, K.; Yoo, J. Do; Lee, S.; Bae, M.; Bae, J.; Jung, W.C.; Han, J.W. A Simple Descriptor to Rapidly Screen CO Oxidation Activity on Rare-Earth Metal-Doped CeO_2: From Experiment to First-Principles. *ACS Appl. Mater. Interfaces* **2017**, *9*, 15449–15458, doi:10.1021/acsami.7b01844.
334. Liu, S.; Wu, X.; Weng, D.; Li, M.; Ran, R. Roles of acid sites on Pt/H-ZSM5 catalyst in catalytic oxidation of diesel soot. *ACS Catal.* **2015**, *5*, 909–919, doi:10.1021/cs5018369.
335. Konstandopoulos, A.G.; Kostoglou, M.; Lorentzou, S.; Vlachos, N. Aspects of multifunctional diesel particulate filters and their efficient simulation. *Catal. Today* **2012**, *188*, 2–13, doi:10.1016/j.cattod.2012.03.022.
336. Shang, Z.; Sun, M.; Chang, S.; Che, X.; Cao, X.; Wang, L.; Guo, Y.; Zhan, W.; Guo, Y.; Lu, G. Activity and stability of Co_3O_4-based catalysts for soot oxidation: The enhanced effect of Bi_2O_3 on activation and transfer of oxygen. *Appl. Catal. B Environ.* **2017**, *209*, 33–44, doi:10.1016/j.apcatb.2017.02.074.
337. Iojoiu, E.E.; Bassou, B.; Guilhaume, N.; Farrusseng, D.; Desmartin-

Chomel, A.; Lombaert, K.; Bianchi, D.; Mirodatos, C. High-throughput approach to the catalytic combustion of diesel soot. *Catal. Today* **2008**, *137*, 103–109, doi:10.1016/j.cattod.2008.02.016.
338. Hernández-Giménez, A.M.; Xavier, L.P.D.S.; Bueno-López, A. Improving ceria-zirconia soot combustion catalysts by neodymium doping. *Appl. Catal. A Gen.* **2013**, *462–463*, 100–106, doi:10.1016/j.apcata.2013.04.035.
339. Tran, Q.N.; Martinovic, F.; Ceretti, M.; Esposito, S.; Bonelli, B.; Paulus, W.; Di Renzo, F.; Deorsola, F.A.; Bensaid, S.; Pirone, R. Co-doped $LaAlO_3$ perovskite oxide for NO_x-assisted soot oxidation. *Appl. Catal. A Gen.* **2020**, *589*, doi:10.1016/j.apcata.2019.117304.
340. Martínez-Munuera, J.C.; Zoccoli, M.; Giménez-Mañogil, J.; García-García, A. Lattice oxygen activity in ceria-praseodymia mixed oxides for soot oxidation in catalysed Gasoline Particle Filters. *Appl. Catal. B Environ.* **2019**, *245*, 706–720, doi:10.1016/j.apcatb.2018.12.076.
341. Filtschew, A.; Hess, C. Unravelling the mechanism of NO and NO_2 storage in ceria: The role of defects and Ce-O surface sites. *Appl. Catal. B Environ.* **2018**, *237*, 1066–1081, doi:10.1016/j.apcatb.2018.06.058.